THEORETICAL AND EXPERIMENTAL STUDIES OF FEMTOSECOND STREAK AND PICOSECOND FRAMING IMAGE TUBES

Martin Ronald Baggs B.A.

A Thesis submitted for the degree of
Doctor of Philosophy of the University of
London and for the Diploma of
Membership of Imperial College

Optics Group
Blackett Laboratory
Imperial College of
Science and Technology
London SW7 2BZ.

November 1983

I DEDICATE
THIS THESIS
TO
MY PARENTS

ABSTRACT

A method of characterising the performance of an electron-optical image tube in terms of its modulation transfer function is described. This is shown to be more physically realistic than the approach based on the Gaussian approximation for the evaluation of the temporal resolution.

The modulation transfer function method was used, in conjunction with a suite of computer programs simulating the paths of photoelectrons through an image tube, in the development of a new subpicosecond streak tube, the Photochron IV. The temporal resolution of this tube was computed to be 0.4 ps, with a limiting value <200 fs when the photocathode is operated close to its cut-off wavelength. It was shown that the streak speed has an optimum value of 3×10^{10} cms^{-1}, above which the temporal resolution becomes degraded. Another design version, the Photochron IV-M, in which the physical size is reduced by 25%, was shown to have a predicted performance comparable to that of the larger tube.

An initial experimental version of the Photochron IV was constructed and incorporated into a streak camera. With the electric field at the cathode restricted to $\leq$ 23 kV cm^{-1}, the temporal resolution was demonstrated to be < 2 ps in the repetitive streak operation, and 0.8 ps in the single-shot mode.

A new framing image tube has been designed to enable the recording of two-dimensional images with exposure times $\sim$100 ps. Two independent deflection configurations have been studied, consistent with the same electron lens. Alternative techniques were considered to achieve multiple framing.

CONTENTS

Page

Chapter 1 THE ULTRAFAST ELECTRON-OPTICAL STREAK CAMERA - AN INTRODUCTION

Chapter 2 THE COMPUTER MODEL

Page

Chapter 5 THE EXPERIMENTAL PHOTOCHRON IV STREAK CAMERA

Chapter 6 THE PHOTOCHRON IV - M MINIATURISED STREAK TUBE

CHAPTER ONE

THE ULTRAFAST ELECTRON-OPTICAL STREAK CAMERA

AN INTRODUCTION

1.1 Introduction

The application of passive mode-locking techniques to continuous wave (cw) ring dye lasers has enabled pulses with durations ∿ 55fs to be produced both reliably and directly (1,2). Further shortening of the pulse width can be achieved by directing the pulse through an optical fiber to impose nonlinear frequency broadening, and then compensating for this by spectral compression with a dispersive delay line. Pulse compression from 90fs to 30fs has been reported using this method (3). The availability of such short pulses allows time resolved spectroscopy on a truly femtosecond time scale (4).

Measurement of hypershort, subpicosecond events has generally been by indirect methods relying upon nonlinear effects, such as two photon fluorescence (5), three photon fluorescence (6), second harmonic generation (5), third harmonic generation (7), etc. Autocorrelators (8) and cross-correlators (9) based on these techniques have been shown to have an excellent intrinsic time resolution capability (∿ 17fs). However, such nonlinear measurements deny the recording of pulse shape information and are insensitive to low intensity background detail.

Of the linear methods of picosecond measurement the simplest involves the use of a photodiode in conjunction with a fast oscilloscope. In practice the temporal resolution is limited by the response time of the oscilloscope, and for the fastest oscilloscope to date (a modified Tektronix 7104), this is $\sim$50ps. For cw mode-locked lasers, a sampling oscilloscope can be used. Commercial sampling heads have a resolution of $\lesssim$ 25ps (e.g. Tektronix S4). In this case it is the photodiode that limits the resolution (risetime $\lesssim$ 35ps - Spectra Physics Model 403B). Using a semiconductor switch (amorphous silicon), the capability of resolving pulses $\lesssim$ 40ps FWHM has been demonstrated (10).

The most widely used linear diagnostic instrument allowing pico/femtosecond resolution is the electron-optical streak camera. It has a superior sensitivity to the nonlinear technique, as evidenced by low intensity fluorescence studies (11), and its linearity of response provides an unambiguous analysis of the luminous event. The streak camera also has the added advantage of simultaneous recording of spatial (12) or spectral (13) information along its slit. A number of streak image tubes have been reported with picosecond resolution (14 - 18), but a subpicosecond response ($\sim$ 0.8ps) has only been achieved in cases where the tube was operated at wavelengths close to the cut-off of the photocathode sensitivity (19, 20).

Apart from the direct duration measurements of mode-locked laser pulses, there are clearly many applications for ultrafast streak cameras. These include laser produced plasma and laser fusion research (21), time resolved spectroscopic studies of molecular dynamics in liquids (4), and of optical excitations in solids (22), direct time-domain measurements of pulse propagation in optical fibers (12), investigations on semiconductor diode lasers (23), the temperature (24) and viscosity (11) dependence of excited state dye fluorescence lifetimes, the studies of biological samples (25) etc.

1.2 Principle of operation

The principle of operation of the streak camera is illustrated by figure 1.1. The light signal being studied is incident on a narrow ($\sim 20\ \mu m$) slit, and imaged via a lens onto the photocathode of the streak tube. Here it is converted into an electron pulse. Since the number of photoelectrons emitted is directly proportional to the incident optical intensity, a linear transformation is attained, and the temporal intensity information is faithfully included in the photoelectron pulse.

The electrons are accelerated and focussed by the electron-optics of the tube onto the phosphor screen where the signal is reconverted into an optical output for subsequent recording. In the streak mode of

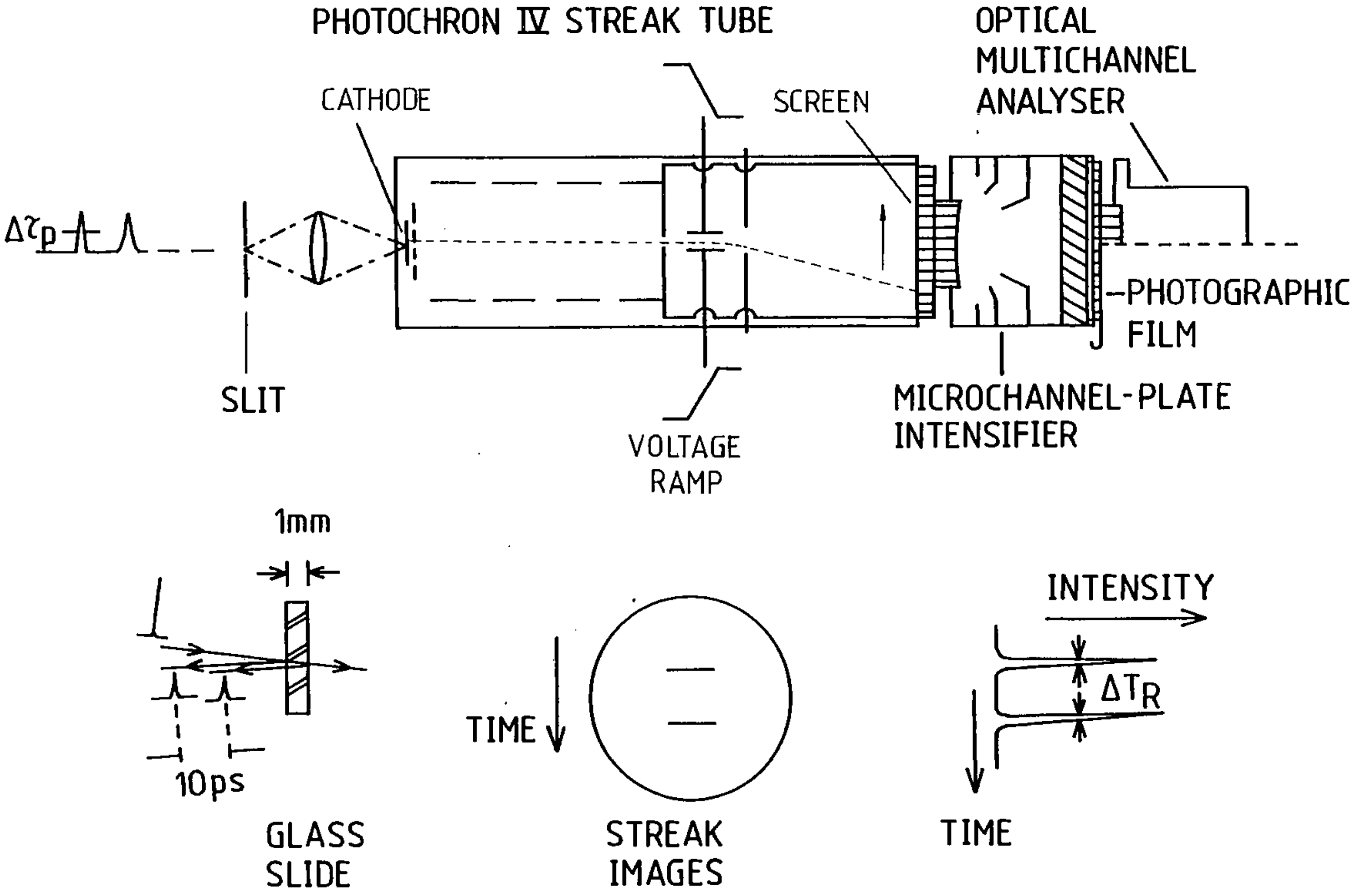

Fig. 1.1 Operating principle of the streak tube.

operation, a linearly time-dependent voltage ramp is applied to the deflector plates so that the slit image is swept across the screen.

Light pulses which are delayed in time will generate correspondingly retarded electron pulses at the photocathode. These will experience different parts of the voltage ramp and so are deflected to different points on the screen. The streak direction spatial dimension (referred to as the x direction throughout this thesis) thus contains the temporal profile of the input signal at the sacrificial expense of spatial information. Linearity of the time scale in the streak direction is guaranteed, as long as the voltage ramp is itself linear. As the photon/electron transformation at the photocathode is linear, examination of the recorded intensity as a function of position at the screen, provides a temporal intensity evolution of the light event.

1.3 Spatial resolution limitations

The image formed on the phosphor screen is limited in quality by the geometrical aberrations of the streak tube electron optics. Of the five first-order aberrations (26), spherical aberration, coma, astigmatism, curvature of the image field, and spatial distortion, the field curvature and astigmatism are the most serious in terms of spatial resolution impairment. By careful design of the electron optics, these aberrations can be minimised, providing optimum spatial resolution ($>$50lp/mm).

If the photoelectrons are proximity focussed onto the screen by the application of a very high extraction electric field (17), the spatial resolution obtained is extremely poor (∿ 4lp/mm), so it appears beneficial to include an electron-optical lens for focussing. The electron lenses generally used are rotationally symmetric and electrostatic (15, 16, 18, 19), although magnetic focussing has also been reported (27). A quadrupolar lens has been employed to independently control the focussing in the orthogonal spatial and temporal directions (28), but the temporal resolution of this streak tube has not been experimentally determined.

Under dynamic conditions, high intensity irradiation of the photocathode can lead to spatial resolution degradation (29). It has been suggested that this arises from a change in the potential across the surface of the cathode due to the high current density extracted (30). This perturbation modifies the equipotentials in the cathode-mesh region so that either a diverging or a converging microlens is produced close to the photocathode, depending on its type. To avoid such problems the cathode surface resistivity should be as low as possible (29), e.g. ∿10 Ω/□.

1.4 Temporal resolution limitations

The basic limitation on the instrumental temporal resolution is imposed by the energy spread of the electrons emitted by the photocathode. This depends on the particular photocathode, the illumination wavelength, the work function, the position and breadth of the electronic level bands, and other properties of the cathode such as the specific type of processing. Unlike conventional glass optics, this electronic chromatic aberration cannot be completely removed.

The distribution of axial velocities leads to a difference in transit times at the deflectors for electrons emitted at the same instant from the same point on the cathode. Consequently, they are deflected to different image positions on the phosphor. The magnitude, δx , of this slit image spread determines the dynamic spatial resolution in the streak direction when the slit size (which is narrow) is neglected. Knowing the streak velocity, v , produced at the screen, the temporal resolution can be obtained from

$$\tau = \delta x / v$$

If the voltage ramp, and hence the streak speed, is increased, the slit image is spread over a larger phosphor area degrading the dynamic spatial resolution. It has been found (ref. section 4.4) that for low voltage ramps the increase in streak velocity more than offsets this effect, but for very high streak speeds the decrease in spatial resolution becomes dominant. The temporal resolution is thus dependent on the writing speed at the phosphor and it should be possible to maximise it by carefully choosing the optimum streak speed (31). Although the temporal resolution is determined by the pre-deflection transit time dispersion and the applied voltage ramp, these are inter-dependent, and cannot be treated separately as in the Gaussian approximation (c.f. section 3.2).

To improve the temporal resolution it is necessary to reduce the time dispersion. Originally it was thought that it mainly built up close to the cathode (32). It was recognised that this could be overcome by the insertion of a high potential, planar mesh electrode in close proximity to the photocathode (33). This creates a high extraction electric field at the cathode, rapidly accelerating the emitted photoelectrons to high velocities. This technique was employed in the Photochron II (14) to provide a resolution <2ps, and finds widespread use in picosecond streak tubes (15, 17, 18).

Further improvement in the instrumental function cannot be achieved by simply increasing the extraction field, since then the transit time dispersion in the mesh-deflector region becomes dominant (34). In fact the temporal dispersion must be minimized over the whole focussing region by deliberate design of the electron optics in conjunction with the high extraction field (see section 4.1).

The optimum temporal resolution of a streak tube is obtained when it is illuminated by light whose wavelength is close to the photocathode long-wave sensitivity threshold. Under these conditions the spread in energies of the photoelectrons is low and so too is the time dispersion. It is thus important to choose an appropriate photocathode since its spectral response characteristic determines the working spectral range of the streak tube, and affects the temporal resolution for a specified wavelength.

The response time of the photocathode will impose a limit on the instrumental function. This is the time taken after illumination for the electrons to be emitted, and depends on the electron ionization and escape times. For cathodes of the S1 and S20 type, the response time should be very short $\sim 10^{-14}$ s (35, 36).

The temporal resolution of the streak image tube should not be limited by the spatial response of the phosphor screen, because this can be $>$ 100 lp/mm (37). Under dynamic operating conditions, the spatial resolution obtained in the streak direction at the screen (which transforms into temporal resolution) is likely to be much worse than this.

The fundamental limit of the electron-optical photochronographic resolution is set by the frequency of the light oscillations, which is $\sim 10^{15}$ Hz. From information theory, in order to time encode information on a carrier wave, the shortest possible signal modulation period must be approximately an order of magnitude greater than the carrier oscillation period. Thus the ultimate time resolution limit should be $\sim 10^{-14}$ s (38).

1.5 Dynamic slit curvature

With the application of a fast voltage ramp to the deflection plates, curvature of the slit image at the screen has been observed (39). This phenomenon is referred to as either dynamic slit curvature or temporal distortion, and is due to the difference in transit times to the deflectors for on and off - axis electrons. The off-axis electrons take a longer time to traverse the focussing region and arrive at the deflectors later than corresponding on-axis electrons; the further off-axis the emission point is, the greater will be this transit time dispersion. As a consequence, the off-axis electrons suffer a larger deflection, striking the phosphor further along the time axis and producing a curved image.

There are three main reasons for the difference in transit times:

(1) The physical distance traversed by the off-axis electrons is slightly longer than that for the on-axis case.

(2) In the initial part of the focussing region, the electrons emitted from the on-axis position intersect the equipotentials before the off-axis photoelectrons.

This is illustrated in figure 1.2 for a three cylinder lens, where the distance of the emission point at the cathode is greatly exaggerated for clarity. Because of this, the on-axis electrons are accelerated to a particular velocity before their off-axis counterparts

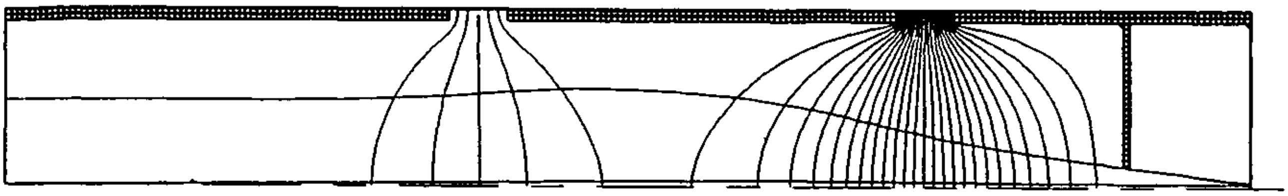

Fig. 1.2. On and off axis electron trajectories.

(3) The force exerted on the photoelectrons, due to the electric fields within the electron lens, can be resolved into a radial and an axial component. Where the equipotentials are normal to the axis, the radial component is zero and the acceleration produced is entirely axial. This is generally the case for electrons emitted on-axis at the cathode, so that their axial velocities are maximised. Where the equipotentials are inclined to the tube axis, a radial acceleration will be present at the expense of the axial component. In this case (for the off-axis electrons) the axial velocity will not be maximised.

As the time of flight along the streak tube is determined only by the axial velocity component, a transit time dispersion between on and off axis electrons will be introduced.

Both effects 2 and 3 above, become less important as the electrons approach the anode because of their convergence towards the electron-optical crossover, and since the equipotential spacing near the anode provides an almost planar equipotential region close to the axis.

The dynamic slit curvature can prove very detrimental to the streak camera instrumental function, particularly if it is used in combination with a linear readout device (c.f. section 1.9), such as an optical multichannel analyser (OMA). Under these conditions it is important that the light sensitive channels of the OMA are aligned along the slit image, which should be normal to the streak direction. If the image is curved, the effective temporal resolution becomes degraded, so it is necessary to mask off all but the central portion of the slit, resulting in a lower signal to noise ratio (40).

Two methods have been reported for reduction or elimination of the temporal distortion. Kinoshita et al (41) have designed and constructed a tube which incorporates a concave photocathode in place of the more usual flat variety. The temporal distortion is thus reduced by decreasing the path lengths for the off-axis electrons. This tube has been used in the streak mode with a fast streak speed to produce picosecond ($\sim$2 ps) resolution without showing noticeable image curvature. However, with this approach, the electric field is no longer uniform and constant in the cathode-mesh region.

In the second method, Niu (42) has adopted the more elegant approach of curving both the photocathode and the mesh electrode in his theoretical design, although this may prove to be problematical in construction. For both approaches, a curved photocathode will shift the electron-optical crossover towards the photocathode and this must be accounted for in the design of the tube.

1.6 Time resolution limited dynamic range

When a streak tube is used in the streak mode to record picosecond or femtosecond events, large photocurrents must be drawn from the cathode, and so significant current densities (~ 100 mA cm^{-2}) will exist within the tube (39). It has been found that for high intensity illumination, the temporal resolution deteriorates while the spatial resolution along the slit is maintained (43, 44, 39, 40). Hence the input intensity will limit the working range where undegraded temporal resolution can be expected. (At extremely high intensities the spatial resolution may also become degraded due to the photocathode effects discussed in section 1.3.)

The upper limit for the time resolution limited (TRL) dynamic range of the streak tube is conventionally taken to be the intensity at which the measured duration, T_M, becomes 20% larger than that of the incident pulse, T_p, after taking account of the camera response. The lower limit is set as the noise level of the system. Then the definition of the TRL dynamic range is taken to be the ratio of the upper and lower limits (39, 40, 45):

$$D.R. = \frac{I(\text{at } T_M = 1.2\ T_p)}{I_{\text{noise}}}$$

The TRL dynamic range is known to be dependent on the temporal duration of the incident pulse, so that the range of intensity over which the camera performance is acceptable becomes more restricted for shorter pulses. Extensive research on the dynamic range of streak tubes has been performed in a number of laboratories (40, 46 - 49), but this has proved a topic of controversy since measurements on similar tubes have shown large inconsistencies (40, 46).

Several theories have been postulated (39, 50, 51) to explain the intensity dependent temporal resolution deterioration, but without complete success. These were based on space charge effects either in or near the photocathode. More recently, an extensive theoretical analysis of space charge effects has been carried out (52) which provides good agreement with experimental observations. In this theory, the space charge introduces a temporal broadening which restricts the upper limit for the dynamic range.

The temporal broadening can be understood as follows. When the photocathode of the tube is illuminated by a picosecond light pulse through a narrow slit, the electron burst produced near the cathode will not have a large axial spread ($\sim$ several microns). As the electron pulse moves along the tube, the space charge within the bundle produces Coulombic repulsion of the electrons, so that the leading electrons are accelerated, while the trailing ones are decelerated. This causes the pulse to spread both spatially and temporally, so that electrons will arrive at the deflectors both earlier and later than the corresponding arrival time for the zero space charge case. This temporal broadening causes the temporal resolution to be impaired, and increases for the larger current densities associated with the higher input intensities required for shorter pulses.

From Niu's results (52) it is clear that the temporal broadening accumulates over the whole electron path from cathode to deflectors, in agreement with earlier calculations (49), and not just close to the cathode as previously suggested (51). However, the broadening is particularly large where the electrons have low velocities for long periods. For Photochron I,II streak cameras this occurs in the mesh-cone region, and space charge effects at the electron-optical crossover have negligible effect on the broadening, as observed experimentally (46, 47, 49).

The temporal broadening of the slit image has been found to be symmetrical, on either side of the result obtained in the absence of space charge, and this is consistent with experimental results (53), unlike an earlier theory (50). It was deduced that variations of the slit width had little effect on the pulse broadening, in agreement with experimental evidence (48, 49). This theory also substantiates the fact that the spatial resolution can be maintained in the slit direction for current densities at which the temporal resolution is seriously degraded (41, 42).

The low limit of the dynamic range is determined by the noise level, and it is not affected by the particular type of mesh used near the cathode (45). This will depend on such parameters as specific type of photocathode processing and electrode surface conditions (54). It is particularly important to minimize the surface contamination by the alkali metal atoms during activation since otherwise increased secondary electron emission is likely. Remotely, rather than in-situ, processed photocathodes should be preferred where possible.

1.7 Single-shot operation

When the ultrafast streak camera is used in the single-shot mode of streak operation, a single fast linear voltage ramp is applied to the deflectors producing a single streaked image at the phosphor. There are several ways of deriving such a ramp, and these will be considered below. To ensure that the temporal resolution is not degraded, and so to obtain a high TRL dynamic range, it is necessary to limit the current density in the tube by reducing the input pulse intensity. Image intensification is then required to enhance the output to a sufficiently recordable level. A brief survey of the types of intensifier used, is presented in section 1.7.2.

1.7.1 Deflection voltage ramp generation

For picosecond and subpicosecond temporal resolution, the writing speed of the streak tube must be high. Consequently the time interval displayed on the phosphor might only be ∿ 250ps, and so the synchronization between the input light pulse and the deflection voltage ramp must be extremely good. Any lack of synchronism (jitter) will cause shot-to-shot variations in the position of the streaked images. Jitter becomes a serious problem at very fast streak speeds since then the image may disappear off screen.

A number of different ramp generators have been used to provide the deflection voltage waveforms for picosecond streak cameras. These include the laser triggered spark gap (39, 44, 55), avalanche transistor stacks (15, 17), Krytron valve circuits (55) and hybrid avalanche transistor -Krytron circuits (40). Of these, the laser triggered spark gap has an intolerable jitter ∿ 1ns, and is seldom used now. The conventional electronic circuits using avalanche transistors and/or Krytron valves can provide extremely fast writing speeds up to 2×10^{10}cms^{-1} (39), but the jitter is still large ∿ 100ps. An alternative means for providing fast voltage ramps with very low jitter makes use of fast semiconductor switches, first suggested by Auston (56).

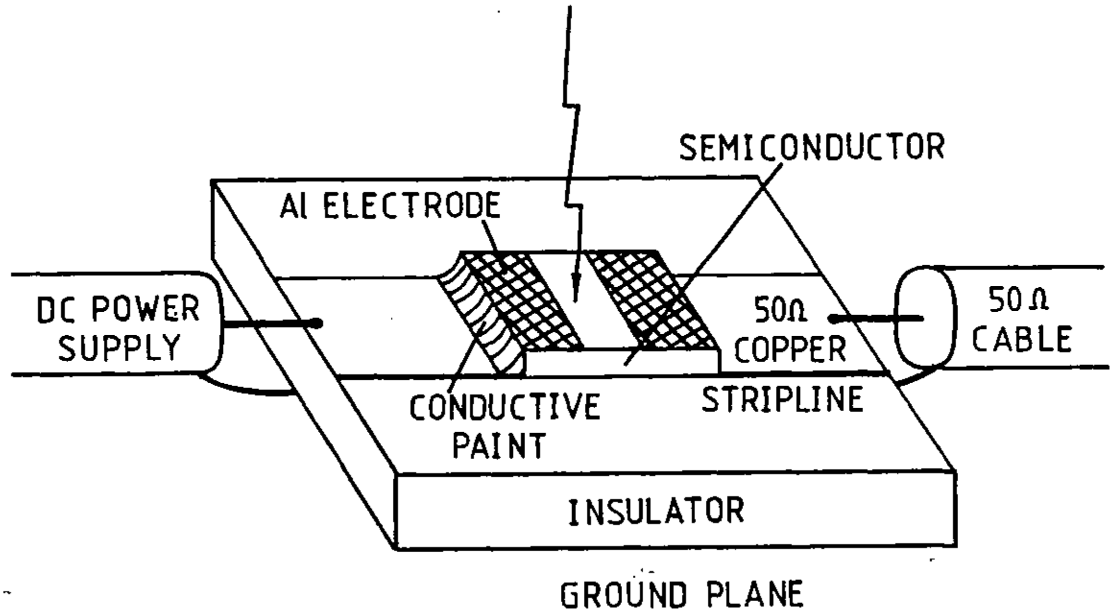

Fig. 1.3 Semiconductor switch structure.

The structure of a semiconductor switch device (also called a photoconductive element - PCE) is shown in figure 1.3 for the microstrip transmission line geometry. The semiconductor is mounted on an insulating substrate, interrupting a 50 Ω transmission line. Initially the resistance of the semiconductor is high (MΩ), and no current is transmitted across the gap in the line. When the semiconductor is photoilluminated at the gap, a high conduction layer is produced in the material by electron -hole pair generation. This reduces the resistance of the semiconductor, switching the device on, and allows current to be transmitted. Thus voltage is switched with a picosecond rise time (56).

Originally the semiconductor material used was nearly intrinsic (i.e. high purity) silicon (56), which has a dark resistance of ∿1MΩ , but this cannot handle d.c. bias voltages larger than 100V. At higher d.c. biases, thermal effects within the material reduce the dark resistance so that the leakage current increases non-linearly until the switch breaks down (57). To avoid this the crystal must be either cooled to liquid nitrogen temperature or the bias voltage should be pulsed. The latter approach was adopted by Margulis (57, 58) for a silicon switch used to generate a voltage ramp of 4.5kV. This provided a writing speed of 2×10^{10}cm s^{-1}, and a long time scale jitter of only ± 15ps. The residual jitter is due to shot-to-shot fluctuations in the amplitude of the voltage switched. This arises from instantaneous differences in the bias at the moment of switching caused by the pulsing of the bias and differences in switching efficiency due to laser pulse amplitude variations (57).

The problem of pulsing the voltage bias is overcome when chromium doped, semi-insulating GaAs is used as the photoconductive medium, since its resistivity ($>10^8\,\Omega$ cm) is very high (several orders of magnitude higher than that of silicon). This enables large d.c. bias voltages (> 2kV) to be withheld without thermal instabilities. Using such a technique, a picosecond streak camera has been operated with jitter as low as ± 2ps (59).

For GaAs the recombination time of the photo-induced carriers is short, ∿100ps, so that if the full deflection time across the screen is ∿ 500ps, the crystal will have become non-conducting before the voltage ramp has been fully switched. This occurs when the switch is included in a 50 Ω transmission line, and leads to poor sweep speeds. To prevent this, the impedance of the deflection arrangement must be increased to ∿1M Ω, since efficient switching prevails while the resistance of the GaAs is less than the load impedance. The current will then flow for a much longer time until the GaAs resistance greatly exceeds that of the load (60). Such a geometry has been used in the single shot experiments to test the Photochron IV streak camera, and will be described in chapter 5.

Semiconductor switch devices have proved a reliable means of producing fast writing speeds for streak cameras with exceptionally low jitter. They are, however, restricted to high power laser applications, since low jitter is only achieved if the switch is saturated every shot by the activating pulse with an energy of 20 - 100 μJ (58, 59).

1.7.2. Image intensifiers

There are generally three main types of intensifier which have been used in conjunction with a streak image tube: the magnetically focussed cascade (15, 39, 40, 53, 55), the electrostatically focussed cascade (55, 61) and the microchannel plate (MCP) intensifier (40, 49, 53, 61).

The magnetically focussed cascade intensifier (e.g. EMI 9693) has been extensively used, particularly in the formative years of picosecond electron-optical chronography. It shows good image uniformity, with spatial resolution ∿40lp/mm, and very low distortion. However, it requires a high operating potential (∿ 35kV) and a large current (∿ 12A) for the solenoid, necessitating additional cooling. To avoid disrupting the electron trajectories within the streak tube through interaction with the large magnetic field, the intensifier must be spatially separated from the phosphor of the streak tube, eliminating fiber optic coupling. The bulky size of this type of intensifier, combined with its requirements on cooling and large power supplies, and the use of lens coupling, makes it inconvenient to use.

The electrostatically focussed cascade intensifier (e.g. Mullard XX 1603) has a spatial resolution ∿ 30lp/mm but suffers from severe image distortion (61). It requires a high voltage (∿ 45kV) across the end plates and so can only be fiber-optically coupled at one end. This type of intensifier is rarely used with streak tubes.

The third type of intensifier, the MCP (e.g. Mullard XX 1332), is becoming increasingly popular for streak camera applications. It is much more compact than the previous two types, and can provide spatial resolution ∿ 40lp/mm. Since it only needs a voltage of about 10kV to operate, it may be fiber-optically coupled at both ends. This is a distinct advantage because, although the detection efficiency for the MCP intensifier is less than that for a cascade intensifier by a factor of 4 (62), the increased coupling efficiency of the fiber optics results in an overall system gain for the MCP which is an order of magnitude larger than for the cascade type (61).

The spatial resolution of the MCP intensifier depends on the channel diameters, which can be <15 μm (63, 64). The open area of the MCP also influences the image quality since primary electrons which strike the front face of the channel plate and are lost, may cause secondary electron emission. These secondaries may be drawn into adjacent channels, contributing to the signal, and thus deteriorating the resolution. Current manufacturing technology can provide open area ratios ∿ 60% (62).

The gain of the MCP is dependent on the potential applied across the ends of the channels, and the ratio of the length to diameter of each channel. By adjusting the applied voltage the gain can be changed without altering the focussing properties of the MCP. The MCP can also be easily gated by modulation of the applied potential, and this allows the use of film as the recording medium, if necessary, in direct contact with the output phosphor without fogging (40).

A major disadvantage of the MCP intensifier is the saturation of the channels (62). When a fast, primary electron signal enters the MCP, the secondary electrons may be stripped from the channel walls faster than they can be replenished by the charging current. This produces an accumulation of positive charge in the channels, and can reduce the gain available for later primary electron signals, if they arrive before channel recovery. This has been found to limit the linear dynamic range at high gain levels because of a reduction in the linearity of the system (40).

As the mechanism of multiplication is independent of the initial process producing the first slow electron in the channel entrance, the MCP can be employed to amplify any spatial distribution of electrons (62). Consequently they have been included directly within the streak tube to provide a compact camera system (63, 64). This has proved particularly suitable for use in the synchroscan mode (see next section), but under single-shot conditions the performance has been limited by MCP gain saturation (64).

1.8 Synchroscan operation

To exploit the repetitive nature of the short pulses obtained from cw mode-locked dye lasers (1 - 3), an alternative method of operation of the streak camera has been developed (65). In this synchroscan mode, the single fast linear ramp is replaced by a repetitive linear driving voltage waveform. In practice this is very difficult to generate, but it is known that the central T/6 portion of one period of a sinusoid, is linear to within 5% (66). Thus a high frequency (e.g. 160MHz) sinusoidally varying voltage waveform is supplied to the deflectors, and only the central part is used for image recording. The frequency of the sinewave is chosen to be identical to that of the repetitive photoluminescent event, or a higher harmonic (see figure 1.4). Then if the input light is accurately synchronized to the linear part of the wave applied to the deflectors, a large

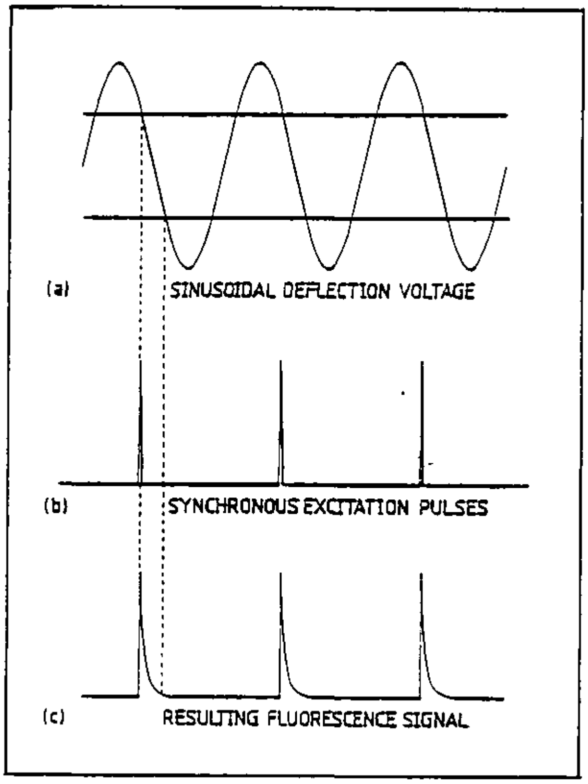

Fig. 1.4 Principle of synchroscan operation.

number of streaked images will be superimposed at the phosphor screen (66). The streak speed and the time window produced at the screen is dependent only on the frequency and amplitude of the driving sinusoidal wave (65).

There are several advantages inherent in this synchronously operating technique:

1. The method allows "real time" pulse monitoring.
2. The accumulation of a large number of streaks eliminates the need for additional image intensification, since the time-resolved output has sufficient intensity for direct recording.
3. The integration of information provides a high signal-to-noise ratio enabling the camera to have

very high sensitivity. Indeed this has been demonstrated in dye fluorescence lifetime measurements (11) where a long lifetime, weak component was discovered, which would have been swamped by background noise in single-shot experiments.

4. The low values of photocurrent required for each individual streak prevent any serious space charge effects within the tube. This ensures that intensity dependent loss of time resolution and TRL dynamic range do not occur. In fact, the system's linear dynamic range may become limited by the readout device employed (66).

The ramp generator should have subpicosecond jitter and good long-term stability so that the streak images do not drift off screen. The usual method for producing a sinewave is to use a tunnel diode-oscillator (64 - 67). A fraction of each laser pulse is directed onto a fast photodiode providing an electrical pulse ∿200 mV. This is then used to trigger a tunnel diode which is biased for monostable operation, supplying a sinewave output at the laser cavity frequency. This is generally frequency doubled and amplified to powers ∿20W (67) before being supplied to the deflection plates. Streak speeds up to 6×10^9 cm s^{-1} have been produced by this method (64).

One disadvantage of the synchroscan streak camera is that its temporal resolution is usually limited by the jitter of the system. This jitter primarily arises because of amplitude fluctuations and pulse dropout in the laser output (66). Since the tunnel diode is set to trigger at a predetermined voltage level, a laser pulse of given intensity illuminating the photodiode will cause the tunnel diode to trigger at an earlier time than would a pulse of lower intensity (see figure 1.5).

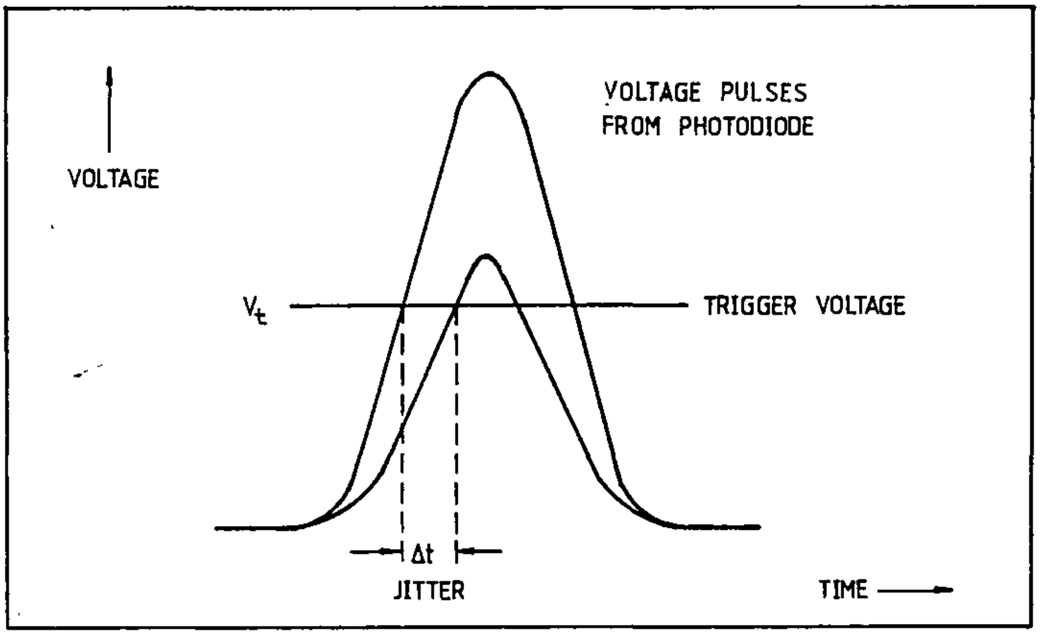

Fig. 1.5 Origin of jitter due to laser pulse amplitude fluctuations.

This jitter can be reduced to minimal levels for certain cavity configurations if alignment is optimised (64, 68). If pulse dropout occurs, the laser pulse generation may stop for a very short period before recommencing at a later, unrelated time. This will lead to a jitter which may be ∿1 - 5ps if the effect is serious.

The feasibility of the synchroscan operation was first demonstrated by Hadland et al in 1974 (69), when 10 pulses from the pulse train of a Nd:YAG laser were superposed at the phosphor screen. This technique has since been extended for use with both synchronously and passively mode-locked cw dye lasers (66, 67). Recently a temporal resolution of 1.2ps was demonstrated for the Photochron II A synchroscan camera (63), and this is the current state-of-the-art. It should be pointed out that when the synchroscan streak camera is used with a synchronously pumped dye laser system, the temporal resolution becomes worse than this by approximately an order of magnitude (67); the best resolution measured for this case was 7ps (70). The reason for this poor performance is probably due to the inherent jitter of the dye laser system arising from the synchronization problems with the pumping pulses.

Although the temporal resolution of a streak camera used under synchroscan conditions is likely to be worse than that obtained from single-shot experiments (c.f. results for the Photochron IV in chapter 5) due to jitter, it has the practical advantage of being much easier to operate, especially since amplification of the laser pulses is not necessary (see chapter 5). However, it should be stressed that for good temporal resolution, the streak camera should be used in conjunction with a highly stable source of light pulses, such as a passively mode-locked cw ring dye laser.

1.9 Image readout devices

Until the late 1970s the most commonly used medium for recording the streaked images was fast photographic film (14, 15, 32, 44). However, film suffers from a number of problems. It needs to be developed, and then scanned by a microdensitometer to provide a density versus position graph, so real-time analysis is impossible. As it shows a nonlinear response to changing light intensity, each film must be individually calibrated, and the microdensitometer results corrected, before any quantitative measurements can be obtained. Up to light intensities at which the space charge effects within the streak tube become important, the film is the only nonlinear element in the camera system, and, as such, will impose a limit on the linear dynamic range (40).

Photographic film is increasingly becoming replaced by electronic readout systems providing quantitative, automatic, and nearly real-time monitoring of the streak camera output. These include a solid-state reticon array of photodiodes coupled to an oscilloscope (71, 72), an SEC vidicon interfaced to a computer (71), an image isocon TV tube combined with a microprocessor display unit (72), and a silicon intensified target (SIT) vidicon camera connected to either a one- (40, 73) or two- (74) dimensional optical multichannel analyser (OMA). Provided that the target is scanned a sufficient number of times (e.g. 10 - 20), the transfer characteristics for the readout system will be linear (40, 73).

Although these electronic readout systems greatly facilitate the ease of use of the streak camera, their limiting spatial resolution is usually low (e.g. 10 lp/mm ref. 70, 25 lp/mm ref. 73). This may impose a limit to the temporal resolution for femtosecond cameras. Also, if the streak images suffer appreciable image curvature, due to temporal distortion (c.f. section 1.5), it becomes necessary to reduce the spatial extent of the slit to retain optimum resolution.

1.10 Conclusions

The aims and limitations of the ultrafast streak camera have been briefly reviewed. There are a wide range of applications for such a diagnostic tool and it is likely that with an improved camera instrumental resolution, these will increase.

The temporal response is mainly limited by the time dispersion of the electrons up to the deflectors, due to their initial energy spread at the cathode, although the streak speed also influences the resolution. These two factors are mutually dependent and cannot be treated separately; this will be discussed in more detail in chapters 3 and 4.

Under dynamic conditions, the camera performance suffers from two principal restraints. Temporal distortion causes the image to become curved for the fast writing speeds associated with optimum temporal resolution and space charge effects within the streak tube deteriorate the temporal resolution if the photocathode illumination is sufficiently intense. The time resolution limited dynamic range defines the operating range of intensities over which the camera temporal response is undegraded. In practice, to maximise the TRL dynamic range and avoid space charge effects, the input light intensity is attenuated and the image on the phosphor is enhanced by image intensification, usually with a fiber-optically coupled MCP intensifier.

The streak camera is usually used in either the single-shot or the synchroscan mode of operation. In the former, a single fast linear voltage ramp is fed to the deflectors, resulting in a single streak image. If a suitable high power laser is available, the ramp is best derived using a semiconductor switch arrangement, since then jitter is low and shot-to-shot reproducibility is good. For synchroscan, a fast sinewave voltage is generated, usually with a photodiode/tunnel diode-oscillator configuration, and this replaces the single ramp. Superposition of a large number of streaked images can result if the frequency of the driving voltage is carefully selected to be an integer multiple of the illuminating pulse frequency, and so image intensification is not required. It is a very much simpler experimental technique than the single-shot case, but its temporal resolution is generally inferior because of the more serious jitter problem.

CHAPTER TWO

THE COMPUTER MODEL

2.1 Introduction

In the design of electrostatically focussed, electron optical imaging systems, a knowledge of the potential distribution of the lens is needed to evaluate the imaging characteristics of the system. Before the advent of fast, digital, electronic computers, the potential distribution was found by making use of analogue methods such as the electrolytic plotting tank (75) or the resistor network (76). When the computer became generally available in the early 1960s, it enabled standard numerical techniques to be applied to electron-optical systems to calculate potential fields and electron trajectories (77). With the extensive development of computer hardware during the last two decades, these techniques have become more widely used in general electron-optical design (78-80), and, more specifically, in the design of fast streak cameras (28, 81, 82). In particular, computer software has been developed in the Laser Group, Imperial College to exploit these numerical methods (83).

2.2. Numerical solution of Laplace's equation

2.2.1 Initialisation of the data

The program suite is restricted to dealing with electrostatically focussed systems which can be mapped onto a two-dimensional grid, so that the field region has a planar representation. Thus only systems which are rotationally symmetric (e.g. the focussing section of an image tube), or which have two-dimensional symmetry (e.g. the deflection region of a streak image tube) can be modelled; those which are explicitly three-dimensional are excluded.

To set up an electron-optical system as data for manipulation by the programs, a uniform, "square mesh", rectangular grid is superimposed onto the cross-section of the region. (If the system is rotationally symmetric its cross-section will be a meridion plane and only the upper half need be considered.) The electrode structure can then be simulated by supplying the computer with the corresponding grid points and their voltages. The boundary grid point potentials must also be given so that the region is completely closed, as required for a numerical solution of the Laplace equation. This is accomplished by extending existing electrodes, and by allowing the potential at non-electrode boundary points to assume a linear or logarithmic variation between electrodes. Generally, these boundary approximations are not critical and will not significantly influence the potential distribution in the region of interest, if the boundary is chosen to be at a sufficient distance.

All points on the grid other than the fixed electrode or boundary points are given an arbitrary potential and are referred to as "free points". It is the potentials of these free points which are recalculated during the numerical solution of Laplace's equation. To discriminate between the free points and the fixed points, the first bit of the 60 bit computer word used to store the potential at a particular grid point, is masked with either a 1 or a 0 for the two respective cases. (This does not affect the value of the potential.)

2.2.2. The finite difference method

Once a data region has been encoded, all the free points must be made to satisfy Laplace's equation. For an axially symmetric region this is given in cylindrical co-ordinates by

$$\frac{\partial^2 V}{\partial r^2} + \frac{1}{r}\frac{\partial V}{\partial r} + \frac{\partial^2 V}{\partial z^2} = 0 \qquad \text{Eq. 2.1}$$

where V(r,z) is the potential at the point (r,z), r and z representing the radial and axial components respectively; in a planar system it becomes

$$\frac{\partial^2 V}{\partial x^2} + \frac{\partial^2 V}{\partial y^2} = 0 \qquad \text{Eq. 2.2}$$

in the normal cartesian co-ordinate system. The solution of either form of the Laplace equation is performed numerically by using the finite difference method (84). This requires the transformation from the partial differential equation representation into a set of difference equations.

Consider a general free point P_o, with co-ordinates (r_o, z_o), which is on the square mesh grid of a rotationally symmetric region. The four neighbouring points $P_1, \ldots, P_4$ are all separated from it by a distance h, where h is the

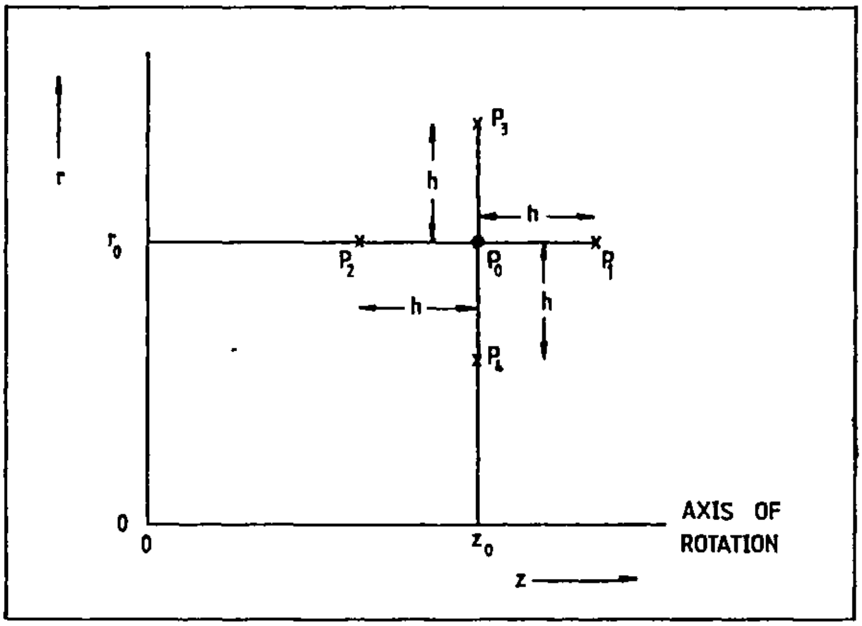

Fig. 2.1. Off-axis free point.

unit length of the square mesh (figure 2.1). By making a Taylor series expansion about the point P_o, the potential V(r,z) is given by

$$V(r,z) = \sum_{i=o}^{\infty} \sum_{j=o}^{\infty} \frac{V_o^{(i,j)}}{i!\ j!} (r-r_o)^i (z-z_o)^j \quad \text{Eq. 2.3}$$

where $$V_o^{(i,j)} = \left(\frac{\partial^{i+j} V}{\partial r^i \ \partial z^j} \right)_o \quad \text{Eq. 2.4}$$

Substituting the co-ordinates of P_1, $(r_o,\ z_o + h)$, into equation 2.3, its potential, V_1, can be related to the potential V_o at point P_o and its derivatives:

$$V_1 = V_o + \left(\frac{\partial V}{\partial z} \right)_o h + \frac{1}{2} \left(\frac{\partial^2 V}{\partial z^2} \right)_o h^2 + \ldots \quad \text{Eq. 2.5}$$

Similar equations can be derived for the potentials V_2, V_3, V_4. If the scale unit h is sufficiently small, terms of third order and higher will be negligible and the Taylor series of equation 2.3 can truncated after $i + j = 2$. Now the potentials $V_1, \ldots, V_4$ must all satisfy Laplace's equation, and hence combining equation 2.5, and its associated equations, with equation 2.1, the following five point difference equation can be derived (84):

$$V_o = \frac{1}{4}(V_1 + V_2 + V_3 + V_4) + \frac{h}{8r_o}(V_3 - V_4) \qquad \text{Eq. 2.6}$$

This expression is not valid for points lying on the axis where $r_o = 0$. If this is the case for the point P_o, then the surrounding six points, shown in figure 2.2, must be considered. By symmetry $V_3 = V_4 = V_5 = V_6$, and, proceeding as above, the axial difference equation can be derived:

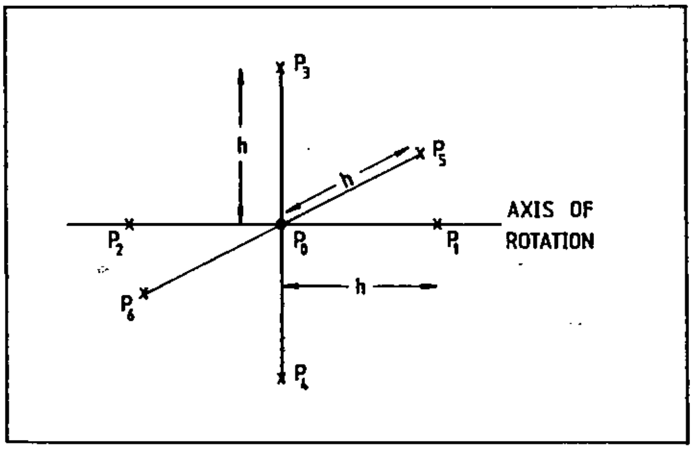

Fig. 2.2 Free point on-axis.

$$V_o = \frac{1}{6}(V_1 + V_2 + 4V_3) \qquad \text{Eq. 2.7}$$

Similarly, if the region is not rotationally symmetric then a Taylor series expansion of the potential, combined with equation 2.2 leads to the difference equation

$$V_o = \frac{1}{4}(V_1 + V_2 + V_3 + V_4) \qquad \text{Eq. 2.8}$$

Equations 2.6 and 2.7 (or 2.8) relate the potential of a free point in the data region to the potentials of its neighbouring four points. For every free point there will be a corresponding five point difference equation, and so a region containing N free points will generate a series of N linear equations with N unknowns. Laplace's equation has thus been approximated by a set of linear difference equations which can be solved by the iterative method described in the next section.

The error introduced by the truncation of the Taylor series expansion after $i + j = 2$ has been shown by Weber (84) to be of the order of h^4. However, all the free point potentials have this truncation error, and, for large regions, these errors all have the same sign. The total error for the system will then be of the order of h^2. Generally h is set to 1mm giving an error of $\sim 10^{-6}$.

2.2.3 Iterative solution of the finite difference equations

The potentials of the free points have initially been given arbitrary values, which, in general, do not satisfy the system of difference equations representing the Laplace equation. To solve this set of equations, the potential of the first free point is re-calculated from the values of its surrounding points using the relevant equation (2.6, 2.7 or 2.8). This is repeated for every free point in the region until all these potentials have been adjusted; this represents one iteration. After one iteration, however, the potential at the first free point will no longer satisfy its difference equation because the potentials of its neighbouring points have been displaced. This is true for all the points, and so further iterations must be effected. As the number of iterations increases, the potential at any point converges towards the value it would achieve after an infinite number of iterations (which would satisfy the difference equations exactly). The iterative procedure is stopped when the potential distribution on the grid satisfies the Laplace equation to within a preset accuracy. This final set of potentials will be determined solely by the electrode structure and boundary points, and is independent of the initial potential distribution.

In the computer program, as the potential of a point is re-evaluated, its old value is immediately replaced by the new value. This method is called successive displacement (84) and requires the storage of only one set of potentials. However, it is important to consider the order in which the grid points are scanned during each iteration, because at any instant during an iteration, some points will have had their potentials re-calculated, while the rest have potentials obtained in the previous iteration. In accordance with Young (85) the set of difference equations must have property A, i.e. the grid points must be classified into a number of groups such that for any point in one group, the potential can be calculated using only points in either the previous or following group. A "chess board" classification is adopted dividing the grid points into two groups (84). Each iteration is then subdivided into two, with first the evaluation of the potentials of one group of points, using only potentials from the second group which have been obtained in the previous "half-iteration", and vice versa. This order of calculation is consistent with property A.

The convergence of the successive displacement method towards the final solution is rather slow. This process can be accelerated by the application of over-relaxation, in which, instead of replacing the potential during an iteration by that just calculated from equation 2.6, a new value, obtained by extrapolation in the direction of change of potential, is substituted (84). Consider a point P, whose potential at the start of the (K + 1) iteration is given by $V_p(K)$. Its potential will be recalculated in this iteration to be $V_p(K + 1)$, but the value stored is given by $V_p'(K + 1)$, where

$$V_p'(K + 1) = V_p(K) + w \left[V_p(K + 1) - V_p(K) \right] \qquad \text{Eq. 2.9}$$

Here, w is called the relaxation factor and over-relaxation corresponds to the case when $w > 1$. (The use of over-relaxation with successive displacement is termed successive over-relaxation).

If the relaxation factor lies in the range $1 < w < 2$, the speed of convergence of the iterative procedure can be improved, but it is important to choose the value of w carefully, because if w is too large, the extrapolated potential will overshoot the final value leading to a low rate of convergence, whilst if w is too small the convergence is not accelerated sufficiently. An optimum value exists for w for which the rate of convergence is maximised but this is usually difficult to determine as it is dependent upon the electrode configuration. In the program, the method described by Carré (86) is used to evaluate the over-relaxation factor, and this is optimised during the iteration process by considering the rate of convergence of the potentials. The iterative procedure is repeated until the largest of the errors $|V_p'(K + 1) - V_p(K)|$ from an iteration is less than a preset limit.

To illustrate the increased speed of convergence obtained by using successive over-relaxation, the potential distribution for the Photochron II (14) data region, which consists of about 6500 grid points, was evaluated to an accuracy of 1 part in 10^5 with w = 1 (i.e. unrelaxed) and with w calculated by Carré's method. The over-relaxed case was solved in 230 cycles, compared with 1000 iterations for the unrelaxed case. The equipotentials in this potential distribution are shown in figure 2.3, using a spacing of 500 V between each contour.

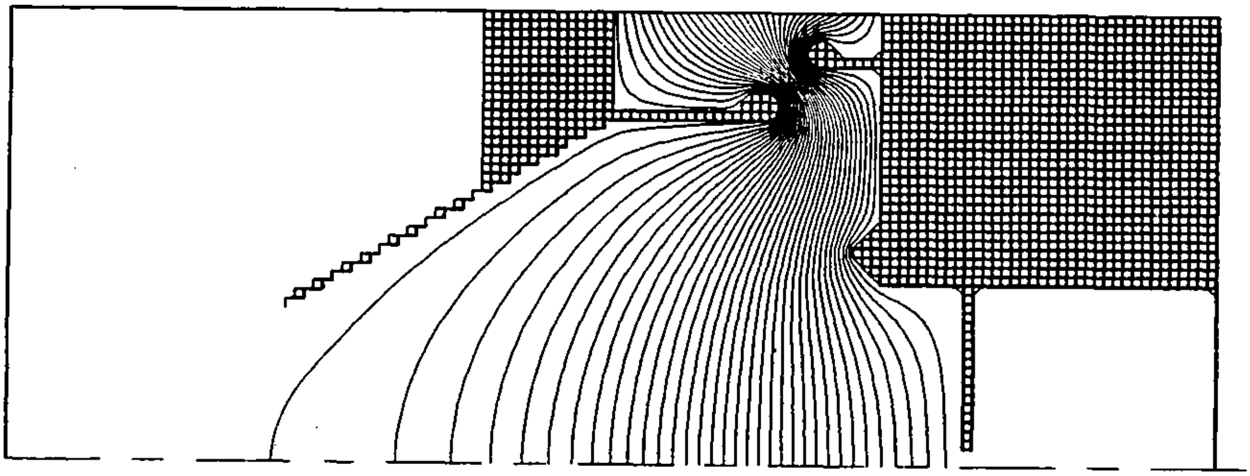

Fig. 2.3 Potential distribution for the Photochron II data region. Contour spacing is 500 V.

2.3 Evaluation of the electric fields

2.3.1 The electric field at the grid points

Once the potential distribution of the region has been established, the next step in the calculation of the electron trajectories is the evaluation of the electric field at all the grid points. This is achieved by solving the equation

$$\underline{E} = - \text{grad}(V) \qquad \text{Eq. 2.10}$$

using Lagrange interpolation and numerical differentiation (87). If a function $y = f(x)$ has known values at the $n + 1$ points (x_o, y_o), (x_1, y_1), ..., (x_n, y_n), its value elsewhere in this range can be found by fitting the n'th order polynomial $P(x)$ through these points

$$P(x) = y_0 L_0^{(n)}(x) + y_1 L_1^{(n)}(x) + \ldots + y_n L_n^{(n)}(x) \qquad \text{Eq. 2.11}$$

where the Langrange coefficients are given by

$$L_j^{(n)}(x) = \frac{(x-x_0)\dots(x-x_{j-1})(x-x_{j+1})\dots(x-x_n)}{(x_j-x_0)\dots(x_j-x_{j-1})(x_j-x_{j+1})\dots(x_j-x_n)} \qquad \text{Eq. 2.12}$$

The gradient dy/dx is then obtained at any of the known points (x_j, y_j) by differentiating equation 2.11 and substituting $x = x_j$.

In calculating the electric field component E_z at any grid point from this method, either 3,4 or 5 points, all lying along the same row, are used (88) with the equation

$$E_z = -\frac{1}{ha_5}(a_oV_o+a_1V_1+ a_2V_2+a_3V_3+a_4V_4) \qquad \text{Eq. 2.13}$$

where, because the points occur at equally spaced intervals, h, the coefficients a_o ..., a_5 are predetermined. The number of points used, and the values of the coefficients of equation 2.13, are governed by the position of the grid point under consideration in relation to the electrodes, as points lying within an electrode must be avoided. There are ten cases employed in the program; these are shown in figure 2.4 where the field is calculated for the point circled using the potentials as indicated. The values of the coefficients, corresponding to each of these cases, are given in table 2.1. Having calculated E_z at any point, the same procedure is adopted to find the component E_r, now using points lying on the same column. In this way, the electric field is stored for every grid point.

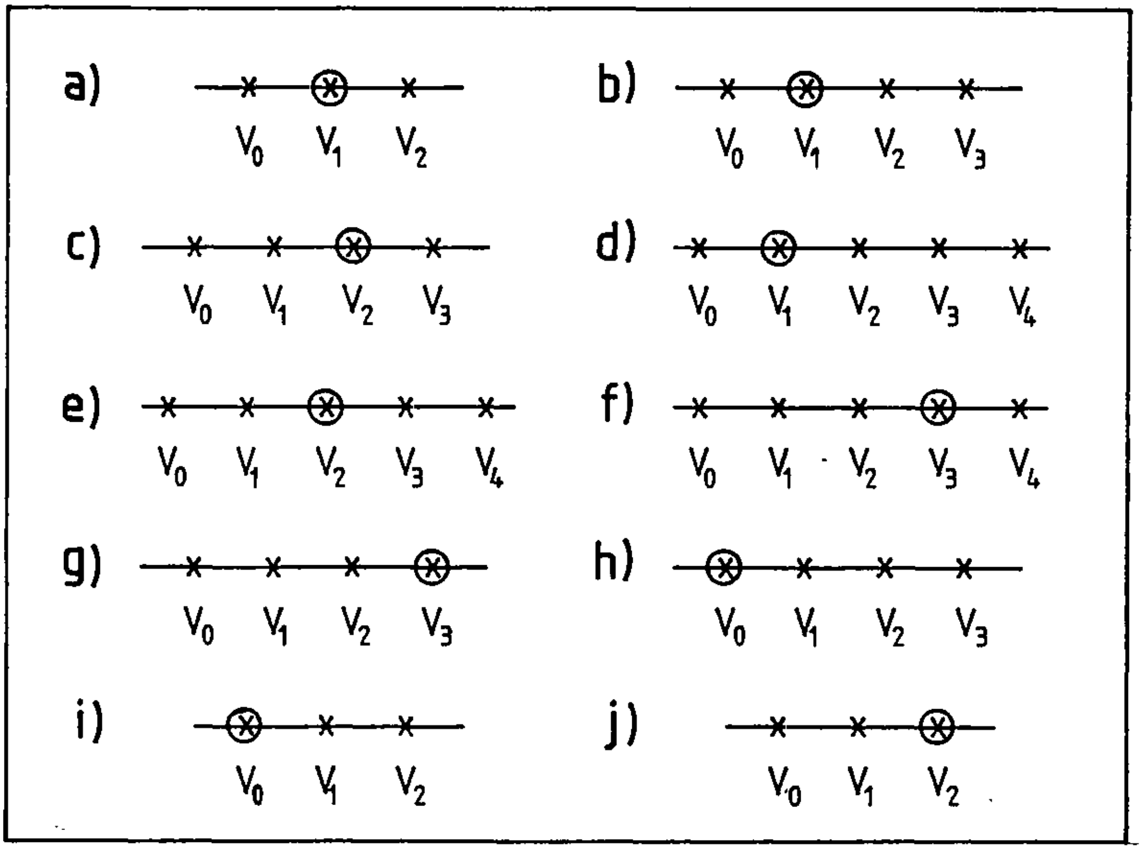

Fig. 2.4 The ten cases used for evaluating the electric field, used with equation 2.13 and the coefficients of table 2.1.

Table 2.1 The coefficients of equation 2.13

Case shown in fig.2.4	a_o	a_1	a_2	a_3	a_4	a_5
a	- 1	0	1	0	0	2
b	- 2	-3	6	-1	0	6
c	1	-6	3	2	0	6
d	- 3	-10	18	-6	1	12
e	1	-8	0	8	1	12
f	- 1	6	-18	10	3	12
g	- 2	9	-18	11	0	6
h	-11	18	-9	2	0	6
i	- 3	4	-1	0	0	2
j	1	-4	3	0	0	2

2.3.2. The electric field within a mesh square

In general the position of an electron during its trajectory through the region does not coincide with a grid point. It thus becomes necessary to be able to calculate the electric field at any point within a grid square. As both the electric field components E_z, E_r are two-dimensional functions, dependent on r and z, this is accomplished by a two-dimensional Lagrange interpolation (89) using 16 grid points surrounding the position of interest, at which E_z, E_r are known.

The grid points to be used are determined by checking the grid square containing the electron, and its surrounding eight squares, until one is obtained for which none of the four corner points lie on an electrode. This square is then taken as the centre of a 4 x 4 matrix providing the 16 grid points (r_o, z_o), ..., (r_3, z_3). If no such square can be found, the electron has either hit an electrode or the electrodes are too close together, and the data region must be re-constructed with new electrode potentials or with a smaller scale.

The method of interpolation is an extension of the one-dimensional case. For each of the four values of r, a Lagrange polynomial is written for interpolation along z, and these are combined in a Lagrangian form. The electric field component E_z at any point is thus given by

$$E_z(r,z) = -\left[L_0^{(3)}(r)\left\{L_0^{(3)}(z)E_z(r_0,z_0)+\ldots+L_3^{(3)}(z)E_z(r_0,z_3)\right\} + \right.$$

$$\left. \ldots + L_3^{(3)}(r)\left\{L_0^{(3)}(z)E_z(r_3,z_0)+\ldots+L_3^{(3)}(z)E_z(r_3,z_3)\right\}\right] \quad \text{Eq. 2.14}$$

with the Lagrange coefficients given by equation 2.12. Similarly, the electric field component along r can be calculated at any point, by replacing E_z with E_r in equation 2.14.

2.4 Calculation of the electron trajectories

2.4.1 Separation into subsystems

In an electrostatic system the equations of motion of an electron can be written in cartesian co-ordinates as

$$\frac{d^2x}{dt^2} = \frac{-e}{m} E_x = \frac{-e}{m}\frac{x}{r} E_r$$

$$\frac{d^2y}{dt^2} = \frac{-e}{m} E_y = \frac{-e}{m}\frac{y}{r} E_r \qquad \text{Eq. 2.15}$$

$$\frac{d^2z}{dt^2} = \frac{-e}{m} E_z$$

where the electron has a charge -e and a mass m. These equations must be solved to evaluate the trajectory of the electron through the system. For this calculation the system can usually be broken down into a number of distinct subsystems which can be treated separately.

For each of the streak and framing image tubes studied in this thesis, a fine mesh electrode has been positioned close to the photocathode for reasons explained in chapter 1; this cathode-mesh region constitutes the first subsystem. The rotationally symmetric focussing lens, from the mesh electrode to the anode, forms the second subsystem. The third subsystem consists of the two-dimensional deflection region containing the deflector plates. The final subsystem is the field-free space between the end of the deflection region and the phosphor screen. (If no deflection is applied, this field free region extends from the end of the focussing data region to the phosphor screen.) Each of the subsystems will be treated below.

2.4.2. The photocathode to mesh region

In the simulation the photocathode and mesh electrode are assumed to be both planar and parallel, as is frequently the case in practice. If any fringing fields are neglected, the equations of motion can be solved analytically for this case. This is a good approximation provided that the emission points of the electrons are not chosen to be close to the edge of the cathode, and that significant bowing of the mesh can be neglected.

For a streak image tube, the slit is set to lie along the y axis, the axis of the tube is defined by the z direction, and any deflection is applied normal to these directions, i.e. in the x direction. Initial values must be chosen for the position (x_c, y_c, z_c) and velocity (v_{xc}, v_{yc}, v_{zc}) of the emitted electron at the cathode. A detailed discussion of these initial conditions is left until chapter 3, but generally the emission energy will lie in the range 0 - 0.6 eV, the slit object height y_c varies from 0 - 5 mm, $x_c = z_c = 0$ mm, and the emission time is set to zero.(It must be noted that for framing image tubes x_c may have a non-zero value since two-dimensional imaging is required.)

With the cathode set at earth potential and the mesh electrode at a potential V_m, a distance d from the cathode, the electric field (and hence the acceleration of the electron) is entirely axial. Then from the equations of motion it follows that

$$v_{zm} = \sqrt{v_{zc}^2 + \frac{2e}{m} V_m}$$

$$t_m = \frac{2d}{(v_{zm} + v_{zc})} \qquad \text{Eq. 2.16}$$

(Here the subscript m refers to values at the plane of the mesh.) As there is no acceleration along x or y, the velocity components in these directions remain unchanged. The position of the electron at the mesh will be

$$x_m = x_c + v_{xc} t_m$$

$$y_m = y_c + v_{yc} t_m \qquad \text{Eq. 2.17}$$

$$z_m = d$$

after a time t_m.

The mesh electrode is set up as the first (bounding) column of the rotationally symmetric data region representing the focussing electron optics, and, as such, is treated as a plane of constant potential. Any microlensing effects due to the small potential variation between the individual filaments of the mesh (90), which may degrade the spatial resolution of the image tube, are ignored because the size ($\sim$15 μm) and shape (square) of these apertures makes it difficult to incorporate them within the present axially symmetric model with a fixed data region grid unit ($\sim$1 mm). This appears to be justified, if the meshes are of sufficient cell density, since it has been found experimentally (91) that the spatial resolution of an image tube with Photochron II geometry (with a limiting resolution $\sim$30 lp/mm) was only degraded if the mesh had $\leqslant$ 20 cells per mm.

A recent simulation of microlensing effects (92) in a mesh of cell density 60 cells per mm, suggested that these effects would limit the spatial resolution to $\sim$ 40 lp/mm at the front end of the streak tube. However, experimental measurements on the constructed Photochron IV tube (c.f. chapter 5), which incorporates a mesh of this density, have established a spatial resolution of $\gtrsim$ 70 lp/mm at the photocathode. This implies that the computer simulation of Roddie (92) may be over-pessimistic, or includes incorrect assumptions, and tends to validate the approximation of disregarding the mesh apertures.

2.4.3. Numerical integration in the focussing region: the Runge-Kutta method

It is not possible to calculate the path of the electron through the data region analytically, as the electric field is not an analytic function of the electron position, and so the equations of motion (eq. 2.15) must be solved by the technique of numerical integration. The known position, velocity and transit time (t_o) of the electron at the mesh electrode are used as the initial conditions in the calculation of its position and velocity at a later time $t_o + dt$. The final values at the end of this time step are then used as the initial conditions for the evaluation of the next step. The procedure is repeated until the electron arrives at the plane of the anode. This multistep method is particularly useful since the step length, dt, can be continuously optimised during the trajectory calculation.

The integration over each step is performed by using a Runge-Kutta method (89,93). The increment to x (Δ x) over the interval between t_i and t_{i+1} is found from this algorithm by evaluating the weighted mean of a number of estimates for Δx obtained at points within the interval (94). Generally, the number of points needed is equal to the order of the approximation required, and this is the same as the highest power of dt retained in the Taylor series expansion (93, 94). In the program, a third-order Runge-Kutta algorithm is used. However, because the set of second order differential equations to be solved (eq. 2.15) are independent of the first order derivatives of x, y and z (the electric field depends only on the position of the electron and not on its velocity), only two integration points are required (94), although the accuracy of the method is still of third order. (The accuracy could be improved by adopting a fourth order algorithm, but this would increase the computation time, as four integration points per step would be needed.)

Using the initial conditions $x_o, \ldots, v_{zo}$, t_o for the first step, and assuming the velocity is constant throughout the step, the electric field is evaluated at the two points

$$(x_o, y_o, z_o)$$
$$(x_o + \tfrac{2}{3}\, v_{xo}\, dt,\, y_o + \tfrac{2}{3}\, v_{yo}\, dt,\, z_o + \tfrac{2}{3}\, v_{zo}\, dt)$$

in the interval $t_o < t < t_o + dt$. With these values for the electric field the following parameters are determined

$$k_x^{(o)} = -dt\, \frac{e}{m}\, E_x(t_o, x_o, y_o, z_o)$$
$$k_x^{(1)} = -dt\, \frac{e}{m}\, E_x(t_o + \tfrac{2}{3}\, dt,\, x_o + \tfrac{2}{3}\, v_{xo}\, dt,\, y_o + \tfrac{2}{3}\, v_{yo}\, dt,\, z_o + \tfrac{2}{3}\, v_{zo}\, dt) \qquad \text{Eq. 2.18}$$

with similar equations for k_y and k_z. Then from Zonneveld's simplified, third-order Runge-Kutta algorithm (94), the values for x and v_x at the end of the step are given by

$$x_1 = x\,(t_o+dt) = x_o+dt\left[\, v_{xo}+\frac{1}{4}\, k_x^{(o)}+\frac{1}{4}\, k_x^{(1)} \right] \qquad \text{Eq. 2.19}$$

$$v_{x1} = v_x(t_o+ dt) = v_{xo} + \frac{1}{4}\, k_x^{(o)} + \frac{3}{4}\, k_x^{(1)}$$

Similar expressions exist for y and z.

Before accepting these values, it is necessary to check the size of the error introduced during this step. This error, due to the truncation of the Taylor series expansion, cannot be determined exactly, but an estimate is obtained by evaluating the size of the third order term used in the series. For this purpose, the electric field must be evaluated at the third point (x_1, y_1, z_1), to enable the calculation of the quantities $k_x^{(2)}$, $k_y^{(2)}$, $k_z^{(2)}$ which are of the form

$$k_x^{(2)} = -dt\,\frac{e}{m}\,E_x(t_1,x_1,y_1,z_1) \qquad \text{Eq. 2.20}$$

The third order terms are then calculated from, (95),

$$\varepsilon_x = \frac{1}{6}\,\frac{d^3x}{dt^3}\,dt^3 \approx \frac{1}{4}\left[\, -k_x^{(o)} + k_x^{(1)} \right] dt$$

$$\varepsilon_{v_x} = \frac{1}{6}\,\frac{d^4x}{dt^4}\,dt^4 \approx \frac{1}{2}\, k_x^{(o)} - \frac{3}{2}\, k_x^{(1)} + k_x^{(2)} \qquad \text{Eq. 2.21}$$

with similar expressions for the third order terms in y and z etc. These six terms (eq. 2.21) are compared with the largest acceptable values for this step, given by $\tau_x dt$,...., τ_{vz} dt, where the preset tolerances denote the maximum contributions of the respective third order terms over one second. If these conditions are satisfied the step is accepted; if not the step is rejected and a smaller step length is used instead. Although three points are used in the step evaluation, the third point is the starting point for the next integration step, and the electric field need only be calculated at two points per step.

In the evaluation of the electron trajectory, the step length is continuously optimised. The optimum step length $\overline{dt}_n$, for a particular step calculated at $t=t_n$, is given by the smallest of the six quantities $(\tau_x{}^{1/2} dt^{3/2})/ \varepsilon_x{}^{1/2}$ (95). Using this value, and that of the optimum step length $\overline{dt}_{n-1}$ calculated at $t=t_{n-1}$, one obtains the next step length at $t=t_{n+1}$ by linear extrapolation

$$dt_{n+1} = \overline{dt}_n + (\overline{dt}_n - \overline{dt}_{n-1})\left(\frac{t_{n+1} - t_n}{t_n - t_{n-1}}\right) \qquad \text{Eq. 2.22}$$

The step length used in the calculation is actually 95% of this value to reduce the probability of step rejection. For the first two steps a fixed step length is used, but after this the step length is determined from equation 2.22.

For a given position and velocity of an electron at the mesh electrode of the data region, it is sufficient to specify just the tolerances $\tau_x, \ldots, \tau_{vz}$, and the initial step length dt for the first two steps to evaluate its trajectory. The initial value for dt is taken to be one hundredth of the approximate time of flight of the electron from the mesh to the anode, whilst the tolerances are generally set as $\tau_x = \tau_y = \tau_z = 10^4$ and $\tau_{vx} = \tau_{vy} = \tau_{vz} = 10^{16}$ (88), although for smaller step lengths, and hence greater accuracy, the tolerances can take smaller values.

For the case of no deflection (i.e. static focus mode of operation), the step-by-step integration is stopped when the electron arrives within 10^{-6}m from the end of the region. This is usually not the anode aperture plane, but a further distance towards the phosphor screen, to take into account the potential leakage through the aperture into the drift (or "field free") section of the image tube. The electron trajectory is easily continued to the phosphor screen, as the velocities are assumed to remain constant in the drift region.

As an example of the trajectories which can be obtained by this numerical technique, figure 2.5 shows the trajectories of 6 electrons through the focussing lens of the Photochron II. These electrons were emitted normal to the cathode with initial energies of 0.3 eV, from points y = 0 up to 5 mm (all with x = 0 mm). Because of the axial symmetry the electrons are shown reflected when they have crossed the tube axis.

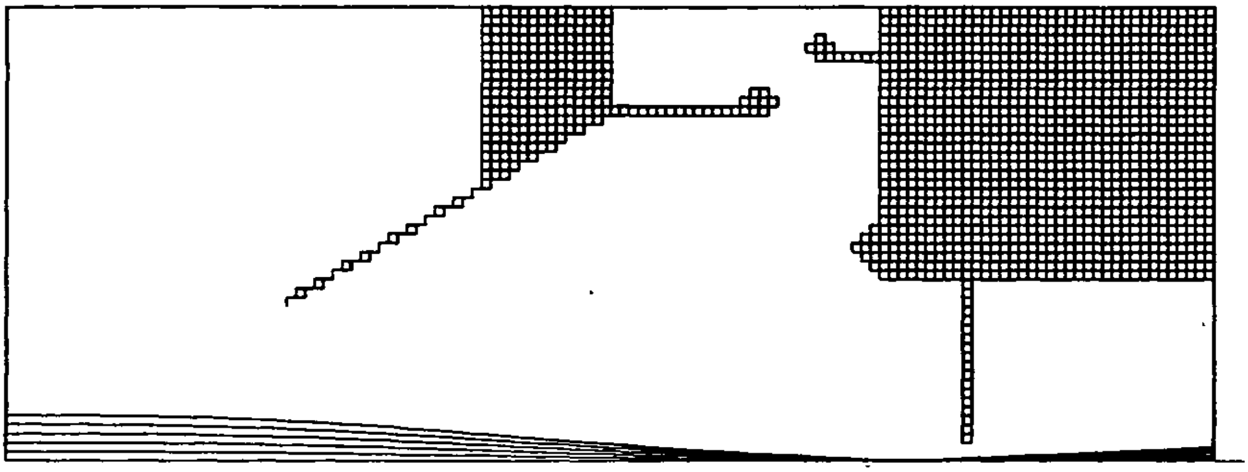

Fig. 2.5 Electron trajectories through the Photochron II focussing region.

2.4.4 The deflection region

If deflection is to be taken into consideration, the trajectory is stopped at the plane of the anode aperture. This plane forms the first column of the two-dimensional data region containing the deflector plates. Because the voltage applied to the deflector plates is linearly time-varying in streak operation, the potential distribution, and the fields, of this deflection region are not static. To accommodate this time dependency, the potential is only allowed to vary through one unit volt when setting up the data region. After solving Laplace's equation (in two dimensions), the time variation is introduced as a multiplicative, time-dependent scaling factor. This quasi-static approach is valid because the conformation of the fractional equipotential contours of the potential distribution (10% of maximum voltage etc.) remain constant throughout time, provided breakdown is avoided; only their magnitudes change with time.

Asymmetric deflection has been used throughout, for the results presented in this thesis. This technique has been widely used in practice (17, 39, 55, 59) because it is more readily realised than symmetric deflection. One plate is held at the anode potential while the deflecting waveform is applied solely to the other plate.

The data region boundary is set to zero volts. The deflector plates are then set to 0V and 1V respectively. The quasi-static potentials and electric fields in the deflection region are evaluated by the methods described in sections 2.2 and 2.3. The resulting potential distribution is indicated in figure 2.6, where the contour steps are 10% (0.1V).

The deflection plate, to which the linearly time dependent ramp is supplied, may be set to a static bias potential V_o so as to deflect the electrons to a chosen position on (or off) the phosphor screen prior to ramp

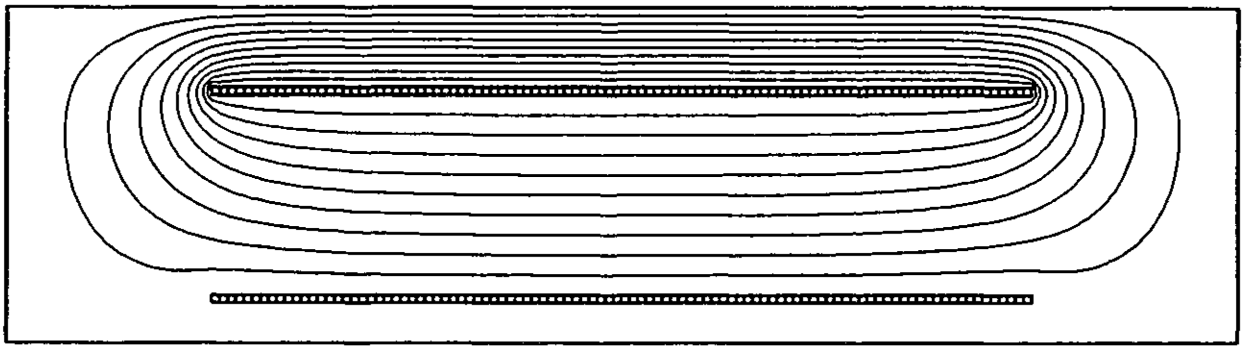

Fig. 2.6 Potential distribution for a deflection region. Contour spacing is 0.1V.

application. It is assumed that the ramp is applied to the deflector at its front (anode) end, so that the waveform will travel along the plate in the same direction as the electrons. Then the time-dependent scaling factor for any point in the region is given by

$$S(t) = V_0 + \frac{dV}{dt}\left(t - \left|\frac{z}{v}\right|\right) \qquad \text{Eq. 2.23}$$

where dV/dt is the slope of the linear ramp. In this equation t is the time which has elapsed since the ramp was switched onto the plates, z is the distance of the point from the front of the plates, and v represents the phase velocity of propagation of the voltage waveform. The potential or electric field for any point at time t, is hence given by the product of its quasi-static value and the relevant scaling factor of equation 2.23.

The trajectory of an electron through the deflection region is evaluated using the third-order Runge-Kutta method, previously outlined, with the known initial conditions at the start of the region. The voltage ramp can be switched on at any time relative to the transit time of the electron. When the electron has reached the end of the deflection region, its path through the field free region to the phosphor screen is computed analytically.

2.5 Summary

A suite of computer programs has been developed to allow the simulation of electrostatic electron-optical systems. The systems modelled can be either completely static, or may incorporate a time-dependent section. In this chapter the methods used in the simulation have been described.

The system must first be set up as a two-dimensional data region, either planar or rotationally symmetric. The potential distribution is obtained by solving Laplace's equation for every free point numerically, using the five point finite difference method and applying successive over-relaxation. The electric field at these points is calculated by the technique of numerical differentiation using Lagrange's interpolation formula. Finally the trajectory of the electrons through the system can be evaluated by numerical integration using a third order Runge-Kutta method. The technique adopted requires only two integration points per step whilst retaining third-order accuracy.

CHAPTER THREE

THE MODULATION TRANSFER FUNCTION METHOD

3.1 Introduction

The temporal resolution of a streak image tube is often obtained by using a method based on the Gaussian approximation (43, 96, 97), in which it is assumed to be composed of a number of discrete, quasi-independent factors. However, for tubes with subpicosecond resolution, this is no longer a physically realistic or accurate approximation.

While the focal properties of a streak tube, such as its paraxial focus, magnification, distortion etc., can be obtained from the computation of a small number of trajectories, this data will not directly yield the spatial and temporal resolutions. The spatial response of both optical (98,99) and electron-optical (100, 101) systems have been widely described by the method of the optical transfer function, which developed from communication theory combined with optical diffraction theory. It is only since the beginning of this decade, however, that this technique has been applied to the field of electron-optical chronoscopy to specify the temporal, as well as the spatial, response of fast streak tubes (34, 102). An important feature of this method is that the interdependency of the acceleration, focus and deflection of the photoelectronic signal can be taken into consideration.

3.2 The Gaussian approximation

The assumptions implicit in this method will first be reviewed by deriving the general equation used. When an input light signal is supplied to a streak tube, the output on the phosphor screen is the convolution of the profile of the original signal and the camera instrumental response function. If the widths (FWHM) of the input and response functions are comparable, as in the case of a femtosecond streak tube recording subpicosecond pulses, the camera instrumental function is obtained by deconvolution of the input function from the output. Generally, this deconvolution is extremely difficult unless simplifying assumptions are introduced regarding the pulse and instrumental profiles.

In the Gaussian approximation both the input pulse intensity profile and the instrumental temporal response function are assumed to be Gaussian, given respectively by

$$I(t) \propto \exp\left(\frac{-4 \ln 2\, t^2}{T^2}\right)$$

$$R(t) \propto \exp\left(\frac{-4 \ln 2\, t^2}{\tau^2}\right)$$

Here T and τ are the respective widths (FWHM) of the two profiles, τ being the camera temporal resolution. The recorded signal at the screen is the convolution of the two profiles, and, from appendix 1, this becomes

$$S(t) \propto \exp\left(\frac{-4 \ln 2\, t^2}{T^2 + \tau^2}\right)\left[1 + \operatorname{erf}\left(\frac{2t\,\tau \sqrt{\ln 2}}{T\sqrt{T^2 + \tau^2}}\right)\right]$$

The error function varies only slowly with time compared with the exponential term, and, in the first order approximation, can be taken as a constant. The FWHM of the recorded signal is given by

$$\tau_{meas} = \sqrt{\tau^2 + T^2}$$

The temporal resolution is limited by the transit time dispersion of the photoelectrons through the streak tube, due to both their initial velocity distribution and the inherent aberrations of the electrostatic focussing and deflection systems, and also by the speed with which the image is streaked across the screen. Generally, the temporal resolution is taken to be a Gaussian combination of these two limitations (39) using a derivation similar to that outlined above:

$$\tau = \left[(\Delta t_{phys})^2 + (\Delta t_{tech})^2\right]^{\frac{1}{2}} \qquad \text{Eq. 3.1}$$

The physical time resolution, Δt_{phys}, is assumed to be composed of a number of distinct quasi-independent factors which are combined in a Gaussian form (97):

$$\Delta t_{phys}^{\;2} = \Delta t_c^{\;2} + \Delta t_{cm}^{\;2} + \Delta t_l^{\;2} + \Delta t_d^{\;2} + \Delta t_{pd}^{\;2} \qquad \text{Eq. 3.2}$$

In this expression Δt_c is the time dispersion of the photoelectrons within the photocathode, and Δt_{cm}, Δt_1, Δt_d, Δt_{pd} are respectively the transit time dispersions in the cathode to mesh region, the focussing electron lens the deflector plates, and the post-deflection section. The technical time resolution, Δt_{tech}, is the time taken by the electron beam to scan a spatial resolution element at the screen, and is given by

$$\Delta t_{tech} = 1/(v \ \delta) \qquad \text{Eq. 3.3}$$

where v is the streak speed of the electrons at the phosphor screen, and δ is the spatial resolution in the streak direction at the screen.

There are a number of assumptions implicit in equations 3.1 and 3.2, and these are listed below.

1) The physical and technical time resolution components can be treated as independent quantities.
2) The time dispersion can be subdivided into a number of discrete components.
3) Each constituent factor of equation 3.2 has the same weight.
4) The input pulse intensity for each contribution has a Gaussian profile.
5) The response function for each contributory factor also has a Gaussian shape.
6) The error function obtained in each derivation can be ignored.

If these assumptions are valid then equation 3.1 will give a good approximation for the temporal resolution, but if any of them is incorrect the result may be inaccurate.

A corollary of the third assumption is that if each of the time dispersion components had an identical value, they would all have the same effect on the deformation of the input signal. This can be shown to be untrue by considering the deflection deviations produced at the screen due to each of the time dispersion components independently. For a pair of parallel deflectors of separation d, it is shown in appendix 2 that to a first order approximation, the deviations due to a) the total time dispersion up to the deflectors Δt_{cd}, b) the time dispersion in the deflectors Δt_d and c) the time dispersion in the post-deflection section Δt_{pd}, are given by the respective equations below

$$\begin{aligned}
\Delta x_1 &= \frac{e}{md}\,\frac{dV}{dt}\,T_d\,T_{pd}\,\Delta t_{cd} \\
\Delta x_2 &= \frac{e}{md}\left(V_o + \frac{dV}{dt}\,T_d\right)T_{pd}\cdot\Delta t_d \qquad \text{Eq. 3.4} \\
\Delta x_3 &= \frac{e}{2md}\left(2V_o + \frac{dV}{dt}\,T_d\right)T_d\cdot\Delta t_{pd}
\end{aligned}$$

In these equations V_o is the applied potential difference between the plates when the electron pulse is at the entry of the deflectors, dV/dt is the slope of the linear deflection ramp, T_d and T_{pd} are the electron transit times in the deflection and post-deflection regions respectively, and e and m are as before.

It is clear from equations 3.4 that if the three temporal dispersions had identical values, the resultant deflection deviations would be different. Hence they do not have the same weight, invalidating assumption three. Consequently they should not be combined in the Gaussian form of equation 3.2. As an example, Δt_{pd} was calculated to be $\sim$ 3.8 ps for the Photochron II when a voltage ramp of 5×10^{12} Vs^{-1} was applied to the deflectors, and the fringing fields were included. If this was used in equations 3.1 and 3.2, the temporal resolution for this tube would be calculated to be much larger than its real value of $\lesssim$ 2 ps (14). Despite its large value, this time dispersion is less important than the earlier contributions of Δt_d and Δt_{cd}, because the deflection deviation that it produces, Δx_3, is significantly smaller than either Δx_2 or Δx_1. This can be seen by substitution of the values of 250 ps and 2.5 ns for the transit times T_d and T_{pd} respectively, and the deflection plate gap of 4 mm. With V_o = 460 V, the value of Δx_3 is only 0.007 mm. This is to be compared with the deflection deviations of 0.10 mm and 0.07 mm produced by the time dispersions of 0.73 ps in the electron lens and 0.84 ps in the deflectors.

To employ equation 3.3, the dynamic spatial resolution in the streak direction must be used, but this has not been directly measured. Usually the spatial resolution, which has been determined for the slit direction under streak conditions, is substituted instead (40). It is shown, in section 3.7, that this value can be significantly higher than the resolution in the streak direction (which contains all the temporal information), thus underestimating the value of Δt_{tech} from equation 3.3.

Finally, and most importantly, the first assumption is not physically realistic. Under the Gaussian approximation, the dynamic spatial resolution along the streak direction has been assumed to be a constant for a particular streak tube even when operating at different writing speeds. For example, this has been taken to be approximately 10 lp/mm at both streak speeds 1×10^{10} cms^{-1} (40) and 2×10^{10} cms^{-1} (14) for the Photochron II. On the contrary, however, it is dependent on both the electron-optical/electronic parameters and the physical time dispersions associated with the electron pulse that is deflected, and is shown in section 3.7 to decrease with increasing streak speed. The physical and technical time resolution factors then cannot be treated independently because the dynamic spatial resolution along x is not a technical characteristic of a particular streak tube.

A more accurate and representative way to evaluate the streak tube temporal resolution, is to determine the dynamic spatial resolution (x) by taking into account all the relevant interdependent factors such as temporal dispersions and geometrical defects, and then to substitute this into equation 3.3. This has been achieved in a method based on transfer function theory.

3.3 Theory of the modulation transfer function approach

If the input signal to an image tube with a linear response has a sinusoidal variation with spatial frequency f_x, the output at the screen will also be sinusoidal, but with a frequency reduced by a factor equal to the magnification of the tube. The image will generally have a lower contrast and may be displaced (i.e. have a phase difference) with respect to the object. The modulation at this frequency is then defined as the image to object contrast ratio, and this gives a measure of the performance of the tube at this particular frequency. If the modulation and phase are obtained for a wide range of spatial frequencies, the curves of modulation and phase versus spatial frequency represent respectively the modulation transfer function (MTF) and the phase transfer function (PTF) of the system. Together these two functions constitute the complex optical transfer function (OTF) which best describes the image quality of a linear system, by relating the intensity distribution in the output plane to that at its input. The MTF is the modulus of the OTF, and the PTF is its imaginary part. To obtain the OTF theoretically, the point spread function (PSF) and the line spread function (LSF) of the system must be evaluated.

The output on the image tube screen for an infinitesimally small point source object will always have a finite size due to the initial distribution of energies and angles of the photoelectrons at the cathode, and the blurring caused by the electron-optical aberrations of the system. The PSF is the three-dimensional surface obtained by plotting the intensity at the screen plane as a function of position (x and y). Although the PSF is difficult to interpret, it contains all the information that is necessary to completely describe the image forming characteristics of the system for the object point considered. If the PSF is given by i(x, y), its integral

$$I(y) = \int_{-\infty}^{\infty} i(x, y)\, dx \qquad \text{Eq. 3.5}$$

represents the LSF, which is drawn as a two-dimensional curve of intensity versus position. This is equivalent to replacing the infinitesimally small point object by an infinitesimally narrow line object (i.e. a delta function) and plotting the intensity at the output plane versus the distance in the direction normal to the length of the object. The LSF is easier to analyse than the PSF although a mathematical transformation is still required to obtain the OTF. Because of axial symmetry a single LSF on axis will contain all the necessary data to quantify the imaging characteristics of the system, but for off axis object points, it is necessary to evaluate two LSFs, in the tangential (x) and radial (y) directions.

The OTF is defined as the Fourier transform of the LSF. This is understood by recognizing that the delta function line object for the LSF contains equal amplitude sine waves of all spatial frequencies. Once the OTF has been calculated, both the MTF and PTF can be derived from it. The MTF is an extremely important function characterising the modulation response for an image tube over a wide range of frequencies. The PTF gives a measure of the asymmetry of the LSF. However, because both the magnitude and direction of the phase may vary for each frequency, this asymmetry cannot be evaluated easily from the PTF, and so the PTF is not usually computed.

This discussion has concentrated on the spatial frequency response of linear imaging devices, but this can be replaced by the temporal frequency to give the temporal performance specifications of the streak image tube. In this case, the input signal will have a sinusoidal variation in time (frequency f_t). By finding the LSF in time now (representing the time dispersion), the temporal modulation transfer function (TMTF) can be derived as described above.

An important property of the MTF is that if a number of incoherently linked systems are used together, the MTF for the combination is simply equal to the product of each individual MTF component (103). This is used to enable the features of a complete streak tube to be obtained from a knowledge of the frequency response of its electron optics and phosphor screen.

3.4 The velocity distribution of the electrons at the cathode

In order to calculate the MTF of an image tube, it is necessary to evaluate a large number of electron trajectories through the system. If physically realistic results are to be obtained, the initial conditions for the electrons at the cathode must be chosen to simulate the velocity distribution. The angular distribution of the photoelectrons is taken to be Lambertian and hence follows a cosine law in the radial angle (26). The initial energy distribution, however, is not an analytic function, but has been measured for an S1 photocathode illuminated by light of wavelength 1.06 μm (104). The half width of this distribution is 0.3 eV (FWHM), and the maximum initial energy of emission of the electrons is $\sim$0.6 eV.

It is not practical to consider electrons with every possible combination of initial energies and angles, so the energy and angular distributions are divided into a number of equally spaced strips, each of which can be represented by a single electron trajectory with an appropriate weighting factor. A total number of 1000 electrons is studied comprising 5 values of energy, 10 values for the radial angle θ and 20 values for the azimuthal angle ϕ. (Angles θ and ϕ are shown defined in figure 3.1a.)

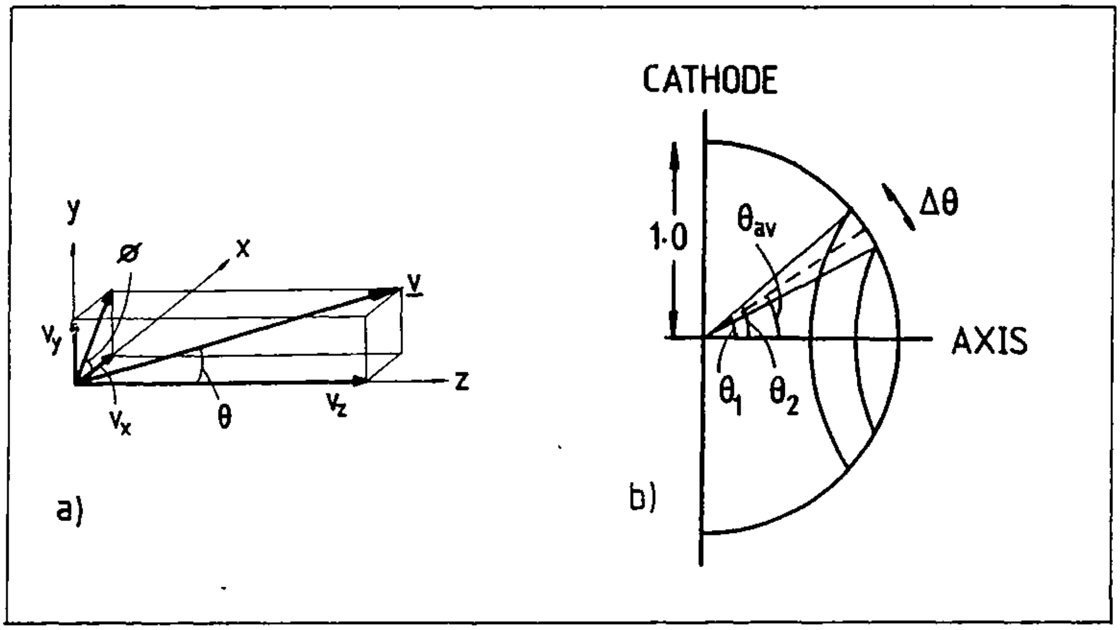

Fig. 3.1 Definition of the angles.

The initial value of the radial angle can vary from 0 to 90 degrees, and this is divided into 10 strips of equal width $\Delta\theta = 9^\circ$. Each strip is described by its midpoint so that the θ values used are 4.5, 13.5, ..., 85.5°. The number of electrons emitted into any of the angular ranges from θ_1 to $\theta_2 = \theta_1 + \Delta\theta$ will be given by the emission probability multiplied by the area of the range (105). For the unit sphere shown in figure 3.1b, this is proportional to

$$\cos\theta \, dA = 2\pi \int_{\theta_1}^{\theta_2} \cos\theta \sin\theta \, d\theta$$

$$= \pi \sin(\Delta\theta) \sin 2\theta_{av}$$

As $\Delta\theta$ is a constant, the appropriate weighting factor for each angular strip is

$$\text{W.F.}(\theta) = N \sin\theta_{av} \cos\theta_{av} \qquad \text{Eq. 3.6}$$

where θ_{av} is the angle used in the electron trajectory for that strip, and N is a constant normalising factor.

The energy distribution is transected into five, 0.12 eV width strips. The number of electrons with energies between E_1 and $E_2 = E_1 + \Delta E$ is similarly given by

$$\int_{E_1}^{E_2} N(E)\, dE \qquad \text{Eq. 3.7}$$

where N(E) is the number emitted with energy E. Because N(E) is not an analytic function now, it cannot be integrated analytically. Instead for each strip, the integral of equation 3.7 is approximated by $N(E_{av}) \cdot \Delta E$ where E_{av} is the central energy of the strip. The normalised values of $N(E_{av})$ used in the program (106) are given in table 3.1

Table 3.1 Energy values and associated weighting factors used.

E_{av} eV	0.06	0.18	0.30	0.42	0.54
$N(E_{av})$	0.023	0.231	0.413	0.288	0.044

The azimuthal angle can take values from 0 to 360 degrees. Twenty strips are used with a constant angular width $\Delta\phi = 18^\circ$, starting at $+9^\circ$, but the distribution of this angle is uniform.

To each of the 1000 electrons emitted at the photocathode, representing a particular energy and angular strip, is associated a weighting factor dependent on the number of electrons which would be emitted in the particular range. It follows from equations 3.6 and 3.7, that the weighting factor for a given energy E_i and θ_i is

$$\text{W.F.}\ (\theta_i,\ E_i) = K \sin(\theta_i) \cos(\theta_i)\ N(E_i)$$

where K is a constant.

3.5 Evaluation of the LSF of an image tube

The 1000 electrons are traced through the image tube (including deflection if required) from the chosen object point on the photocathode as far as the plane at which the MTF is to be obtained. A spot diagram can be generated by plotting the position of each electron at this plane, as shown in figure 3.2a.

The LSF is obtained from this spot diagram as follows. The spatial distribution of electrons is divided into 100 strips with a strip width of d/100, where d is the difference between the largest and smallest values in the direction of integration. The number of electrons in each strip is counted by adding up their associated weighting factors. This number of electrons plotted against the position of each strip, taken to be at its central value, provides the LSF (refer eq. 3.5). As an

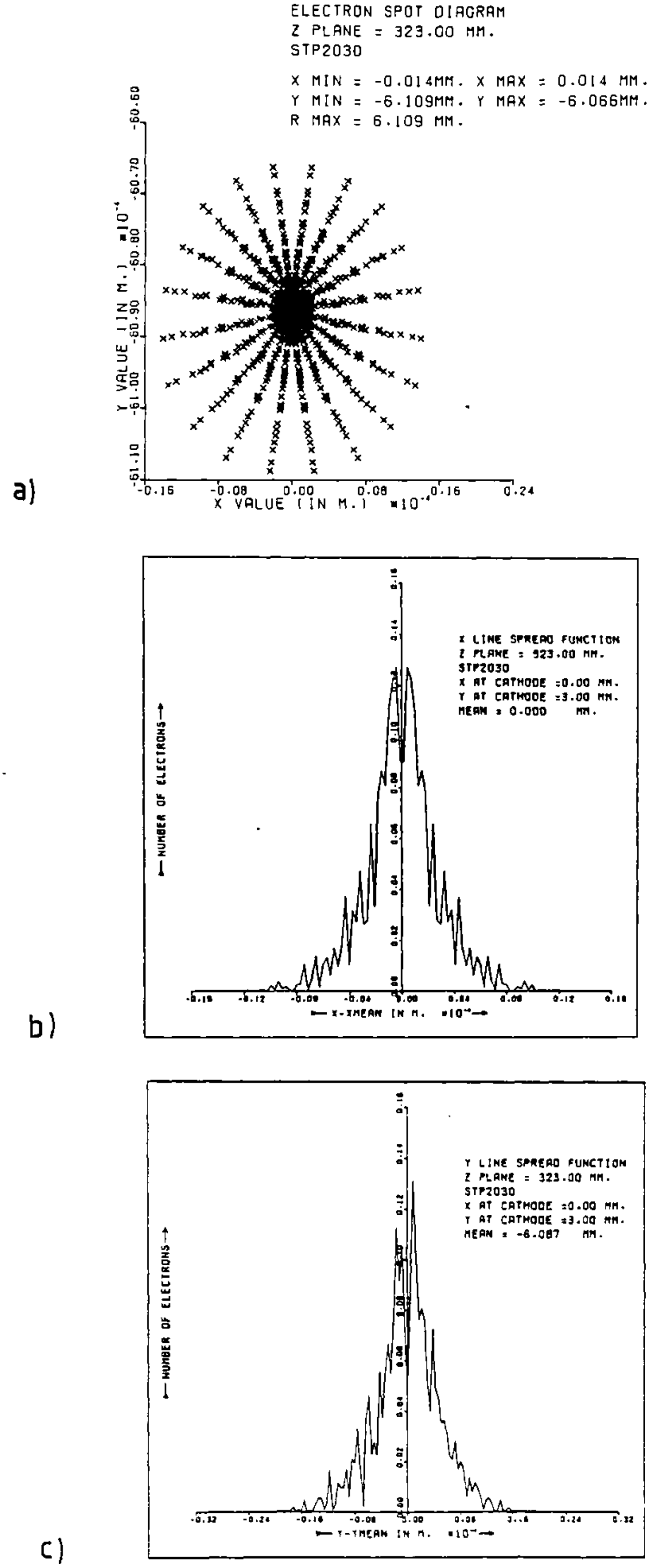

Fig. 3.2 Spot diagram and corresponding LSF s for the Photochron II.

example, figures 3.2 b and c show the LSFs in both the x and y directions obtained from figure 3.2a.

3.6 Calculation of the MTF

3.6.1 The spatial MTF

Once the LSF has been established at a given plane, the modulation at a particular frequency in this plane follows directly from a Fourier analysis of the LSF, as indicated for the x direction in equations 3.2 below:

$$A_1 = \frac{\int_{-\infty}^{\infty} LSF_x \cos(2\pi f_x x)\, dx}{\int_{-\infty}^{\infty} LSF_x \, dx}$$

$$A_2 = \frac{\int_{-\infty}^{\infty} LSF_x \sin(2\pi f_x x)\, dx}{\int_{-\infty}^{\infty} LSF_x \, dx} \qquad \text{Eq. 3.8}$$

$$\text{Modulation } (f_x) = (A_1^2 + A_2^2)^{\frac{1}{2}}$$

The modulation is normalised to a value of unity at zero frequency. The integration need only be performed across the width of the spot, and so the effective limits become the values of x for the first and last strips of the LSF.

The modulation is calculated at 100 equally spaced values of the frequency from zero up to a chosen maximum, which can be changed for each new curve. The MTF is then displayed by plotting the modulation at each frequency. This is indicated in figure 3.3 for the MTF curves obtained from the two LSFs of figure 3.2.

Although the MTF defines the performance of the system in a given direction at a specific plane for a wide range of image frequencies, it is still useful to be able to characterise the system by a single number, and to this end, the concept of limiting resolution is retained.

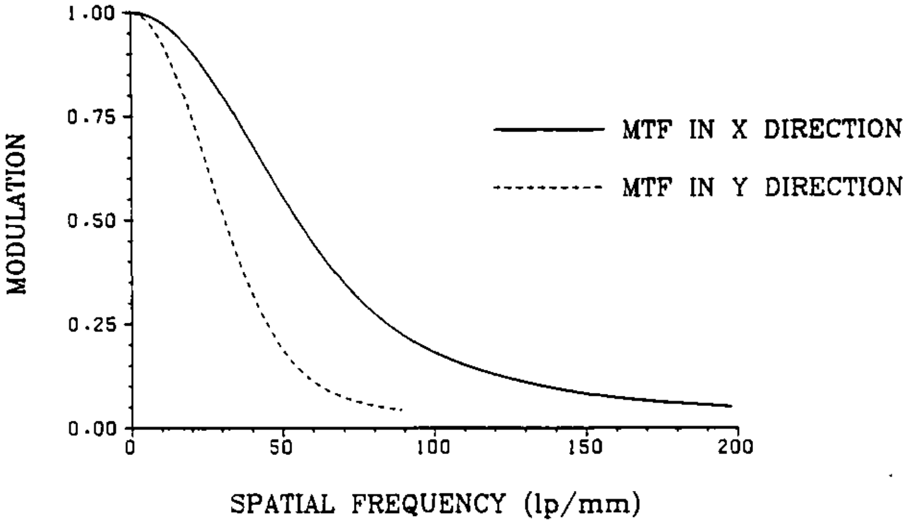

Fig. 3.3 MTF curves calculated from the LSFs of figure 3.2.

The limiting resolution is taken to be the frequency at which the modulation has fallen to a value of 5%, as this should be near the limit of detection of the eye (107). The limiting resolution is evaluated in the program, by establishing between which two frequencies the modulation falls below 5% and then using a linear interpolation between these values.

A problem which sometimes occurs in the evaluation of the MTF is the generation of spurious spectra referred to as aliasing (108). This originates from both the finite number of electrons considered, and the fact that the

LSF is calculated using only 100 strips corresponding to sampling the true LSF at these discrete values (fig. 3.4a). The Fourier transform of the sampling function is another comb function in the frequency domain. The MTF obtained by Fourier analysing the calculated LSF will be equal to the convolution of the true MTF and this new comb sampling function (fig. 3.4b). If the sampling rate used in obtaining the LSF is too low, the MTF will be overlapped by its alias. Although aliasing is not common, when it occurs the modulation begins to increase at high frequencies. An example of this effect is shown in figure 3.4c. For this case, the limiting

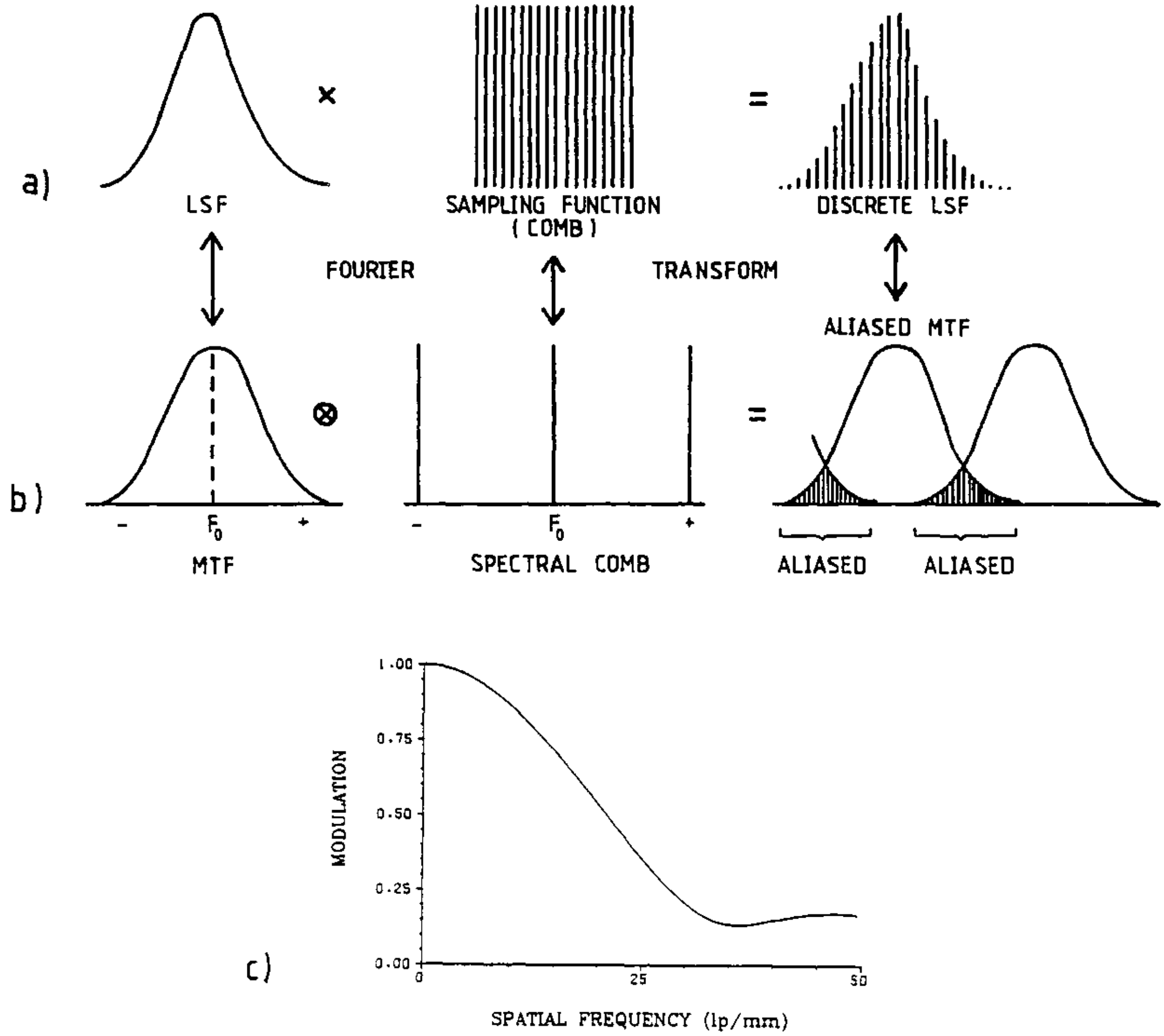

Fig. 3.4 The problem of aliasing.

resolution can no longer be defined as the frequency for 5% modulation, but is now approximated to the value at which the modulation starts to increase.

3.6.2. The Temporal MTF (TMTF)

The temporal LSF (LSF_t) can be evaluated in exactly the same way as the spatial LSF described in section 3.5, at any plane up to the deflectors, by summing the number of electrons in each strip of the unidimensional temporal spot diagram. This represents the distribution of the number of electrons as a function of their time dispersion. It can be used to calculate the TMTF as outlined above, to give a value for the time dispersion up to the plane under consideration.

If the electrons undergo a time dependent deflection however, the temporal information is transformed into spatial information at the screen (refer section 1.2). Hence the TMTF must now be found by transformation of the spatial MTF in the streak direction (MTF_x), by the multiplication of each spatial frequency with the applied streak speed at the phosphor. The LSF_t at the phosphor will still contain the information on the total transit time dispersion in the tube (including deflection time dispersion), but this is not the same as the temporal resolution obtained from the transformed TMTF.

Since in streak operation the slit of the camera is usually restricted (c.f. section 1.5), the object point at the cathode used for all dynamic MTF results is (0,0).

3.6.3 The MTF of the phosphor screen

The above discussion has centred on the MTF of the electron optics of the image tube. In practice it is customary to convert the manipulated electronic signal back into an optical signal via a fluorescent phosphor screen. It is therefore important to consider the effect of the phosphor on the performance of the image tube, by evaluating an overall MTF for the system including this phosphor. This is achieved by making the assumption that the screen has a linear imaging response, (i.e. doubling the number of electrons striking the screen, doubles its fluorescence), and then invoking the multiplication rule. The MTF of the total system is the product of the MTFs of the electron optics and the phosphor.

Johnson (109) has shown that the experimentally obtained MTF data for a P20 type phosphor is well described by the equation

$$M(f) = \exp\ (-f/f_c)^n \qquad \text{Eq. 3.9}$$

where $n = 1.1$, and f_c is a frequency constant found from fitting the experimental results. In the experimental streak tube studied, however, P11 type phosphor screens have been used. The MTF response for a phosphor of this type has been measured by Delori (37), and its limiting resolution was found to be 132 lp/mm. Making the assumption that the device index, n, for a P11 type is also 1.1, the frequency constant is calculated to be 48.7 lp/mm. With these values for n and f_c, equation 3.9 is used to give an approximate MTF curve for a P11 type phosphor screen (fig. 3.5). Although this curve gives a slightly pessimistic fit to Delori's measurements, it may give a generally optimistic prediction for the performance of most P11 phosphors.

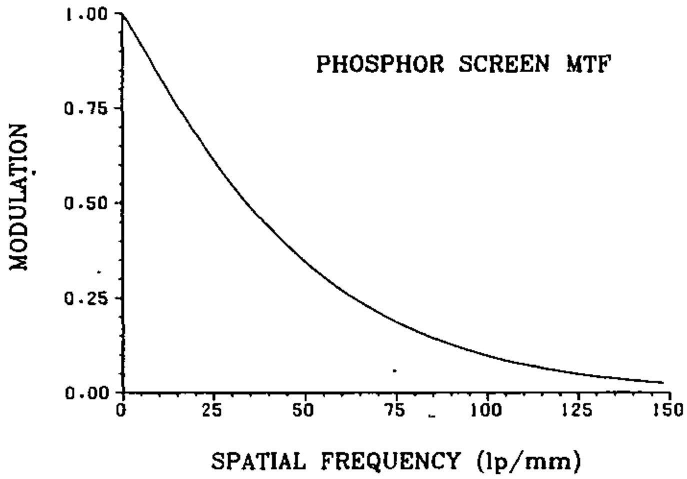

Fig. 3.5 Phosphor screen response used in the calculations.

In general, the results presented in this thesis will include the screen response unless explicitly stated otherwise. The main effect of including the phosphor in the system is to reduce the modulation at high frequencies; when the modulation has fallen to a low value the modification of the system response by the phosphor is small.

3.7 MTF results for the Photochron II

To illustrate the use of the MTF curves in describing the performance of a streak tube, the Photochron II has been studied under both static and dynamic conditions. For simulation in the focus mode, six cathode object points have been taken lying along the slit direction with $y = 0 - 5$ mm (all have $x = 0$ mm). The MTF in the slit direction for each of these points is shown in figure 3.6 at the paraxial focus plane ($z = 323$ mm).

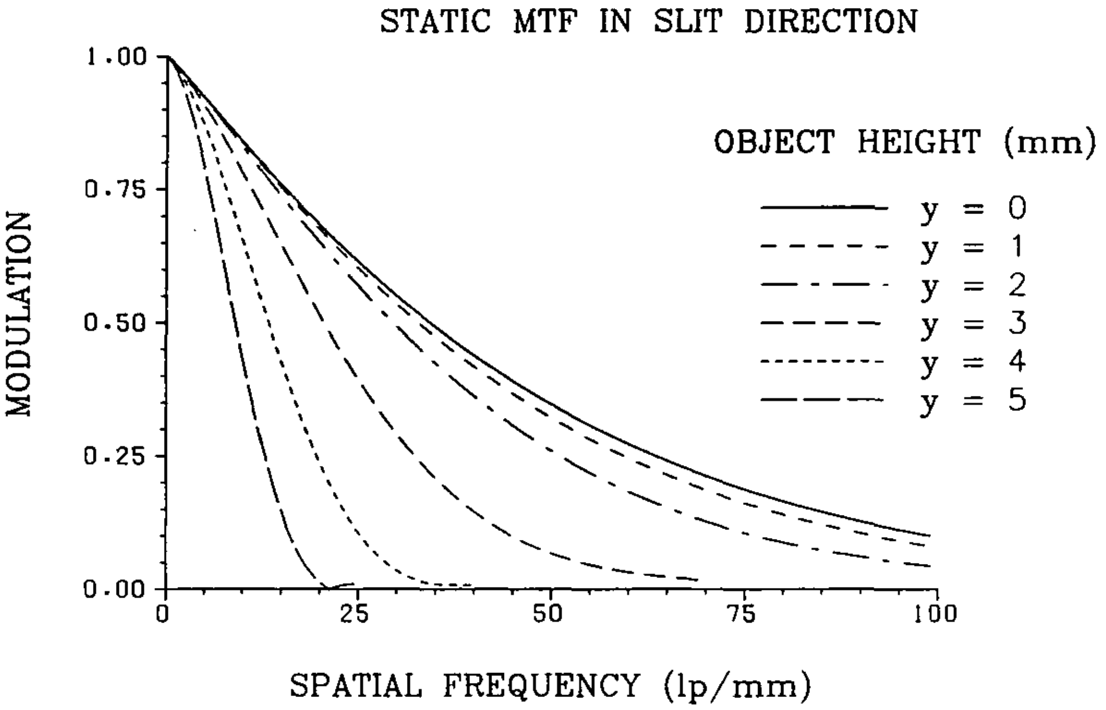

Fig. 3.6. MTF_y curves at paraxial focus of the Photochron II.

It is clear from figure 3.6 that the spatial resolution (along the slit) at the paraxial focus decreases monotonically with increasing slit height. This is due to the increase in lens aberrations off axis, in particular field curvature (26). The curves of field curvature and astigmatism are shown in figure 3.7. A compromise plane can be found, closer to the cathode, at which the overall spatial resolution (along both the slit and streak directions) is optimised for the extended object. This compromise plane is at z = 316 mm. The limiting static spatial resolution for each cathode object point, at this plane is given in table 3.2. The theoretical static resolution for the Photochron II is 32 lp/mm, with a magnification of -1.97, i.e. 63 lp/mm

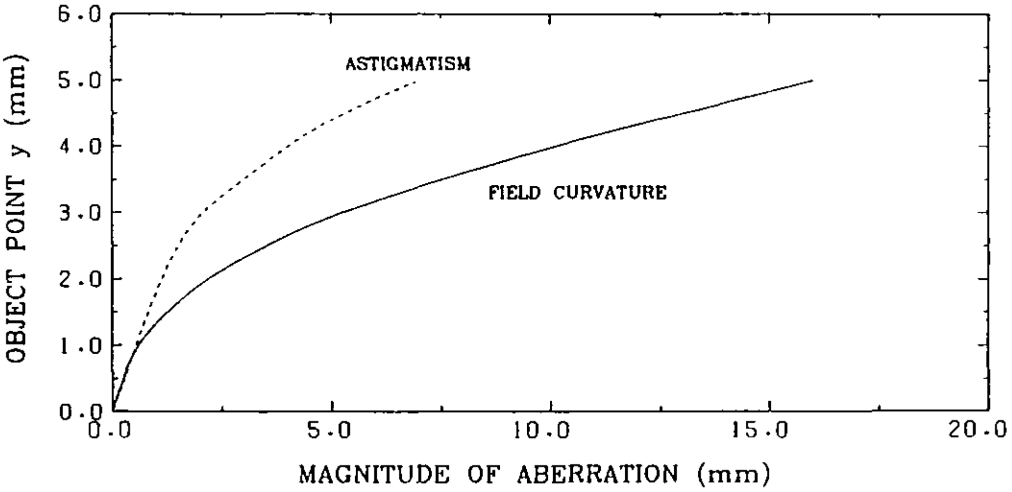

Fig. 3.7 Photochron II aberration curves.

Table 3.2. Photochron II static results at z = 316 mm.

Object point mm	Res. x lp/mm	Res. y lp/mm	Magnification
0	37	37	
1	39	40	-1.96
2	44	54	-1.96
3	62	105	-1.97
4	118	79	-1.98
5	87	32	-1.98

at the cathode. Experimentally the static resolution has been observed to be 40 lp/mm at the cathode, and the magnification was -1.95 (40). The experimentally measured resolution is lower than that predicted theoretically due to a number of detrimental effects. These include the quality of the input optics, misalignment and tolerancing of the electrodes during construction, and degradation of the signal-to-noise ratio (and hence contrast) at the screen. This latter effect is due to the increase in noise from secondary electron emission in the tube, particularly at the mesh, and also the reduction in the signal-to-noise due to the finite transmission of the mesh. None of these resolution - degrading effects has been considered in the MTF results in this thesis.

The performance of the Photochron II has been theoretically studied in streak operation for six different writing speeds: 1.0, 1.5, 3.1, 6.25, 12.5 and 25.0 cm/ns. The MTF in the streak direction at these writing speeds is shown in figure 3.8. It is quite apparent that the spatial resolution along the direction of streak does not remain constant as the writing speed is increased, as has previously been assumed (14, 40). As the voltage ramp becomes faster the spatial resolution in the deflection direction becomes degraded. This phenomenon will be treated in more detail in chapter 4.

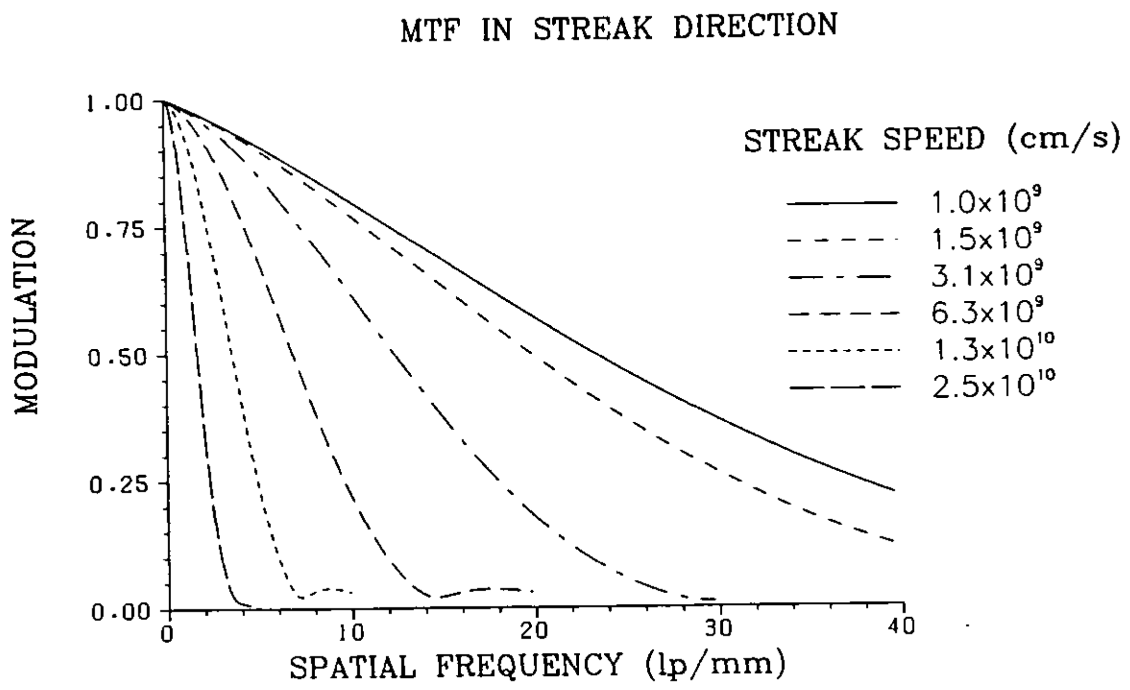

Fig. 3.8 MTF_x for Photochron II in streak mode.

The MTFs shown in figure 3.8 contain the information on the temporal resolution of the tube at these streak speeds. Converting these curves into TMTFs, the variation of temporal resolution with writing speed is presented in figure 3.9. Although the dynamic spatial resolution along x decreases with increasing streak speed, at first

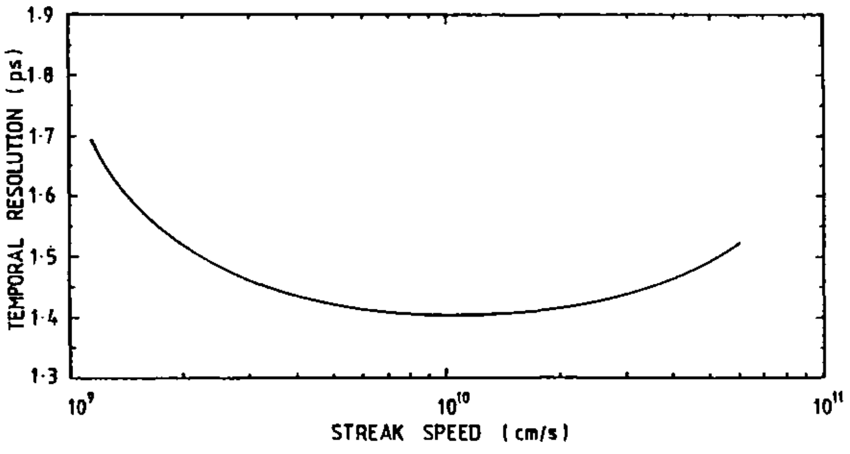

Fig. 3.9 Variation of temporal resolution with streak speed.

the rate of decrease is slower than the rate of increase of the writing speed (c.f. chapter 4). An optimum streak speed exists, namely 1.25 x 10^{10} cm s^{-1}, at which the temporal resolution is minimised (at a value of 1.4 ps). This is in agreement with the conclusions of Kinoshita et al (31).

The temporal resolution of a Photochron II has been experimentally investigated when the photocathode was subjected to conditions similar to those simulated in the MTF calculations (14). An S1 tube was illuminated with 3 ps pulses at 1.06 μm. The streak images, recorded at a writing speed of 2 x 10^{10} cm s^{-1}, were reported to have widths (FWHM) ∿3 ps. Bird (14) concluded a camera temporal resolution of 0.8 ps by a Gaussian combination of a transit time dispersion of 0.7 ps and a technical time resolution of 0.5 ps. The time dispersion is of the correct order of magnitude (c.f. section 3.2), but the latter component was calculated assuming a dynamic spatial resolution of 10 lp/mm. It can be seen from figure 3.8 that this is an optimistic assumption, and in practice it may be reduced by a factor of 2 at this writing speed. By taking into account both the time dispersions and the deflection fields, the temporal resolution was calculated to be ∿1.4 ps at this streak speed. With such a temporal resolution, the pulses of duration ∿3 ps would be recorded without significant broadening.

Another photocathode frequently used in sealed-off Photochron streak tubes is the S20. Although the initial energy distribution of the photoelectrons is not well known compared to the S1 photocathode (104), Bryant (40) has estimated the halfwidth and the average energy to be ∿ 0.3 eV when the S20 cathode is illuminated by light of wavelength ∿600 nm (e.g. mode-locked Rhodamine 6G dye laser pulses). Under such operating conditions the initial energy distribution will be similar to that used for the MTF calculations of this chapter, and hence the experimental results should be comparable to the predicted values. The temporal resolution of the S20 Photochron II was reported to be 1.4 ps (40, 53) when studying its dynamic range using 2 ps pulses and a writing speed of 10^{10} cm s^{-1}. This figure is in excellent

Table 3.3 Comparison of theoretical and experimental results.

Characteristic	Theory	Experiment
Magnification	-1.97	-1.95
Static resolution at cathode	63 lp/mm	40 lp/mm
Temporal resolution	1.41 ps	1.4 ps
Writing speed (cms^{-1})	$1.25x10^{10}$	$1x10^{10}$

agreement with the theoretically predicted temporal resolution of 1.41 ps at a streak speed of $1.25x10^{10}$ cms^{-1} The theoretical and experimental results obtained for this tube are summarised in table 3.3.

3.8 Conclusions

It has been shown that the Gaussian approximation is not a physically realistic method for estimating the temporal resolution of a streak image tube. This is because the dynamic spatial resolution in the streak direction is dependent on both the time dispersions in the tube and the deflection voltage ramp used. To this end, a computer program has been developed to calculate the TMTF of a streak tube under dynamic conditions.

The performance of the streak tube can be evaluated in both the focus and streak modes of operation by calculation of its MTFs from LSFs determined from a number of known electron trajectories. The MTF approach takes into account both the chromatic aberration of the electron signal and the geometrical aberrations of the focussing lens, and, in streak operation, the aberrations and fringing fields associated with the deflectors.

An important feature of the MTF method is that the frequency response of a total system can be obtained from a knowledge of the MTF curves for the separate linear components of the system by using the multiplication rule. This has been used to evaluate the performance of a streak tube including its phosphor screen, by describing the response of the phosphor with a semi-empirical expression. Although the MTF represents the frequency response for a wide range of frequencies, the concept of limiting resolution, defined at 5% modulation, is still retained.

The MTF approach has been used to describe the performance of the Photochron II. The method has been shown to give good agreement between the theoretical predictions and experimentally measured values (see table 3.3). Therefore, the MTF description of image tube performance has been adopted and applied for the estimation of the characteristics of other tube designs, notably the Photochron IV (chapter 4) and the Photochron IV-M (chapter 6) streak tubes, and a Photochron framing tube (chapter 7).

CHAPTER FOUR

THE PHOTOCHRON IV FEMTOSECOND STREAK IMAGE TUBE

4.1 Design considerations

As explained in chapter 1, to achieve subpicosecond resolution a fundamental requirement is the reduction of the temporal dispersion in the streak tube. It was originally thought that this could be achieved by increasing the extraction electric field close to the cathode (32). However, theoretical studies of the Photochron II with extraction fields of both 20 and 50 kV cm^{-1} at the cathode have shown that this is insufficient to reduce the temporal dispersion across the whole slit (34). Table 4.1 shows the temporal dispersion associated with electrons emitted from object points 0 - 5 mm with a spread of energy 0 - 3 eV for the two cases cited. It is clear from these results that although

Table 4.1

Slit height mm	Temporal dispersion in ps	
	Photochron II (20 kV/cm)	Photochron II (50 kV/cm)
0	0.76	0.44
1	1.06	0.74
2	1.37	1.20
3	1.85	1.82
4	2.50	2.43
5	3.10	3.04

the time dispersion for the on-axis electrons is reduced by increasing the electric field, there is little change in the off-axis time dispersions.

The fact that there is significant temporal dispersion outside the photocathode - mesh region is underlined by the results presented in table 4.2 for the standard Photochron II with a range of values for the initial energy spread of the photoelectrons emitted from y = 0 mm. Indeed, for initial energy spreads $\gtrsim 0.15$ eV, this becomes the dominant factor in the pre-deflection time dispersion. Thus to improve the temporal resolution, the time dispersion must be reduced throughout the image tube, not just close to the cathode.

Table 4.2

Initial energy eV	Temporal dispersion in ps		
	Photocathode to mesh	Mesh to deflectors	Photocathode to deflectors
0 - 0.075	0.25	0.19	0.31
0 - 0.15	0.35	0.39	0.48
0 - 0.3	0.41	0.65	0.76
0 - 0.6	0.54	1.05	1.25
0 - 1.2	0.77	1.96	2.20

Another important point to consider in the design of subpicosecond resolution streak cameras is the dynamic range over which the time resolution remains undegraded (c.f. section 1.6). It has been shown (52) that the temporal broadening of the input pulse, due to the Coulombic repulsion in the electron signal, occurs mainly in the region of the tube where the electron velocity is low for comparatively long times. This is illustrated in table 4.3 which is reproduced from reference 52. It can be seen that for the Photochron II, under the particular

Table 4.3 Temporal broadening for the Photochron II; input pulse duration = 3 ps, current density = 120 mA/cm^2

Region	Pulse broadening ps	% of total
Cathode - mesh	0.127	5.7
Mesh - cone	2.0	89.8
Cone - deflectors	0.1	4.5

operating conditions assumed, 90% of the temporal broadening occurs in the mesh-cone region where the potential is between approximately 800 V and 1 kV. To reduce this temporal broadening, and hence increase the dynamic range by virtue of smaller space charge effects, the regions where the electons have low velocities must be minimized by maximising the potentials.

A femtosecond resolution streak tube, the Photochron III, was designed theoretically (83, 110) using as preconditions reduced temporal dispersion by increased electric fields, and faster streak speeds obtained from an improved deflection sensitivity. This tube was a precursor of the Photochron IV (111), and has a similar cathode - mesh arrangement and four electrode type geometry. The deflection sensitivity was increased by reducing the anode potential to 10 kV thus lowering the energy of the electrons being deflected.

Two main problems were later found to occur in this tube. The first was that, although the lower operating (anode) potential increases the deflection sensitivity of the tube, as explained above this is only at the expense of larger space charge related effects and hence a lower TRL dynamic range. Secondly, the electron-optical crossover was located too far from the anode aperture (∿ 10 cm towards the cathode). This requires a larger aperture which has the detrimental effect of increasing the interaction between the focussing and deflection fields through field leakage.

The Photochron IV, on the other hand, has been designed to achieve subpicosecond resolution by maximising the electric fields and potentials throughout the photocathode to anode region. The high potentials employed reduce the space charge problems but increase the speed of the electrons at the deflector plates, hence reducing the deflection sensitivity. This has been compensated for by increasing the length of the drift section (∿ 190 mm), so that it is approximately the same as that of the focussing region (210 mm), and improving the deflection geometry. This results in a deflection sensitivity of 3 cm/kV at the screen. The structure of the tube together with its theoretical performance will be described in the following sections of this chapter.

4.2 Description of the Photochron IV

4.2.1. The focussing region

The electrode configuration of the Photochron IV streak tube is shown schematically in figure 4.1, in which the nomenclature subsequently used is defined. A flat mesh is positioned 2 mm from the planar photocathode. The application of 10 kV to the mesh, with respect to the grounded cathode, ensures a substantial electric field of 50 kV/cm close to the cathode. The electrons are accelerated by this large field to relatively high velocities, reducing the temporal dispersion in the post-mesh region. However, these high velocities make it difficult to focus the electron beam emerging from the mesh.

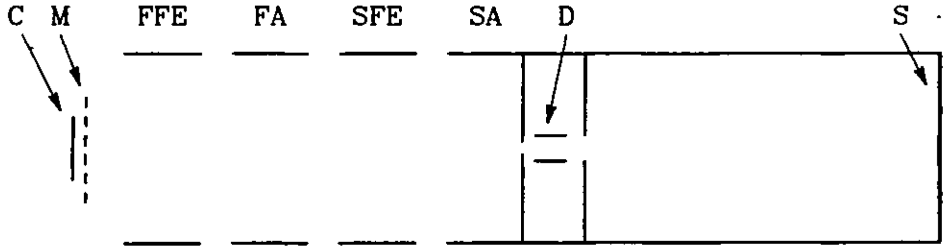

C	PHOTOCATHODE	SA	SECOND ANODE
M	MESH	D	DEFLECTOR PLATES
FFE	FIRST FOCUS ELECTRODE	S	SCREEN
FA	FIRST ANODE		
SFE	SECOND FOCUS ELECTRODE		

Fig. 4.1 Schematic of the Photochron IV.

It is inappropriate to use a single focussing lens with a low focus voltage because of the requirement of maximised potentials. Instead, two inter-dependent focussing lenses, consisting of four coaxial, equi-diameter cylinders, are used. The first lens is composed of the mesh, the first focus electrode and the first anode cylinder. It has the four-fold function of focussing and further accelerating the electrons, adjusting the position of the crossover, and reducing the temporal distortion. The second focussing lens, made up of the first anode, second focus electrode and second anode, is mainly used to position the image plane, although it also has the function of minimizing the aberrations and the temporal dispersion.

Using the computer model described in chapter 2, an optimum design was obtained for the combination of the two lenses by considering not only the spatial and temporal resolutions, and dynamic range, but also the interaction between the focussing and deflection systems. That this interaction must be minimized in order to achieve high-fidelity electron deflection can be understood as follows. If the position of the crossover is too far from the anode aperture, then the size of this aperture, and also the deflection plate separation, will be unavoidably large, leading to a poorer deflection response to the applied linear voltage ramps. Moreover, the detrimental influence of the strong deflection fringe fields on the focussing electrostatic field can be minimized by having a small anode aperture.

For the optimum design the four electrodes are of length 42 mm with diameters of 44 mm, and all inter-electrode spacings in the focussing section are 10 mm. The electrode voltages used in the Photochron IV are indicated in table 4.4. The resulting potential distribution is shown in figure 4.2. It is evident that the objective of high potentials and electric fields has been achieved. This is further illustrated by the axial potential distribution of figure 4.3, which shows that the potential is always greater than $\sim$ 6.5 kV on axis. This can be compared to the lowest axial potential of 0.8 kV in the Photochron II. It is important to note that the potential in the immediate vicinity of the mesh drops by approximately 2 kV creating a repulsive force on the electrons. Any secondary electrons emitted at the mesh must have a kinetic energy of greater than 2 keV

Table 4.4

Electrode	Cathode	Mesh	FFE	FA	SFE	SA
Potential (kV)	0	10	8	24	5	18

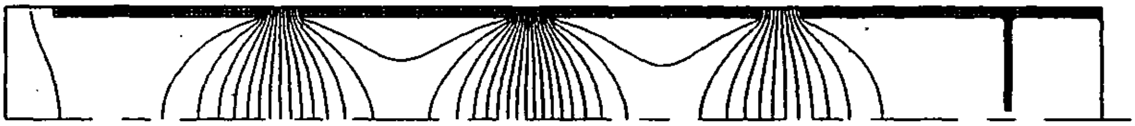

Fig. 4.2 Equipotentials for the Photochron IV; contour spacing is 1 kV.

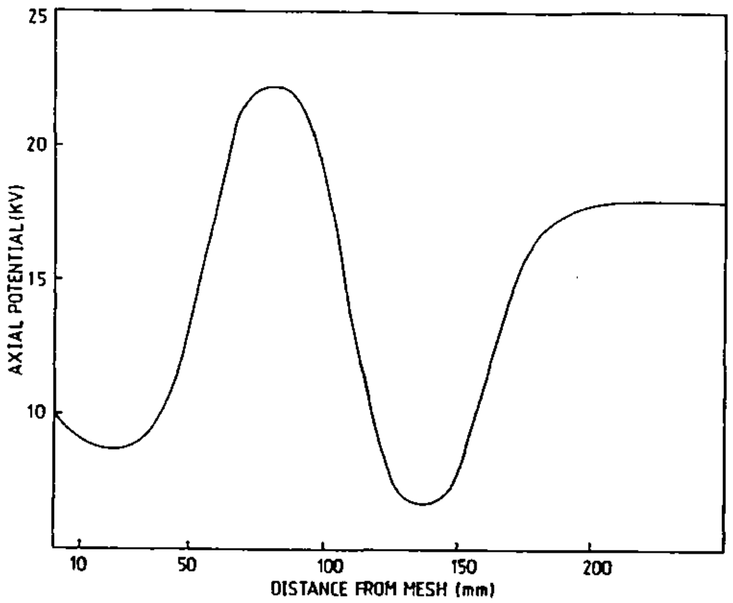

Fig. 4.3 Axial potential distribution in the mesh-anode region.

to overcome this potential barrier, thus significantly reducing the background noise in the tube.

4.2.2 The deflection geometry

An initial design for the deflection region of the tube was obtained by computing a small number of electron trajectories. Applying a static bias deflection voltage, the deflection sensitivity of the arrangement could be evaluated. The effect of a particular deflection system (used with the aforementioned focussing lens design) on the electrons was studied by considering the two boundary electrons in the beam, for a given emission energy. The initial conditions for the two electrons were $x = y = 0$ mm, $\Phi = 0^{o}$, $\theta = \pm 90^{o}$ and $E = 0.1$ eV. By evaluating the paths of these electrons through the focussing region and then through the deflection system with the application of a voltage ramp of 5×10^{12} Vs^{-1}

(equivalent to a streak speed $\geqslant 1\times10^{10}$ cm s^{-1}), their spatial (and hence temporal) separation at the screen was determined. This temporal separation (T.S. in table 4.5) gives a convenient indication of the temporal response of the overall system.

The deflection systems considered were parallel plate structures, as shown in figure 4.4. To achieve a good deflection sensitivity at the phosphor, the plate separation, d, should be small. However, if it is too small the photoelectrons may get too close to the deflector plates, and so experience the adverse fringing fields. The compromise value of d was set to be 3 mm. Also the length of the plates, L, should be as large as possible without introducing significant detrimental time dispersions within this region.

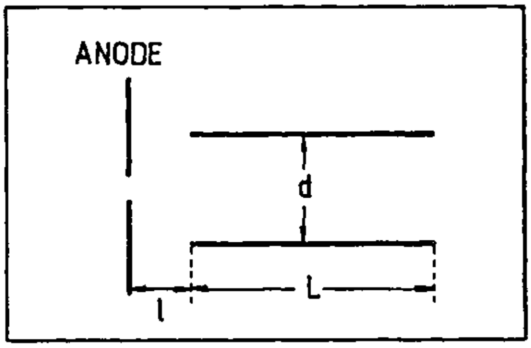

Fig. 4.4 Deflection geometry.

Different values of l and L were investigated, and some of the results are summarised in table 4.5. Because the electron-optical crossover occurs approximately 40 mm from the anode (towards the cathode) in this streak tube, it is necessary to keep the deflection plates

Table 4.5 Deflection geometry results

l mm	L mm	T.S. ps	Def. sens. cm/kV
10	15	0.44	2.70
5	15	0.34	2.77
3	15	0.27	2.77
3	17	0.24	3.09
3	20	0.25	3.59
2	17	0.34	3.07
*3	17	0.23	3.06

as close as possible to the anode, ensuring that the electrons do not approach the plates as they enter the deflection system. This separation was chosen to be l = 3 mm. As the length of the deflectors increase, the temporal response (T.S.) for the given ramp passes through a minimum, with the optimum value being L = 17 mm. This occurs because at small values of L the deflection sensitivity, and hence the streak speed, will be low but at large values of L the electron trajectories become close to the plates as they leave the deflectors. This leads to an increased time dispersion due to their greater interaction with the large fringing fields at these positions.

For the optimum plate dimensions of d = 3 mm, L = 17 mm the effect of reducing l to 2 mm is to degrade the temporal response due to the more severe initial fringing fields imposed by the greater proximity of the equipotentials. A final improvement to the temporal response was made by including a second aperture plate 3 mm away from the exit of the deflectors (see fig. 4.1).

The results for this geometry are shown asterisked in table 4.5. This plate has a large rectangular aperture (10 mm x 3 mm), and establishes a constant equipotential at the anode/screen potential. Although its original purpose was to limit the penetration of the fringing fields along the drift section of the tube, another beneficial use of the plate is described in chapter 5.

4.3 Static performance

The effective useful area of the cathode of the Photochron IV has been influenced by the need to minimise the curvature of the slit image which occurs upon applying the fast streak voltage ramps. The pre-deflection temporal dispersions and distortions have been calculated at the anode plane for the photocathode slit heights up to 5 mm. The results for the Photochron IV (PC IV) are presented in table 4.6, along with those of the Photochron II (PC II) as a comparison. Because the

Table 4.6

Slit height mm	Temporal disp.(ps) PC II	PC IV	Temporal dist.(ps) PC II	PC IV
0	0.76	0.26		
1	1.06	0.31	0.74	0.20
2	1.37	0.35	2.92	0.77
3	1.85	0.45	6.57	1.72
4	2.50	0.51	11.69	3.08
5	3.10	0.60	18.27	4.76

temporal resolution of the Photochron IV is ∿ 400 fs (see next section), it is necessary to restrict the overall extent of the slit object at the photocathode to ∿ 4 mm (i.e. ±2 mm off axis) under dynamic conditions. This enables a small anode aperture, of 2 mm diameter, to be used, which reduces the interaction of the focussing and deflection sections.

The static resolution performance, for the cathode object points y = 0, 1, 2, 3 (with x = 0 mm) has been obtained using the MTF technique described in chapter 3. Figure 4.5 shows the variation of the radial (y) static resolution with axial position, close to the paraxial focus plane at 405 mm. To achieve optimum spatial

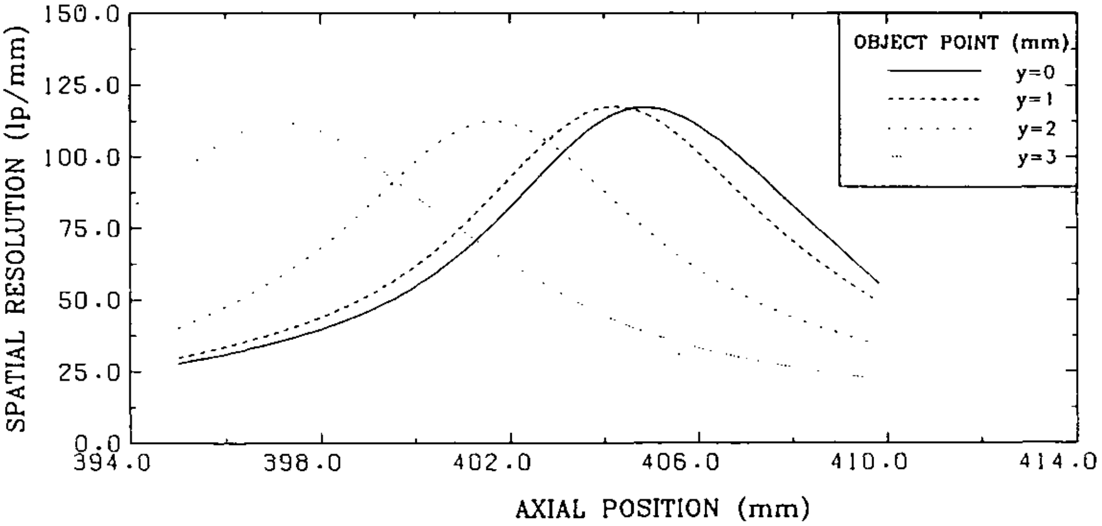

Fig. 4.5 Variation of static resolution in slit direction with axial position.

resolution across the whole of the image it was decided that the phosphor should be positioned at the plane z = 401 mm whilst retaining the same focussing potentials.

The performance predicted at this compromise plane is summarised in table 4.7. It is clear that the electron-optical magnification of the Photochron IV is -1.97, and the theoretical static spatial resolution is $\geqslant$ 64 lp/mm at this plane.

Table 4.7 Static results at the optimum plane of z = 401 mm.

Slit height mm	Spat. res. x lp/mm	Spat. res. y lp/mm	Magnification
0	74	64	
1	67	73	-1.965
2	83	120	-1.967
3	120	73	-1.969

4.4 Temporal resolution of the Photochron IV

4.4.1 Excluding the phosphor screen response

The Photochron IV has been studied under streak conditions for a number of applied deflection voltage ramps. (In each case the bias voltage was chosen so that the deflected images were positioned as close to the centre of the screen as possible, since this is the area used in practice.) The variation of the limiting dynamic spatial resolution in the streak (x) direction with axial position is shown in figure 4.6a for different voltage ramps. Multiplication of each spatial resolution by the correct corresponding streak speed allows the transformation of figure 4.6a into figure 4.6b, where the temporal resolution is shown as a function of axial position for each voltage ramp.

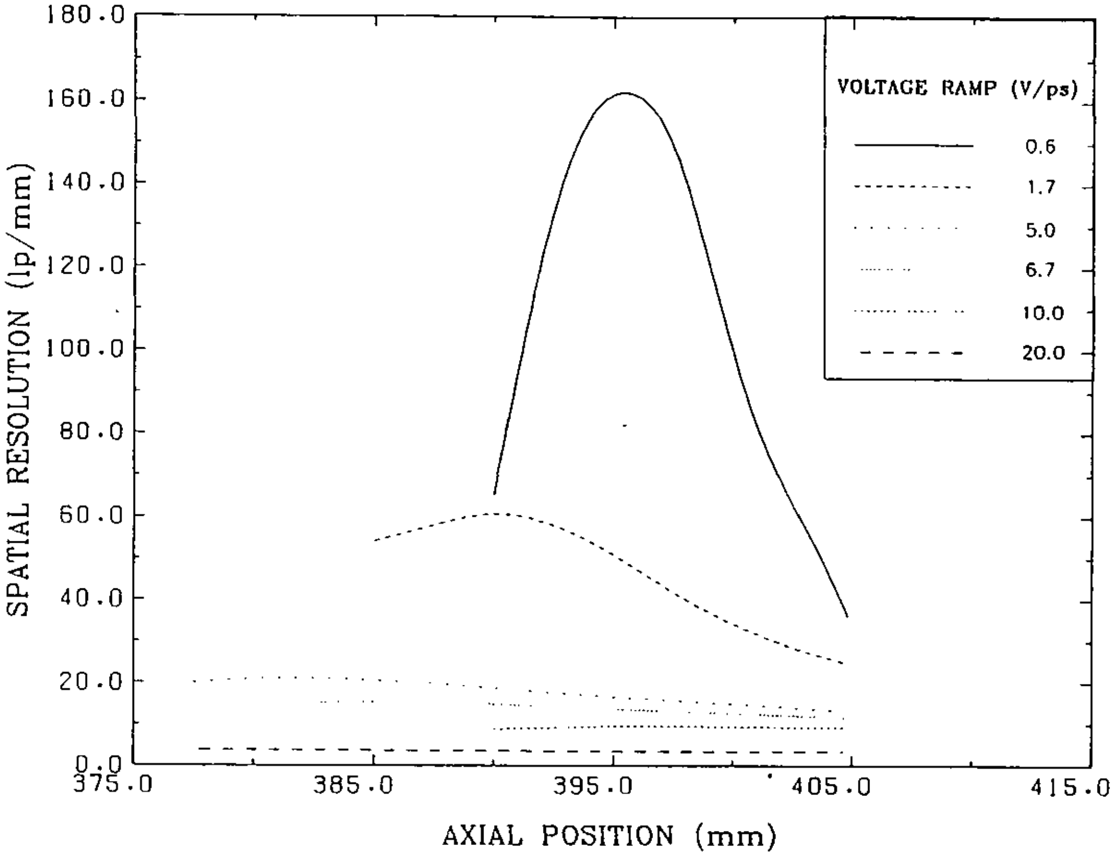

Fig. 4.6a Dynamic spatial resolution (streak direction) as a function of axial position. The phosphor screen response is not included.

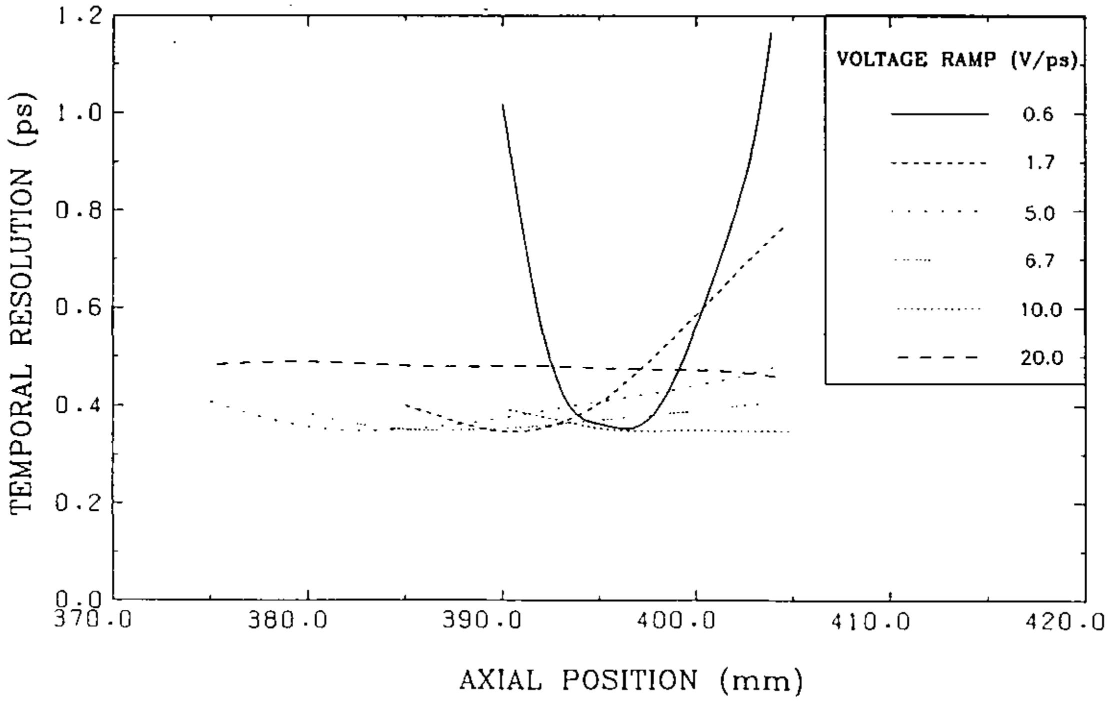

Fig. 4.6b Temporal resolution curves obtained from fig. 4.6a.

It can be seen from figure 4.6a that at low voltage ramps (and hence low streak speeds), the spatial resolution in the streak direction is still high even after deflection. However, at the lowest streak speed, the limiting resolution falls off very sharply away from the peak position. As the voltage ramp increases, the spatial resolution along x deteriorates due to the spread of the image, and the curve flattens. This arises principally from the time dispersion in the electron beam prior to deflection.

Although the spatial resolution is degraded, at ramps lower than 2 x 10^{13} Vs^{-1} (equivalent to 6 x 10^{10} cms^{-1} writing speed) this is almost compensated for by the increase in streak speed. The optimum temporal resolution at each voltage ramp remains nearly constant at approximately 0.34 ps, as shown in figure 4.6b. For very large voltage ramps, the decrease in spatial resolution becomes larger than the corresponding increase in writing speed, resulting in a poorer temporal resolution. This effect will be explained in section 4.6.

An interesting point which arises from these results is the possibility of achieving a temporal resolution as good as 0.33 ps at very low streak speeds (e.g. 1.85 x 10^9 cms^{-1}). This follows directly from the high predicted value of 165 lp/mm for the dynamic spatial resolution along x. However, this has been calculated considering only the electron optics of the tube. In practice the phosphor screen will impose an upper limit on the spatial resolution, and this is dealt with in the next section.

4.4.2. Inclusion of the phosphor screen response

With the inclusion of the phosphor screen (refer section 3.6.3) the calculated spatial and temporal results presented in figures 4.6a and b become the curves of figure 4.7. The spatial resolution is diminished by the phosphor screen response, but this occurs primarily at the lowest streak speeds where the resolution was initially very high. This leads to a reduction in the temporal resolution as shown in figure 4.7b.

It should still be possible to achieve subpicosecond resolution with low voltage ramps but two further considerations make it unlikely in practice. Firstly, in single-shot operation, to minimise space charge broadening, it is necessary to attenuate the input pulse intensity and then intensify the image at the screen (c.f. chapter 1). The intensifier used will itself limit the spatial resolution. For the MCP intensifier used with the experimental version of this streak tube, described in chapter 5, (Philips 21 XX) the limiting resolution is ∿ 45 lp/mm (112). This will further reduce the temporal response at low writing speeds, and at the lowest streak speed of 1.85×10^9 cms^{-1} considered, will limit the temporal resolution to 1.2 ps.

Secondly, at low streak speeds, the temporal curve shown in figure 4.7b is quite narrow, producing a small effective "depth of focus" for the temporal resolution. Then even a small displacement along the axis results in a significant reduction in the temporal resolution. At the

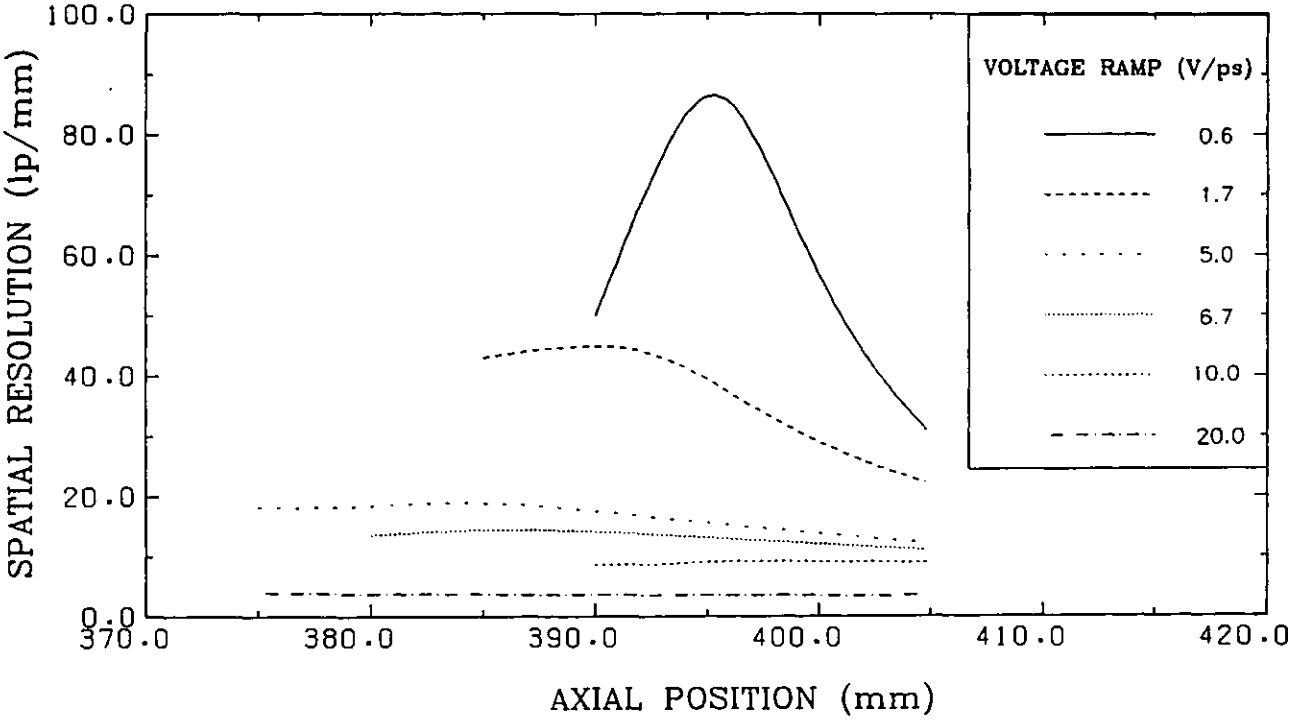

Fig. 4.7a Dynamic spatial resolution (streak direction) as a function of axial position, with phosphor screen response included.

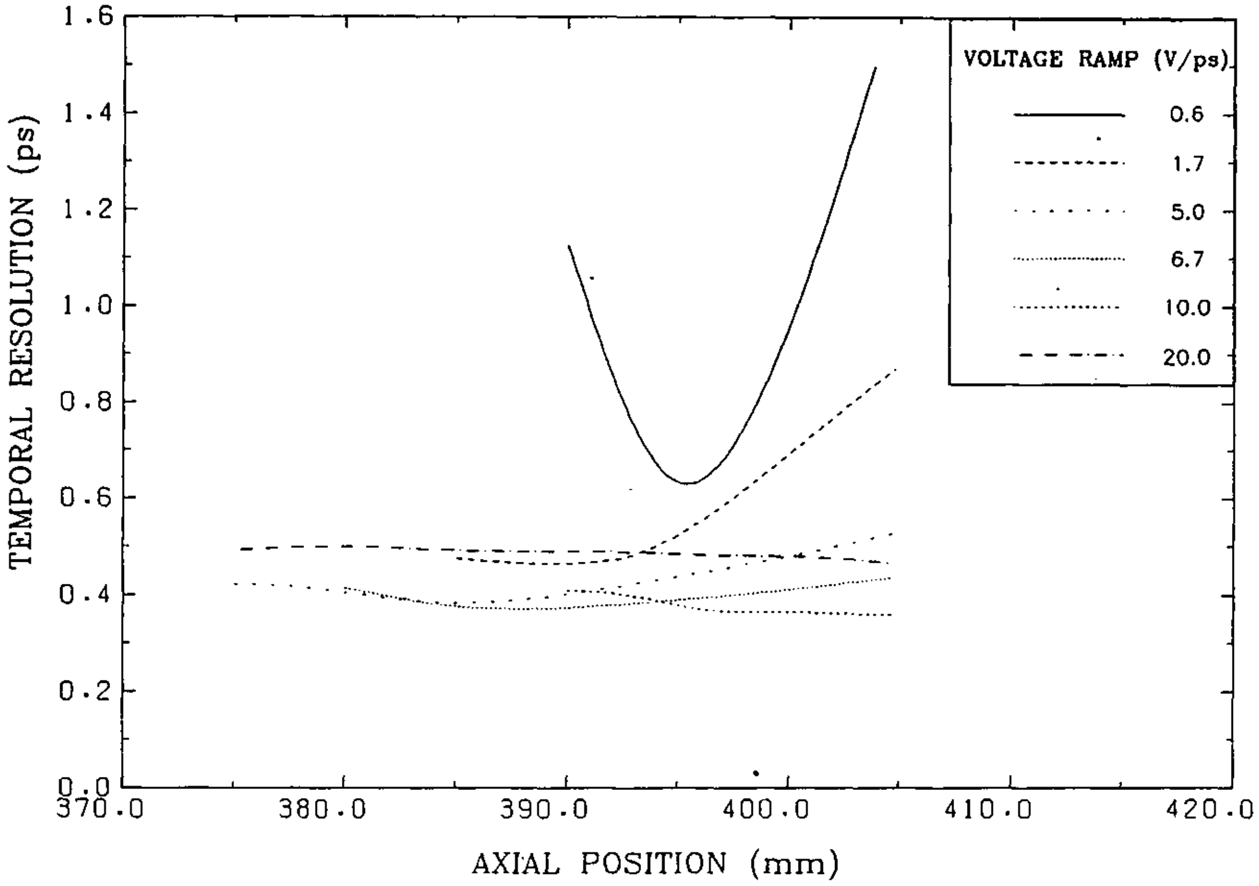

Fig. 4.7b Temporal resolution curves obtained from fig. 4.7a.

optimum plane (z = 401 mm) the response is no longer subpicosecond. On the other hand, at high voltage ramps (e.g. 1 x 10^{13} Vs^{-1}) the tube response has a large effective "depth of focus" and retains a subpicosecond value for a wide range of axial positions.

4.4.3 Optimum streak speed

It is obvious from figure 4.7b that a streak speed exists for which the temporal resolution is optimised. This is further evidenced in figure 4.8 in which the actual TMTF curves at the optimum plane for the Photochron IV are shown for four streak speeds. This is in qualitative agreement with the conclusions of Kinoshita et al (31), although the time dispersion of the photoelectrons at the entry of the deflectors was ignored in their model, and with the previous suggestions of an optimum streak speed (55, 113).

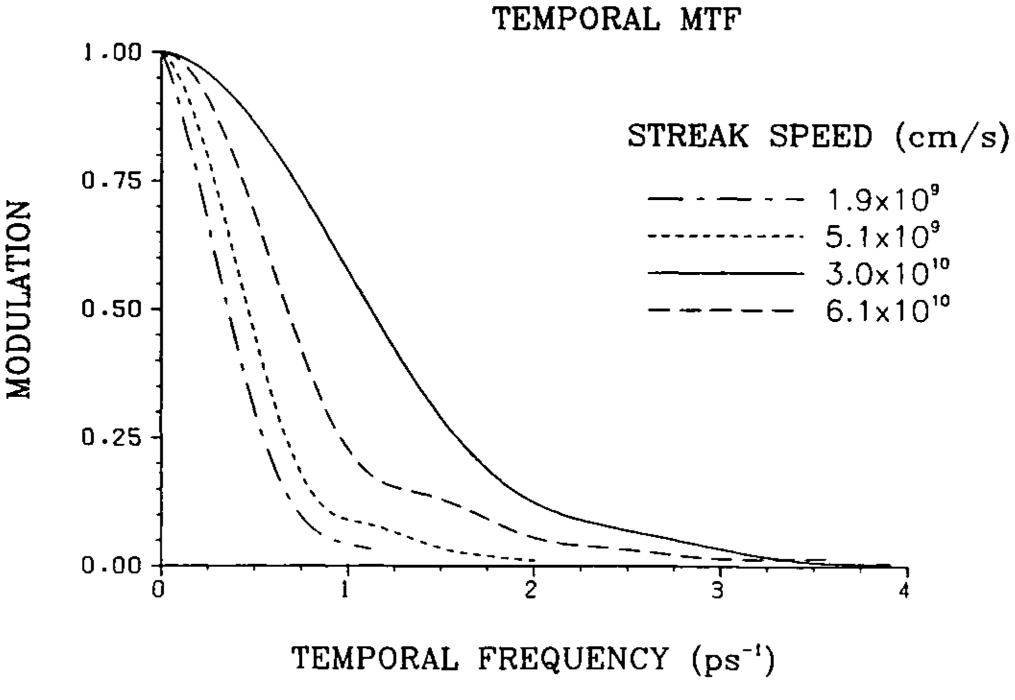

Fig. 4.8 TMTF curves at the optimum plane z = 401 mm.

At writing speeds lower than the optimum value the temporal resolution is limited by the spatial resolution capability of the phosphor screen (and also the image intensifier, although this is ignored in the computational analysis). At streak speeds higher than the optimum value the increased temporal dispersion within the deflectors causes a deterioration in the resolution from its best value (see section 4.6).

Another interesting feature which is evident in figure 4.7b, is that the best temporal resolution for each voltage ramp does not occur at the same plane. This is because complex dynamic deflection defocussing effects tend to shift the position of best spatial resolution (i.e. focus in the x direction after deflection) towards the cathode at higher voltage ramps. As a result, the optimum streak speed varies slightly in the range 2-3 x 10^{10} cms^{-1} as the axial position is displaced from 390 mm towards 405 mm (see fig. 4.9). At the best screen position of 401 mm, the optimum writing speed is 3 x 10^{10} cms^{-1}, resulting in a temporal resolution of 0.37 ps at the centre of the screen.(This is for an initial energy spread of 0-0.6 eV).

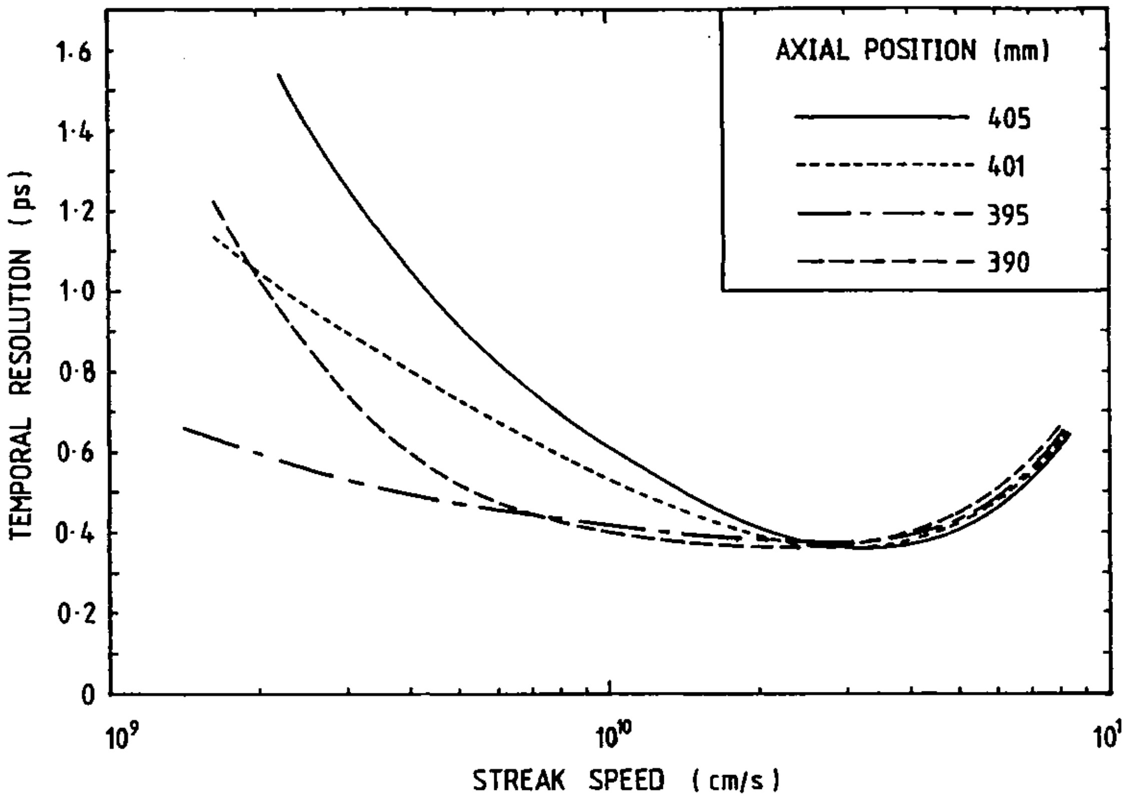

Fig. 4.9 Variation of temporal resolution with streak speed for four axial positions.

4.4.4. Variation of temporal resolution across the screen

The variation of the temporal resolution as the streak image is deflected to different positions on the phosphor screen (z = 401 mm) is indicated in table 4.8. These results at the optimum writing speed of 3 x 10^{10} cms^{-1}, show that the resolution remains relatively constant, with a value of approximately 0.4 ps, over the radius of the screen.

Table 4.8

Deflection on screen (mm)	0	6	12	24
Temporal resolution (ps)	0.37	0.41	0.41	0.45

This can be explained simply as follows. For the large voltage ramp used (1×10^{13} Vs^{-1}), a large bias potential is needed to display the streaks at the centre of the screen. The fringing fields at the entry of the deflection region are then large. However, for larger deflections smaller bias voltages are required, so the initial fringing fields are small. But now the fringe fields at the exit of the deflectors will be much larger. The net result is a temporal resolution which is essentially constant across the screen.

4.4.5 Limiting temporal resolution

When the cathode of the streak tube is illuminated at a wavelength close to the threshold of its photosensitivity, the resulting initial energy spread of the photoelectrons is very small, approximately 0 - 0.2 eV, with a FWHM of 0.1 eV. The TMTF has been evaluated at the plane z = 401 mm for the Photochron IV operated at the optimum streak speed, with these initial conditions. This is shown in figure 4.10, along with the similar curve for the Photochron II.

The limiting temporal resolution predicted theoretically for the Photochron IV is 180 fs. This is a fourfold increase on the corresponding limit of 0.69 ps for the Photochron II. (There is good agreement between this theoretical value and the measured experimental limit (19) of approximately 0.8 ps for the Photochron II.)

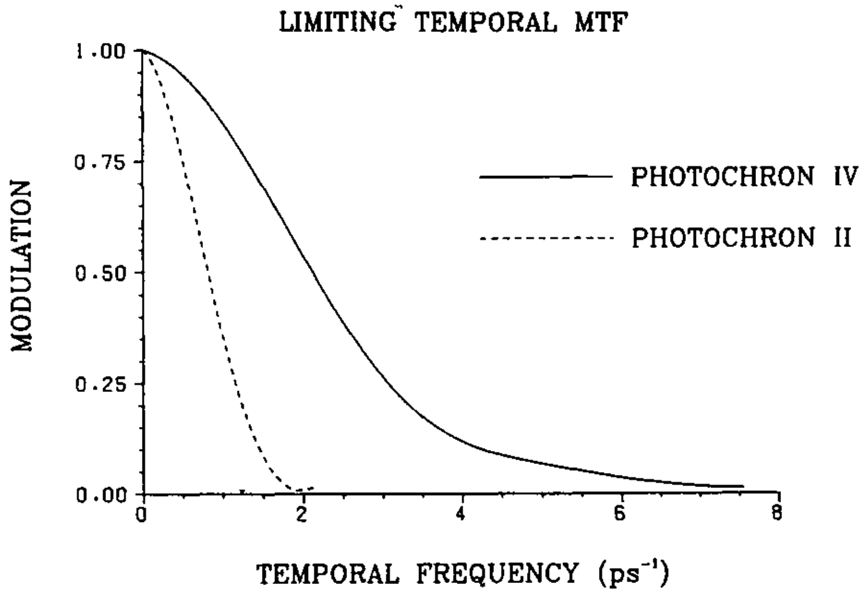

Fig. 4.10 TMTFs for Photochron II and IV tubes when the initial energy spread is 0 - 0.2 eV.

4.5 Dynamic spatial resolution in the slit direction

The calculated spatial resolution along the slit direction at the phosphor has been found to depend on the voltage ramp supplied to the deflectors. This is indicated in figure 4.11, where the MTF_y curves for four streak speeds are shown at the screen plane of $z = 401$ mm. At the optimum streak speed, the dynamic spatial resolution along the slit is 64 lp/mm.

Superficially, it may not be obvious that this spatial resolution should show a streak speed dependency, since the electron velocities along the y direction remain unaffected by the application of time dependent electric fields in the two-dimensional (x,z) deflection region. However, it is explained in section 4.6 that all the electrons experience an axial deceleration during their trajectories through the deflectors, the magnitude

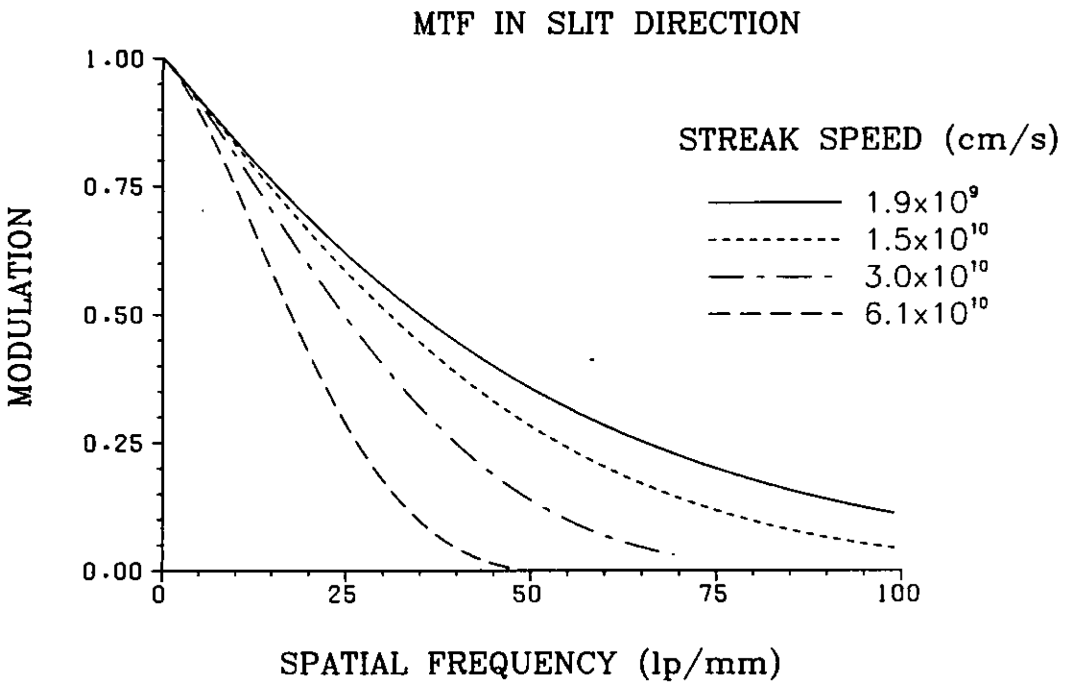

Fig. 4.11 Dynamic MTF_y curves at z = 401 mm.

of which depends upon their respective paths through the fringe fields. For larger amplitude voltage ramps, the axial velocities suffer larger reductions. The transit times to a given z plane then become larger causing a bigger LSF_y because the y component velocities are constant. This leads to a lower MTF-derived limiting spatial resolution. The plane at which this spread is least, and the spatial resolution is a maximum, tends to be shifted towards the cathode (and hence lower transit time).

4.6 Influence of the deflection fringing fields on temporal resolution

At high streak speeds the temporal resolution is limited by the increased degradation of the spatial resolution (along the streak direction). This effect is caused by the influence of the deflection fringing fields.

Initially the voltage on the top deflection plate is set to a negative bias and an ongoing positive ramp is applied. The value of the axial component of the electric field, E_z, is positive for all the photoelectrons, throughout the deflection region. This is particularly important where it has a high value, and this occurs close to the entrance and exit of the deflectors where the fringe fields exist. The electric field E_z induces a repulsive force on the electrons and they are decelerated. The magnitude of this field (and hence the deceleration) is position - dependent, so that electrons closer to the top deflection plate will be retarded by a larger amount than electrons close to the bottom deflector. This introduces a transit time dispersion for the electron signal within the deflection region.

At the slow streak speeds used in the calculation, the fringing electric fields are small. The deceleration of the photoelectron axial velocities is low, and so under these conditions the deflection - induced time dispersion is small. The spread of the slit image at the phosphor, and hence the temporal resolution of the tube, is thus dominated by the pre-deflection time dispersion.

For larger amplitude voltage ramps, the magnitude of the fringing fields becomes larger, leading to an increased deflection-induced time dispersion. Also, the

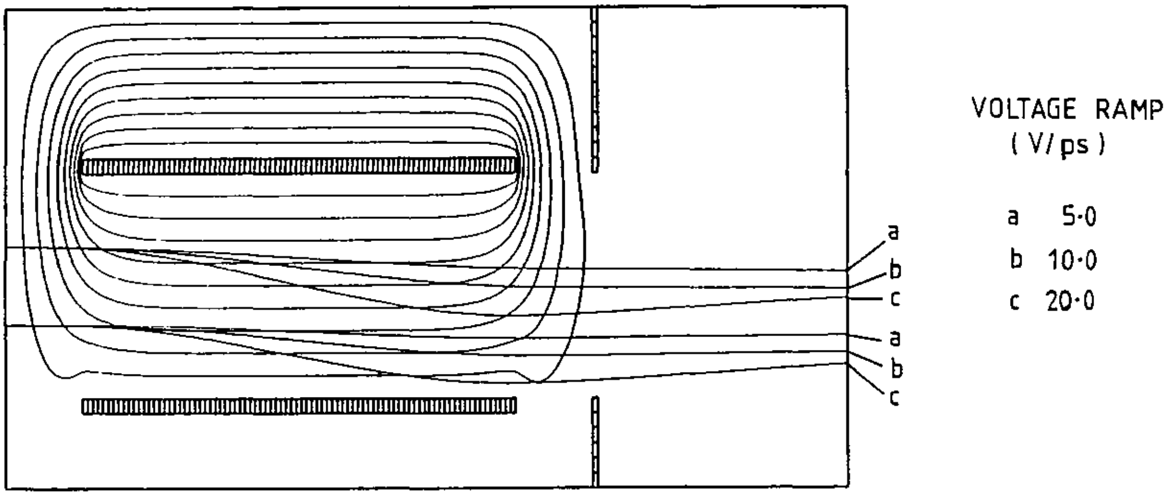

Fig. 4.12 Electron beam boundary trajectories through the deflection region for different applied voltage ramps.

electrons suffer an increased deviation towards the lower deflection plate, so that the influence of the fringing fields at the exit of the deflectors increases. With the application of a very large voltage ramp (e.g. 2×10^{13} Vs^{-1}) the deviation of the electron trajectories within the deflectors is large, as shown in figure 4.12. Some electrons may approach the bottom deflection plate where the fringe fields are most serious. The transit time dispersion within the deflection region due to these fields becomes large, and will cause the image at the phosphor to be spread over a bigger area. This will degrade the spatial resolution. Thus, there is a deflection voltage ramp dependent time dispersion, due to the fringe fields, within the deflectors which will limit the temporal resolution at high streak speeds.

4.7 Time resolution limited dynamic range

The TRL dynamic range (see section 1.6) of the Photochron IV has been studied by Niu (52). Assuming input pulses of duration 1,3 and 10ps, the variation of the ratio of the measured pulse width to the actual pulse duration (τ_r' / τ_r), has been calculated as a function of the current density. The results obtained are reproduced in figure 4.13

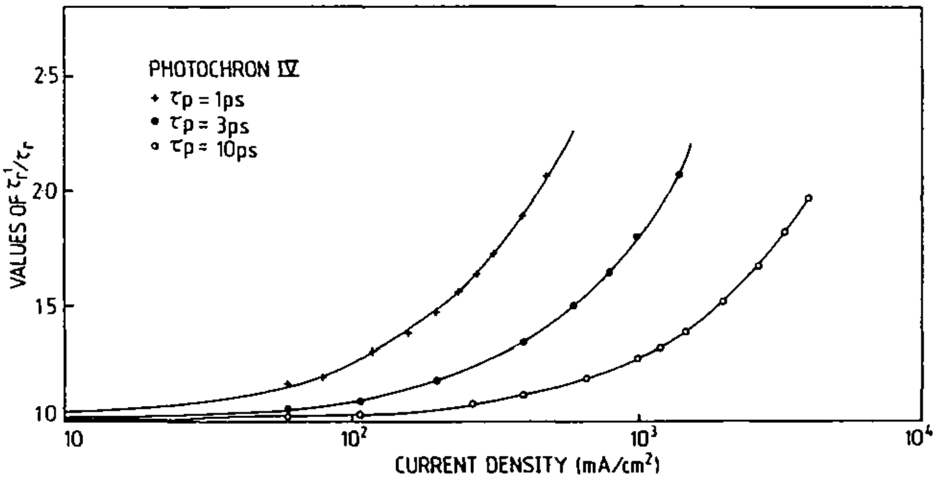

Fig. 4.13 Variation of (τ_r' / τ_r) as a function of current density for three input pulse durations.

To calculate the dynamic range from these curves, it is necessary to establish the noise equivalent current density which is temporal resolution dependent. By assuming the values of 0.5 ps and 2 ps for the temporal resolution, the dynamic ranges obtained for the curves of figure 4.13 are presented in table 4.9. It can be seen from these results that the effective dynamic range increases considerably for longer light pulses.

Table 4.9

Pulse duration ps	Temporal resolution ps	Dynamic Range
1.0	0.5	82
3.0	0.5	227
10.0	0.5	723
3.0	2.0	911
10.0	2.0	2891

4.8 Conclusions

In conclusion, the Photochron IV streak image tube has been designed theoretically to achieve state-of-the-art femtosecond resolution over a wide spectral range, with an improved dynamic range. In this design, not only is the electric field at the photocathode increased, but the fields throughout the focussing region are maximised.

Table 4.10 Theoretical performance characteristics of the Photochron II and IV streak tubes.

Characteristic	PC IV	PC II
Extraction electric field (kV/cm)	50	20
Static resn. at screen (lp/mm)	64	32
Magnification	-1.97	-1.97
Temp. resn. ($\Delta\varepsilon$ = 0 - 0.6 eV)	0.37ps	1.41ps
Limiting temp. resn.	180fs	0.69ps
Optimum streak speed (cms^{-1})	$3\text{x}10^{10}$	$1.25\text{x}10^{10}$
Temp dist. at r = 2 mm	0.77ps	2.92ps
Dynamic range	911	150

The salient characteristic performance figures for the Photochron IV are summarised in table 4.10. The corresponding theoretical results for the Photochron II are also presented for direct comparison. The temporal resolution of the Photochron IV is subpicosecond and is markedly superior to that for the earlier Photochron II. When the tube is operated at wavelengths close to the cut-off of sensitivity of the photocathode, the resolution is likely to be truly femtosecond. The TRL dynamic range of the Photochron IV is also larger than that of the Photochron II, as seen in the table for the comparable conditions of a tube time resolution of 2 ps with an input pulse of 3 ps.

An important conclusion which has been drawn from this work is that an optimum streak speed exists for which the best temporal resolution is attained. This results from the deterioration of the dynamic spatial resolution along the streak direction at higher streak speeds, due to a deflection - induced temporal dispersion which arises from the large influence of the fringe fields. It is worth noting here that the optimum streak speed is not necessarily the same for different streak tubes.

CHAPTER FIVE

THE EXPERIMENTAL PHOTOCHRON IV STREAK CAMERA

5.1 Introduction

In the construction of an experimental version of the theoretically designed Photochron IV streak tube first preference was given to the use of "off-the-shelf" components and available technology. To accommodate this constraint, the electrode diameters have had to be reduced to 42 mm.

For this slightly modified version, the potential applied to the second focussing electrode would have to be increased to 5.35 kV to retain the same paraxial focus plane. Under these conditions the best compromise image plane is located at a distance of 402 mm from the cathode. Both the static and dynamic performances of this tube are very similar to those previously described (in chapter 4), for example the temporal resolution at the optimum streak speed of 3×10^{10} cms^{-1} is also 0.37 ps.

5.2 Construction of the streak image tube

An experimental version of the Photochron IV streak tube was fabricated in collaboration with the Electron Tubes Division of Thorn - E.M.I. The metal electrode parts (e.g. the focussing cylinders, the mandrel, spacer rings, the deflection plates and mechanical jigs) were prepared

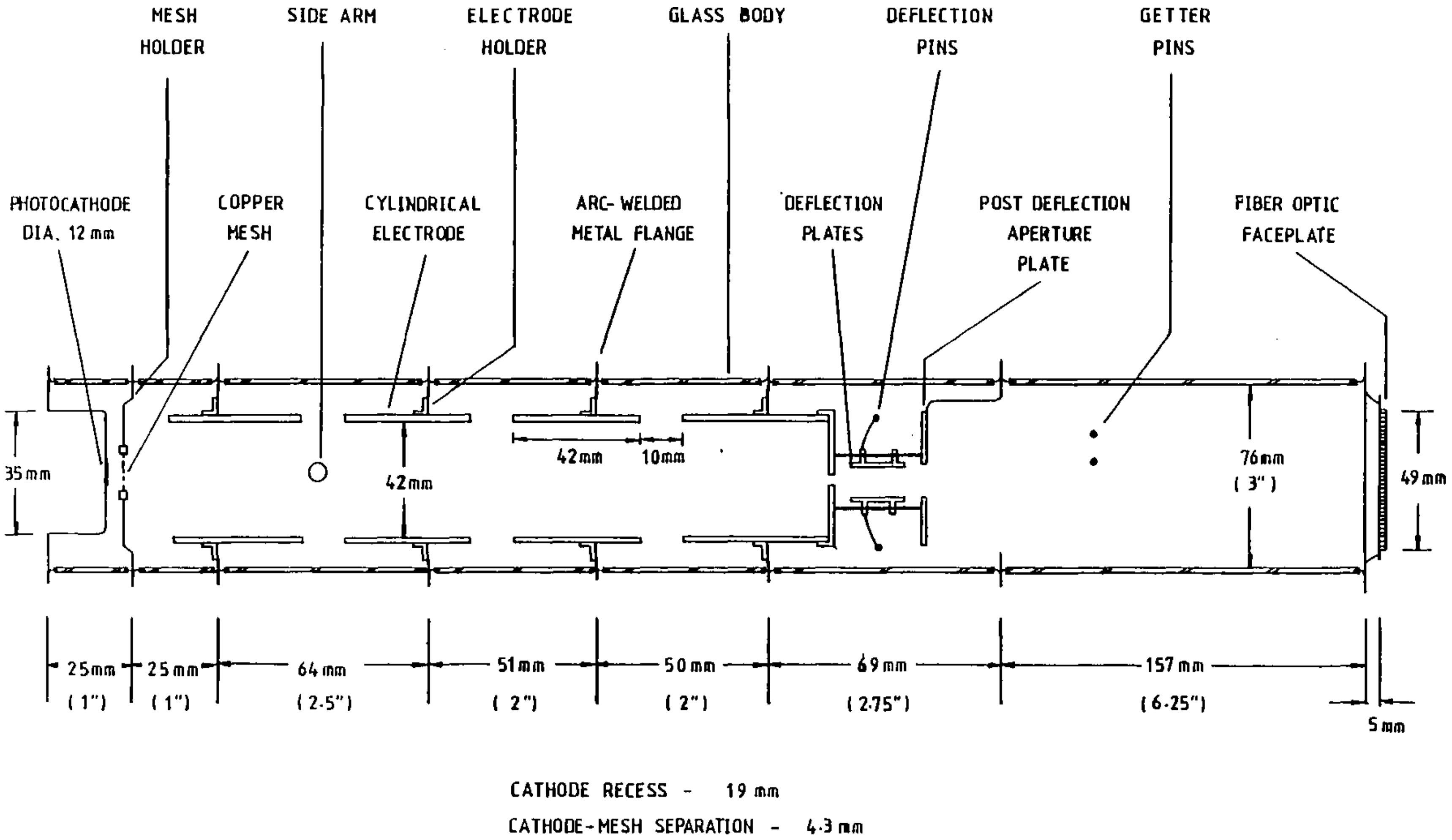

Fig. 5.1 Cross-sectional schematic of the constructed Photochron IV.

in the workshops of the Optics Group, Imperial College prior to inclusion in the streak tube.

The four polished, stainless steel focussing electrodes were positioned, relative to the micromesh electrode, using a tubular metal mandrel and spacer rings to an accuracy ~50 μm, with axial and concentrical tolerances ~25 μm. Once positioned, a stainless steel annulus was spot welded to the electrode. The electrode was then fixed in place by securing the annulus between the two metal flanges of adjoining glass envelope pieces (see fig. 5.1). These were argon arc-welded together using industrial technology.

The deflection arrangement is shown in figure 5.2. The deflector plates (17 mm x 15 mm) were machined at Imperial College, from stainless steel. Two small metal holders were spot-welded to machined lugs on each deflector to locate the ceramic rods used (two per plate) to secure the deflectors in position between the anode aperture and the

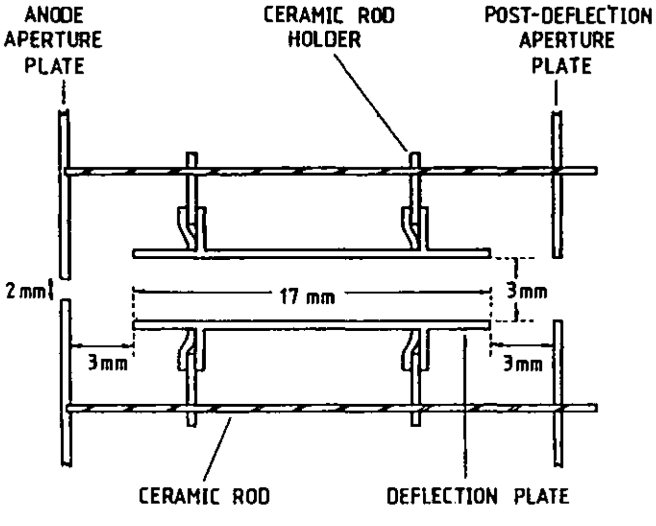

Fig. 5.2 Arrangement used for the deflection section.

post-deflection aperture. This plate was thus electrically isolated from the anode. The assembly was clamped in position with a removable, locking spacer, and brazed to form a permanent, prefabricated arrangement for inclusion in the streak tube.

The deflection arrangement was spot-welded to the second anode electrode. The electrical connections to the deflectors were made by gold-plated nickel wire to two deflection pins sealed in the glass wall. The capacitance of the deflection plate arrangement is low ($\sim$ 1 pF) so the rise time of the voltage ramps applied will be limited by the inductance of the circuit.

The mesh used in this tube is a standard E.M.I., 60 cells per mm, copper micromesh spot-welded under tension between two thin metal retaining rings. The transmission of the mesh is $\sim$ 30%, and its diameter is 17 mm. Two problems arise with this type of mesh support. The first is that the retainer rings suffer surface blemishes at the spot-weld marks, and these can cause field emission at high voltages (114). Secondly, the retainer ring stands "proud" of the mesh, so that this ring is closer to the photocathode than is the mesh. Thus the electric field is maximised at the edge of the mesh support rather than at the mesh. Also with the application of high electric fields, the meshes can rupture if they are not completely flat. To avoid any such problems, which might have delayed the evaluation of the camera performance characteristics, the cathode -

mesh separation was chosen to be 4 mm rather than 2 mm for the initial experimental tube. (In fact, in practice this separation was 4.3 mm, so limiting the extraction electric field to 23.3 kV cm^{-1}). The mesh is located in a stainless steel holder secured between two metal flanges, which are arc-welded together.

The streak tube has a P11 type phosphor deposited on a 49 mm diameter fiber-optic faceplate which was arc-welded onto the back end of the tube. The front-end was sealed-off by arc-welding a zinc crown glass window to it.

An S20 photocathode was activated on the front window, the chemicals needed being introduced via the two glass side-arms shown in figure 5.1. Prior to activation, the window had a layer of chromium vacuum-evaporated onto it for electrical conduction. The central 12 mm diameter area has approximately a 50% transmitting, conducting layer, whilst the remaining area has a much thicker chromium deposit.

The tube had a zirconium getter included in it. This can be fired by application of current, to absorb any gas left after bakeout. The final vacuum within the tube should be better than 10^{-8} Torr. Because of the use of readily available glass envelope sections, of diameter 76 mm ($\sim$3"), the overall length of the sealed-off image tube is $\sim$445 mm ($\sim$17.5"), corresponding to a cathode-screen distance approximately 25 mm longer than originally intended in the computed design study.

The streak tube has been mounted within the streak camera chassis as illustrated in figure 5.3. In operation, the phosphor screen is grounded to the stainless steel body, and so the cathode end is electrically insulated from the body via a nylon insulator. A sheet of printed circuit board has been included for mounting the deflection circuitry, and to isolate the focussing section of the tube from any RF applied when the tube is used in the synchroscan mode of operation. Not shown in figure 5.3 is the outer casing made from stainless steel sheet.

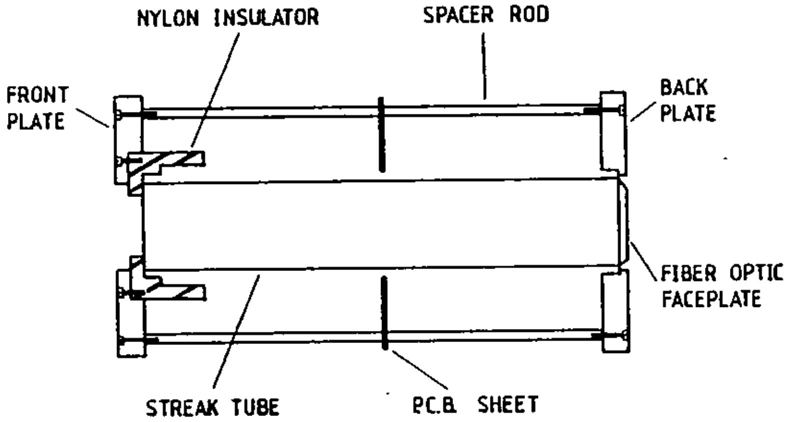

Fig. 5.3 Streak camera chassis.

5.3 Static performance of the Photochron IV

To minimise the number of power supplies required to provide the voltages to the electrodes, and hence to simplify the system and reduce the likelihood of voltage ripple affecting the results, a voltage divider network was employed to derive the necessary potentials. For a supply EHT voltage of -18 kV the voltages supplied to the mesh, the first and second focus electrodes could be independently adjusted in the respective ranges -8/-9 kV, -9/-10 kV, and -12/-13 kV. The photocathode voltage was fixed at -18 kV and the second anode was grounded, with the phosphor screen, to the camera body. The voltage of +6 kV was applied independently to the first anode.

Using a Baum projector (115), the image of a resolution test chart was focussed onto the cathode of the Photochron IV. The variable voltages were adjusted until the image of the Baum chart formed at the centre of the screen was optimally focussed, as seen through a microscope. A typical set of operating potentials is indicated in table 5.1. The static spatial resolution of 70 lp/mm has been measured at the photocathode for both the x and y directions, and the electron-optical magnification was determined to be -2.1 (116). This corresponds to a limiting resolution of 33 lp/mm at the centre of the phosphor screen.

Table 5.1

Electrode	Cathode	Mesh	FFE	FA	SFE	SA
Potential (kV)	-18.0	-8.75	-9.86	+6.0	-12.36	0.0

With the tube focussed, the variation of the limiting spatial resolution across the phosphor screen was studied by applying symmetrical deflection voltages of ±V to the deflection plates. In this case, the deflection sensitivity was measured to be 3.69 cm/kV. (This is in agreement, to within 6%, with the extrapolated theoretical value of 3.5 cm/kV at the plane z = 430 mm.) The resulting curves of spatial resolution versus deflection voltage

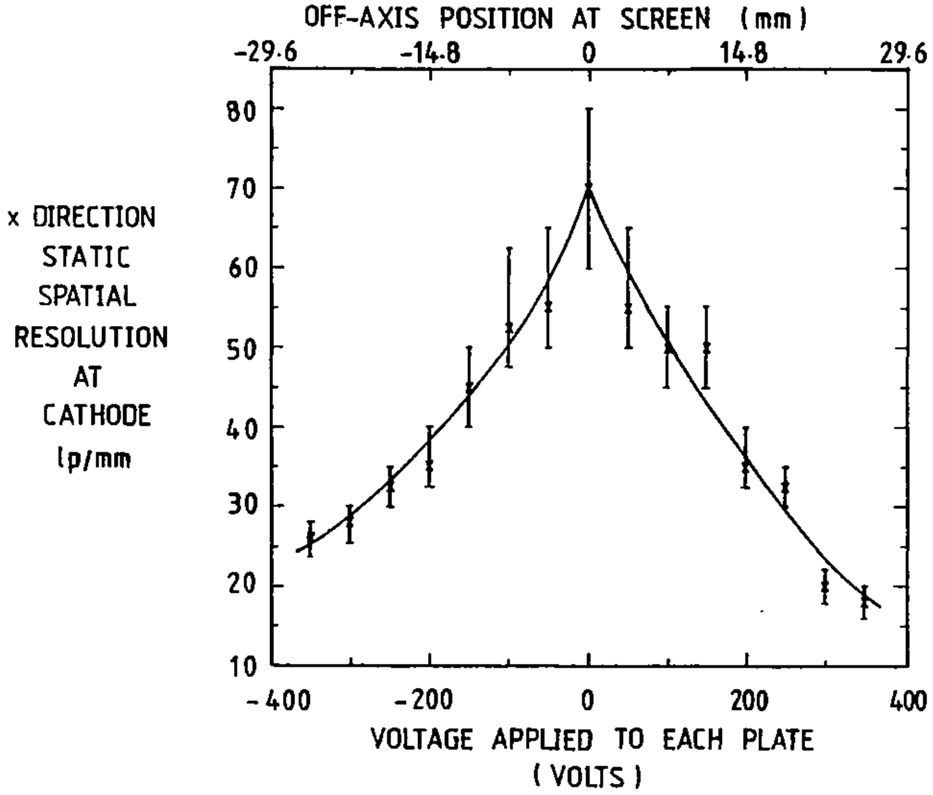

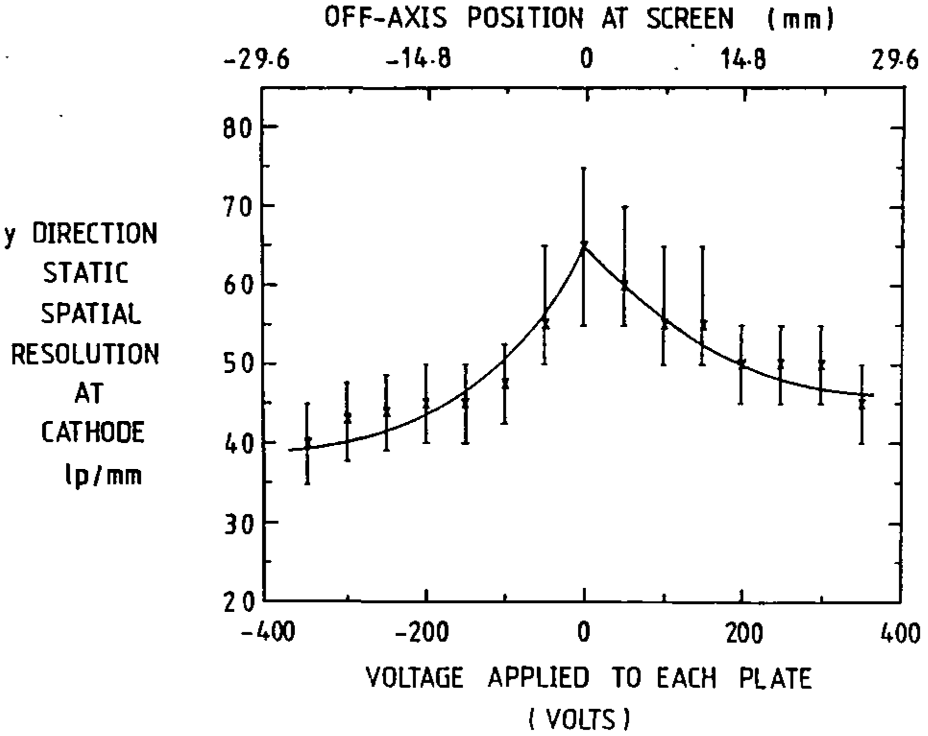

Fig. 5.4 Static spatial resolution as a function of phosphor position.

(and hence position) are presented in figure 5.4 for both the x (streak) and y (slit) directions. In these curves, the error bars are larger for high spatial resolution because of the greater difficulty in making quantitative measurements at high resolution.

It can be seen that both curves are asymmetric about the zero (or screen centre) position. This indicates that there is some misalignment in the focussing section. There are a number of possible causes of this misalignment: a) the axiality and concentricity of the four cylindrical electrodes is initially good, but these may be distorted when the tube is heated during bakeout; b) the cathode and/or the mesh may be in a position which is not normal to the axis of the tube; c) the phosphor may be misaligned with respect to the axis. In all likelihood, it is a combination of these effects which is causing the asymmetric response.

The spatial resolution decreases in both directions at large off-centre screen positions. This is due to deflection defocussing effects (26). The tube does seem to suffer some astigmatic deflection aberration, as evidenced by the drop in resolution in the x direction compared to that in the y direction at the same off-axis position. However, there is little or no sign of astigmatism near the centre of the screen. It is possible to improve the spatial resolution off-centre in the x and y directions by refocussing the image tube to select a compromise plane, but this is achieved at the expense of lower spatial resolution at the centre of the screen, and generally has not been practiced. In streak experiments, it is the central 22 mm section of the phosphor which is used, and for this region the spatial resolution at the photocathode is >40 lp/mm.

5.4 Synchroscan operation of the Photochron IV

5.4.1 The ring dye laser system

The source of the hypershort light pulses used to test the Photochron IV in both the synchronously operated, and single-shot, experiments was a colliding pulse, passively mode-locked, cw ring dye laser (68) shown in figure 5.5. The gain medium was a 1.5×10^{-3} M solution of Rhodamine 6G and the saturable absorber was DODCI (3,3 diethyloxadicarbocyanine iodide) at a concentration of 2×10^{-4} M, both dissolved in ethylene glycol. Both dye jets were situated at the focus of a folding section made up of two 100% reflecting, 10 cm focal length mirrors. The Rh 6G was pumped by an unmode-locked cw Argon ion laser.

The DODCI was positioned a quarter of the way round the laser cavity to allow the Rh 6G the same gain recovery time after depletion by each of the two counter-propagating pulses (2).

A tuning wedge was included in the cavity to select the laser pulse wavelength of 617 nm at which largest gain results (117). Two of the cavity mirrors were 100% reflecting, while the output mirror had a reflectance of 98%.

With this system pulses of duration as short as 200 fs are produced, with an average output power of 5 mW. The round-trip time of the laser cavity is ∿12 ns and this is equivalent to an output pulse frequency of 82 MHz.

5.4.2 Experimental arrangement

The Photochron IV has been studied in the synchroscan mode, and the experimental arrangement used is shown in figure 5.5. One of the two output pulses from the cw ring dye laser system was directed through a Michelson type optical delay. The mirrors were set so that the delay between the two subpulses was 33 ps. These subpulses were incident on a 30 μm width slit, and were then focussed by a 4:1 demagnifying lens onto the photocathode of the streak tube.

The second output pulse from the dye laser was directed into a photodiode. This provided the voltage signal used to trigger a tunnel diode-oscillator, which produced a sinusoidal waveform with a frequency of 82 MHz. This was frequency doubled to 164 MHz and amplified to a power of the order of 10 W, before being used to drive the deflector plates via a high -Q coupling coil in close proximity to a copper loop

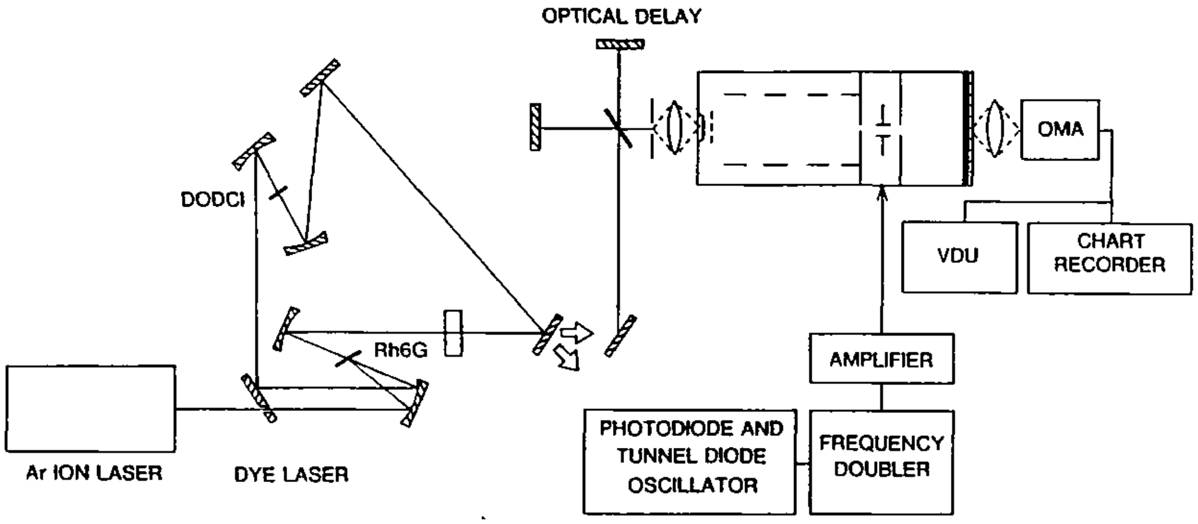

Fig. 5.5 Experimental arrangement of the Photochron IV synchroscan streak camera and passively mode-locked cw ring dye laser.

attached to the deflection pins.

The output of the streak tube was focussed onto the silicon intensified target (SIT) vidicon camera by a relay lens with magnification of x 4. The vidicon has a useful area of 12.5 mm (long) x 10 mm (high) containing 500 diodes each separated by 25 μm. Charge leakage between adjoining diodes in this array limits the effective spatial resolution to 15 lp/mm. The vidicon was part of an optical multichannel analyser (OMA), type B & M Spektronik OSA 500. This has a data storage capability of 30 memories of 499 channels. The scanning time for 500 channels is 32 ms, so that the OMA output seen on the visual display unit is an integration of approximately 10^6 pulses. Hard copy could be taken using a chart recorder.

5.4.3 Synchroscan results

The application of an RF power of 9 W to the deflector plates produced a measured streak speed of ∿ 4 x 10^9 cms^{-1} at the phosphor screen. The power efficiency of the Photochron IV can be compared favourably to that of the Photochron II where an RF power of 20 W was needed to provide a similar streak velocity (65). The intensity profiles of a pair of recorded streak images, showing a temporal resolution of 2.2 ps are reproduced in figure 5.6a. The theoretical temporal resolution for the Photochron IV with an extraction electric field of 25 kV/cm at the cathode is 1 ps at this writing speed, but this is for a single linear ramp. The slight discrepancy is probably due to an averaged jitter component (see chapter 1).

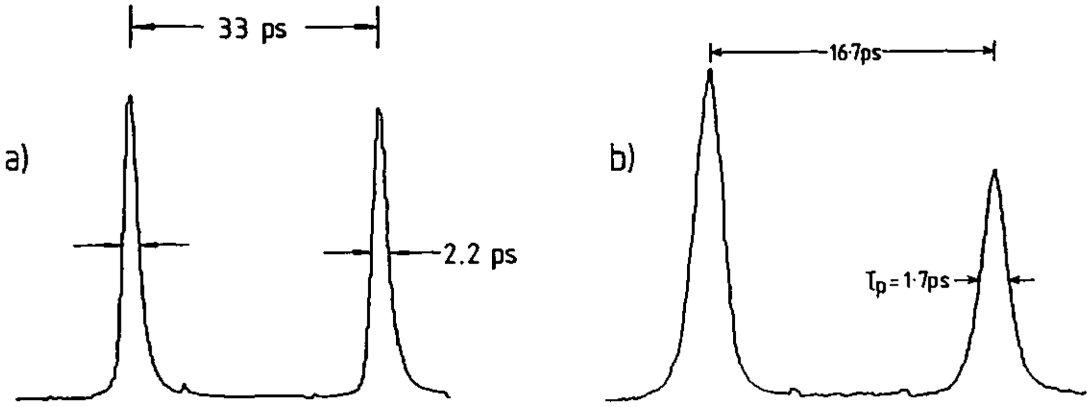

Fig. 5.6 Intensity profiles of streak images recorded in synchroscan operation with anode potential of a) 18 kV, b) 15 kV.

The low photocurrents and current densities in the streak tube operated synchronously (66) ensure a high dynamic range. This relaxes the requirements, described in chapter 4, of high voltages and electric fields throughout the focussing region. To increase the deflection sensitivity, the voltages applied to the Photochron IV were all reduced by 17%, so that the electrons acquired a final energy of 15 keV prior to deflection. (The static width of the slit was measured to be 8 channels under these conditions, instead of 7 channels for the usual operating potentials.) Combining these lower voltages with a shorter coupling loop to increase the amount of coupled radiation to 12 W, provided a faster writing speed of $\sim 6.5 \times 10^9$ cms^{-1}. The measured temporal resolution for this case was 1.7 ps (see figure 5.6b).

5.4.4 Multipactor discharge

It has been noticed during the synchroscan experiments, that sometimes a glow discharge is observed in the deflection region, resulting in a fogging of the screen information. This effect is known as multipactor discharge and has been observed by other workers (118, 119). This is usually only a serious problem at particularly high RF powers.

Stray, low energy electrons between the deflection plates are accelerated to one of the deflectors upon application of RF voltage. If the voltage is high enough, these can produce secondary electrons when they collide with the electrode surface. If the synchronization is correct these secondaries may be attracted to the opposite deflection plate as shown in figure 5.7, creating associated secondaries of their own at this plate. Replication of this process leads to electron

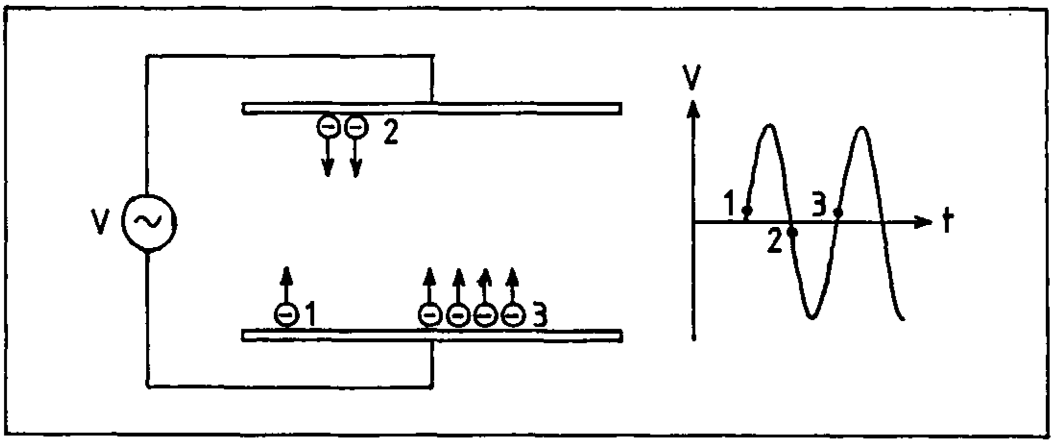

Fig. 5.7 Origin of multipactor discharge.

multiplication. If it is sufficiently high this can initiate ionization of gas molecules or alkali metal atoms on the deflection plate or glass surfaces by electron bombardment. The luminescence produced irradiates the photocathode generating a large enough background noise to swamp the signal being studied at the screen. This ionization also reduces the effective life of the tube by degradation of the photocathode.

The multipactor discharge depends on the secondary electron emission ratio of the electrode surfaces, the spacing between the deflector plates, and the strength and frequency of the applied RF signal. Kinoshita et al (119) have tried reducing the discharge by suppression of the secondary electron emission. They have shown that by preventing the adhesion of alkali metal vapour molecules to the surface of the deflectors during activation of the photocathode, it is possible to eliminate the discharge. However, this is not completely feasible in the fabrication of the Photochron IV tube, and a certain amount of contamination of electrode surfaces is likely.

One method for eliminating the discharge has been found to be the application of a small electric field in the deflection region, whose lines of force lie parallel to the axis of the tube (120). This removes the low energy stray electrons from the region between the deflection plates without noticeably affecting the high energy signal electrons. This electric field has been applied by changing the potential on the second anode to -200 V whilst leaving the post-deflection aperture plate at earth potential. No multipactor discharge was observed even with an RF power as high as 20W.

A preferable arrangement is to apply the field so that the stray electrons are attracted in a direction away from the phosphor screen. This has been achieved by supplying the anode with a voltage as low as +40 V, again leaving the post-deflection aperture plate at 0 V, and has eliminated the discharge. From these results, it can be concluded that when the Photochron IV streak tube is used in the synchroscan mode of operation, a small, non-zero, potential should be applied to the anode aperture plate to remove any high - RF discharge problems.

5.5 Single-shot operation of the Photochron IV

5.5.1 The Photochron IV streak camera

The Photochron IV streak camera arrangement used for the single-shot experimental studies is shown schematically in figure 5.8. The slit, of width 16 μm, is focussed into the photocathode by a Tektronix f1.3, 80 mm focal length lens. The lens has a demagnification

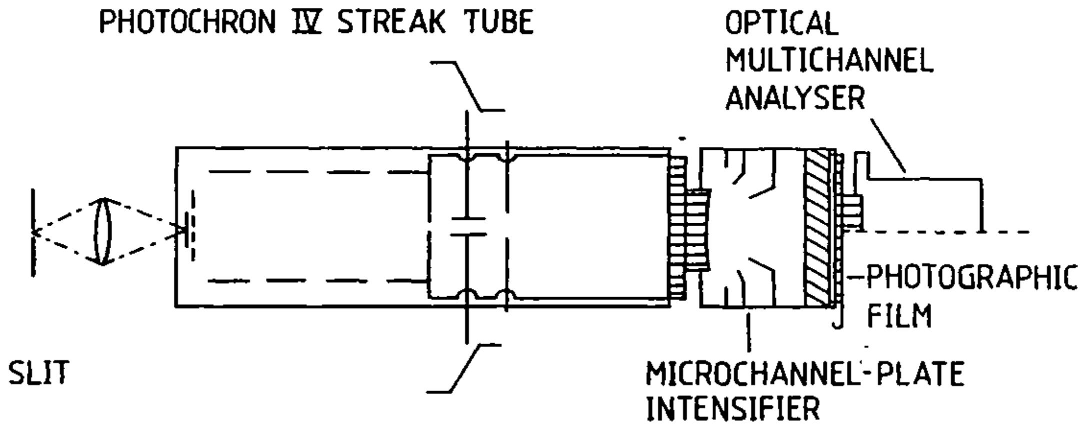

Fig. 5.8 Schematic of the Photochron IV single-shot streak camera.

of x 1.85, so that the overall magnification between the slit and its image on the phosphor screen is x 1.1.

A Philips 21 XX image intensifier is coupled to the output of the streak tube by a 20 mm long, 20 mm diameter fiber-optic cylinder, and is held in position by a spring-loaded pressure plate. The intensifier is an inverting, microchannel plate (MCP) intensifier with electrostatic self-focussing, and has fiber-optic input and output windows. It has a 19 mm diameter photocathode, and a magnification of x 1.5. The operating potentials, in kilovolts, are -5.4, -4.5, -3.5, -1.1, and 0 for the cathode, MCP input, MCP output, anode, and screen respectively. This intensifier provides a nominal light gain $\sim 10^5$ (112). Although the limiting spatial resolution is high, being 50 lp/mm, this drops very quickly to only 15 lp/mm at 45% contrast (112).

The limiting static resolution of the camera has been measured both with and without the intensifier, using a standard 1951 USAF resolution test chart positioned at the slit plane. The results obtained are presented in table 5.2. It can be seen that although the spatial resolution of the streak tube itself is good, the addition of the input lens and the MCP intensifier place a severe limitation on the overall camera response. For maximum resolution, whilst still retaining sufficient light through-put, the lens was usually operated at f5.6 in the single-shot experiments. Clearly for future work, input optics with better MTF characteristics would

Table 5.2 Spatial resolution at screen plane for the streak camera.

Experimental conditions	Resn. x lp/mm	Resn. y lp/mm
Streak tube	33	33
Streak tube + Lens (f1.3)	23	20
Streak tube + Lens (f5.6)	26	23
Streak tube + Lens (f1.3) + MCP	13	10
Streak tube + Lens (f5.6) + MCP	14	14

be required, and this is true also for the image intensifier and detector used.

5.5.2 The four stage dye amplifier

The energy of the output pulses from the ring dye laser, described in section 5.4.1, is ∿20 pJ with a peak power ∿100 W (117). This is insufficient to activate a GaAs photoconductive element, used to derive the deflection voltage ramp (see chapter 1), and so amplification is necessary. The amplifier used is a 4 stage dye amplifier (117) providing a gain ∿ 2×10^7.

Kiton red was used as the first stage dye, while Rhodamine 101 was used for the other stages. The first three dye cells were pumped transversely and the fourth stage pumped longitudinally. Each amplification stage was isolated by either spatial filters or saturable absorbers to reduce the amount of amplified spontaneous emission (ASE), otherwise this ASE would deplete the gain from the following amplifying stages. It would also be directed back into the ring system, eventually destroying the DODCI by photodissociation.

The four dye amplification stages were pumped by the frequency-doubled output from a Q switched Nd:YAG oscillator. These pulses at 532 nm, were produced at a repetition rate of 10 Hz. They had a duration of approximately 15 - 20 ns, an energy of 150 mJ and provided peak powers of 10 MW.

To acquire maximum amplification the dye laser pulses must arrive at the amplifier dye cells at the peak of the Nd:YAG pulse. This synchronisation was achieved by triggering the Pockel's cell Q-switch from the 82 MHz frequency sinewave voltage produced by the tunnel diode circuitry (see section 5.4.2) via an electronic trigger (117). The measured jitter between the Q-switched pulse and the dye laser pulse was ∿ 1ns. Under these conditions, the peak power of the dye laser pulses after amplification was ∿2 GW, with a relatively small pulse broadening to 0.25 ps.

5.5.3 The deflection voltage ramp generator

The driving voltage applied to the deflection plates was produced by the circuit of fig. 5.9, using a semi-insulating, Cr-doped GaAs switch, with a recombination time of ∿100 ps (57). The deflection circuit operates as follows. When a voltage of V = 3 kV is applied, initially the voltage at A is 3 kV, while B is at 0 V, since the GaAs is not conducting. Upon irradiating the GaAs switch, its resistance drops to $\lesssim 1\ \Omega$, and the voltages at A and B become identically equal to 1.5 kV. Since the voltage at A has dropped by 1.5 kV, the voltage at C must also drop by this same amount. Conversely, the potential at both B and D increases by 1.5 kV. Then, because of the applied bias voltages, the voltage to the deflection plates change from + 750 V to -750 V, and vice versa, producing symmetrical deflection. The high values of resistors R_1 and R_2 ensure that the GaAs switch

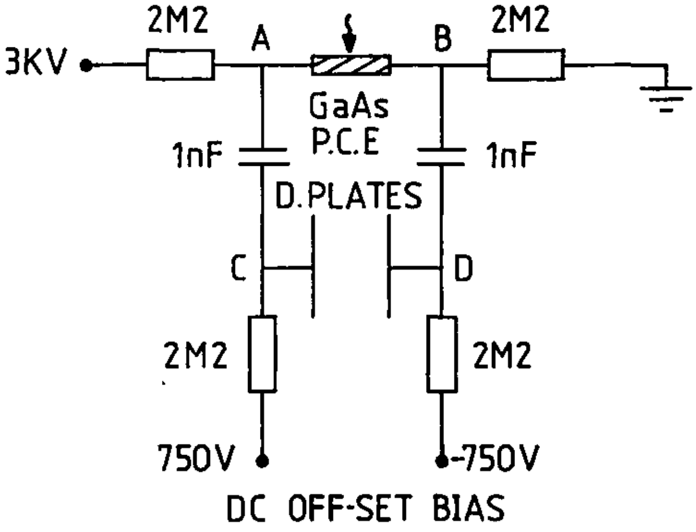

Fig. 5.9 Deflection voltage ramp generator circuit.

remains conducting for up to ∿1ns, since efficient switching will prevail until the resistance of the GaAs has returned to a value significantly greater than R_1 or R_2 (see section 1.7.1).

The switch deflection arrangement was mounted from the PCB sheet (included in the camera body - see section 5.2), directly above the deflection pins to minimize any stray inductance. The amplified laser pulse was tightly focussed onto the switch by a cylindrical lens. Initially a GaAs switch with a 1 mm gap between the silver-painted electrodes was used, with an applied voltage of 3 kV. For later experiments this was replaced by another GaAs switch with a gap dimension of 0.8 mm so that the light pulses could be focussed more tightly onto the switch. This causes increased saturation, providing a longer switch time hence reducing the jitter. In this case the voltage was reduced to 2.5 kV, to avoid damaging the switch.

The writing speed produced by the switch circuit is dependent upon the energy of the light irradiating it, so that any fluctuations in the intensity of the amplified pulses can lead to varying streak velocities. With the GaAs arrangement, the best observed streak speed was 2×10^{10} cms^{-1} at the phosphor. The jitter of the images at the screen was low, as expected for a semiconductor switch circuit (58).

5.5.4 The experimental arrangement

The single-shot experimental arrangement used to test the Photochron IV streak camera is shown in the block diagram of figure 5.10. The gigawatt amplified pulses were directed through a manually-operated camera shutter onto a pellicle beam splitter. Approximately 90% of each pulse was used to irradiate the semiconductor switch deflection drive circuit, while the other 10% was sent to an optical delay line, consisting of three 1 mm thick microscope glass slides, separated by 1.5 mm. This provided a set of 6 subpulses, with temporal separations of 10 ps, by the 4% quasi-normal reflections from the front and back surface of each slide (e.g. see fig. 1.1). After attenuation, by neutral density filters, these subpulses were directed into the streak camera. The manual camera shutter ensured that only one set of subpulses illuminated the cathode of the streak tube at a time.

The streak camera has been used with both film and OMA recording of the output signal. In the former

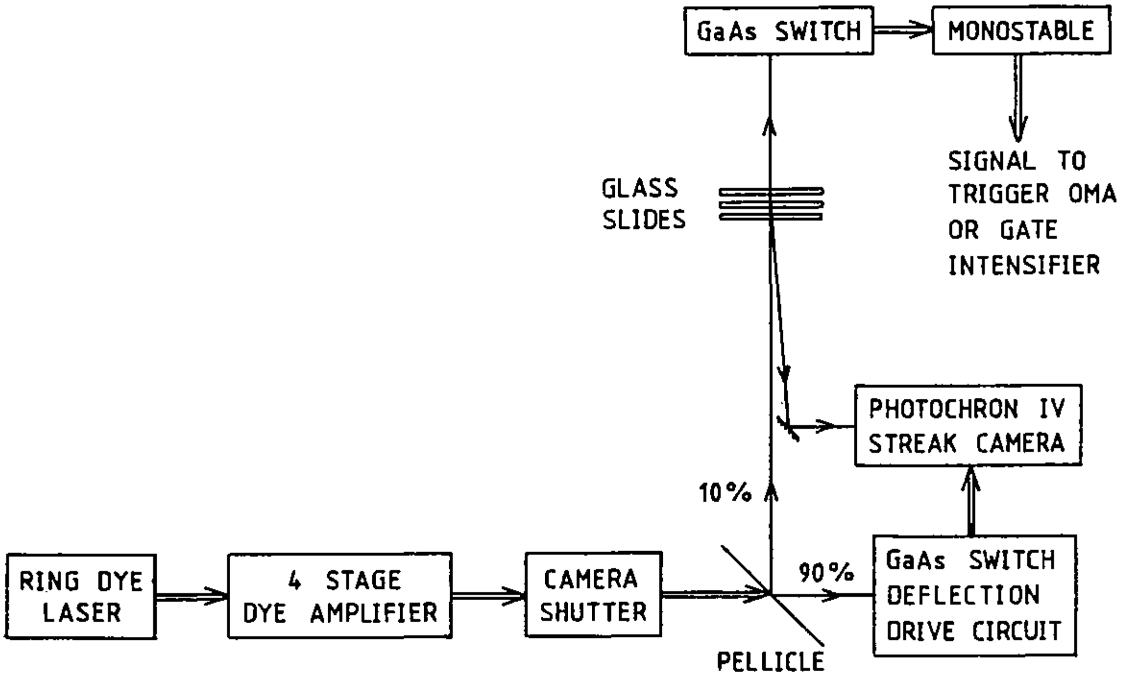

Fig. 5.10 Block diagram of the single-shot streak camera experimental arrangement.

instance, Ilford HP5 (ASA 400), 35 mm photographic film was in direct contact with the output fiber-optic window of the MCP intensifier. The large, accumulative background on the intensifier screen caused severe fogging of the film, and it was necessary to gate the intensifier to operate only for the short time prior to, and during, camera illumination. This was achieved by running the intensifier with its cathode at -4.4kV, so that the emitted electrons initially experience a repulsive electric field between the cathode and the MCP. Applying a -1 kV pulse to the cathode, to reduce its voltage to -5.4 kV, hence gated it "on". The -1 kV pulse was synchronised to the amplified laser pulse by using the light transmitted through the glass slide optical delay line to drive another GaAs switch (see fig. 5.10). This was connected to a 555 monostable which generated a 40 μs, 15 V pulse to drive the -1 kV pulser.

5.5.5 Results

A typical set of streaked images recorded on film, is shown in figure 5.11. The dynamic slit curvature problem is evident in the results. The main problem, experienced with direct film recording was the excessively granular quality of the images. Also the requirement of microdensitometry of these results proved inconvenient, disallowing real-time, on-line presentation of temporal information from the camera.

For these reasons, the results were generally recorded using the OMA described in section 5.4.2. The signal from the 555 monostable was now used to externally trigger the OMA, which was preset to integrate 10 scans. The slit was masked so that only the central ~3 mm was used.

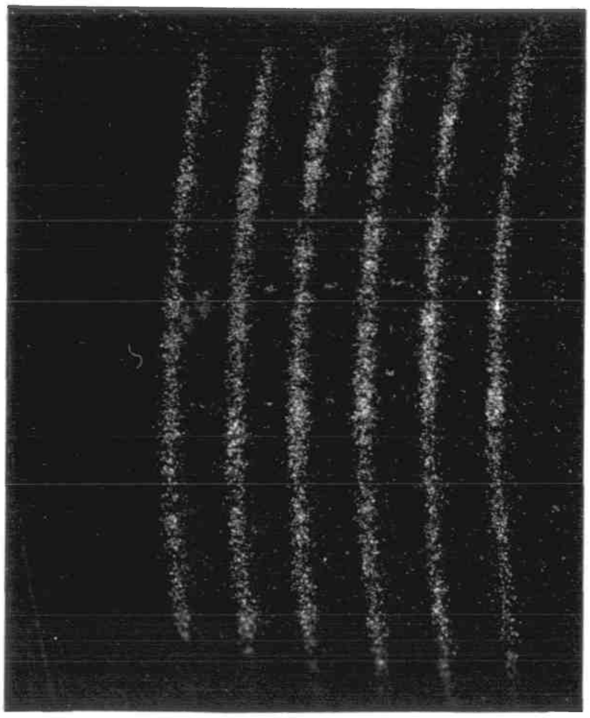

Fig. 5.11 Typical streak images recorded on film.

With this arrangement, the best temporal resolution was measured to be 0.8 ps for the camera, as illustrated in figure 5.12 where the temporal intensity profile for the streaks is reproduced. This subpicosecond resolution is for the camera inclusive of the OMA. Deconvolution of the OMA spatial response leads to a Photochron IV streak camera instrumental function of ∿0.7 ps. This is in excellent agreement with theoretically predicted resolution of 0.7 ps for this experimental camera with the streak speed of 2×10^{10} cms^{-1},obtained from the TMTF shown in figure 5.13.

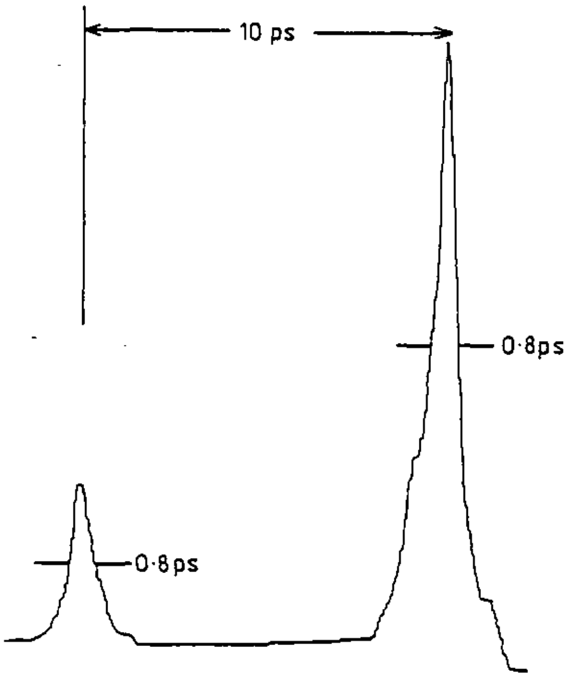

Fig. 5.12 Intensity profiles of the best streak images recorded under single-shot conditions.

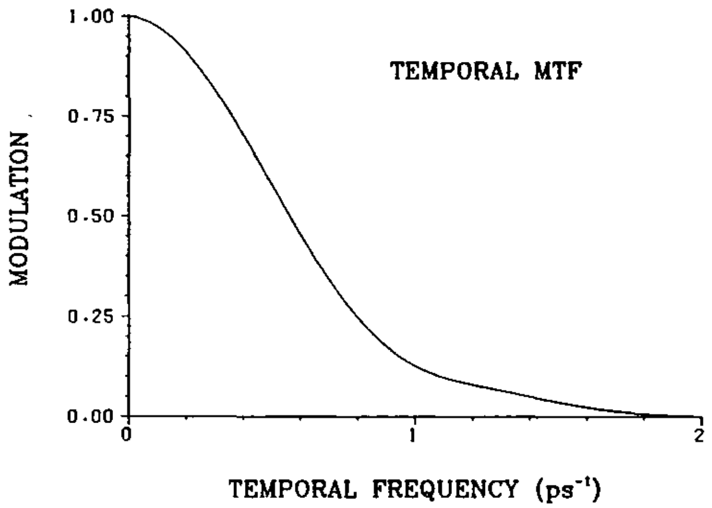

Fig. 5.13 TMTF for the experimental Photochron IV at a streak speed of 2 x 10^{10} cms^{-1}.

5.6 Conclusions

The construction of an initial, experimental Photochron IV streak image tube has been described. For this prototype tube, the extraction electric field has been restricted to 23 kV/cm (by increasing the cathode-mesh separation) to avoid any field emission and mesh rupture effects, which might have proved detrimental to the expeditious characterisation of the camera. A static spatial resolution of 33 lp/mm at the phosphor screen, for an electron-optical magnification of -2.1, has been measured.

The tube has been incorporated in a streak camera, and tested under dynamic conditions. In the synchroscan mode of operation the best camera temporal resolution was measured to be 1.7 ps, limited by the jitter of the testing setup, while the single-shot camera has been shown to have an overall resolution of 0.8 ps.

When the triggering jitter is reduced to a subpicosecond value, this Photochron IV streak camera should have a subpicosecond resolution for both synchroscan and single-shot operation. Further improvements with this particular tube could be made by replacing the camera input lens by a better quality optic, and employing an intensifier and detector with better spatial MTF response.

CHAPTER SIX

THE PHOTOCHRON IV-M MINIATURISED STREAK TUBE

6.1 Introduction

The Photochron IV streak tube, described in detail in the previous two chapters, has a length greater than 400 mm. For many applications, a sealed-off tube with these dimensions would be perfectly adequate. However, some areas of research, such as laser induced plasma and fusion studies (21), may require the inclusion of the streak tube in a target chamber having a restricted volume for diagnostics (121). Under these circumstances, the Photochron IV may be excessively large. For this reason a miniaturised version, named the Photochron IV-M, has been designed with a reduced diameter and a length ∿300 mm, similar to that of the Photochron II (14).

6.2 The Photochron IV-M design

Although the Photochron IV-M is essentially a scaled-down version of the Photochron IV, it has been found necessary to alter the relative operating potentials and electrode dimensions. The reasons for this are explained in section 6.2.2, but first the design analysis method which has been employed will be described.

6.2.1 The analysis method

Although the MTF method can fully characterise the performance of an image tube, the evaluation of an MTF is lengthy in terms of computer time. Because of this, a time-saving, if somewhat more simplistic, method (106) for analysing tube designs has been used to provide an initial design prior to detailed MTF characterisation. In this method, a crude calculation of such parameters as the focus, crossover, field curvature, temporal dispersion and temporal distortion are obtained by evaluating a small number of electron trajectories.

The paraxial focus of the tube is established by following the path of an electron emitted from $r = 0$ mm on the cathode, at an angle $\theta = 10^{\circ}$, until it intersects the axis of the tube. The electron-optical crossover can be found in a similar way by considering the intersection with the axis of an electron emitted normal to the cathode from $r = 1$ mm. To obtain the field curvature for a particular off-axis object distance, two electrons are initiated from the same point on the cathode, one normally and the other with an angle $\theta = 10^{\circ}$. The position at which they meet to form an inverted image is taken to be the focus plane for this off-axis height. The field curvature is then taken to be the separation of this plane from the paraxial focus.

The temporal dispersion is calculated from the difference in times of flight at the paraxial focus of two electrons from a given cathode radius with $\theta = \pm 90^{\circ}$. Finally, the temporal distortion is the transit time difference at the deflector plane of an electron emitted from a height r in a direction normal to the cathode, and one emitted directly along the axis. For the work described in the next section, the energy of these electrons is set to 0.3 eV.

6.2.2 Modifications to the standard Photochron IV

The Photochron IV-M has an identical cathode-mesh geometry to its standard-sized counterpart, but a scaled-down electrode structure. Initially, the scaling factor was $\sim$ 0.75 for all electrodes, so that each electrode was 30 mm long with a 30 mm diameter, and all inter-electrode spacings were 8 mm. The application of the Photochron IV voltages (see table 4.4) to these reduced electrodes resulted in too short a focal length.

The variation of the focussing potential applied to the second focus electrode, to reposition the paraxial focus at the required distance of approximately 300 mm from the cathode, is shown in figure 6.1a. Also shown in this figure is the effect on the field curvature, for r = 2 mm at the photocathode. (This cathode point is used for the field curvature, temporal dispersion and distortion results shown in the figures 6.1 - 6.3.) It can be seen that a focussing potential of $\sim$ 5.6 kV is needed, but as the voltage increases the field curvature becomes worse. In figure 6.1b the variation of both the

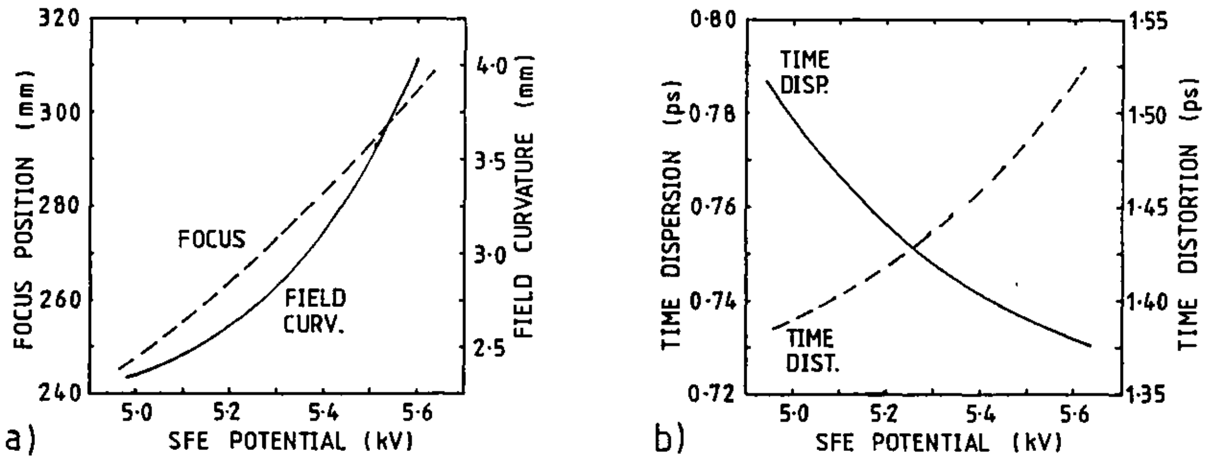

Fig. 6.1 Effect of changing the potential of the second focus electrode.

time dispersion and time distortion with this focus potential is presented. For the range of voltages considered the crossover remains almost constant at $z = 119$ mm (the anode aperture is positioned at $z = 154$ mm).

With a voltage of 5.6 kV on the second focus electrode, the focus is 305 mm from the photocathode, but the field curvature is quite large. To reduce this, the voltage applied to the first focus electrode was reduced, whilst keeping $V_{SFE} = 5.6$ kV. This has the effect of decreasing both the field curvature and the temporal dispersion as shown in figure 6.2a, whilst leaving the temporal distortion virtually unchanged. However, as indicated in figure 6.2b, it also has the detrimental effect of shifting both the focus and the crossover

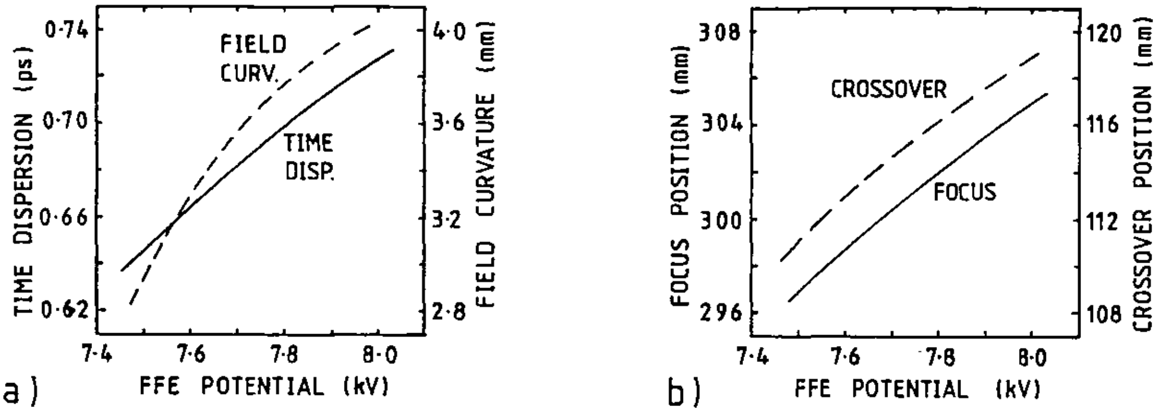

Fig. 6.2 Effect of changing the potential of the first focus electrode.

closer towards the photocathode. The focus was reset to the position z = 310 mm by increasing the potential of the second focus electrode to 5.7 kV, but this was achieved without significantly shifting the crossover.

It is necessary to keep the distance between the crossover and the anode aperture as small as possible, to ensure that the electron beam size in the deflection region, and hence the deflection plate separation, can be minimised, thus maximising deflection sensitivity. This also has the advantage of allowing a small anode aperture diameter, reducing the interaction of the focussing and deflection fringing fields.

To this end, the variation of the position of the anode aperture was studied by changing the length of the second anode electrode, while keeping the inter-electrode separations constant. The focussing electrode potentials were set at 7.5 kV and 5.7 kV respectively. The crossover remains almost independent of the position of the anode aperture over the range considered, so the separation of the crossover from this aperture (d_{CA}) decreases linearly with the electrode length. The focus and the field curvature both increase, though, as the length of the second anode decreases, as indicated in figure 6.3, and it is

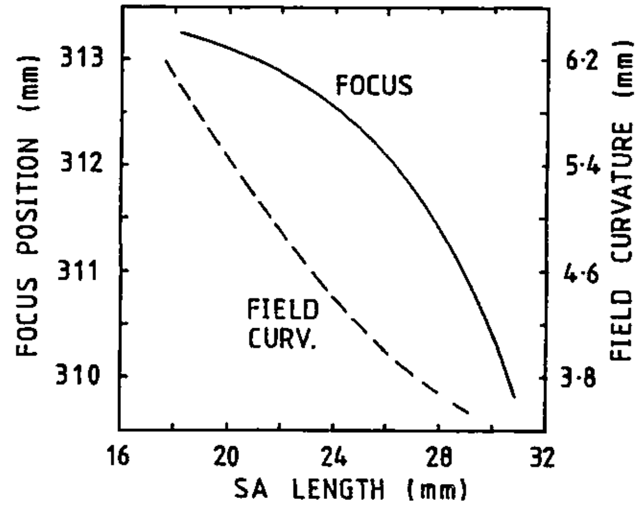

Fig. 6.3 Effect of changing the length of the second anode electrode.

necessary to trade-off the undesired, increased field curvature with the reduced value of d_{CA}. For this range of second anode lengths, the temporal dispersion is constant at the improved value of 0.65 ps, and the temporal distortion is also constant at ∿ 1.56 ps.

The version of the Photochron IV-M chosen for MTF performance characterisation then has the familiar four, coaxial, cylindrical electrode structure of the standard Photochron IV. All four electrodes have a diameter of 30 mm. The first three have lengths of 30 mm, whilst the second anode has a length of 22 mm; all inter-electrode separations are 8 mm. Both the cathode-mesh region and the deflection section have a geometry identical to those of the Photochron IV. The operating potentials for the Photochron IV-M streak tube are indicated in table 6.1.

Table 6.1

Electrode	Cathode	Mesh	FFE	FA	SFE	SA
Potential (kV)	0	10	7.5	24	5.7	18

6.3 Static theoretical results

Using the photoelectron initial energy spread of 0-0.6 eV the MTF response of the Photochron IV-M has been considered for slit object points y = 0, 1, 2, 3 mm at the cathode. The variation of the limiting static spatial resolution (along the slit direction) with axial position is shown in figure 6.4.

The focal plane for electrons emitted from the on-axis position at the cathode is 313 mm, but the resolution for the off-axis points is low due principally to field curvature. The magnitude of both the field curvature and astigmatism, for the object points considered, are plotted in figure 6.5. (These values have been determined from the MTF curves.) A compromise plane at z = 306 mm has been selected for which the static spatial resolution in both the x and y directions is optimised along the slit image. The limiting spatial resolution values derived from the MTF curves, are given in table 6.2 The static resolution for the Photochron IV-M is $\gtrsim$ 43 lp/mm at the

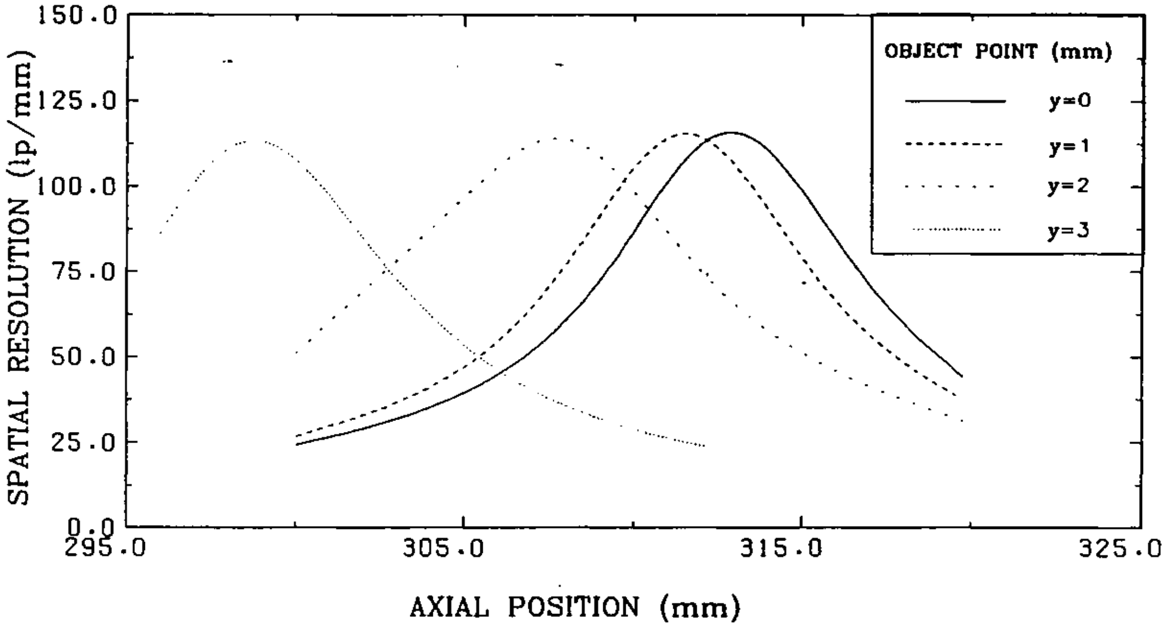

Fig. 6.4 Variation of static resolution (y direction) with axial position.

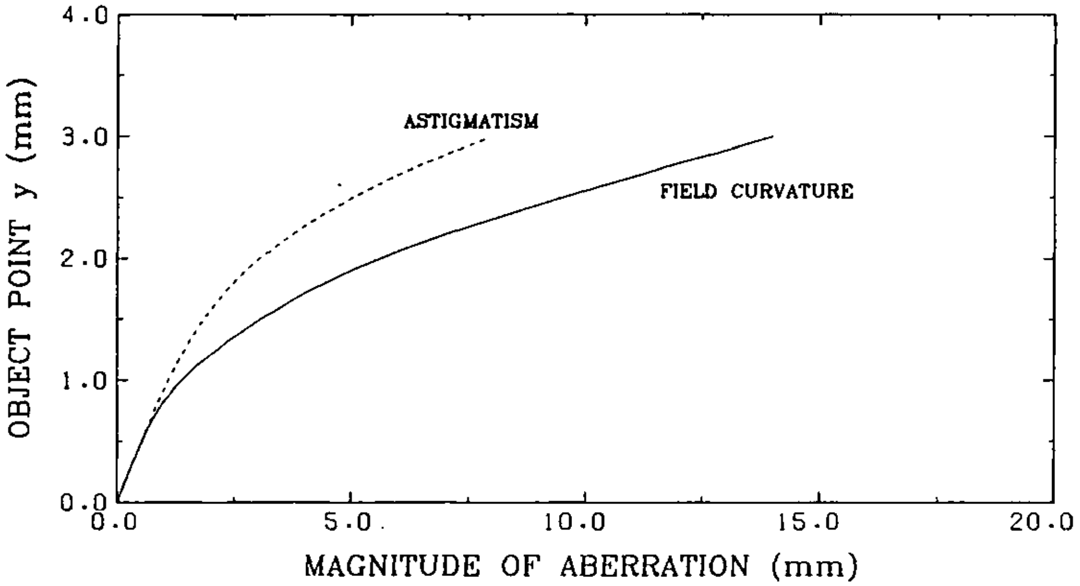

Fig. 6.5 Aberration curves for the Photochron IV-M.

screen, and its electron-optical magnification is -2.2. It can be seen from this table, that there is very little spatial distortion of the image.

Table 6.2 Static results at the optimum plane of $z = 306$ mm.

Slit height mm	Spat. res. x lp/mm	Spat. res. y lp/mm	Magnification
0	43	43	
1	46	52	-2.166
2	60	106	-2.168
3	124	45	-2.168

6.4 Temporal resolution

The Photochron IV-M has been studied theoretically under dynamic asymmetric deflection conditions, with the application of a number of time-dependent, linear voltage waveforms, with slopes ranging from 0.8×10^{12} to 2.4×10^{13} Vs^{-1}. With the reduced deflection sensitivity of 2.45 cm/kV (due to the reduced length of the drift section), these ramps provide writing speeds in the range $2 \times 10^9 - 6 \times 10^{10}$ cms^{-1} at the compromise plane. For each different voltage ramp, the electrons have been generated at the point $x = 0$, $y = 0$ mm at the cathode.

The variation of the temporal resolution with axial position for each voltage ramp is shown in figure 6.6. As observed in the Photochron IV, it is possible to obtain subpicosecond temporal resolution even at low streak speeds, but the positioning of the image plane (i.e. focussing) would be extremely critical. At the lower, streak speeds the real time resolution is likely to be worse than this due to the resulting degradation of the high dynamic spatial resolution (streak direction) by the limited response of the peripheral equipment, such as the input relay lens and the image intensifier.

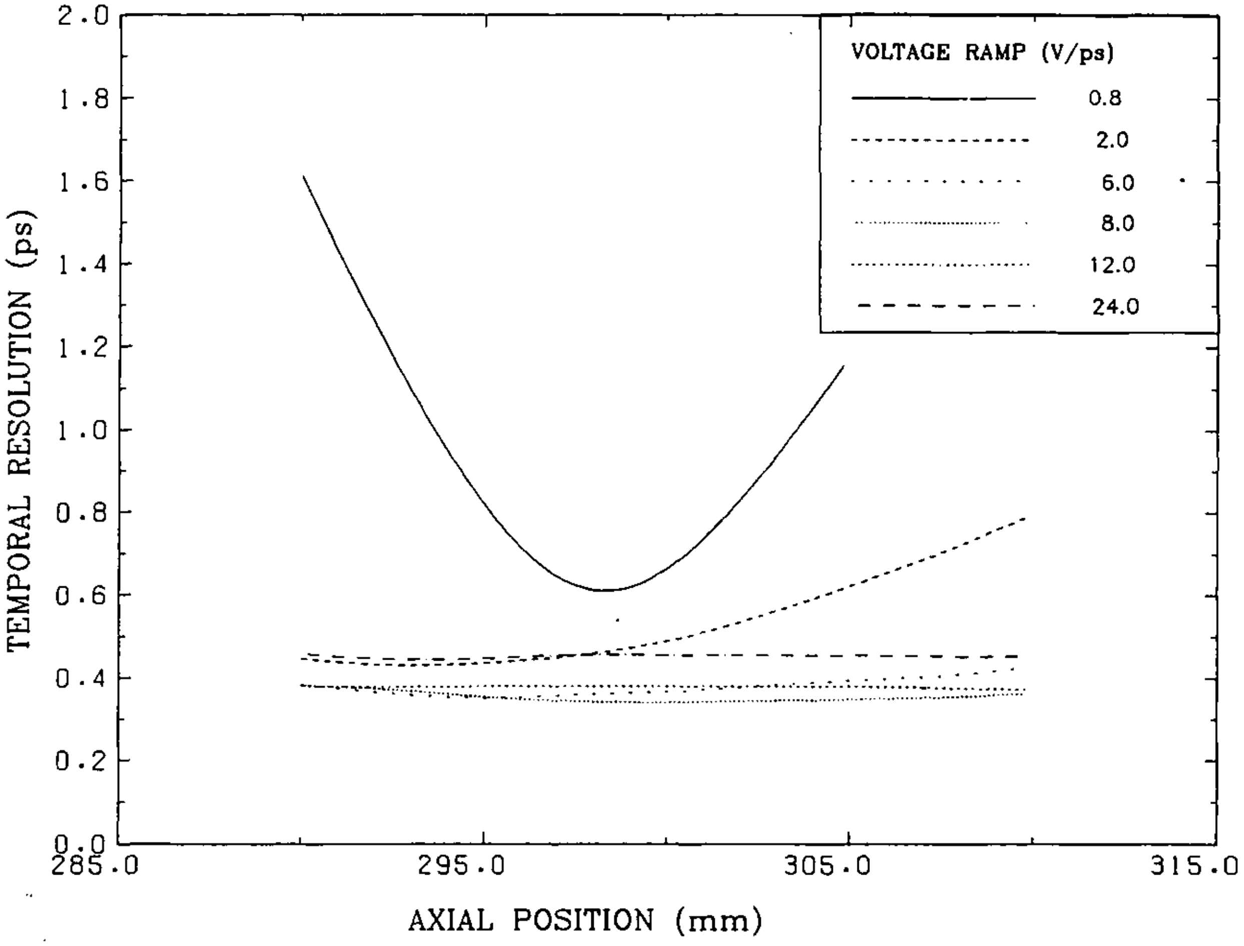

Fig. 6.6 Temporal resolution as a function of axial position.

The actual dependence of the temporal resolution on the streak speed at the compromise plane is shown in figure 6.7. There is an optimum streak speed of 2×10^{10} cms^{-1} for the best temporal resolution of 0.35 ps. This is as established for the Photochron IV (ref. section 4.4.3), but the value for this optimum writing speed is slightly lower now. The reason for the degradation of the temporal resolution with increasing streak speed above this value has been explained previously (ref. section 4.6).

The limiting temporal resolution has been obtained by assuming an initial electron energy spread of 0-0.2 eV, consistent with the illumination of the photocathode close to its long-wavelength cut-off. The MTF obtained at the compromise plane, with a writing speed of 2×10^{10} cms^{-1} is shown in figure 6.8. The limiting response, obtained from the curve, is 190 fs for this streak tube.

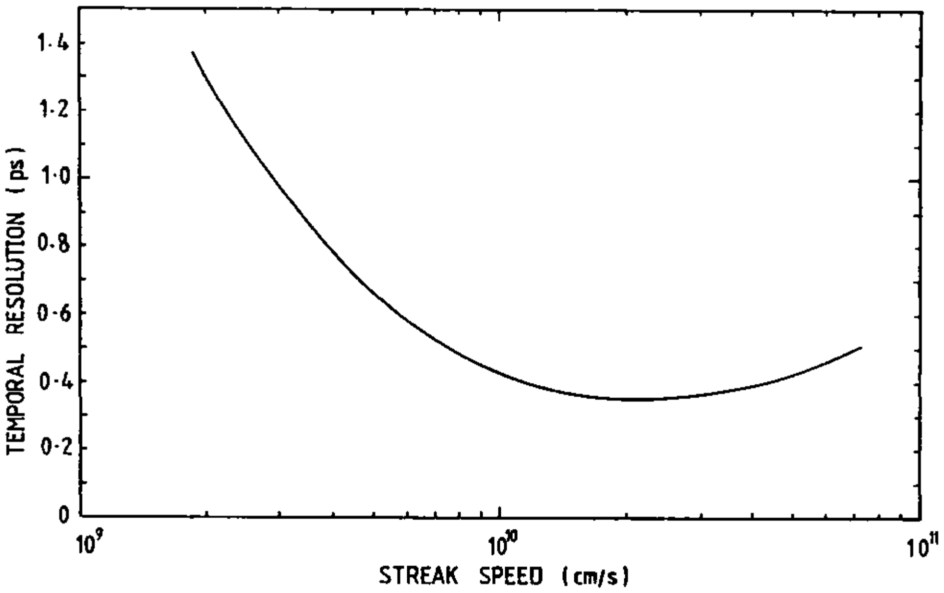

Fig. 6.7 Variation of temporal resolution with streak speed at z = 306 mm.

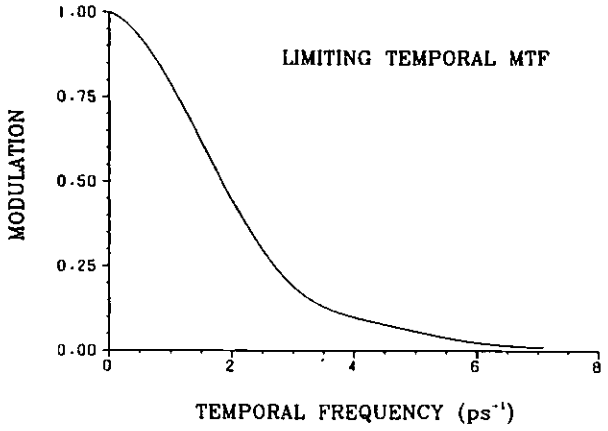

Fig. 6.8 TMTF for an initial energy spread of 0-0.2 eV.

6.5 Comparison of the Photochron IV and IV-M

The pre-deflection temporal dispersion and temporal distortion values for the two versions of the Photochron IV are given in table 6.3. The temporal dispersion of the Photochron IV-M is smaller and increases less markedly with slit height. This is understandable since the length of both the focussing section and the overall cathode-phosphor dimensions are smaller, resulting in reduced dispersion of the transit times.

Table 6.3

Slit height mm	Temporal dispersion (ps)		Temporal distortion (ps)	
	PC IV	PC IV-M	PC IV	PC IV-M
0	0.26	0.24		
1	0.31	0.26	0.20	0.28
2	0.35	0.29	0.77	1.10
3	0.45	0.34	1.72	2.40
4	0.51	0.40	3.08	4.30
5	0.60	0.41	4.76	6.80

The temporal distortion, on the other hand, is a more severe problem in the scaled-down tube for identical emission points at the cathode. It is likely that to minimise the dynamic slit curvature problem, the spatial extent of the slit image on the photocathode must be limited to ± 2mm, which is consistent with the use of an anode aperture diameter $\lesssim$ 2 mm.

The other salient characteristics of the Photochron IV and IV-M streak tubes are summarised in table 6.4. The static resolution is lower at the best compromise plane, in the miniature tube, but this is to be expected since the electron-optical aberrations at a particular off-axis point become worse as the electrode diameter is reduced (26, 122).

Because the temporal dispersion prior to deflection is smaller, the temporal resolution of the Photochron IV-M is slightly superior, although both show a response < 0.4 ps, at their optimum streak speeds. These optimum streak speeds are comparable but are not identical. This is due to slight variations in the beam size at the deflectors for the two tubes. The limiting temporal resolution (when the cathode is illuminated close to its threshold of sensitivity) is <200fs for both streak tubes.

Table 6.4 Theoretical performance characteristics of the Photochron IV and IV-M streak tubes.

Characteristic	PC IV	PC IV-M
Length (mm)	401	306
Diameter (mm)	44	30
Static res. at screen (lp/mm)	64	43
Magnification	-2.0	-2.2
Field curvature (r=2 mm)	4mm	5mm
Astigmatism (r=2mm)	3mm	3mm
Deflection sensitivity (cm/kV)	3.0	2.5
Temporal resolution (ε=0-0.6 eV)	0.37ps	0.35ps
Limiting temporal resolution	180fs	190fs
Optimum streak speed (cms^{-1})	$3x10^{10}$	$2x10^{10}$
Dynamic range	911	1700

The TRL dynamic ranges of the two versions of the Photochron IV have been evaluated (116) assuming an input pulse duration of 3 ps and a camera response of 2 ps. The value for the Photochron IV-M is better than that for the Photochron IV, because of the reduction of the mesh-anode distance. The low potential region in the focussing section is now smaller, and so too is the transit time of the photoelectrons in this part of the tube. This leads to lower Coulombic interactions and to a larger dynamic range.

6.6 UHV demountable version of the Photochron IV-M

A demountable version of the Photochron IV-M has been constructed by Phillips (123) for inclusion in an ultra-high vacuum (UHV) chamber. The constructional details are reproduced in figure 6.9.

The mesh holder and the four cylindrical electrodes were mounted from glass support rods via tungsten pins. The copper micromesh used had a pitch of 60 cells/mm and was held in position by three stainless steel clips. The deflection plates were incorporated into a high-Q resonant deflector circuit made entirely from high conductivity polished copper. The aluminium backed P11 phosphor screen was spot welded onto the end of the drift section electrode. The tube could be used to study the properties of a variety of fabricated photocathodes, by transporting the cathode, activated in another section of the chamber, via a railway line system, to the streak

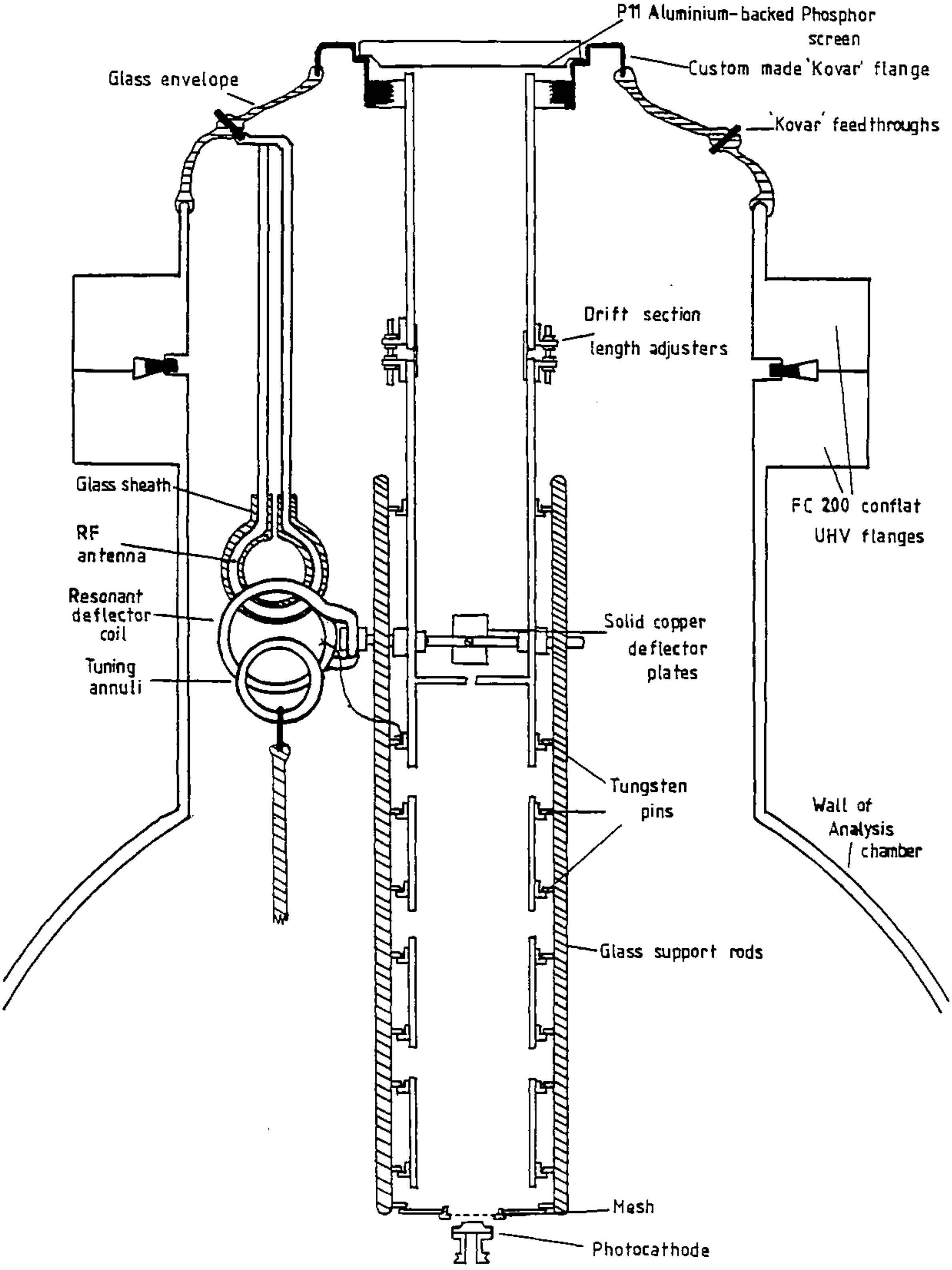

Fig. 6.9 The constructed, demountable Photochron IV-M.

tube. The cathode could be finally positioned accurately parallel to the mesh by a spectrometer mainipulator.

To test the static spatial resolution of the streak tube, a 1951 USAF resolution chart was focussed, by a 135 mm f3.5 camera lens, onto a previously fabricated S1 photocathode. Deriving the correct voltages from a divider network, the streak tube was operated in the positive potential mode with the cathode grounded and +18 kV on the screen. After optimising the focus potentials, all the elements of group 5 on the USAF resolution chart could be resolved (123). Allowing for the magnification of the input lens, this corresponds to a static resolution of 51 lp/mm at the photocathode of the tube, and was limited by the range of the test chart. This suggests that the limiting static spatial resolution should be even closer to the theoretically predicted value of 95 lp/mm at the cathode (c.f. table 6.2).

The demountable Photochron IV-M was also tested dynamically in the synchroscan mode of operation, using as a test source pulses from a synchronously mode-locked Rhodamine B cw dye laser. For this laser configuration, the durations of the pulses have been measured by non-linear techniques to be ∿ 1 ps (124).

The experimental arrangement used by Phillips is shown in figure 6.10 (123). Each output dye laser pulse was sent through a Michelson type optical delay line, producing two subpulses separated by 100 ps as a temporal

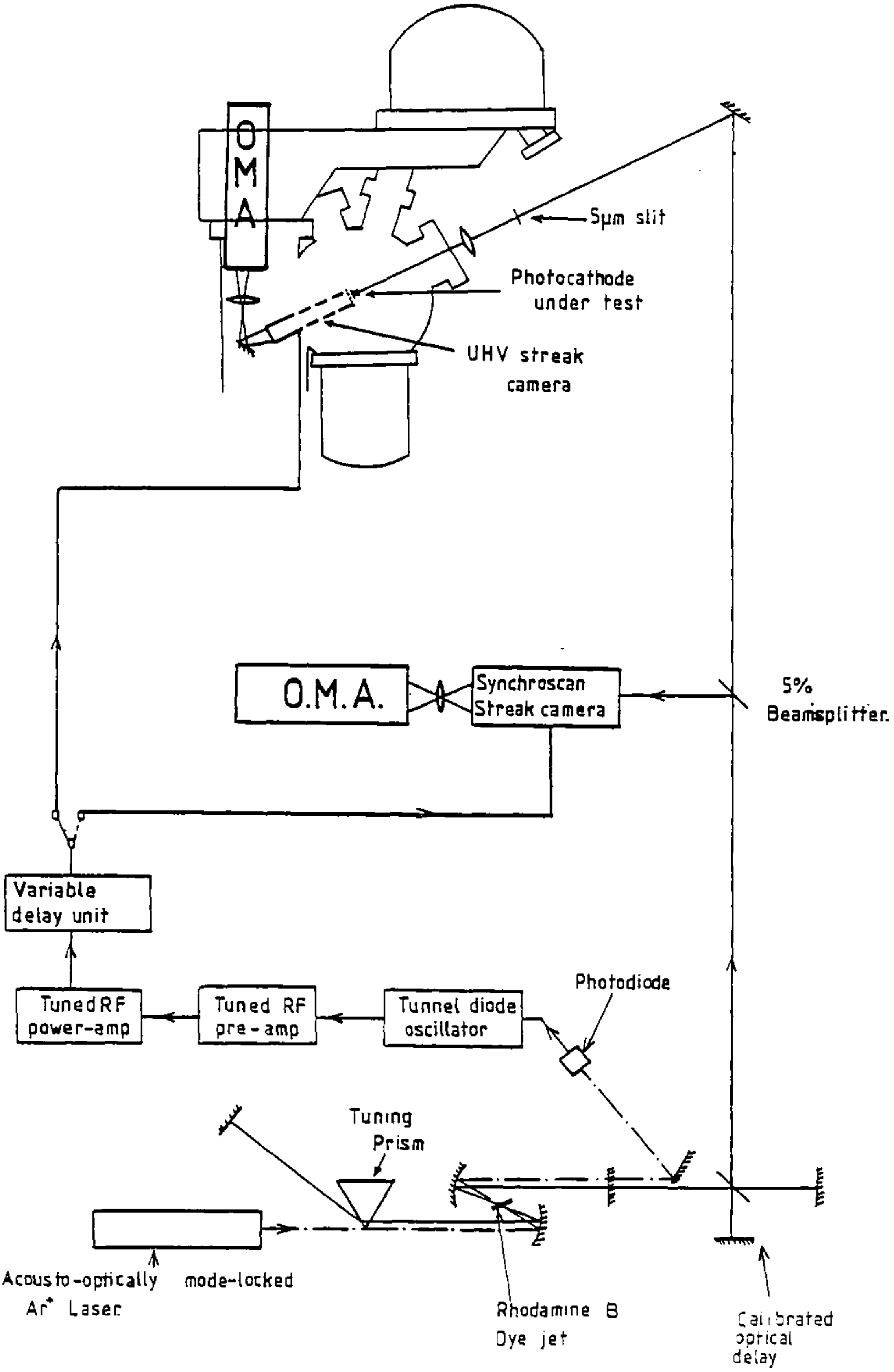

Fig. 6.10 Experimental arrangement for synchroscan tests of the Photochron IV-M.

calibration. These subpulses were then incident on a 5 μm wide slit, and focussed into the streak tube. The output image on the screen of the Photochron IV-M was recorded on an OMA. A second synchroscan streak camera, a sealed-off Photochron II tube, was used simultaneously as an independent check on the measured pulsewidth.

The RF deflection wave, applied to the deflectors of both streak tubes, had a frequency of 138.8 MHz and was derived from the mode-locked dye laser pulse train using a photodiode/tunnel diode oscillator circuit. After amplification this signal provided a streak writing speed of 1.8×10^9 cms^{-1} at the phosphor of the Photochron IV-M. Under these conditions, the recorded pulsewidths were ∿18 ps for both streak cameras (123). Since the Photochron II has a temporal resolution of 1 - 2 ps, this suggests that the recorded value of 18 ps was primarily a measure of the jitter of the system. The fact that no broadening was observed with the Photochron IV-M indicates that the measured pulsewidth only represents a pessimistic upper limit for the temporal resolution of this demountable tube (in fact the rsolution should be significantly better than this). If this tube was tested in synchroscan mode with subpicosecond pulses from a passively mode-locked cw ring dye laser, in which the system jitter was also subpicosecond (68), its temporal resolution should be < 1 ps, with an ultimate value of 0.35 ps predicted from theoretical calculations.

6.7 Conclusions

The Photochron IV streak image tube has been scaled down in size (and slightly modified) to make it compatible with both smaller streak camera systems and for inclusion in limited volume demountable test chambers. The theoretical study of this miniature tube has indicated a comparable performance to the Photochron IV. Indeed, both the temporal resolution and the TRL dynamic range of the Photochron IV-M should be superior to those of its larger-sized counterpart, although there is more severe time distortion in the smaller tube.

A demountable, experimental version of the Photochron IV-M has been constructed. Preliminary dynamic tests have shown a time resolution of <18 ps but this has been limited by the jitter in the testing laser system.

When a sealed-off version of the Photochron IV-M is constructed and tested with the subpicosecond pulses obtainable from a passively mode-locked cw ring dye laser, its single-shot temporal resolution should be 0.35 ps if it is not limited by the anciliary equipment. In synchroscan operation, the jitter of this type of laser system can be reduced to a subpicosecond value, so the temporal resolution of the tube under these conditions should also be subpicosecond.

CHAPTER SEVEN

THE PICOSECOND PHOTOCHRON FRAMING IMAGE TUBE

7.1 Introduction

In applications such as laser-induced compression of matter and thermonuclear fusion research (21) there is a need to complement streak camera data with information from a sequence of discrete, two-dimensional spatial images (frames). Since currently available commercial cameras can only provide frame exposure times ∿1ns with modest spatial resolution (∿4 lp/mm) at the limit of operation (125), substantial research effort has concentrated on a variety of techniques whereby picosecond resolution of the frames can be acheived. These techniques will be briefly reviewed here.

An ultra-fast optical shutter based on the optical Kerr effect has been used to demonstrate frame recording with exposures as fast as 5 ps (126). Multiple frame separation was achieved using such a Kerr cell in combination with a slow electron-optical streak camera. With this technique it should be possible to reduce the exposures into the femtosecond regime (127), although it cannot be used in the X-ray spectral region due to the lack of suitable Kerr cell materials.

Lieber has reported a plategate shutter tube (128), which makes use of a passive microchannel plate, with interspersed deflection electrodes, to both collimate and shutter the electron beam. Theoretical frame durations of 1 ps have been claimed for this tube, but have not been demonstrated experimentally.

An ingenious technique for fast, single-frame image production by making use of the good temporal resolution of a streak camera has been suggested by Cheng et al (129). A fiber-optic image dissector is used to encode the two-dimensional event under study onto the one-dimensional slit of streak camera. With a prototype 7 x 7 array dissector used in conjunction with an S20 streak tube, 20 ps duration frames have been recorded, but the spatial resolution was only 2 lp/mm. The main limitation of this technique is the low number of pixels ($\sim$100) available along the slit, but also computer data processing is required to regenerate the two-dimensional format from the recorded image.

Another method of picosecond framing involves image dissection within a conventional streak camera (130). In this case, a mask is inserted at the front of the camera to select a discrete matrix of object points. After streak operation, the recorded image has to be digitized prior to data processing. This technique has successfully provided five frames of duration 13 ps with a spatial resolution of 6 lp/mm. However, there is a significant delay between the recording of the experimental information, and the availability of the computer generated, two-dimensional framed images.

An alternative type of framing camera is that of the gated, proximity - focussed image intensifier (131, 132), which allows the use of a large (∿ 35 mm diameter) cathode area. Recent research (133) has shown that this type of camera is capable of producing a single exposure of 50 - 100 ps with high resolution (12.5 lp/mm). To achieve multiple frames requires a multiplex array of several gated image intensifiers. This has been demonstrated in the nanosecond regime (134, 135), but may prove problematic in circumstances of restricted diagnostics volume. Multiple (400 ps) framing has also been reported for a gated image intensifier by including a 5 pinhole input structure at the photocathode (136). Here the additional frames are achieved at the expense of smaller object size.

Kalibjian has designed a dissector-restorer image tube specifically for multiple framing (137, 138). This tube consists of a modified RCA C73435 streak tube, whose phosphor screen has been replaced by a metal diaphragm containing three slit apertures, and a restoring electron lens section. Initial research showed a triplet of 125 ps framed images of a 2.5 mm x 2.5 mm pattern, but this suffered from large jitter. Further work has concentrated on improving the jitter to ∿10 ps and increasing the object size to 3.2 mm x 4.2 mm. Under these conditions, the three frame exposures had durations of 250 ps with spatial resolution of 5 lp/mm (139). The main problem with this tube is its complicated electrode structure, in which the additional restorer section leads to lower image quality.

Current, ongoing research by Hall et al (140) has resulted in a prototype framing tube which incorporates a slow-wave, helix deflection structure in a Photochron I type streak tube. The deflection voltage takes the form of a staircase wave generated by a non-saturated photoconductive element, and the frames are obtained at each plateau. Initial results suggest subnanosecond frame exposure ($\sim$500 ps) but with very poor spatial resolution.

The Photochron framing image tube (141), which is described in this chapter, has been designed to achieve multi-framing, with (i) frame exposure times $\lesssim$100 ps, (ii) interframe periods of $\leqslant$250 ps, and (iii) a dynamic spatial resolution $\geqslant$10 lp/mm at the photocathode. The basic concept has some features that are similar to those of the shutter tube proposed by Walters et al (142) and later developed by Huston et al in a camera system (143, 144), in which nanosecond resolution has been demonstrated (Imacon 790 framing camera - ref. 125).

7.2 Method of operation and design constraints

The method of frame generation imposes several constraints on the design of the image tube, and these will be outlined in this section. The photoelectrons emitted from the cathode are focussed by an electrostatic electron-optical lens through the anode aperture into the deflection section and hence onto the phosphor screen.

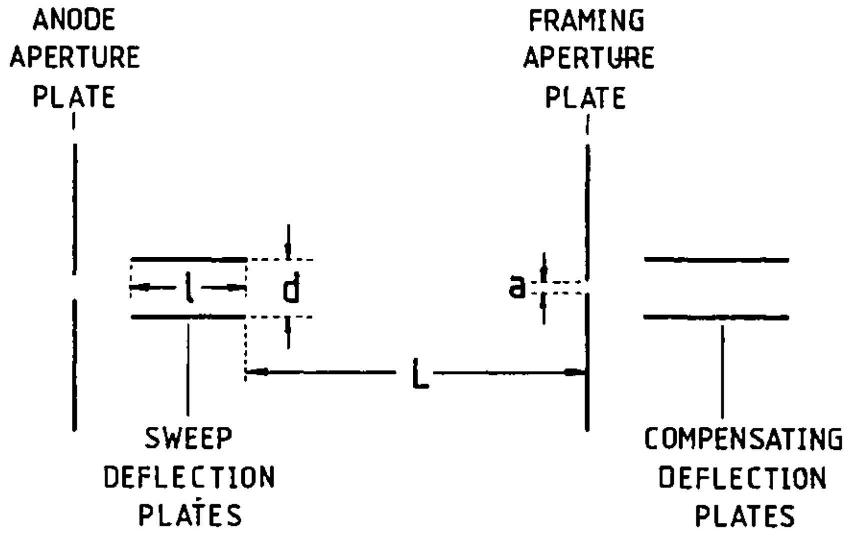

Fig. 7.1 Deflection section geometry.

A simplified deflection geometry is shown in figure 7.1. When a time-dependent deflection voltage is applied to the sweep deflectors, the electron beam is streaked across the aperture in the metal diaphragm, referred to as the framing aperture plate. This defines a short temporal transmission of electrons through the aperture, the rest being intercepted. The deflection voltage introduces a transverse velocity to the electron beam, and this would cause the image to appear smeared (or blurred) at the screen. To secure spatial resolution information at the phosphor, this transverse velocity is removed by the application of an inverted - polarity, deflection voltage to another set of deflectors - the compensating deflection plates. This provides a stationary image at the screen. If the temporal gradients ($K = dV/dt$) of the two voltage waveforms are identical in magnitude, then the only pre-requisite for stationarity in the image is that the deflection sensitivities of the sweep and compensator deflectors must also be identical (143).

The frame exposure time can be obtained from the following simplified analysis. The speed with which the electron beam is swept across the framing aperture is given by

$$v = K.S \qquad \text{Eq. 7.1}$$

where K is the slope of the voltage waveform (in V s^{-1}) and S is the deflection sensitivity of the sweep deflectors at the framing aperture plate (in cm V^{-1}). Ignoring such effects as deflection fringing fields, effective electron beam width and chromatic aberration for this qualitative analysis, the deflection sensitivity for the parallel plate network is, (26),

$$S = \frac{1\ (1/2 + L)}{2\ Vd} \qquad \text{Eq. 7.2}$$

where the dimensions are as defined in figure 7.1, and V is the anode voltage. The frame exposure time, T, is the time taken for the electron beam to scan across the aperture. If the aperture has a diameter, a, it follows from equations 7.1 and 7.2 that this framing time is

$$T = \frac{a}{v} = \frac{2\ Vad}{K\ 1\ (1/2 + L)} \qquad \text{Eq. 7.3}$$

For short exposures, equation 7.3 implies that, with a particular anode voltage V, (i) the speed of the streaking voltage ramp should be maximised, (ii) the size of the framing aperture, and the gap separation of the sweep deflection plates, d, should be small, (iii) the distance L from the sweep deflectors to the framing aperture should be as large as possible, and (iv) the sweep plate length, l, should be maximised.

From requirements (ii) and (iii) it follows that the electron beam entering the framing section of the tube should be constrained by the focussing electron lens to have an extended, narrow waist, with the electron-optical crossover region positioned beyond the anode aperture. This precludes the use of a curved photocathode. (Ideally this crossover would occur at the framing aperture plane, but, because of restrictions due to the sweep deflection geometry, it should actually be shifted towards these deflectors.) Thus the focussing lens must be a weak electron lens.

Originally this type of tube was operated with either a sinusoidally time-varying, or sawtooth voltage waveform applied to the deflector plates (143, 144), but this only produced nanosecond exposure times. From requirement (i), to achieve picosecond framing it is desirable to use the fastest ramps available. Because of this, the linearly time-dependent voltage ramps provided by photoconductive elements (56 - 59) are likely to be used. For this case, the operation is summarised diagrammatically in figure 7.2.

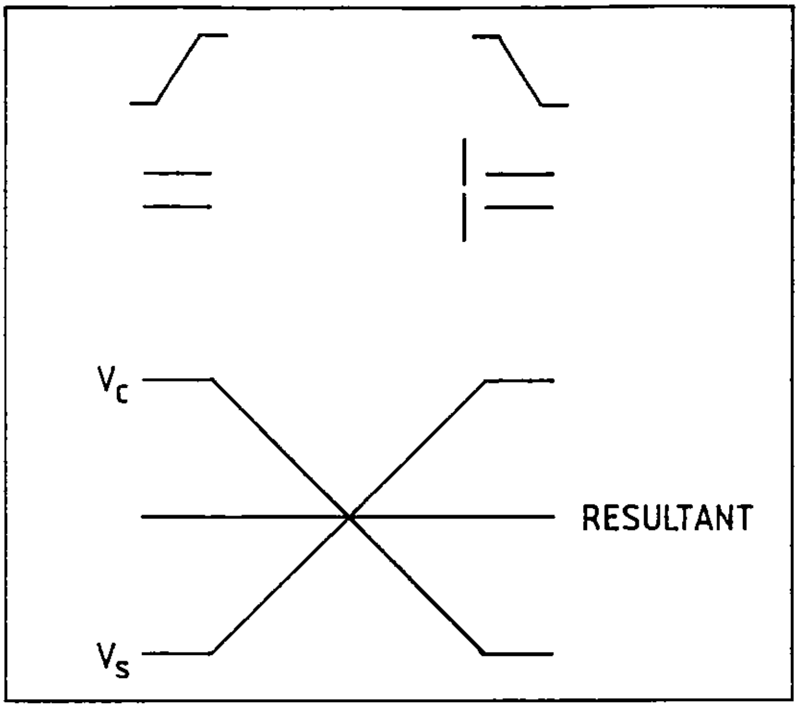

Fig. 7.2 Principle of framing operation.

7.3 Design concepts of the focussing lens

The weak lens chosen to focus the electron beam is shown schematically in figure 7.3. (The deflection structure is omitted in this figure, and will be dealt with in section 7.5). This is a three cylinder lens with an extraction mesh connected electrically to the first electrode. The mesh is spaced 2.5 mm from the photocathode, and with a voltage of 5 kV applied to it,

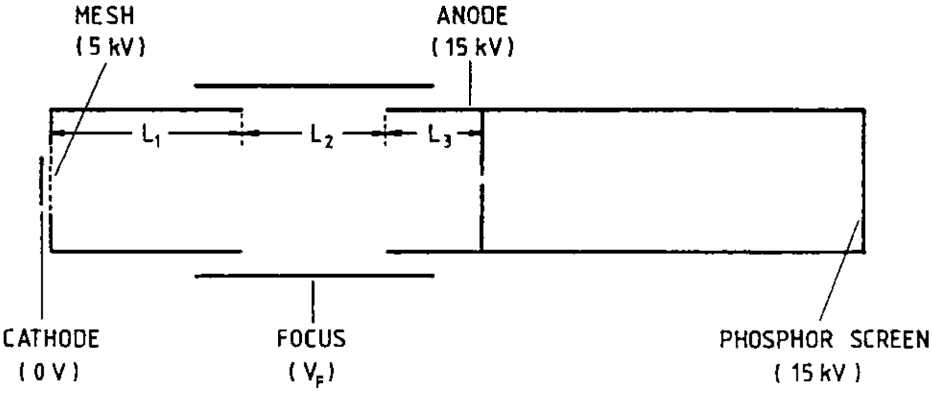

Fig. 7.3 Schematic of the weak electron lens studied.

provides an extraction electric field of 20 kV cm^{-1} to limit the temporal dispersion of the electrons. The mesh electrode and anode cylinders have diameters of 42 mm, and initial lengths of 78 mm and 30 mm respectively. The voltage applied to the anode is 15 kV. The central focussing electrode was selected to be of a larger diameter (60 mm) to reduce the polishing requirements on its ends, and was chosen to have an initial length of L_2 = 90 mm.

To understand the importance of the parameters L_1, L_2, L_3 and V_F (defined in fig. 7.3) in the design of the weak lens, each was varied in turn whilst holding the others constant. The effects were studied by evaluating the trajectories of 48 electrons, of which 8 were emitted from each cathode object point y = 0, 1, ..., 5 mm (x = 0 mm). The initial angular values of these were $\theta = 0^o, 10^o, \pm 90^o$ with $\phi = 0^o, 90^o$ and the electron initial energy used was 0.1 eV. The performance was generally defined by considering the paraxial focus and the field curvature, which were calculated as described in chapter 6, and the distance D between the minimum beam spot size for all 48 electrons and the anode. (In the curves shown later in this section, the field curvature used is the magnitude of the value for r = 2 mm on the cathode.)

The effect of varying the focussing voltage is shown in figure 7.4. With increasing potential the lens becomes weaker, and the focus shifts further away from the photocathode (fig. 7.4a). So too does the minimum beam spot size with a corresponding increase of D, but the field curvature becomes worse (see fig. 7.4b). For the following results a value of V_F = 2.1 kV was selected.

Figure 7.5 indicates the effect of changing L_1. As L_1 increases the focus moves towards the photocathode,

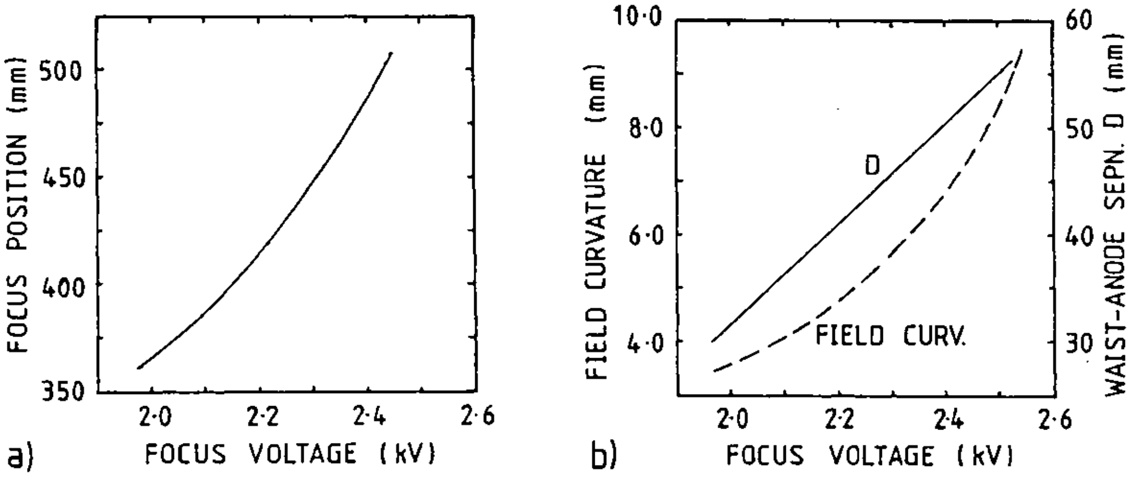

Fig. 7.4 Effect of altering the focus voltage.

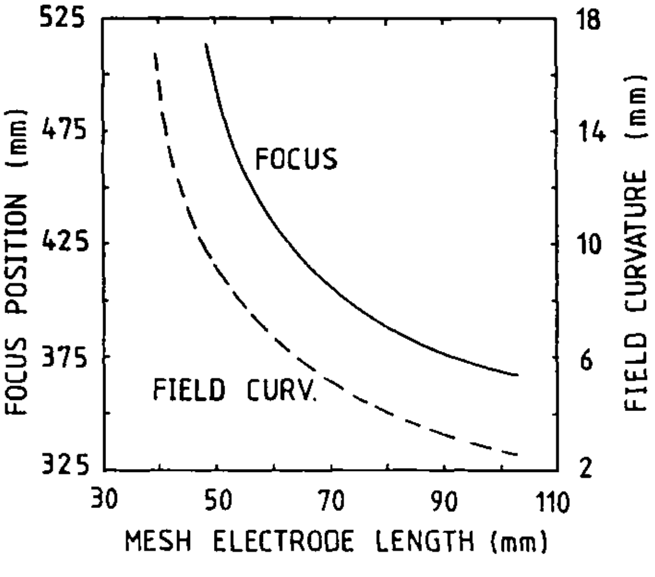

Fig. 7.5 Effect of changing the length of the first electrode.

since the lens is becoming stronger. The field curvature also decreases with increasing L_1. The value of D changes only slightly in the range 32 - 37 mm as L_1 goes from 30-100mm. Therefore it is desirable to have $L_1 > 60$mm.

Variation of L_2 provides the effects shown in figure 7.6. The focus plane is shifted closer to the cathode as L_2 is increased, and the magnitude of the field curvature decreases. The position of the smallest beam waist remains almost constant, but since the anode position changes with L_2, the value of D decreases with an increasing value of L_2. From this, it can be concluded that L_2 should lie in the range 60 mm $< L_2 <$ 100 mm.

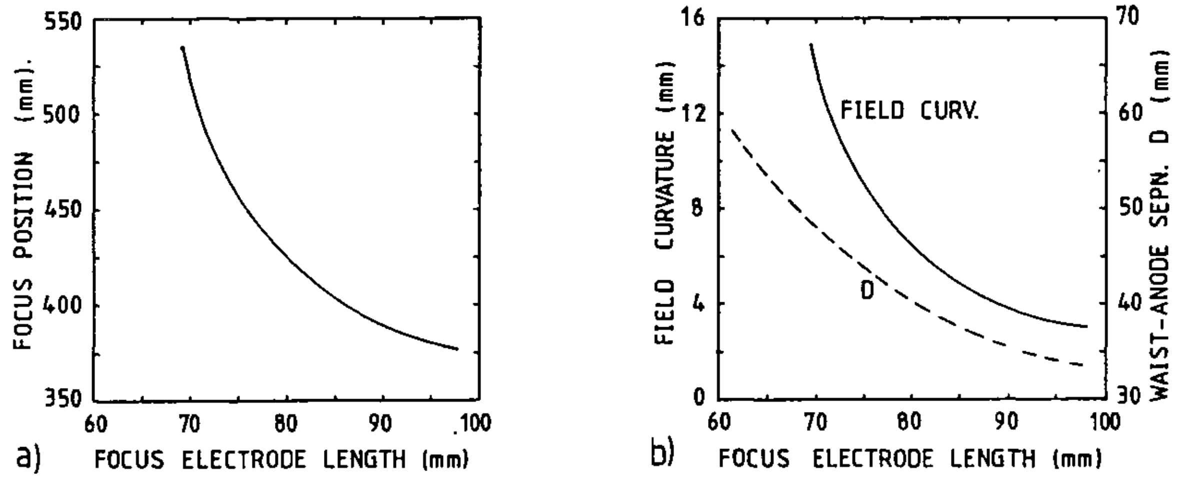

Fig. 7.6 Effect of varying the length of the focus electrode.

Changing the value of L_3 has been found to have very little effect on the size of the field curvature, which remains at $\sim$ 4 mm. Its effect on the focus is also small (see fig. 7.7), but the minimum beam size position is almost independent of L_3, so that D increases as L_3

decreases. This imposes the need to keep $L_3 \lesssim 30$ mm.

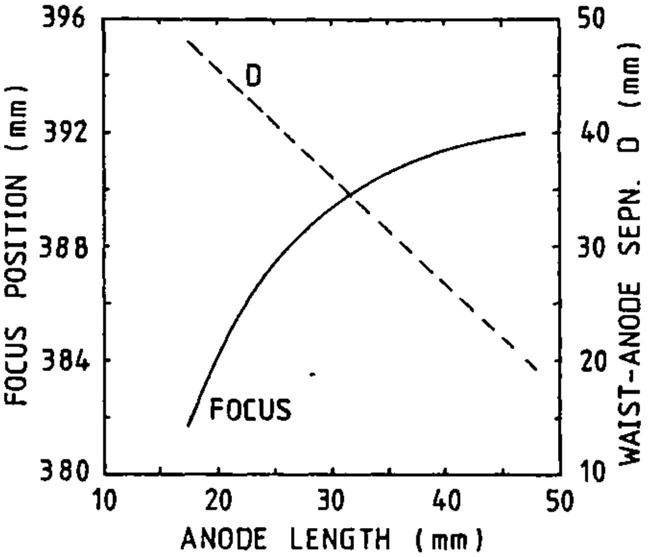

Fig. 7.7 Effect of changing the length of the anode.

Because of constructional difficulties which could arise upon fabrication of the lens type described above (145), the final design incorporated three equidiameter, cylindrical electrodes, with inter-electrode spacings of 10 mm. The diameter chosen was 58 mm, since standard stainless steel tube is commercially available with this internal diameter. The lengths of the electrodes are 76 mm, 67 mm, 29 mm for L_1, L_2, L_3 respectively, based on the previous discussion. With the focussing voltage set at 2 kV the paraxial focus is 438 mm from the photocathode, while the value of D is 43 mm. The equipotential contours set up by this lens arrangement are illustrated in figure 7.8.

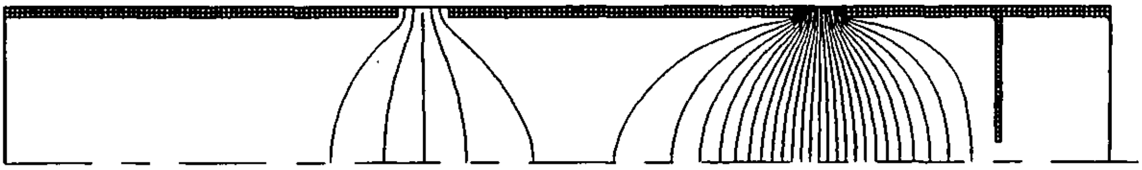

Fig. 7.8 Potential distribution for the focussing lens of the Photochron framing tube; contour spacing is 500 V.

7.4 Static MTF results

The static performance of the framing tube described above, and shown in figure 7.8, has been studied theoretically by analysing electron trajectories from five cathode object points using the MTF method discussed in chapter 3. Since the framing tube records two-dimensional information the object points had to be chosen across the whole cathode area, but because of axial symmetry only one quadrant needed to be studied. The five object points used were (0,0), (0,1.5), (0,3.0), (1.5,1.5) and (3.0,3.0) where these represent (x,y) in mm.

The static resolution in the y direction is plotted against axial position, for each of these points in figure 7.9. (In the cases where x = y on the cathode, the spatial resolution curves will be identical in the two orthogonal directions due to symmetry.) It is evident that the electron-optical aberrations degrade

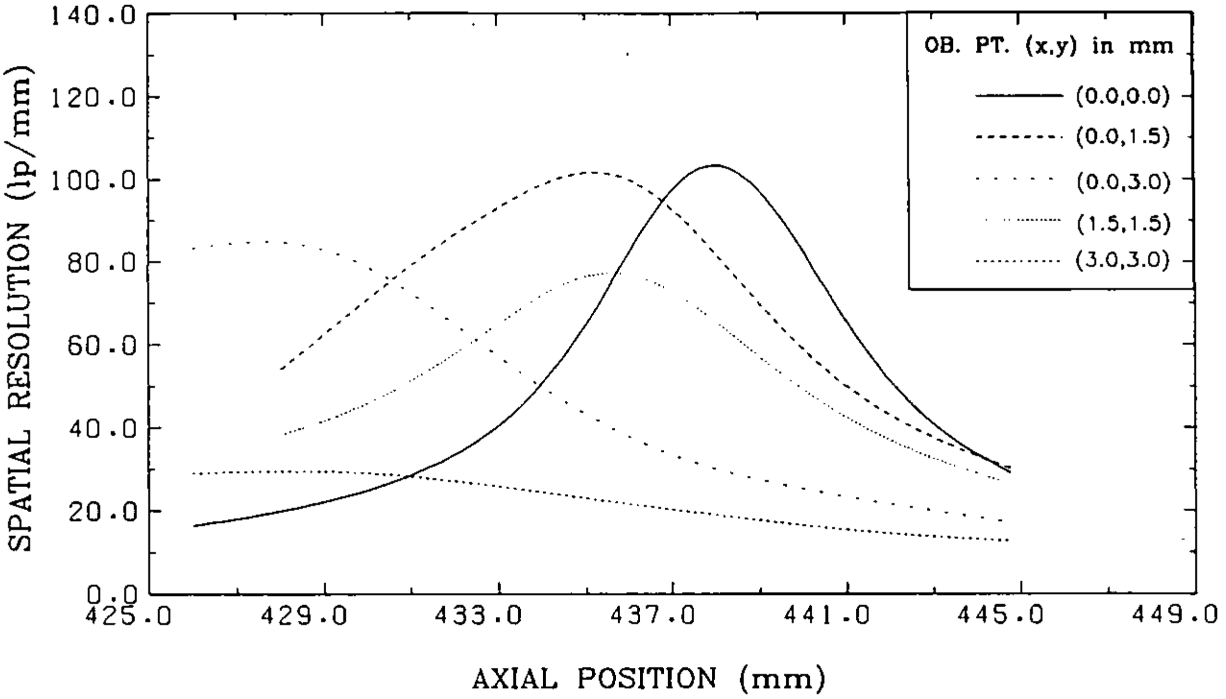

Fig. 7.9 Variation of static resolution in the slit direction with axial position.

the resolution for off-axis objects.

The spatial resolution for the furthest off-axis point (3,3) is clearly $\lesssim$ 30 lp/mm. If this is initially ignored, the best compromise plane for optimum resolution across the phosphor is chosen to be z = 434 mm. At this plane the spatial resolution is $\gtrsim$ 45 lp/mm for all object points within a radius ∿ 3 mm at the cathode; at the point (3,3) the resolution has dropped to 24 lp/mm. Extending the usable cathode radius to ∿ 3.5 mm by inclusion of the point (2.5,2.5), the spatial resolution over the whole image at the screen plane (z = 434 mm) is still $\gtrsim$ 40 lp/mm, as seen in figure 7.10. The electron-optical magnification is -1.50, with a spatial distortion of 1.3% at the furthest point considered.

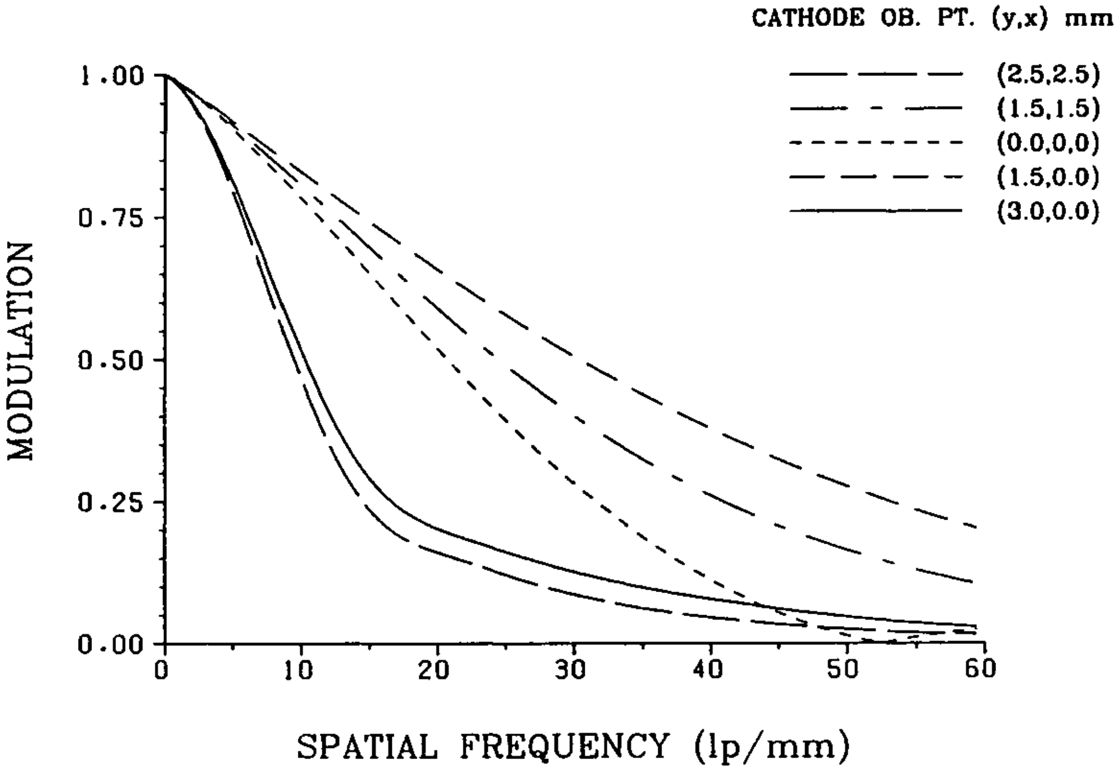

Fig. 7.10 Static MTF_y curves at optimum plane of z = 434 mm.

Although the electron beam has its minimum waist size at a distance 43 mm from the anode aperture, it was found that the framing aperture plate could be positioned further from the anode, so increasing the value of L in equation 7.3, but in doing so some electrons are lost by collision with the framing aperture diaphragm. The distance of this diaphragm from the anode, and the diameter of its framing aperture, was studied by considering the spot diagram of the electrons at different z planes. The percentage of electrons which are intersected by the aperture plate was estimated for different aperture radii. This is illustrated for the object point (3.0,3.0) in figure 7.11, for the plane at the optimum separation of 65 mm from the anode. Figure 7.12a shows the resulting curves for the object points (3.0, 3.0) and (0,3.0) at this plane (z = 259.5 mm). For

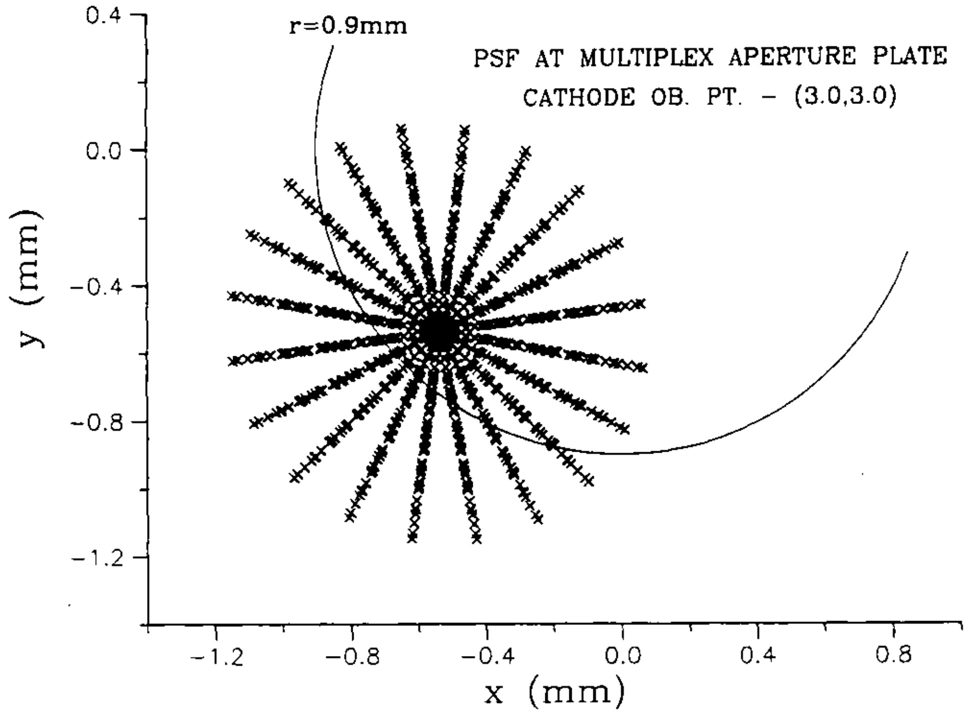

Fig. 7.11 Spot diagram at framing aperture plate plane.

cathode emission points within these values, very few electrons would be lost. Therefore the framing aperture can have a diameter of 1.8 mm while still retaining a usuable cathode size of 6 mm x 6 mm. The diameter of the anode is established to be 3.5 mm from figure 7.12b.

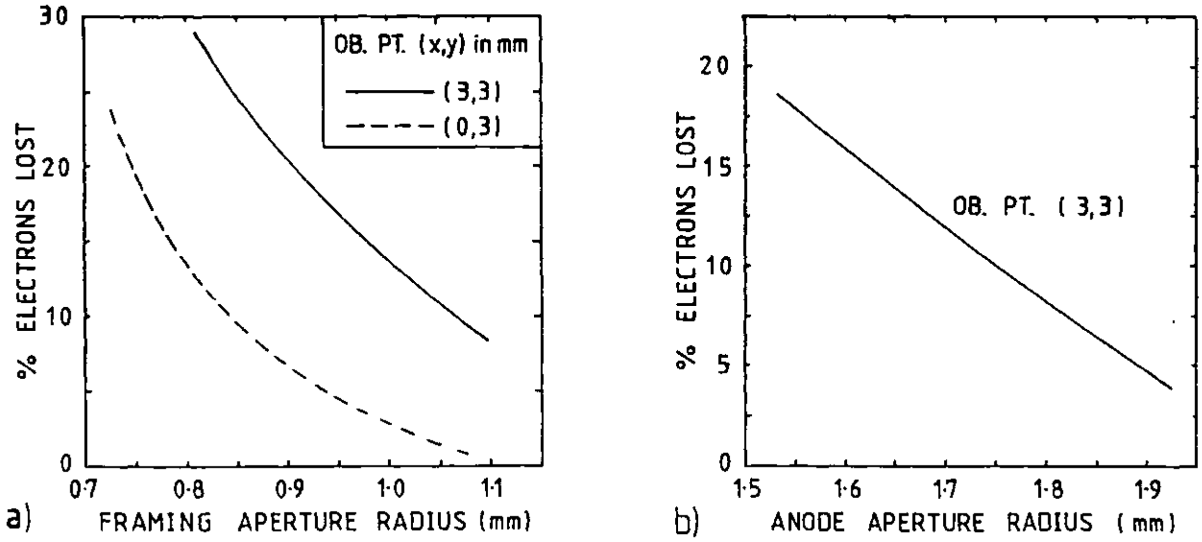

Fig. 7.12 Number of electrons lost at the two aperture planes as a function of the aperture radius.

7.5 Multiple frame generation - I

7.5.1 Principle

One method of producing multiple framed images with this tube is to include more than one aperture in the framing aperture plate. This is shown in figure 7.13, in which the deflection arrangement consists of three framing apertures in the framing (or multiplex) aperture plate, and three pairs of compensating deflection plates, whose deflection sensitivity is identical to that of the sweep deflectors.

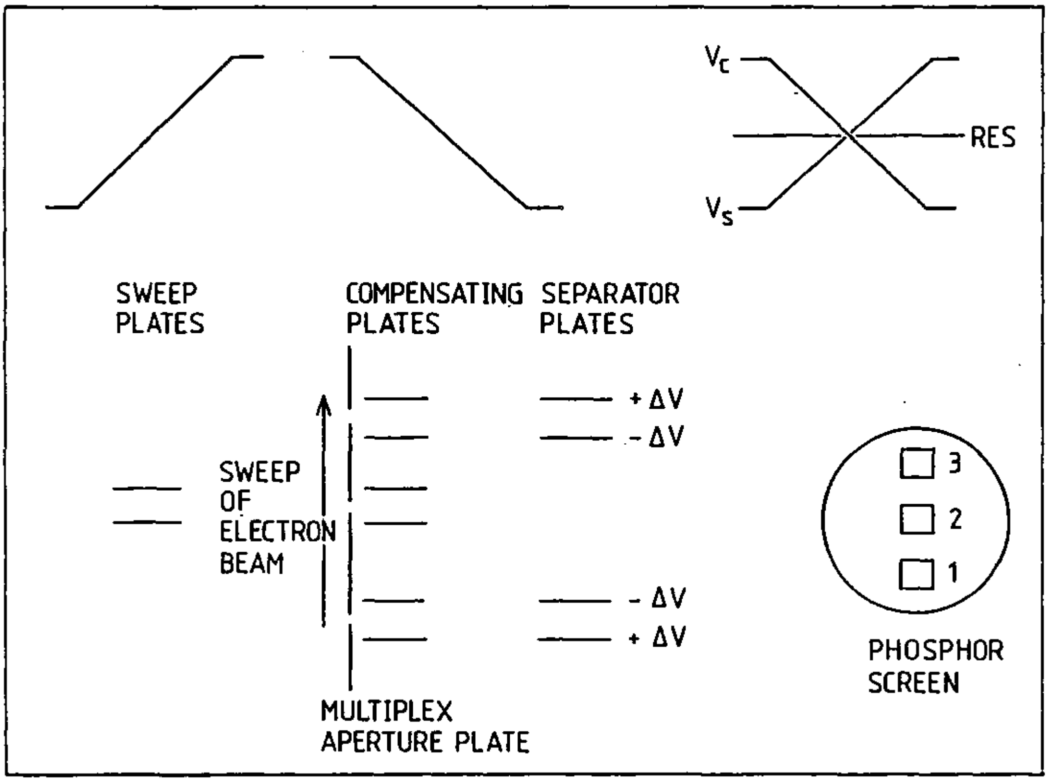

Fig. 7.13 Multiple frame generation.

Initially the electron beam is deflected to a pre-selected "closed" position, either above or below the three apertures, by applying a d.c. bias voltage to the sweep plates. When a single, fast, linearly time-varying voltage ramp is supplied to these deflectors, the beam is scanned across the three apertures producing three temporal transmissions. Application of the accurately synchronised, in-phase, duplicate but inverted waveform to the three pairs of compensating plates removes the introduced transverse velocity but would result in a spatial superposition of three generated frames at the phosphor. To overcome this several techniques can be employed. Two further sets of deflectors, referred to as the separator plates (fig. 7.13), can be included in the deflection region. By maintaining them at appropriate d.c. bias voltages of inverse polarity, spatial discrimination of the three frames is achieved. In this scheme, however, the deflection section becomes rather complex.

In two alternative techniques, the need for the separator plates is eliminated. The first of these is illustrated in figure 7.14. In this case the inverted voltage ramps are supplied to the three pairs of compensating deflectors with carefully chosen phase differences, so that the resulting effect of combining the sweep and compensating voltages is a net d.c. voltage bias of $\pm \Delta V$ for the top and bottom pairs of deflection plates respectively; the central pair suffer no overall bias. Another, related, technique for spatially separating the three images is to keep the phases of the voltage ramps supplied to the sweep and compensating deflectors synchronised accurately, but to maintain suitable d.c. bias voltages on the top and bottom pairs of compensating plates (see figure 7.15).

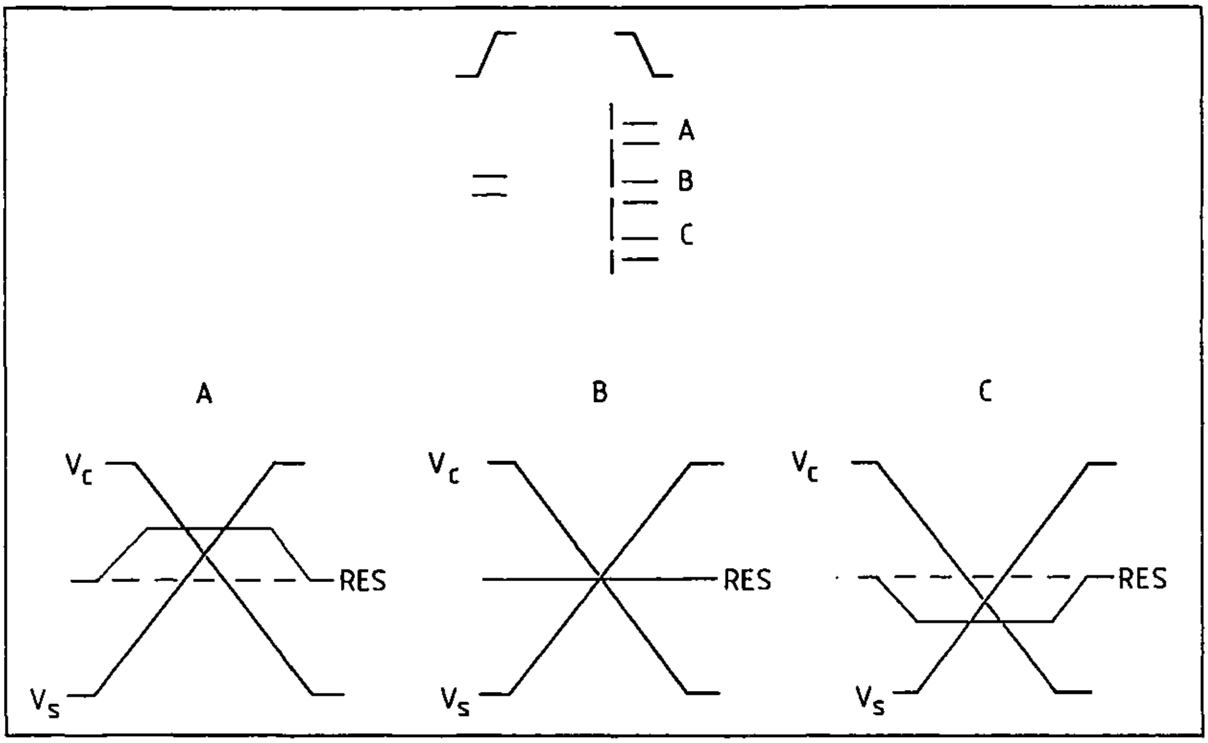

Fig. 7.14 Frame discrimination by dephasing the sweep and compensating voltage waveforms.

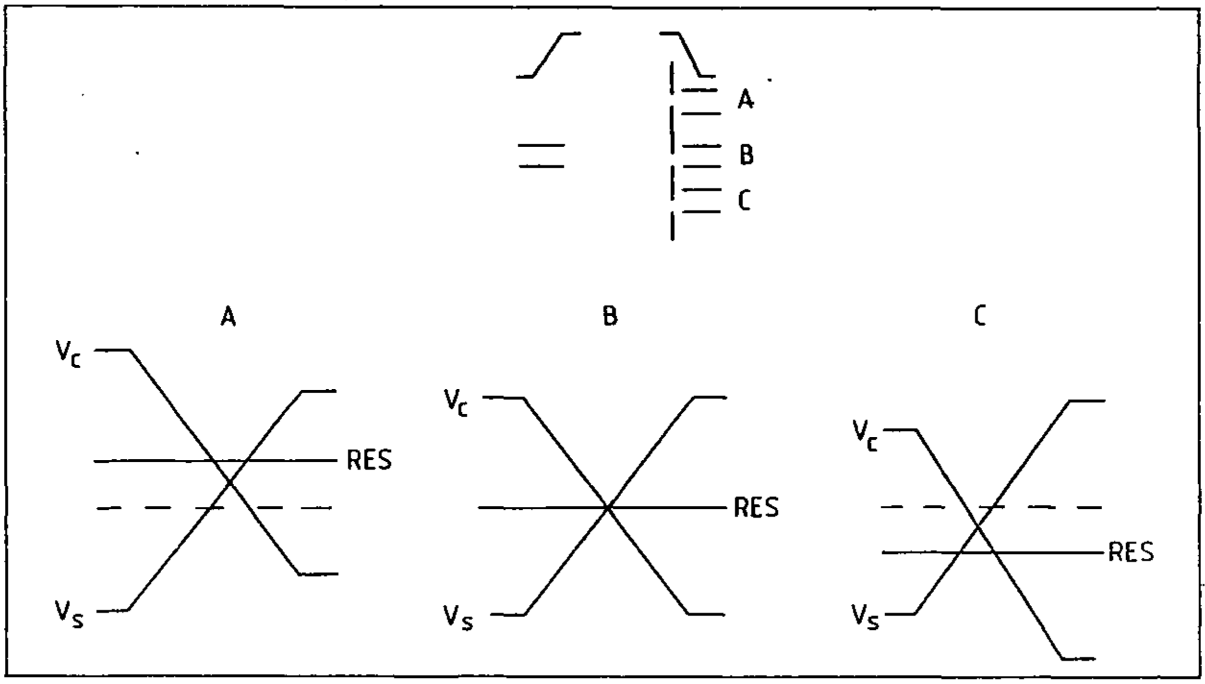

Fig. 7.15 Frame separation by application of suitable d.c. bias voltages to the compensating deflectors.

In all these cases, a further pair of deflection plates (the shift plates), orientated orthogonally to the others, would be included in the framing image tube as indicated in figure 7.16. Application of a staircase voltage waveform to this pair of plates would allow a sequence of "triplet" framed images to be displayed on the phosphor screen.

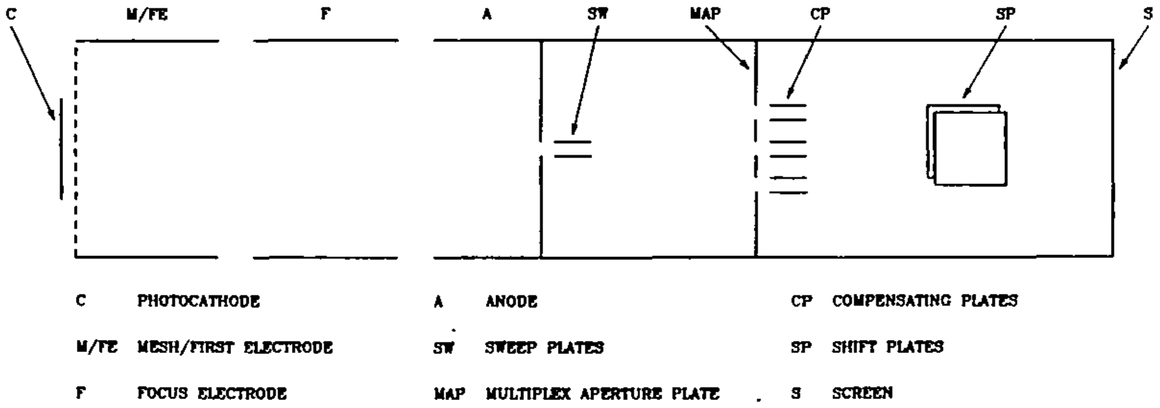

Fig. 7.16 Schematic of the Photochron framing tube, version 1.

7.5.2 Dimensions of the deflectors

A simplified analysis of the deflection geometry has been used to determine the dimensions of the sweep and compensating deflectors. The parameters used are defined according to figure 7.17. With values chosen for d, and l_1, the deflection voltage V_1 required to deflect the electron beam to the centre of the first aperture (distance G from the axis) is calculated using equation 7.2. The deflection sensitivity at the phosphor screen S_1 (in mm V^{-1}) of the sweep deflectors is determined, and by equating this to the corresponding value for the compensating plates (from eq. 7.2), the length l_2 is

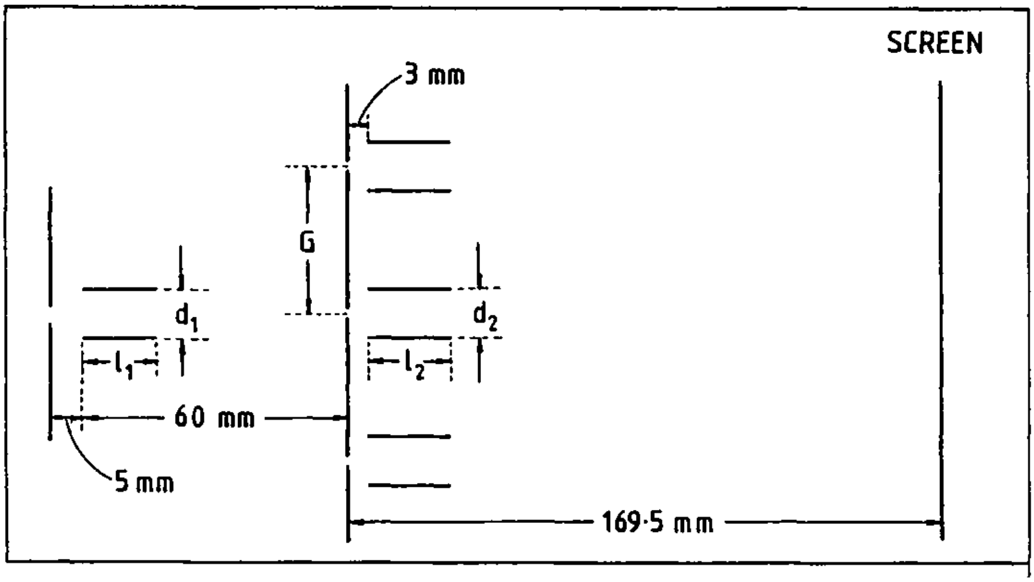

Fig. 7.17 Deflection geometry dimensions.

determined to be

$$l_2 = 166.5 - \sqrt{2.77 \times 10^5 - 6 \times 10^4 .\ S_1 d_2}\ \text{mm} \qquad \text{Eq. 7.4}$$

where d_2 is pre-selected. If the electron beam does not hit the compensating deflector plates, this value of l_2 is satisfactory, otherwise d_2 is incremented and l_2 re-evaluated. The values of l_2 and d_2 can be calculated for a range of values of l_1 and d_1.

There are a number of assumptions implicit in this analysis, and these are:- (i) the axial velocity v_z of the electrons is constant; (ii) the diameter of the electron beam is small compared to the deflection plate separation; (iii) the electric field between the plates is uniform over the length of the plates and is negligible beyond their ends, i.e. no fringing fields; (iv) the displacement given to the electron within the deflection region is negligible compared with the displacement produced at the screen.

The gap between the apertures was chosen to be 7mm. For each value of d_1 = 3.6, 3.8, 4.0, 4.2 mm, the values of l_2 and d_2 were calculated for l_1 = 5 - 11 mm. The results are presented in table 7.1.

For ease of fabrication the length of the sweep plates should be at least 7 mm. Also, it is necessary to keep the voltage required to deflect the beam across the aperture as low as possible (i.e. < 2kV), since it becomes more difficult in practice to supply very high voltage ramps. A final constraint is that the value of d_2 should be kept small, otherwise the separation between each pair

Table 7.1 Framing tube version I compensating plate dimensions for variations in l_1, d_1 with G = 7 mm.

d_1 = 3.6mm

l_1 mm	V_1 kV	l_2 mm	d_2 mm
5.0	2.63	6.5	3.4
6.0	2.21	8.3	3.6
7.0	1.91	10.3	3.8
8.0	1.69	12.4	4.0
9.0	1.51	15.5	4.4
10.0	1.37	19.0	4.8
11.0	1.26	22.8	5.2

d_1 = 3.8mm

l_1 mm	V_1 kV	l_2 mm	d_2 mm
5.0	2.78	6.2	3.4
6.0	2.33	7.4	3.4
7.0	2.02	9.7	3.8
8.0	1.78	11.8	4.0
9.0	1.60	14.0	4.2
10.0	1.45	17.1	4.6
11.0	1.33	20.6	5.0

d_1 = 4.0mm

l_1 mm	V_1 kV	l_2 mm	d_2 mm
5.0	2.92	5.5	3.2
6.0	2.46	7.1	3.4
7.0	2.12	8.7	3.6
8.0	1.88	10.6	3.8
9.0	1.68	13.2	4.2
10.0	1.53	15.5	4.4
11.0	1.40	18.7	4.8

d_1 = 4.2mm

l_1 mm	V_1 kV	l_2 mm	d_2 mm
5.0	3.01	5.3	3.2
6.0	2.58	6.7	3.4
7.0	2.23	8.3	3.6
8.0	1.97	10.1	3.8
9.0	1.77	12.0	4.0
10.0	1.60	14.0	4.2
11.0	1.47	17.0	4.6

of compensating plates will be less than the deflector spacing in that pair (d_2), and the cross-coupling capacitance becomes large. In this case, some shielding would be needed.

With the above requirements in mind, the best values for the deflector plate dimensions are likely to be
l_1 = 8 mm, d_1 = 4.0 mm for the sweep plates, and
l_2 = 10.6 mm and d_2 = 3.8 mm for the compensating plates. The widths of these deflectors are chosen to keep the capacitances identical and as low as possible, so possible values would be 10 mm and 7.2 mm for the sweep and compensating deflectors respectively, providing a theoretical capacitance of ∿ 0.2 pF (ignoring any cross-capacitance effects).

7.6 Multiple frame generation - II

7.6.1 Principle

Another method of producing multiple frames is to simplify the deflection section to include just a single framing aperture and one pair of compensating plates (see figure 7.18). This is a more feasible design from the constructional viewpoint of an experimental prototype tube.

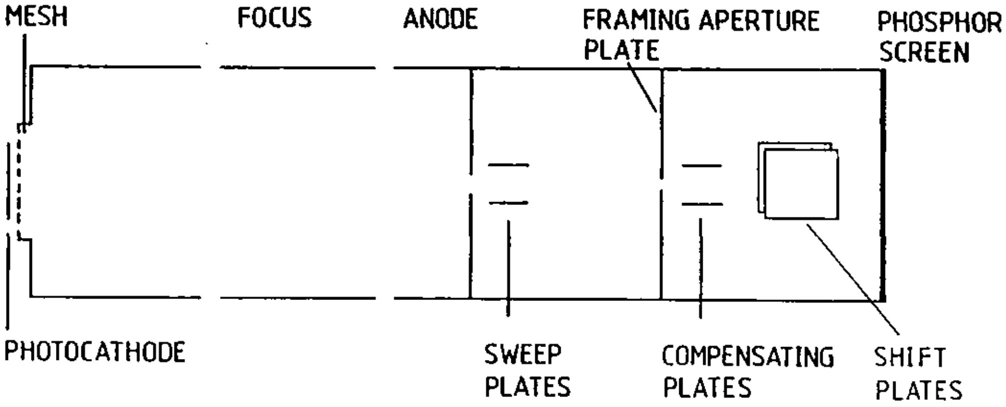

Fig. 7.18 Schematic of the Photochron framing tube, version 2.

Applying a symmetrical triangular voltage waveform to the sweep deflectors, the electron beam is scanned across the framing aperture twice, hence defining two short exposures. The duplicate, inverted waveform is supplied to the compensating plates. By suitably de-phasing this wave with respect to the sweep voltage wave, as shown in figure 7.19, spatial discrimination of the two images is achieved. If an appropriate staircase voltage waveform is supplied to the shift plates, a series of frame "doublets" could be produced.

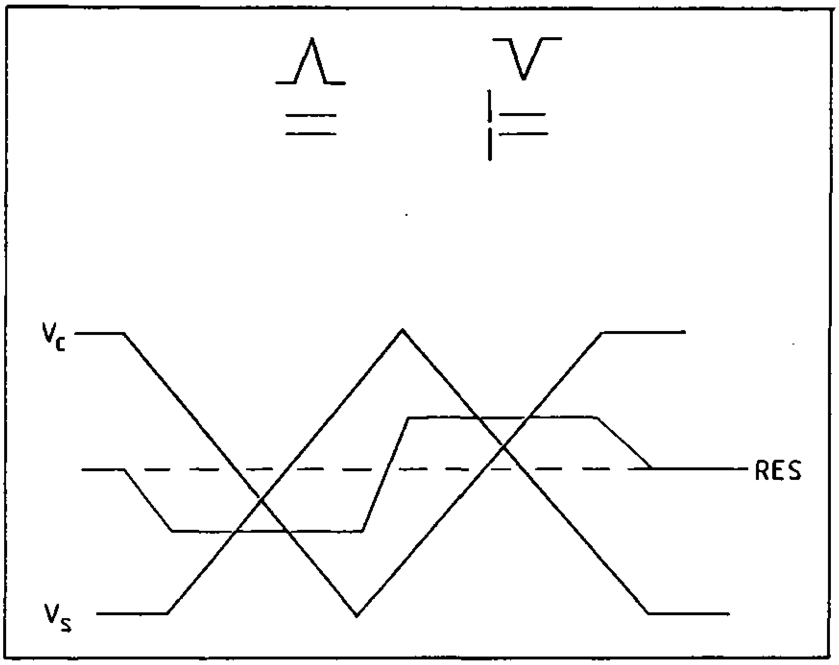

Fig. 7.19 Multiple frame generation with triangular waveforms.

The triangular voltage wave required for this technique could be derived from a semiconductor switch device if the recombination time is very short. It has been shown that GaP can have such a recovery time as short as $\sim$ 60 ps (146), and can switch voltages $>$ 5 kV. The feasibility of obtaining the triangular voltage pulses has thus been demonstrated.

7.6.2 Dimensions of the deflectors

The procedure adopted in designing the deflection system for this second scheme was similar to that described in section 7.5.2. Now, the voltage V_1 is that required to deflect the electron beam a distance 1.8 mm off axis, which is equivalent to shuttering the tube "off". Since the electron beam has a defined diameter of 3.5 mm at the anode aperture, for a chosen usable cathode area of 6 mm x 6 mm, the value of d_1 was set to be 4.4 mm. The resulting values of V_1, l_2 and d_2 for the selected values of l_1 are presented in table 7.2.

Table 7.2 Framing tube version II compensating plate dimensions for different sweep plate lengths

l_1 mm	V_1 V	l_2 mm	d_2 mm
7.0	600	8.9	4.0
8.0	530	10.2	4.0
9.0	476	12.1	4.2
10.0	432	13.4	4.2
11.0	396	14.8	4.2
12.0	366	16.2	4.2
13.0	341	17.6	4.2

To maintain sufficient deflection sensitivity, the length of the sweep plates was set to be 11.0 mm, so the dimensions for the pair of compensating plates are l_2 = 14.8 mm with d_2 = 4.2 mm. The widths of these two sets of deflection plates were selected as being 11.0 mm and 7.8 mm for the sweep and compensating deflectors respectively, so that the capacitance of each set should be identical, with the low value of 0.24 pF. (In practice the measured value is likely to be higher but will be limited by any stray capacitances.)

The dimensions of the orthogonally orientated, shift deflectors were chosen by considering the size of the deflected electron beam passing between them. The width of the shift plates is 20 mm and their separation is 20 mm. They are positioned 20 mm from the end of the compensating deflectors to reduce the interaction between the two deflection fields. The length of the plates is chosen to be 25 mm to maintain a deflection sensitivity ∿ 9 mm/kV. The spatial separation of the 9 mm x 9 mm images at the screen requires a voltage of 1 kV to be supplied to the shift plates.

7.7 Frame exposure time

7.7.1 Multiplex aperture design

For this design, the deflection sensitivity of the sweep plates at the multiplex aperture plate is 0.37 cm/kV. It should be possible to apply a voltage ramp of 5.4×10^{12} Vs^{-1} to these deflectors, as this has been produced experimentally before (ref. the single-shot tests on the Photochron IV, section 5.5). This would provide a streak speed of 2.0×10^{9} cms^{-1} at the framing apertures. With the diameters of these apertures being 1.8 mm, the frame exposure time is predicted to be 90 ps from equation 7.3.

The interframe period is determined by the gap between the apertures and the speed of deflection. Since the minimum distance between the apertures is 5.2 mm, with the above streak speed, the interframe, "off", time should be ∿260 ps.

7.7.2 Design version 2

In this case, the sweep plates have a sensitivity of deflection of 0.45 cm/kV at the framing aperture diaphragm. With an applied voltage ramp of 5.4×10^{12} Vs^{-1} the electron beam would be swept across the framing aperture at a speed of 2.4×10^{9} cms^{-1}. This leads to a predicted frame exposure time ∿74 ps.

The interframe period for this design is dependent on the separation of the positive and negative parts of the triangular waveform, and hence on the recombination time of the semiconductor. It should be possible to achieve interframe times $<$ 500 ps with suitable choice of semiconductor material (146).

7.8 Conclusions

An image tube has been designed specifically for multiple, picosecond, framing operation. This incorporates a weak electrostatic lens to provide an electron beam which has a long narrow waist in the crossover region. This is consistent with the use of either of the two types of deflection geometry studied. The lens has an electron-optical magnification of -1.5 and provides a static spatial resolution at the screen $\geqslant 40$ lp/mm for a useable area of 5 mm x 5 mm on the photocathode.

Two independent schemes for the deflection configuration have been developed. One employs three apertures and three sets of compensating deflectors, with a single applied linear voltage ramp, whilst the other has a single framing aperture but provides multiple frames by using a triangular voltage ramp. The frame exposure time for either case is < 100 ps if the voltage ramp is $\geqslant 5 \times 10^{12}$ Vs^{-1}.

In the multiplex aperture design, the deflection plate separation within each pair of compensating deflectors should be small to avoid any cross-capacitance effects between these different sets of deflectors. This scheme may prove inconvenient, so that the second version of the framing tube may be superior experimentally because of its greater constructional simplicity. The multiplex aperture version also has the added disadvantage that the best values chosen for the sweep deflector plate dimensions may constrain the size of the anode aperture, further restricting the usable cathode area.

Under dynamic conditions the spatial resolution in the image will become degraded due to such effects as deflection-induced aberrations, non-perfect voltage waveforms which may not be accurately synchronised, and space-charge effects. In the theoretical simulation for the Photochron IV streak image tube, the dynamic spatial resolution in the streak direction after deflection by a voltage ramp of 5×10^{12} Vs^{-1} was calculated to be ∿ 15 lp/mm (ref. section 4.4). Taking this into account, it is estimated that the dynamic spatial resolution, at the screen, of the framed images should be ⩾ 10 lp/mm.

CHAPTER EIGHT

GENERAL CONCLUSIONS

The linearity and sensitivity of response has established the picosecond streak camera as an important diagnostic tool in many areas of research (21 - 25). The information which it provides can be complemented by the two-dimensional data available from fast framing image tubes (121 - 141). With the improvement of the resolution capabilities of both types of high speed camera, the number of applications will be expected to increase substantially in the future.

To study electron-optical image tube designs, a computer model has been used to evaluate the electron trajectories (c.f. chapter 2). The current model does not allow the simulation of electrode misalignments (e.g. tilting or non-concentricity), or mesh effects, such as bowing at large extraction fields and microlensing through the individual cell apertures. Although these effects do not seem to pose significant problems in the current tube designs (as evidenced in the experimental tests), they should be explicitly included in the design of the next generation of streak and framing image tubes. To accommodate this, the computer programs will need to be extended to three-dimensions, and refined to accept a variable grid size as opposed to the constant square-grid currently used.

To analyse the computed electron trajectories, and hence characterise the performance of the image tubes, the modulation transfer function method has been developed (34). This approach, which is more physically realistic than the Gaussian approximation, has the important advantage of allowing the specification to be quantified over a large range of spatial or temporal frequencies, and not just at the limiting value. The MTF method has been comprehensively adopted, and used in the design of the new Photochron IV streak tube, which shows a theoretical temporal resolution of 0.4 ps with an ultimate limiting value < 200 fs.

The Photochron IV has demonstrated a static spatial resolution of 70 lp/mm at the photocathode, which is approximately twice that of its predecessor, the Photochron II. It is clear, then, that to exploit the full potential of this tube, and any future improved designs, the peripheral instrumentation used must have non-limiting response capabilities. For instance, it is no longer sufficient for this equipment to have good limiting resolution since it is the general shape of the MTF curve which is important. Because the total camera system response is the convolution of each individual MTF, the requirement now is for an input lens, image intensifier and detector all with a good MTF response over the whole range of frequencies.

It has been found from theoretical considerations that an optimum streak speed exists for the Photochron IV with a value of 3×10^{10} cms^{-1}, above which the temporal resolution deteriorates. However, in principle, this tube could achieve subpicosecond resolution even at relatively low streak speeds, due to its high spatial resolution along the streak axis, provided that this is not degraded by the imaging response of the anciliary equipment (e.g. the OMA).

An initial, experimental Photochron IV tube has been constructed, wherein the cathode extraction field was restricted to 23 kV cm^{-1}. Under single-shot conditions the temporal resolution was measured to be 0.8 ps for a writing speed of 2 x 10^{10} cms^{-1} at the phosphor. It is very unlikely that subpicosecond resolution will be attained at much lower streak speeds than this for the present camera arrangement, since the spatial resolution is limited to 15 lp/mm by the OMA used.

It is intended that the next experimental Photochron IV streak tube to be constructed should have the designed cathode-mesh spacing of 2.0 mm, so allowing an electric field of 50 kV cm^{-1} to be maintained at the cathode. To reduce any detrimental effects caused by the spot-weld blemishes at the surface of the mesh retaining ring (c.f. chapter 5), the micromesh should be secured between this ring and a profiled holder, so that the surface defects are positioned further from the cathode than is the flat mesh. Even so, it is still possible that field emission (114) would occur. This may impose severe problems at very high electric fields, and may require the electric field to be pulsed, by applying a gating voltage pulse to the mesh, rather than be maintained d.c. The streak camera arrangement used with an up-to-specification Photochron IV should include improved input and output instrumentation, so that the camera temporal response is limited solely by the streak tube.

The Photochron IV has been adapted to make it compatible with inclusion in a demountable target chamber. This miniature Photochron IV-M has the advantage of a smaller pre-deflection temporal dispersion, but has a poorer deflection sensitivity. Its dynamic performance has been shown to be comparable to that of the standard sized Photochron IV. A demountable version of the Photochron IV-M has been tested in the synchroscan mode of operation. The temporal resolution was limited by the jitter of the testing system to be $\lesssim 18$ ps.

It should be feasible to further improve the temporal response of the Photochron IV streak tube by refining the deflection geometry. If the deflection plates were profiled in shape to follow the paths of the electrons, the majority of the electrons would always intersect the electric field lines normally, and so would not suffer axial deceleration. There would then be very little deflection-induced temporal dispersion.

Further enhancement of the temporal response would then require a reduction of the pre-deflection time dispersion, probably by using a shorter length focussing section, as in the Photochron IV-M, or by increasing the extraction electric field at the cathode and redesigning the electron-optical lens. A novel approach would be to include an electron mirror within the streak tube, after the lens but prior to the deflection section. Since the fastest electrons will travel further into the retarding potential region of the mirror before being reflected, than will their slower counterparts, the transit times at the deflection plates may be equalised. With careful design of this mirror it may be possible to eliminate or at least significantly reduce the predeflection transit time dispersion.

It should be possible to make use of the improved dynamic spatial resolution of the Photochron IV along the slit, in the X-ray region of the spectrum, where high spatial resolution may be more desirable than extremely fast temporal resolution. To achieve subpicosecond resolution at these spectral wavelengths it is expected that it would be necessary to further increase the extraction electric field above 50 kV cm^{-1}, but this may require improvements to the current production technology.

The fundamental limit on the temporal resolution of an electron-optical streak camera is set to $\sim$10 fs by the frequency of the light oscillations (c.f. chapter 1), the time dispersion within the photocathode (35, 36), and the time dispersion of the glass optics used (38). It is likely that a streak tube, whose low dispersion focussing lens is allied with an elaborate deflection configuration (such as that suggested above), could achieve a theoretical temporal response better than 100 fs.

A framing image tube has been designed which utilises a weak electrostatic focussing lens combined with either of two independent deflection sections. For both design versions it should be possible to achieve multi-framing, with frame exposure times <100 ps. Since the exposure time of the images is determined by the diameter of the framing aperture, this could be further reduced by limiting this aperture size, in applications where only a small object size is needed at the cathode. It is expected that the initial Photochron framing image tube constructed will be of the single framing-aperture design, since this is likely to be simpler to fabricate than the more complex multi-deflector version.

The next generation framing camera is likely to be scaled down in both physical size, to allow for inclusion in test chambers of restricted diagnostic volume, and voltage. The latter would provide an increased deflection sensitivity, and would facilitate the incorporation of internal intensification thereby further reducing the overall length of the camera.

Using a photoconductive element it is possible to switch voltages ~ 5 kV with rise times ~ 10 ps. Under these conditions the voltage ramp applied to the deflection plates could be $\sim 5 \times 10^{14}$ $\mathrm{Vs^{-1}}$, so that in principle subpicosecond exposure frames could be generated with this type of framing image tube. However, in practice the rise time of the voltage ramp will be limited by the stray inductances and capacitances in the tube and its associated electrical connections, and also the capacitance of the deflection plates. Improvements to the design of the deflection plate arrangement should enable the frame exposure time $\lesssim$ 10 ps to be attained in the near future.

Clearly, further refinements to current streak and framing tube designs are possible. The overall objective will be to achieve the best temporal and spatial resolutions while retaining the maximum dynamic range of operation. This may well involve substantial development to the electronic read-out systems as well, so that concentration on the "active" image tube element may be a luxury in this thesis that cannot be guaranteed for the future!

APPENDIX ONE

DERIVATION OF THE GAUSSIAN APPROXIMATION EQUATION

Let the input intensity profile and the camera instrumental response functions both have Gaussian forms, represented by respectively

$$I(t) = \exp\left(-\frac{4\ \ln 2\ t^2}{T^2}\right)$$

$$R(t) = \exp\left(-\frac{4\ \ln 2\ t^2}{\tau^2}\right)$$

where T is the FWHM of the input pulse, and τ is the camera temporal resolution. The resultant output signal at a time t is the convolution of these functions:

$$S(t) = \int_{-\infty}^{t} R(t^1 - t)\ I(t^1)\ dt^1$$

$$= \int_{-\infty}^{t} \exp\left[-\frac{4\ \ln 2\ (t^1-t)^2}{\tau^2}\right] . \exp\left[-\frac{4\ \ln 2\ {t^1}^2}{T^2}\right] dt^1$$

$$= \int_{-\infty}^{t} \exp\left\{-4\ \ln 2\left[\frac{{t^1}^2}{\tau^2} - \frac{2t\ t^1}{\tau^2} + \frac{t^2}{\tau^2} + \frac{{t^1}^2}{T^2}\right]\right\} dt^1$$

$$= \int_{-\infty}^{t} \exp\left\{-4\ \ln 2\left[{t^1}^2\frac{(T^2 + \tau^2)}{T^2\tau^2} - \frac{2tt^1}{\tau^2} + \frac{t^2}{\tau^2}\right]\right\} dt^1$$

Completing the square this becomes

$$S(t) = \int_{-\infty}^{t} \exp\left\{-4\ \ln 2\left[\left(\frac{t^1\sqrt{T^2 + \tau^2}}{T\tau} - \frac{tT}{\tau\sqrt{T^2+\tau^2}}\right)^2 + \right.\right.$$

$$\left.\left. + \frac{t^2}{\tau^2} - \frac{t^2T^2}{\tau^2(T^2 + \tau^2)}\right]\right\} dt^1$$

$$S(t) = \exp\left(-\frac{4\ \ln\ 2\ t^2}{T^2 + \tau^2}\right) \int_{-\infty}^{t} \exp\left[-4\ \ln\ 2\left(\frac{t^1\sqrt{T^2+\tau^2}}{T\tau} - \frac{tT}{\tau\sqrt{T^2+\tau^2}}\right)^2\right] dt^1$$

Make the substitution

$$x = \frac{t^1}{\tau T}\sqrt{T^2+\tau^2} - \frac{tT}{\tau\sqrt{T^2+\tau^2}}$$

When $t^1 = t$, x is given by x_1 where

$$x_1 = \frac{t\tau}{T\sqrt{T^2+\tau^2}}$$

therefore

$$S(t) = \exp\left(-\frac{4\ \ln\ 2\ t^2}{T^2+\tau^2}\right) \int_{-\infty}^{x_1} \exp(-4\ \ln\ 2\ x^2)\ \frac{T\tau}{\sqrt{T^2+\tau^2}}\ dx$$

The integral can be written as

$$\int_{-\infty}^{x_1} \exp\ (-4\ \ln\ 2\ x^2)dx = \int_{-\infty}^{0} \exp(-4\ \ln\ 2\ x^2)dx + \int_{0}^{x_1} \exp(-4\ \ln\ 2\ x^2)dx$$

But $\int_{-\infty}^{0} \exp\ (-a^2x^2)dx = \int_{0}^{\infty} \exp\ (-a^2x^2)dx = \frac{\sqrt{\pi}}{2a}$

$$\therefore \quad \int_{-\infty}^{x_1} \exp(-4\ \ln\ 2\ x^2)dx = \frac{\sqrt{\pi}}{2\sqrt{4\ln 2}} + \int_{0}^{x_1} \exp(-4\ln 2\ x^2)dx$$

Making the substitutions $y = 2\sqrt{\ln 2}\, x$, $y_1 = 2\sqrt{\ln 2}\, x_1$, this latter integral becomes

$$\int_0^{y_1} \exp(-y^2) \frac{dy}{2\sqrt{\ln 2}}$$

The error function is defined as

$$\operatorname{erf}(z) = \frac{2}{\sqrt{\pi}} \int_0^z \exp(-w^2)\, dw$$

Thus $s(t) = \dfrac{T\tau}{\sqrt{T^2+\tau^2}} \exp\left(-\dfrac{4\ln 2\, t^2}{\tau^2+T^2}\right)\left[\dfrac{\sqrt{\pi}}{4\sqrt{\ln 2}} + \dfrac{\sqrt{\pi}}{2}\dfrac{\operatorname{erf}(y_1)}{2\sqrt{\ln 2}}\right]$

Finally, the signal at time t is

$$S(t) = \frac{T\tau}{\sqrt{T^2+\tau^2}} \frac{\sqrt{\pi}}{4\sqrt{\ln 2}} \exp\left(-\frac{4\ln 2 t^2}{\tau^2+T^2}\right)\left[1 + \operatorname{erf}\left(2\frac{\sqrt{\ln 2}\, t\, \tau}{T\sqrt{\tau^2+T^2}}\right)\right]$$

In this equation the only two terms which are time dependent are the exponential term and the error function. The approximation generally made is that the product of these two terms is small compared with the exponential terms, and so the error function may be ignored. The width of the signal at half maximum then occurs when

$$\frac{1}{2} = \exp\left(-\frac{4\ln 2\, t^2}{\tau^2+T^2}\right)$$

$$\therefore \quad 4t^2 = \tau^2 + T^2$$

$$\therefore \quad t = \pm\frac{1}{2}\sqrt{\tau^2+T^2}$$

The FWHM is then, $t_{FWHM} = \sqrt{\tau^2+T^2}$.

APPENDIX TWO

DERIVATION OF THE DEFLECTION DEVIATIONS

Ideal case of zero temporal dispersion

Consider a pair of parallel plate deflectors with a separation d, and whose initial potential difference is V_o. In the ideal case, the electron beam arrives at the entry to the deflectors with zero temporal dispersion, at a time which is taken to be t = 0. The ramp applied to the plates is K Vs^{-1}. Then making the assumptions that the electrons have no transverse velocity components, and that there are no fringing fields, the uniform electric field at time t is given by

$$E(t) = -\frac{(V_o + Kt)}{d} \qquad \text{Eq. A1}$$

$$\therefore \quad \text{Acceleration } (t) = \frac{e}{md}(V_o + Kt) \qquad \text{Eq. A2}$$

where -e and m are respectively the charge and mass of the electron.

The transverse velocity at the exit of the deflector plates can be obtained by integrating the acceleration over the initial and final times. If the time of flight in the deflectors is T_d, then

$$v_x(\text{exit of deflectors}) = \int_o^{T_d} \frac{e}{md}(V_o + Kt)dt \qquad \text{Eq. A3}$$

$$= \frac{e}{md}\left(V_oT_d + \frac{KT_d^{\,2}}{2} \right) \qquad \text{Eq. A4}$$

To a first approximation the deflection of the electron beam in the deflector plates can be ignored compared with the deflection at the screen. This deflection is given by the product of the velocity v_x and the transit time in the drift region T_{pd},

$$x_{screen} = \frac{e}{md}\left(V_o T_d + \frac{KT_d^2}{2} \right) T_{pd} \qquad \text{Eq. A5}$$

Time dispersion in the electron lens

Now consider the case when there is a time dispersion Δt_{cd} in the electron focussing region. Assume that the electrons arrive at the entry of the deflectors between times t = 0 and t = Δt_{cd}. The former case produces a deflection at the screen given by equation A5. For the latter case (the slowest electrons), the field which these electrons experience will be $E(t + \Delta t_{cd})$. Therefore the velocity at the start of the drift region (end of deflection region) will be, using equation A3

$$v_x = \int_o^{T_d} \frac{e}{md} (V_o + Kt + K\Delta t_{cd})\, dt$$

$$= \frac{e}{md} (V_o T_d + \frac{KT_d^2}{2} + K \Delta t_{cd} T_d)$$

The deflection at the screen in this case is

$$x_1 = \frac{e}{md} (V_o T_d + \frac{KT_d^2}{2} + K \Delta t_{cd} T_d) T_{pd} \qquad \text{Eq. A6}$$

Hence the deflection deviation (in the first approximation) due to the temporal dispersion up to the deflectors is given by the difference of equations A6 and A5:

$$\Delta x_1 = \frac{e}{md} K \, T_d \, T_{pd} \, \Delta t_{cd}$$

Time dispersion in the deflection region

For the case when the temporal dispersion is assumed to be zero in the pre-deflection section, all the electrons arrive simultaneously at the deflectors at t = 0. If there is a temporal dispersion Δt_d within the deflection region, the time of flight of the electrons through the deflectors will lie in the range $T_d \leqslant t \leqslant T_d + \Delta t_d$. The electrons which take the longest time to traverse the deflection region will have a final transverse velocity of

$$v_x = \int_0^{T_d + \Delta t_d} \frac{e}{md} (V_o + Kt) \, dt$$

$$= \frac{e}{md} \left[V_o (T_d + \Delta t_d) + \frac{K}{2} (T_d + \Delta t_d)^2 \right]$$

from equation A3. The resulting deflection at the screen is then

$$x_2 = \frac{e}{md} (T_d + \Delta t_d) \left[V_o + \frac{K}{2} (T_d + \Delta t_d) \right] \quad \text{Eq.A7}$$

The deflection deviation due to the temporal dispersion within the deflection region is hence the difference of equations A7 and A5:

$$\Delta x_2 = \frac{e}{md} (V_o \, \Delta t_d + K \, T_d \, \Delta t_d + \frac{K}{2} \Delta t_d^{\,2}) \, T_{pd}$$

To a first-order approximation this can be rewritten as

$$\Delta x_2 = \frac{e}{md} (V_o + K\,T_d)\,T_{pd}\;\;\Delta t_d$$

provided $\Delta t_d << T_d$.

Time dispersion in the drift region

Consider the case when there is no temporal dispersion up to and through the deflection region. All the electrons will leave the deflector plates with the same velocity v_x, given by equation A4. Suppose that there is a temporal dispersion Δt_{pd} in the drift region. The electrons which take the longest transit time will suffer a deflection

$$x_3 = \frac{e}{md} (V_o\,T_d + \frac{KT_d^2}{2})\;(T_{pd} + \Delta t_{pd}) \qquad \text{Eq. A8}$$

The resulting deflection deviation due to this temporal dispersion is:

$$\Delta x_3 = \frac{e}{md} (V_o + \frac{K}{2}\,T_d)\,T_d\;\;\Delta t_{pd}$$

REFERENCES

1. J.M. Halbout and C.L. Tang,
IEEE J. Quant. Elect., Vol. QE - 19, p. 487, 1983

2. R.L. Fork, B.I. Greene and C.V. Shank,
Appl. Phys. Lett., Vol. 38, p. 671, 1981.

3. C.V. Shank et al,
Appl. Phys. Lett., Vol. 40, p. 761, 1982.

4. C. Kalpouzos et al,
"Picosecond Phenomena III", Ed. K.B. Eisenthal,
Springer-Verlag series in chemical physics 23,
New York, p. 221, 1982.

5. H.E. Rowe and T. Li,
IEEE J. Quant. Elect., Vol. QE - 6, p. 49, 1970.

6. P.M. Rentzepis, C.J. Mitschele and A.C. Saxman,
Appl. Phys. Lett., Vol. 17, p. 122, 1970.

7. R.C. Eckardt and C.H. Lee,
Appl. Phys. Lett., Vol. 15, p. 425, 1969.

8. A. Kalpaxis et al,
Rev. Sci. Inst., Vol. 53, p. 960, 1982.

9. J.M. Halbout and C.L. Tang,
Appl. Phys. Lett., Vol. 40, p. 765, 1982.

10. D.H. Auston, P. Lavallard, N. Sol and D. Kaplan,
Appl. Phys. Lett., Vol. 36, p. 66, 1980.

11. J.R. Taylor, M.C. Adams and W. Sibbett,
J. Photochem., Vol. 12, p. 127, 1980.

12. J.P. Willson, W. Sibbett and P.G. May,
p. 149 of reference 4.

13. R.S. Marjoribanks et al,
Opt. Comm., Vol. 44, p. 113, 1982.

14. P.R. Bird, D.J. Bradley and W. Sibbett,
Adv. Elect. and Elect. Phys., Vol. 40 A, p. 51, 1976.

15. S.W. Thomas, G.R. Tripp and L.W. Coleman,
Proc. 10th I.C.H.S.P., p. 127, 1972.

16. A. Lieber,
Proc. 13th I.C.H.S.P.P., p. 521, 1978.

17. Y. Tsuchiya, E. Inuzuka, Y. Suzuki and W. Yu,
Proc. 13th I.C.H.S.P.P., p. 517, 1978.

18. M. Ya. Schelev,
Proc. 14th I.C.H.S.P.P., p. 75, 1980.

19. D.J. Bradley and W. Sibbett,
Appl. Phys. Lett., Vol. 27, p. 382, 1975.

20. P.G. May and W. Sibbett,
Appl. Phys. Lett., Vol. 43, p. 624, 1983.

21. M.H. Key,
Phil. Trans. R. Soc. London A, Vol. 298, p. 351, 1980.

22. J.G. Fujimoto, T.K. Yee and M.M. Salour,
Appl. Phys. Lett, Vol. 39, p. 12, 1981.

23. J. Chen, W. Sibbett and J.I. Vukusic,
Elect. Lett., Vol. 18, p. 426, 1982.

24. J.R. Taylor, M.C. Adams and W. Sibbett,
Appl. Phys. Lett., Vol. 35, p. 590, 1979.

25. e.g. "Biological events probed by ultrafast laser spectroscopy",
Ed. R.R. Alfano, Academic Press, New York, 1982.

26. O. Klemperer and M.E. Barnett,
"Electron Optics", Cambridge University Press, 3rd Edition, 1971.

27. C.B. Johnson, J.M. Abraham, E.H. Eberhardt and L.W. Coleman,
Proc. 12th I.C.H.S.P., S.P.I.E. Vol. 97, p. 56, 1976.

28. G. Clement, C. Loty, J.P. Roux and C. Chancel,
Proc. 11th I.C.H.S.P., p. 130, 1974.

29. V.V. Korobkin, A.A. Malyutin and M.Ya. Schelev,
Proc. 9th I.C.H.S.P., p. 232, 1970.

30. R. Kalibjian,
J. Appl. Phys., Vol. 46, p. 4875, 1975.

31. K. Kinoshita, T. Kato and Y. Suzuki,
Proc. 14th I.C.H.S.P.P., p. 199, 1980.

32. E.K. Zavoiskii and S.D. Fanchenko,
Sov. Phys. Doklady, Vol. 1, p. 285, 1956.

33. D.J. Bradley,
U.K. Patent Spec. 31167/70, 1970,
U.S. Patent 3761614, 1973.

34. H. Niu, W. Sibbett and M.R. Baggs,
Rev. Sci. Inst., Vol. 53, p. 563, 1982.

35. W.E. Spicer and F. Wooten,
Proc. IEEE, Vol. 8, p. 1119, 1963.

36. C.C. Phillips,
Private communication.

37. F.C. Delori,
Ph. D. Thesis, London University, 1971.

38. E.K. Zavoisky and S.D. Fanchenko,
Appl. Opt., Vol. 4, p. 1155, 1965.

39. W. Sibbett,
Ph. D. Thesis, The Queen's University of Belfast, 1973.

40. S.F. Bryant,
Ph. D. Thesis, London University, 1978.

41. K. Kinoshita, N. Hirai, and Y. Tsuchiya,
Proc. 15th I.C.H.S.P.P., S.P.I.E. Vol. 348, p. 222
1982.

42. H. Niu,
Proc. 15th I.C.H.S.P.P., S.P.I.E. Vol. 348, p. 231, 1982.

43. D.J. Bradley et al,
Adv. Elect. and Elect. Phys., Vol. 33 B, p. 1145, 1972.

44. A.J. Alcock, M.C. Richardson and M. Ya. Schelev,
Proc. 9th I.C.H.S.P., p. 191, 1970

45. S.W. Thomas and R.L. Peterson,
Proc. 15th I.C.H.S.P.P., S.P.I.E. Vol. 348, p. 190, 1982.

46. W. Friedman, S. Jackel, W. Seka and J. Zimmermann,
Proc. 12th I.C.H.S.P., S.P.I.E. Vol. 97, p. 544, 1976.

47. P. Dooley, V.I. Little, S.Sim and S. Majumdar,
Proc. 12th I.C.H.S.P., S.P.I.E. Vol. 97, p. 80, 1976.

48. S.W. Thomas and G.E. Phillips,
Proc. 13th I.C.H.S.P.P., p. 471, 1978.

49. D.R. Hull and N.J. Freeman,
J. Phys. E., Vol. 13, p. 685, 1980.

50. S. Majumdar,
Proc. 12th I.C.H.S.P., S.P.I.E. Vol. 97, p. 24, 1976.

51. R. Kalibjian,
Proc. 13th I.C.H.S.P.P., p. 452, 1978.

52. H. Niu and W. Sibbett,
Rev. Sci. Inst., Vol. 52, p. 1830, 1981.

53. D.J. Bradley, S.F. Bryant, J.R. Taylor and W. Sibbett,
Rev. Sci. Inst., Vol. 49, p. 215, 1978.

54. R. Kalibjian,
Proc. 13th I.C.H.S.P.P., p. 460, 1978.

55. W.E.D. Sleat,
Ph. D. Thesis, The Queen's University of Belfast, 1973.

56. D.H. Auston,
Appl. Phys. Lett., Vol. 26, p. 101, 1975.

57. W. Margulis,
Ph. D. Thesis, London University, 1981.

58. W. Margulis, W. Sibbett, J.R. Taylor and D.J. Bradley,
Opt. Comm., Vol. 32, p. 331, 1980.

59. W. Knox and G. Mourou,
Opt. Comm., Vol. 37, p. 203, 1981

60. W. Margulis,
Private communication.

61. G.E. Phillips and S.W. Thomas,
Proc. 13th I.C.H.S.P.P., p. 508, 1978.

62. P. Schagen,
"Advances in image pickup and display", Ed. B. Kazan, Academic Press, New York, Vol. 1, p. 1, 1974.

63. K. Kinoshita and Y. Suzuki,
Proc. 13th I.C.H.S.P.P., p. 504, 1978.

64. W. Sibbett, W.E. Sleat, J.R. Taylor and J.P. Willson,
Proc. 15th I.C.H.S.P.P., S.P.I.E. Vol. 348, p. 217, 1982.

65. W. Sibbett,
Proc. 15th I.C.H.S.P.P., S.P.I.E. Vol. 348, p. 15, 1982.

66. M.C. Adams,
Ph. D. Thesis, London University, 1979.

67. M.C. Adams, W. Sibbett and D.J. Bradley,
Adv. Elect. and Elect. Phys., Vol. 52, p. 265, 1979.

68. J.P. Willson, W. Sibbett and W.E. Sleat,
Opt. Comm., Vol. 42, p. 208, 1982.

69. R. Hadland, K. Helbrough and A.E. Huston,
Proc. 11th I.C.H.S.P., p. 107, 1974.

70. W. Sibbett, W.E. Sleat and J.R. Taylor,
Paper presented at the Royal Institution symposium, "Picosecond chemistry and biology", Nov. 1982,
To be published by Interscience, London.

71. J.C. Cheng et al,
Proc. 12th I.C.H.S.P., S.P.I.E. Vol. 97, p. 311, 1976.

72. C. Cavailler, N. Fleurot, D. Mazatud and R. Verrecchia,
Proc. 14th I.C.H.S.P.P., p. 347, 1980.

73. D.J. Bradley, S.F. Bryant and W. Sibbett,
Rev. Sci. Inst., Vol. 51, p. 824, 1980.

74. Y. Tsuchiya, C. Horiguchi, H. Iida and K. Kamiya,
Proc. 14th I.C.H.S.P.P., p. 350, 1980.

75. M. Bowman-Manifold and F.H. Nicoll,
Nature, Vol. 142, p. 39, 1938.

76. D.C. DePackh,
Rev. Sci. Inst., Vol. 18, p. 798, 1947

77. C. Weber,
Philips Technical Review, Vol. 24, p. 130, 1962.

78. "Image processing and computer aided design in electron optics", Ed. P.W. Hawkes, Academic Press, London, 1973.

79. W.B. Herrmannsfeldt,
Stanford Linear Accelerator Centre Report, SLAC-226, 1979.

80. P.W. Hawkes,
J. Phys. E., Vol. 14, p. 1353, 1981.

81. M.R. Alpern,
Proc. 9th I.C.H.S.P., p. 207, 1970.

82. V.P. Degtyareva et al,
Proc. 14th I.C.H.S.P.P., p. 354, 1980.

83. D.J. Bradley, K.W. Jones and W. Sibbett,
"Ultra-short laser pulses", The Royal Society, London, p. 71, 1980.

84. C. Weber,
"Focusing of charged particles", Ed. A. Septier, Academic Press, New York, Vol. 1, p. 45, 1967.

85. D. Young,
Trans. Am. Math. Soc., Vol. 76, p. 92, 1954.

86. B.A. Carré,
Comp. J., Vol. 4, p. 73, 1961.

87. W.E. Milne,
"Numerical Calculus", Princeton University Press, New Jersey, 1949.

88. K.W. Jones,
Private communication.

89. C.F. Gerald,
"Applied Numerical Analysis", Addison-Wesley,
Massachusetts,
2nd Edition, 1978.

90. B.J. Mayo and A.W. Bennett,
Adv. Elect. and Elect. Phys., Vol. 33 A, p. 571, 1972.

91. W. Sibbett,
Private communication.

92. A.G. Roddie, J.G. Edwards, T. Murphy and S. Maisey,
National Physical Laboratory Report DES 72, 1981.

93. B. Carnahan, H.A. Luther and J.O. Wilkes,
"Applied Numerical Methods", John Wiley, New York,
1969.

94. J.A. Zonneveld,
"Automatic Numerical Integration", Mathematisch
Centrum, Amsterdam, 2nd Edition, 1970.

95. C. Weber,
Philips Research Reports Supplements, No. 6, 1967.

96. V.V. Korobkin, A.A. Maljutin and M.Ya. Schelev,
J. Photog. Sci., Vol. 17, p. 179, 1969.

97. R. Kalibjian, C.F. McConaghy and L.W. Coleman,
Rev. Sci. Inst., Vol. 45, p. 776, 1974.

98. K.R. Barnes,
"Monographs on Applied Optics No. 3", Hilger,
London, 1971.

99. W.T. Welford,
"Aberrations of the symmetrical optical system",
Academic Press, London, 1974.

100. A.M. Stark, D.L. Lamport and A.W. Woodhead,
Adv. Elect. and Elect. Phys., Vol. 28 B, p. 567,
1969.

101. J.C. Richmond,
Adv. Elect. and Elect. Phys., Vol. 40 B, p. 519,
1976.

102. V.N. Platanov,
Proc. 14th I.C.H.S.P.P., p. 357, 1980.

103. W.T. Welford,
Optica Acta, Vol. 18, p. 401, 1971.

104. N.A. Soboleva, A.G. Berkovsky, N.D. Checnik and
R.E. Eliseev,
"Photoelectronic Devices", Science, Moscow, 1965.

105. E. Munro,
Private communication.

106. H. Niu,
Private communication.

107. A. Rose,
"Vision, human and electronic", Plenum Press, New York, 1974.

108. H.P. Lavin,
"Photoelectronic Imaging Devices Vol. 1", Ed. L.M. Biberman, Plenum Press, New York, 1971.

109. C.B. Johnson,
Adv. Elect. and Elect. Phys., Vol. 33 B, p. 579, 1972.

110. D.J. Bradley and K.W. Jones,
Proc. 15th I.C.H.S.P.P., S.P.I.E. Vol. 348, p. 237, 1982.

111. W. Sibbett, H. Niu and M.R. Baggs,
Rev. Sci. Inst., Vol. 53, p. 758, 1982.

112. Philips 21 XX Microchannel plate image intensifier, Technical information.

113. G. Jean-Francois et al,
Proc. 11th I.C.H.S.P., p. 190, 1974.

114. S.F. Essig,
Adv. Elect. and Elect. Phys., Vol. 12, p. 73, 1960.

115. W.A. Baum,
Adv. Elect. and Elect. Phys., Vol.16, p. 391, 1962.

116. W. Sibbett, H. Niu and M.R. Baggs,
Proc. 15th I.C.H.S.P.P., S.P.I.E. Vol. 348, p. 271, 1982.

117. P.G. May,
Ph. D. Thesis, London University, 1983.

118. A.J. Hatch,
Nucl. Inst. and Methods, Vol. 41, p. 261, 1966.

119. K. Kinoshita, K. Shinoda and Y. Suzuki,
Proc. 15th I.C.H.S.P.P., S.P.I.E. Vol. 348, p. 227, 1982.

120. M.C. Adams, M.R. Baggs, W. Sibbett and W.E. Sleat,
U.K. Patent Application, Agents Ref. No. PQ 20 925, 1983.

121. D.T. Attwood et al,
Proc. 14th I.C.H.S.P.P., p. 85, 1980.

122. P. Grivet,
"Electron Optics", Pergamon Press, Oxford, 2nd English Edition, 1972.

123. C.C. Phillips,
Ph. D. Thesis, London University, 1983.

124. P.G. May et al,
Opt. Comm., Vol. 42, p. 285, 1982.

125. e.g. Imacon 675,
Hadland Photonics Ltd., Bovingdon, Herts.

126. M.C. Richardson and K. Sala,
Appl. Phys. Lett., Vol. 23, p. 420, 1973.

127. J. Etchepare et al,
Appl. Phys. Lett., Vol. 43, p. 406, 1983.

128. A.J. Lieber and H.D. Sutphin,
Appl. Opt., Vol. 18, p. 745, 1979.

129. J.C. Cheng, L.G. Multhauf and G.R. Tripp,
Proc. 12th I.C.H.S.P., S.P.I.E. Vol. 97, p. 218, 1976.

130. H. Niu, T. Chao and W. Sibbett,
Rev. Sci. Inst., Vol. 52, p. 1190, 1981.

131. E. Laviron and C. Delmare,
Proc. 9th I.C.H.S.P., p. 198, 1970.

132. G. Clement,
Adv. Elect. and Elect. Phys., Vol. 33 B, p. 1131, 1972.

133. A.K.L. Dymoke-Bradshaw, J.D. Kilkenny and J. Westlake,
Conference on High Speed Photography,
Videography and Photonics, San Diego, 1983,
Proceedings to be published as S.P.I.E. Vol. 427.

134. L.V. Gavganen et al,
Proc. 8th I.C.H.S.P., p. 41, 1968.

135. A.J. Lieber and H.D. Sutphin,
Rev. Sci. Inst., Vol. 42, p. 1663, 1971.

136. N. Fleurot et el,
Proc. 15th I.C.H.S.P.P., S.P.I.E. Vol. 348, p. 772, 1982.

137. R. Kalibjian,
Proc. 12th I.C.H.S.P., S.P.I.E. Vol. 97, p. 269, 1976.

138. R. Kalibjian and L.W. Coleman,
Proc. 13th I.C.H.S.P.P., p. 447, 1978.

139. R. Kalibjian, S. Thomas, J.P. Henz and R.L. Peterson, Proc. 15th I.C.H.S.P.P., S.P.I.E. Vol. 348, p. 201, 1982.

140. T.A. Hall, C. Kler and E. McGoldrick, Annual Report to the Central Laser Facility Committee, 1983, Rutherford Appleton Laboratory Report RL-83-043, 1983.

141. W. Sibbett, M.R. Baggs and H. Niu, Proc. 15th I.C.H.S.P.P., S.P.I.E. Vol. 348, p. 267 1983.

142. F. Walters, R.A. Chippendale and R.P. Brown, Proc. 6th I.C.H.S.P., p. 357, 1962.

143. A.E. Huston and F. Walters, Adv. Elect. and Elect. Phys., Vol. 16, p. 249, 1962.

144. A.E. Huston and R.B.A. Harris, Adv. Elect. and Elect. Phys., Vol. 33 B, p. 1109, 1972.

145. M.C. Adams, Private communication.

146. W. Margulis and W. Sibbett, Opt. Comm., Vol. 37, p. 224, 1981.

NOTES

I.C.H.S.P. - International Congress on High Speed Photography.

I.C.H.S.P.P. - International Congress on High Speed Photography and Photonics.

S.P.I.E. - Society of Photo-Instrumentation Engineers.

ACKNOWLEDGEMENTS

I would like to thank Professor D.J. Bradley for introducing me to the field of high speed photography, and for supervising me through my first year. I would also like to thank my supervisor, Dr. Wilson Sibbett for his excellent guidance and endless encouragement throughout this work.

I gratefully acknowledge the help and advice of all the members of the Laser Group, in particular: Drs. Walter Margulis, Paul May and Bill Sleat, and Mr. Richard Eagles, for their assistance with the experimental evaluation of the Photochron IV streak camera; Dr. Chris Phillips for building and testing the demountable Photochron IV-M; Dr. Eric Munro and Mr. Keith Jones for their helpful discussions about the computer programs.

I would like to thank all the technical staff of the Optics Group, and Dr. Martin Adams and Mr. Phil Grigg of Thorn-EMI Electron Tubes Division, for their help in the construction of the experimental Photochron IV.

I would like to express my thanks to everyone in the Laser Group and the Optical Design Group for making the period of my Ph.D. project so enjoyable.

Special thanks are due to Fiona Scroggs for typing this thesis, and to Walter Margulis for the hours spent proof-reading it.

Finally I am indebted to both the Science and Engineering Research Council, and Thorn-EMI Electron Tubes Division Ltd. in Ruislip, for their financial support during this work.

PUBLICATIONS

Theoretical evaluation of the temporal and spatial resolutions of Photochron streak image tubes

H. Niu,[a] W. Sibbett, and M. R. Baggs

Optics Section, Blackett Laboratory, Imperial College, Prince Consort Road, London SW7, England

(Received 3 November 1981; accepted for publication 7 January 1982)

A method involving modulation transfer functions has been used to study the temporal and spatial resolutions of Photochron streak tubes. This is shown to be a much more physically realistic and reliable approach for the evaluation of the temporal resolution of a streak camera than that based on the commonly applied Gaussian approximations. The results obtained from the temporal modulation transfer functions (TMTF) indicate that the increase of the electric field near the photocathode is an insufficient condition to ensure the best temporal resolution. It is also shown that there is an optimum streak speed for which the camera instrumental function is a minimum, and theoretical estimates are given for the Photochron I, II, and IV streak image tubes.

PACS numbers: 06.60.Jn, 42.80.Qy

INTRODUCTION

The most widely used direct and linear technique for studying ultrashort luminous phenomena is electron-optical chronoscopy[1] where subpicosecond temporal resolution ~1 ps has already been demonstrated experimentally.[2] The theoretical estimate of the instrumental function of the streak cameras is generally derived by assuming it to be made up of a number of discrete contributory factors which are combined using a Gaussian approximation.[3,4] Bulygin *et al.*[5] suggested an alternative contrast-temporal method with which to study the performance of streak tubes, but the values of the estimated temporal resolutions were unrealistically optimistic.

To successfully design streak tubes to provide resolution of $\lesssim 0.5$ ps then it is imperative that a reliable and accurate method is used to predict their performance. In this paper it is shown that it is unrealistic to consider the time resolution of a subpicosecond streak camera to arise from discrete quasi-independent contributions to which a Gaussian approximation can be applied. We suggest that the temporal resolution should be inferred from a temporal modulation transfer function which is evaluated by taking into account all the interactive aspects of acceleration, focus, and deflection of the photoelectronic signal.

I. THE GAUSSIAN APPROXIMATION METHOD

The Gaussian approximation is usually applied in the form given in Eq. (1),[6-8]

$$\Delta\tau_{\rm inst} = [(\Delta\tau_{\rm phys})^2 + (\Delta\tau_{\rm tech})^2]^{1/2}, \tag{1}$$

where $\Delta\tau_{\rm inst}$ is the instrumental function of the streak tube and $\Delta\tau_{\rm phys}$ and $\Delta\tau_{\rm tech}$ represent the physical and technical time resolution components, respectively, that contribute to the overall resolution and can be quantified according to Eqs. (2) and (3).

$$\Delta\tau_{\rm phys}{}^2 = \Delta\tau_C{}^2 + \Delta\tau_K{}^2 + \Delta\tau_L{}^2 + \Delta\tau_D{}^2 + \Delta\tau_{pD}{}^2, \tag{2}$$

where $\Delta\tau_C$ is the time dispersion of the photoelectrons in the photocathode and $\Delta\tau_K$, $\Delta\tau_L$, $\Delta\tau_D$, $\Delta\tau_{pD}$ are the transit time dispersions in the photocathode-to-mesh region, the focusing electron lens, the deflector plates, and the post-deflection sections, respectively.

$$\Delta\tau_{\rm tech} = 1/\nu\delta, \tag{3}$$

where ν is the streak speed of the electrons at the phosphor screen and δ is the spatial resolution in the direction of the streak.

Examination of the transit of an ultrashort pulse of photoelectrons between the photocathode and screen of a streak tube indicates that the imposed instrumental or response function is not properly described by Eqs. (1)–(3). We shall first substantiate this statement in physical terms and then in a later section it will be confirmed by some theoretical results.

Ideally, if all of the photoelectrons in the electron signal were emitted instantaneously from a single point on the cathode, and arrived simultaneously at the entry of the deflectors via a perfect electron lens, and subsequently deflected by an ideal deflector configuration, then the streak image displayed on the screen would faithfully represent the temporal features of the input optical pulse. Unfortunately, this is never the case and as a result of the initial energy and angle distributions of the electrons emitted at the photocathode and the inherent defects in the electrostatic focusing and deflection systems, the temporal structure of the streak image is to some extent a deformation of that of the incident pulse. It is therefore necessary to quantify this deformation in the most appropriate and accurate manner possible. This is particularly important in the consideration of the limiting performance of the femtosecond streak image tubes that are currently being developed.

According to Eq. (2), all of the constituent factors are given the same weight. Thus it follows that if they had equal value then they would play the same role in the deformation of the original signal. This ought not to be the case because if we consider that the deflection net-

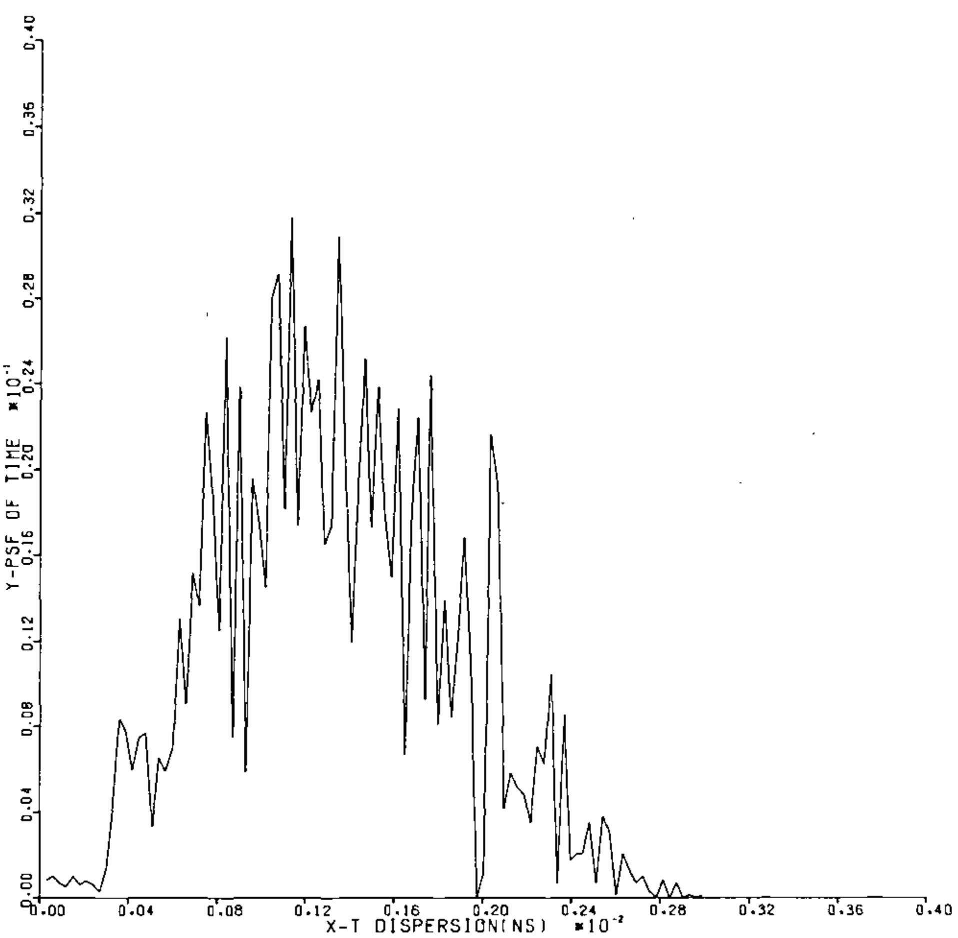

FIG. 1. Temporal line spread function for Photochron II.

work is a pair of parallel plates, then the following relationships can be deduced to a first approximation:

$$\Delta x_1 = \frac{\eta}{d}\dot{V}\tau_p\tau_F\Delta\tau_S\,, \tag{4a}$$

$$\Delta x_2 = \frac{\eta}{d}(V_0 + \dot{V}\tau_p)\tau_F\Delta\tau_D\,, \tag{4b}$$

$$\Delta x_3 = \frac{\eta}{2d}(2V_0 + \dot{V}\tau_p)\tau_p\Delta\tau_{pD}\,, \tag{4c}$$

where

$$\Delta\tau_S{}^2 = \Delta\tau_C{}^2 + \Delta\tau_K{}^2 + \Delta\tau_L{}^2\,. \tag{4d}$$

Δx_1, Δx_2, and Δx_3 are the deflection deviations that are registered at the screen due to the temporal dispersions $\Delta\tau_S$, $\Delta\tau_D$, and $\Delta\tau_{pD}$, respectively. V_0 is the applied potential difference between the plates when the electron pulse is at the entry of the deflector, and τ_p and τ_F are the electron transit times in the deflection and post-deflection regions, respectively. $\dot{V}$ is the slope of the time-varying linear deflection voltage ramp, d is the separation of the streak plates, and η is the electron charge-to-mass ratio.

It is clear from equations (4a)–(4c) that $\Delta\tau_S$, $\Delta\tau_D$, and $\Delta\tau_{pD}$ do not have the same weight. Consequently, it is wrong to combine them using the Gaussian approximation given in Eq. (2). For instance, when a high-speed voltage ramp $\sim 5 \times 10^{12}$ V s^{-1} is applied to the deflectors of a Photochron II streak tube, then $\Delta\tau_{pD}$ can be shown to be $\sim$3.8 ps when the influence of fringing fields is included. Substitution of this value into Eq. (2) would obviously give a ridiculous value for its limiting time resolution. Despite the relatively large magnitude of $\Delta\tau_{pD}$, the contribution to the deflection deviation Δx_3 that arises from it is still significantly smaller than either Δx_2 or Δx_1.

With regard to Eq. (3), the dynamic spatial resolution δ in the streak direction cannot be directly measured

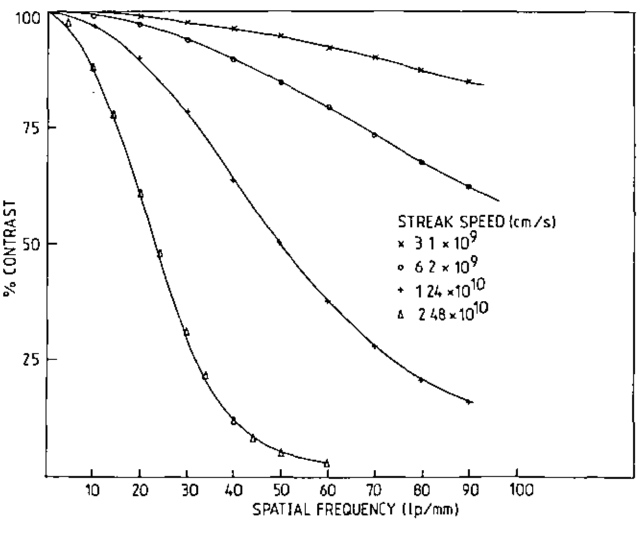

FIG. 2. MTF in slit direction for Photochron II for four streak speeds.

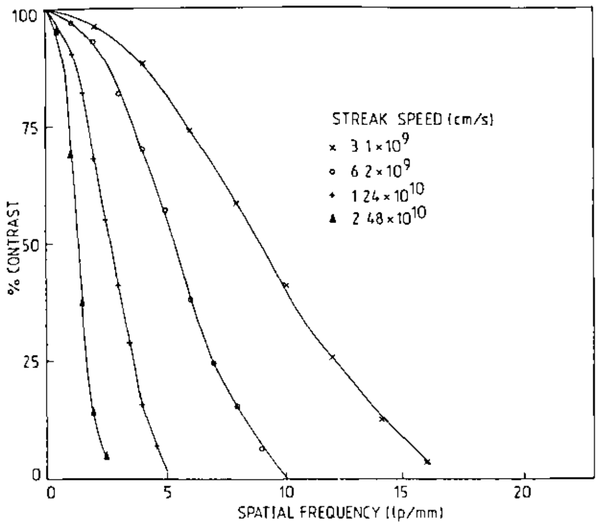

FIG. 3. MTF in streak direction for Photochron II.

experimentally under conditions of picosecond and subpicosecond resolution. It is seen from the results discussed later that the value of the spatial resolution in the direction normal to that of the streak (referred to here as the slit direction) is always significantly higher than δ and so must never be substituted into Eq. (3). It must also be emphasized that the dynamic spatial resolution in the streak direction is dependent on the streak speed involved. Under the conditions of high-speed deflection, then an increase in streak velocity generally induces a decrease in δ and, consequently, there exists an optimum streak speed at which the best time resolution is ensured. This was also concluded by Kinoshita *et al.*[9] but their model ignored the temporal dispersion of the electrons entering the deflection region.

It is our view that the so-called physical and technical time resolution limits of a streak tube cannot be treated as separate or distinct entities. The dynamic spatial resolution δ is not a technical characteristic of a particular streak tube because it is determined by both the electron-optical/electronic parameters and the physical time dispersions associated with the electron pulse that is deflected. In other words, the instrumental function of a streak tube can be determined by using Eq. (3), provided the spatial resolution δ has been inferred from calculations that contain all of the relevant interdependent factors such as temporal dispersions and geometrical aberrations. To this end we have investigated the approach based on modulation transfer functions which is described in the next section.

II. THE MODULATION TRANSFER FUNCTION METHOD

The optical transfer function (OTF) has general application in optics and electron optics for the evaluation of image quality.[10,11] The suitability of this type of approach to the theoretical estimation of the spatial and temporal resolution of electron-optical image tubes has already been given some preliminary consideration by Niu[12] and Bulygin *et al.*[13] In this paper we describe a relatively comprehensive study of the modulation transfer functions associated with Photochron streak tubes.

The basis of our method can be understood by considering an image tube for which the input optical signal is sinusoidally varying in space with a frequency f_x. If a linear response is assumed, then the image registered on the phosphor screen should also have a sinusoidal spatial variation at f_x, but in all likelihood the output image will have a different phase and lower contrast. The ratio of the output to input contrasts, i.e., the modulation, then gives a measure of the performance of the tube at the particular frequency f_x. When a comprehensive range of frequencies is taken, then the resulting plot of modulation vs spatial frequency gives the modulation transfer function (MTF) of the system. Alternatively, when the input signal has a sinusoidal variation with time (frequency f_t) rather than space, then the curve of contrast against temporal frequency is the temporal modulation transfer function TMTF.

The TMTF of a given streak tube design has been determined by using a suite of computer programs. The

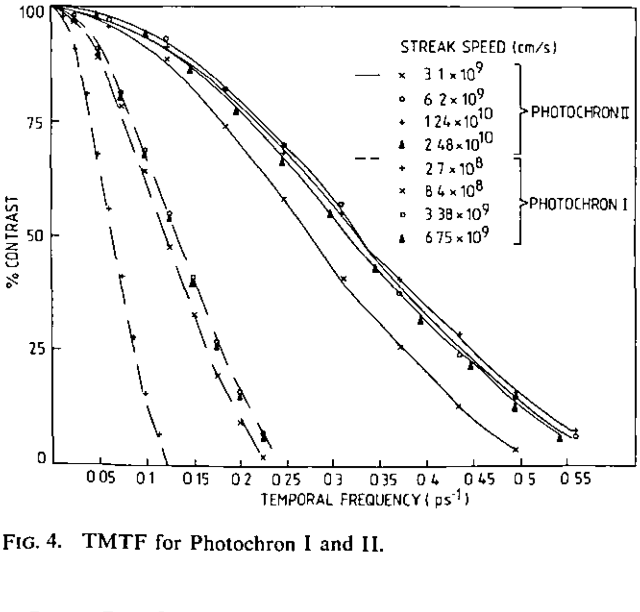

FIG. 4. TMTF for Photochron I and II.

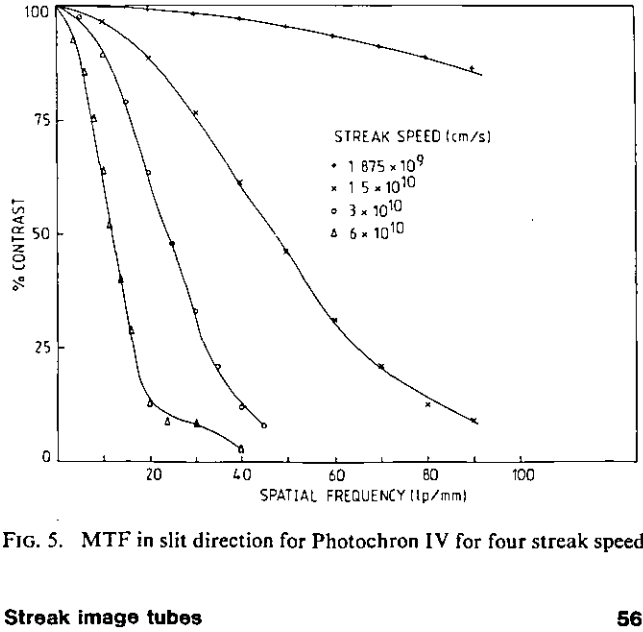

FIG. 5. MTF in slit direction for Photochron IV for four streak speeds.

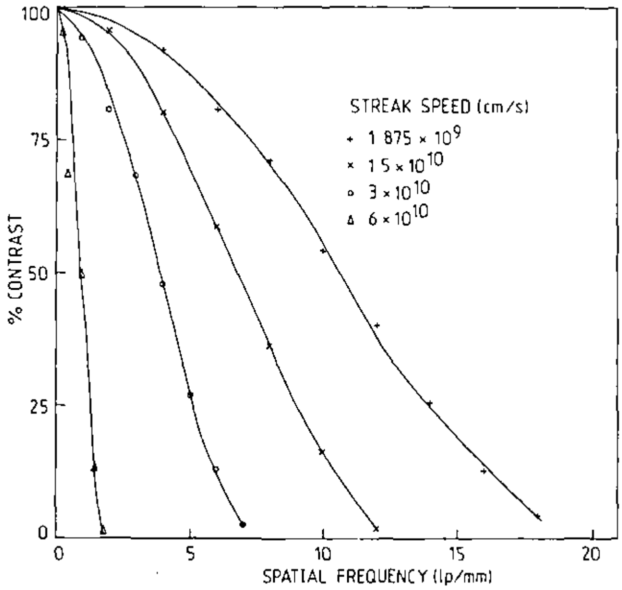

FIG. 6. MTF in streak direction for Photochron IV.

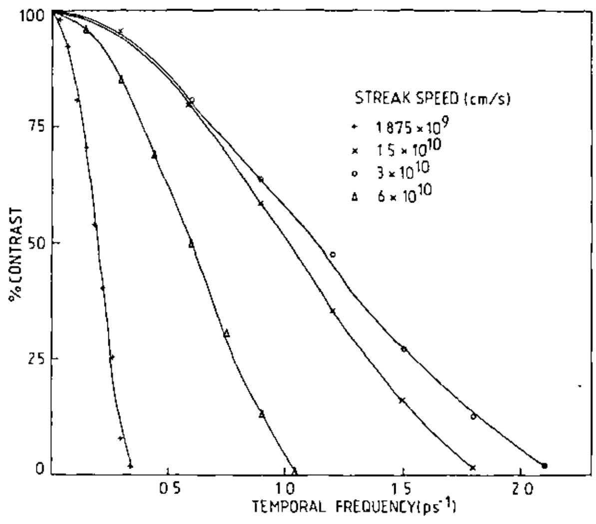

FIG. 7. TMTF for Photochron IV.

structure of the rotationally symmetric focusing electrodes is fitted to the points on a selected rectangular grid. The potential at each point on this grid is obtained by solving Laplace's equation iteratively with an accelerated successive over-relaxation routine.[14] From this potential distribution the electric field at each grid point can be evaluated using the 4 × 4 formula[15] and then electrons can be traced from the photocathode to the deflection region by the Runge–Kutta method.[16] For the nonrotationally symmetric deflection region the structure has to be set up in two dimensions on a rectangular grid with the five-point difference formula and solving the plane Laplace's equation to include the quadratic terms.[17] To economize on computing time, the superposition theorem was used to calculate deflection fields for different applied voltage bias and ramp gradients. The electron could then be traced through the deflection section while applying the deflection, static deflection, dynamic (i.e., time-varying) deflection, or a combination of bias and dynamic deflection. When the dynamic deflection is involved then the time variation of the voltage waveform and the propagation of the voltage in the deflectors has to be included in the calculations. On leaving the deflection region the electrons are assumed to travel in an entirely field-free region and their trajectories are finally computed to the plane of the phosphor screen.

The overall performance of a particular streak tube is assessed by evaluating both the spatial and temporal modulation transfer functions. To do this, 1000 electrons are assumed to emanate from a discrete point with a cosine-dependent angular distribution and an initial energy distribution which simulates the photoemission from an S1 photocathode when illuminated at a wavelength of 1.06 μm.[18]

Although all of the electrons have the same spatial and temporal origins, the effects of the distribution of initial angles and energies of emission and electron-optical defects in the focusing lens and deflection system result in a recorded image of finite size at the phosphor. This distribution of electrons at the screen plane is described by the so-called point spread function (PSF). Once the PSF is known at a given plane along the axis of the tube (z direction), it may then be integrated in the x, y, and t directions to obtain the respective line spread function (LSF). This is achieved in the program by dividing the image spot into a large number of strips and summing the total number of electrons in each strip. This can be done for both x, y spatial directions and the time (t) direction. Plotting the number of electrons as a function of relative position coordinates gives the LSF. The MTF and phase can then be evaluated from a Fourier analysis of the LSF as indicated for the time direction in Eqs. (5a)–(5d):

$$A_1 = \frac{\int_{-\infty}^{+\infty} \mathrm{LSF}_t \cos(2\pi f_t \cdot t)\, dt}{\int_{-\infty}^{+\infty} \mathrm{LSF}_t\, dt}, \tag{5a}$$

$$A_2 = \frac{\int_{-\infty}^{+\infty} \mathrm{LSF}_t \sin(2\pi f_t \cdot t)\, dt}{\int_{-\infty}^{+\infty} \mathrm{LSF}_t\, dt}. \tag{5b}$$

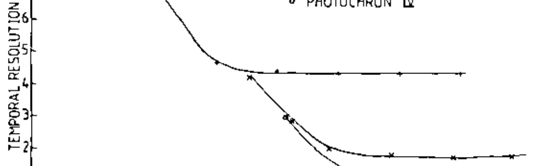

FIG. 8. Variation of temporal resolution with streak speed for Photochron I, II, and IV.

TABLE I. Temporal resolution limits.

Deflection from center of screen (mm)	0	6	12	24
Temporal resolution (ps)	0.6	0.51	0.48	0.66

$$\text{Modulation } M \text{ at } f_t = (A_1^2 + A_2^2)^{1/2}. \tag{5c}$$

$$\text{Phase } \phi \text{ at } f_t = \tan^{-1}\left(\frac{A_2}{A_1}\right). \tag{5d}$$

The TMTF can be calculated at any plane prior to the deflectors and at the screen, but the LSF$_t$ must be computed differently. Up to the deflection section, the LSF$_t$ represents the distribution of the number of electrons as a function of their time dispersion at the specific location where the temporal performance of the streak tube is assessed. At the screen plane, however, the LSF$_t$ is obtained by transforming the spatial LSF in the streak direction into the temporal LSF for a given streak speed.

The limiting time resolution or instrumental function of a streak image tube is taken to be the time at which the modulation has fallen to a value of 5% in the TMTF curve. A similar definition is used for the spatial resolutions in the x (streak) and y (slit) directions. For the streak camera, then the SMTF associated with the phosphor screen, fiber optics, intensifier, and coupling optics must also be included in the estimation of the spatial resolution of the total system.

III. RESULTS

The MTF program has been used to study the temporal and spatial characteristics of the Photochron I, II, and IV streak tubes. An example of the temporal line spread function is shown in Fig. 1 for the Photochron II. It can be seen that at least 1000 electron trajectories are required to produce an adequately smooth line spread function from which the MTF can be determined with acceptable accuracy. Figures 2–4 illustrate the MTF's of the Photochron II tube[2,19] in the slit, streak and time (includes curves for Photochron I[20]) directions as displayed at the plane of the phosphor screen for several streak speeds. Similarly, the MTF's for the Photochron IV[21] are given in Figs. 5–7. For all three streak tubes the spatial resolution in both streak and slit directions decreases as the streak velocity is increased, but the decrease is much greater for the streak direction. It is also clearly evident from Fig. 4 (for Ph I, II) and Fig. 7 (for Ph IV) that there is an optimum streak velocity above which the temporal resolution actually deteriorates. This is indicated in Fig. 8 which shows the variation of temporal resolution as a function of streak speed for the Photochron I, II, and IV tubes. Therefore, the contribution of the deflection system to the camera instrumental function cannot be reduced indefinitely by a continued increase in the streak speed. This is the result of the degradation in the spatial resolution arising from the time dispersion of the electrons at the entry of the deflection region, where the voltage gradient and the fringe field effects of the deflectors are changing very rapidly. When the rate of increase of streak speed is slower than the decrease in the spatial resolution, then the overall temporal resolution inevitably falls below an optimum value.

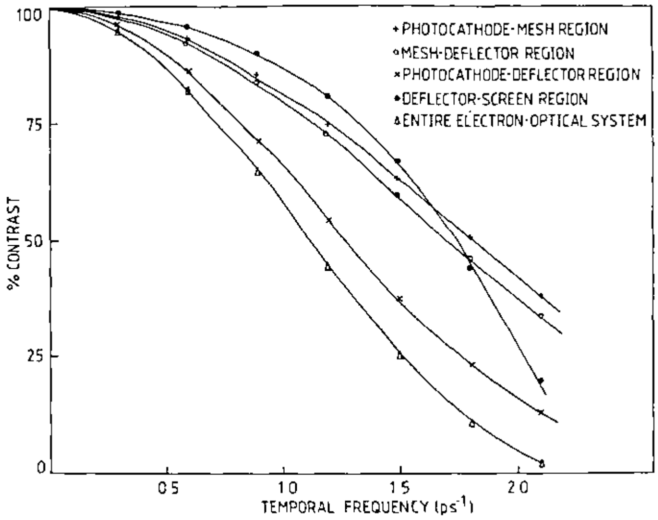

FIG. 9. TMTF' for the various constituent regions of the electron optics in the Photochron IV.

In Table I the temporal resolution limits are given for the streak image when deflected to different positions on the screen. These data imply that the time resolution is relatively constant even for large deflections away from the center of the screen. This can be understood on the basis that under conditions of a fast voltage ramp applied to the deflectors, then the streaks will be displayed near the center of the screen for a large bias and away from screen center for smaller bias levels. In the former case, the geometrical aberrations are small but the fringe field experienced by the electrons at the entry of the deflection region is large, while in the latter, the geometrical aberrations are more severe but the fringe field effects are less. When combined, these effects offer some mutual

TABLE II. Variation of spatial resolution.

Displacement from optimum image plane (mm)	−3	−2	−1	0	+1	+2	+3	+14	+16
Spatial resolution in slit direction (lp/mm)	21.5	23	25	27.4	30.5	33.3	37	60	54
Spatial resolution in streak direction (lp/mm)	7.06	7.08	7.09	7.1	7.07	7.06	7.05	6.4	6.3
Temporal resolution at optimum streak speed (ps)	0.473	0.471	0.470	0.469	0.471	0.472	0.473	0.52	0.53

TABLE III. Temporal dispersion.

Initial energy (eV)	Temporal dispersion (ps)		
	Photocathode mesh	Mesh deflector	Photocathode deflector
0-0.075	0.25	0.19	0.31
0-0.15	0.35	0.39	0.476
0-0.3	0.41	0.645	0.769
0-0.6	0.54	1.05	1.25
0-1.2	0.77	1.96	2.2

TABLE IV. Temporal dispersion.

Temporal dispersion (ps) \ Slit height above axis (mm) / Electric field (kV/cm)	0	1	2	3	4	5
20 (PH. II)	0.76	1.06	1.37	1.85	2.5	3.1
50 (PH. II)	0.44	0.74	1.2	1.82	2.43	3.04
50(PH. IV)	0.26	0.31	0.35	0.45	0.51	0.6

compensation so that the temporal resolution across the screen remains essentially constant.

Results are presented in Table II which show the variation of the spatial resolution (in the slit and streak directions) and temporal resolution as a function of the displacement of the image plane away from the optimum location for best time resolution in the Photochron IV tube. It is clear that the temporal resolution does not depend critically on a precise location of the image plane, and it has been deduced from our calculations that at the plane for optimum spatial resolution in the slit direction (displacement = +14 mm) the theoretical temporal resolution is only degraded to 0.52 ps. From this it may be inferred that it is not possible to improve the temporal resolution appreciably by a change in the position of the image plane or equivalently by changing the focus condition which is in contrast to the conclusion reached by other authors.[9]

The TMTF's associated with the various constituent regions of the electron optics in the Photochron IV streak tube are given in Fig. 9 for the condition of optimum streak speed of 3×10^{10} cm s^{-1} so that the relative contributions to the overall temporal modulation transfer function can be readily distinguished. Additional TMTF's have been calculated for the Photochron II where the temporal dispersion arising in the photocathode-to-mesh and mesh-to-deflector regions of the tube have been determined for several values of the initial energy range of the photoelectrons. These results (see Table III) confirm that the contribution of the mesh-to-deflector region to the predeflector time dispersion is significant for small initial energy spreads and becomes a dominant factor for energy spreads $\lesssim$0.15 eV.

The simple exercise of merely increasing the electric field in the vicinity of a streak tube photocathode is insufficient to ensure that the instrumental function is improved by virtue of a reduced temporal dispersion. This fact has been illustrated by calculating the time dispersion associated with electrons emitted from several heights on a Photochron II for applied electric fields of 20 and 50 kV cm^{-1} near the photocathode. For the sake of comparison the dispersions have also been evaluated for the Photochron IV for an electric field of 50 kV cm^{-1} at the photocathode and a selection of the calculated results are presented in Table IV. Although the electric fields for the Photochron II and IV can be arranged to

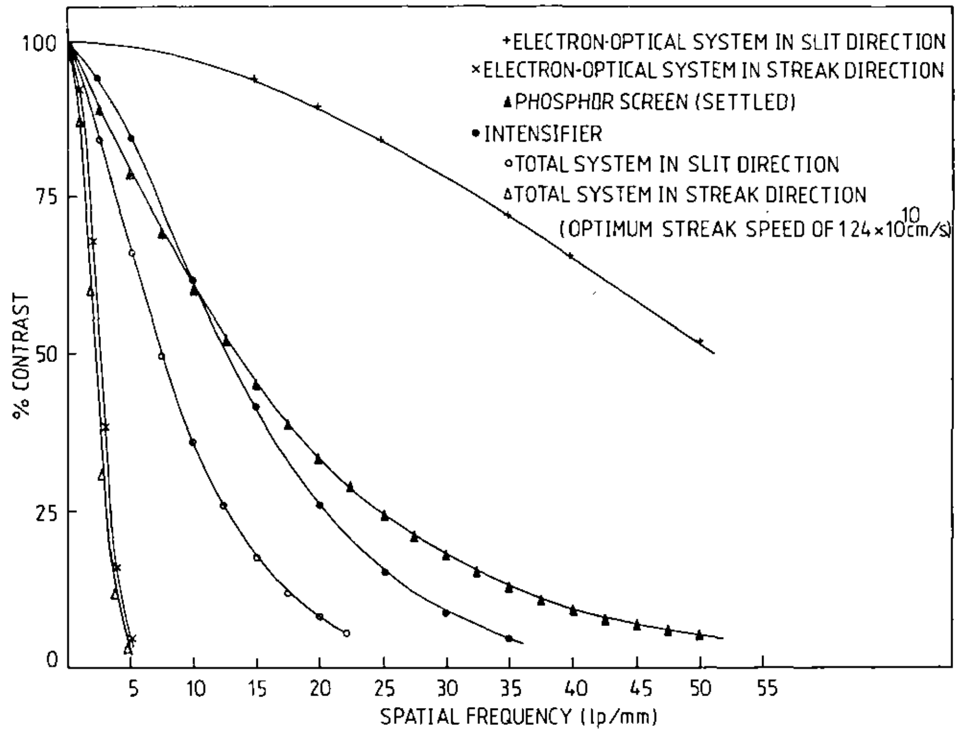

FIG. 10. MTF in slit and streak directions for individual and combined parts of the Photochron II streak camera.

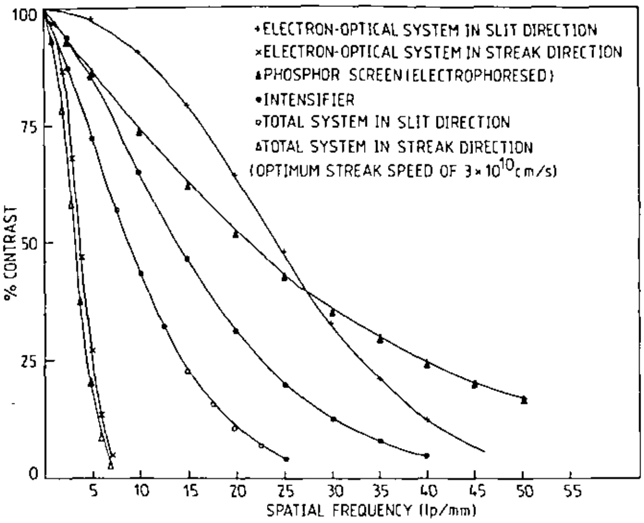

FIG. 11. As Fig. 10, but for the Photochron IV streak camera.

be equal, the temporal dispersions are much smaller in the Photochron IV because high electric fields and potentials are established in the photocathode-to-deflector region. Another interesting feature that comes from these data is that although the on-axis temporal dispersion of the Photochron II is reduced from 0.76 to 0.44 ps, the off-axis dispersion remains virtually unaltered despite the increase in electric field by a factor of 2.5.

It has been mentioned that the results just presented apply entirely to the electron optics of the streak tubes. When the MTF of the phosphor screens and the intensifiers are included, then the overall system MTF can be obtained. In the case of the spatial resolution in the streak direction, then it is to be expected that for its low magnitude $\lesssim$10 lp/mm the observed resolution will not be significantly degraded. However, the spatial resolution in the slit direction is much higher (see Figs. 2 and 5) and it suffers noticeably as indicated in Figs. 10 and 11 for the Photochron II and IV cameras, respectively. The limiting spatial resolution $\sim$23 lp/mm for the Photochron II single-shot camera which can be deduced from this theoretical consideration agrees closely with the experimental value already reported for streak operation.[22]

We conclude that our calculations of the spatial and temporal characteristics of electron-optical streak cameras give accurate results when based on the method using modulation transfer functions. It is clear that the temporal resolution which is predicted for the Photochron IV streak tube that is currently under construction should be $\lesssim$0.5 ps over a relatively wide spectral range.

ACKNOWLEDGMENTS

The financial support of the Paul Instrument Fund of the Royal Society is gratefully acknowledged. One of us (MRB) was supported by a CASE studentship from the Science and Engineering Research Council and another (HN) was supported by the Chinese Academy of Sciences.

[a)] Permanent address: Xian Institute of Optics and Precision Mechanics, Xian, China.

[1] E. V. Zavoisky and S. D. Fanchenko, Appl. Opt. **4**, 1155 (1965).

[2] D. J. Bradley and W. Sibbett, Appl. Phys. Lett. **27**, 382 (1975).

[3] V. V. Korobkin, A. A. Malyutin, and M. Ya. Schelev, J. Photogr. Sci. **17**, 179 (1969).

[4] e.g., R. D. A. Maurice, *Convolution and Fourier Transforms* (Pentech Press, London, 1976).

[5] V. S. Bulygin, Yu. A. Drozhbin, and B. M. Stepanov, Proc. of 12th ICHSPP (1976), p. 68.

[6] D. J. Bradley, B. Liddy, and W. E. Sleat, Opt. Commun. **2**, 391 (1971).

[7] R. Kalibjian, C. F. McConaghy, and L. W. Coleman, Rev. Sci. Instrum. **45**, 776 (1974).

[8] V. V. Korobkin, B. M. Stepanov, S. D. Fanchenko, and M. Ya Schelev, Opt. Quant. Electron. **10**, 367 (1978).

[9] K. Kinoshita, T. Kato, and Y. Suzuki, Proc. 14th ICHSPP (1980) (Moscow).

[10] K. R. Barnes, *Monographs on Applied Optics* No. 3 (Hilger, London, 1971).

[11] A. M. Stark, D. L. Lamport, and A. W. Woodhead, Adv. Electron. Electron Phys. **28B**, 567 (1969).

[12] H. Niu, paper presented at the Conference for the Founding of the Optical Society of China (Peking, Dec. 1979) (paper to be published in Acta Optica Sinica).

[13] V. S. Bulygin, Yu A. Drozhbin, and B. M. Stepanov, paper presented at 14th Inter Congress on High Speed Photography and Photonics (Moscow, October 1980) (paper to be published in Proceedings of 14th ICHSPP).

[14] B. A. Carré, Comput. J. **4**, 73 (1961).

[15] R. A. Buckingham, *Numerical Methods* (Pitman, London, 1959).

[16] C. F. Gerald, *Applied Numerical Analysis* (Addison, Wesley, Massachusetts, 1978), p. 257.

[17] C. F. Gerald, *Applied Numerical Analysis* (Addison, Wesley, Massachusetts, 1978), p. 347.

[18] N. A. Soboleva, A. G. Berkovsky, N. D. Checnik, and R. E. Eliseev, *Photoelectronic Devices* (Science, Moscow, 1965), p. 124.

[19] P. R. Bird, D. J. Bradley, and W. Sibbett, Adv. Electron. Electron Phys. **40A**, 51 (1976).

[20] D. J. Bradley, B. Liddy, W. Sibbett, and W. E. Sleat, Appl. Phys. Lett. **20**, 219 (1972).

[21] W. Sibbett, H. Niu, and M. R. Baggs (to be published).

[22] D. R. Hull and N. J. Freeman, J. Phys. E **13**, 685 (1980).

Photochron IV subpicosecond streak image tube

W. Sibbett, H. Niu,[a] and M. R. Baggs

Optics Section, Blackett Laboratory, Imperial College, Prince Consort Road, London SW7 2BZ, England

(Received 20 November 1981; accepted for publication 26 January 1982)

The electrode configuration and electron-optics of a newly designed streak image tube (Photochron IV) are described. The results of our theoretical studies show that the Photochron IV can have a limiting temporal resolution ~0.2 ps when the photocathode is illuminated near the long wavelength cutoff and subpicosecond resolution $\lesssim 0.5$ ps in the UV/visible/NIR spectral regions and ~1 ps for 1-keV x rays. This streak tube design also possesses the features of a good dynamic range and reduced temporal distortion.

PACS numbers: 42.80.Qy

INTRODUCTION

Picosecond[1-8] and subpicosecond ($\lesssim 0.7$ ps)[9,10] time resolutions have already been reported for some electron-optical streak cameras, but there is still the need for further developments to provide improved spatial resolution and dynamic range with instrumental functions reduced to ~0.1 ps in the visible spectral regions and ~1 ps at x-ray wavelengths. Relevant applications include the direct duration measurement of hypershort mode-locked laser pulses,[11] time-resolved spectroscopic studies of molecular dynamics on a subpicosecond time scale,[12] and plasma kinetics in the picosecond regime.[13]

It is widely known that a primary consideration for improving the temporal resolution of streak image tubes is the increase in electric fields in the vicinity of the photocathode. Recent theoretical studies[14] have shown that this can not be regarded as a sufficient condition to ensure an adequate improvement in the instrumental function of Photochron streak tubes. In fact we have presented data which indicate that the temporal dispersion in a bunch of photoelectrons is often greater in the focusing electrode region than in the photocathode-to-mesh regions[14] and that space charge effects that limit the dynamic range are usually more serious in the post-mesh region of the streak tubes.[15] Additional conclusions were that the space-charge effect in the crossover region did not contribute significantly to temporal dispersion or pulse broadening and that an optimum streak speed exists at which the best temporal resolution is obtained.

From the theoretical analysis of the Photochron I and II tubes, it became clear that the limitations on their performance did not arise from intrinsic defects of the so-called pinhole electron-optical systems in contrast to earlier allegations.[16] In this paper we decribe a new streak tube called the Photochron IV in which pinhole electron optics have been retained but where the major features in the design are maximized electric fields and potentials throughout the overall photocathode-to-anode region, so that the temporal resolution and dynamic range are optimized.[14] The performance of this tube has been evaluated theoretically and estimates are given for the expected spatial resolutions, temporal resolution, temporal distortion, and dynamic range for streak operation at both UV/visible/NIR and x-ray wavelengths. In most instances, a comparison between the Photochron IV and Photochron II streak tubes is included.

I. DESCRIPTION AND PERFORMANCE OF PHOTOCHRON IV STREAK TUBE

The electrode configuration of the Photochron IV streak image tube is shown schematically in Fig. 1. The six electrodes which constitute the pre-deflection section include a flat photocathode and mesh arrangement that is common to earlier Photochron tubes and four coaxial equidiameter cylinders which are designated in sequence from the mesh as the first focus electrode, first anode, second focus electrode and second anode. The equipotential distribution that can be established by this electrode geometry is shown in Fig. 2.

The mesh, or alternative electrode, has a separation of 2 mm from the photocathode and the applied potential difference is 10 kV. This ensures not only a substantial electric field near the photocathode, but also that the electrons are accelerated to relatively high velocities. While this serves to reduce the temporal dispersion in the post-mesh region, it also gives rise to a "rigid" electron beam that is difficult to focus. A single strong focusing lens applied with low potential is inappropriate for this purpose and so the design includes two focusing lenses. The first focus electrode and first anode form the

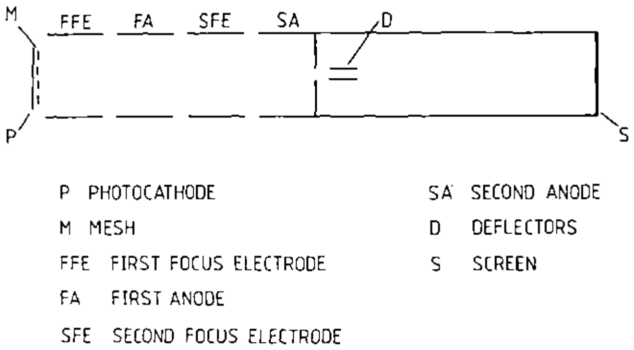

FIG. 1. Electrode configuration of Photochron IV.

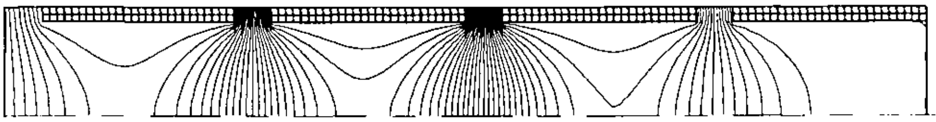

FIG. 2. Equipotential distribution associated with Photochron IV-type geometry.

first focusing lens which has the four-fold function to focus the electron beam, further accelerate the photoelectrons, adjust the position of the crossover, and reduce temporal distortion. The second focusing lens (second focus electrode and second anode) also plays a multiple role in that it is mainly used to position the image plane and to minimize the geometrical and chromatic aberrations and the temporal dispersions. These lenses are interdependent and so an optimum design had to be obtained for the combination.

The typical voltages at which the electrodes are maintained are included in Table I. Taken with Fig. 3 which illustrates the potential distribution on axis, it is clearly evident that the objective of establishing high electric fields and potentials has been realized. It is significant to note that the lowest potential on axis is ~6.5 kV compared to 0.8 kV in the Photochron II tube. This feature also ensures that secondary electrons emitted from the mesh do not reach the phosphor screen and thus the tube noise is subdued. As well as ensuring the best possible values for the spatial/temporal resolutions and dynamic range, particular attention must also be given during the design studies to minimize the interactions between the electron lenses and the deflection network. An example of this relates to the location of the crossover, because if it is too far from the anode aperture, then the dimensions of the deflector plates and anode aperture will be unavoidably large. When the crossover is near the anode, then the geometry of the deflectors can be arranged to give a high-fidelity response to the fast time-varying linear deflection voltages. Moreover, the detrimental influence of the strong deflection fringe field on the focusing electrostatic field can be minimized by having a small anode aperture. On the basis of this understanding, an appropriate location of the crossover and suitable size of aperture have been determined from a computer analysis of the electron trajectories in the image tube.

The deflectors for the Photochron IV have been designed by taking into consideration the fringe field, the variation and transmission of the deflection voltage wave, the flight times of the electrons through the deflectors, and the temporal spread of the electrons at the entry of the deflection region. The influence of the fringe field on both sides of the deflectors has also been evaluated and steps have been taken to reduce the detrimental effects and also improve the streak performance.

Some of the characteristic performance figures are given in Table II for the Photochron IV and also for the Photochron II so that comparisons can be made directly. The electron-optical magnification is ~2 in both cases but in the static or focus mode, the spatial resolution at the photocathode of the Photochron IV is almost twice that of the Photochron II. From calculations involving the temporal modulation transfer function of the deflectors[14] it has been deduced that the temporal resolution of the Photochron IV is an optimum for a streak speed of 3×10^{10} cm s^{-1}. Taking this streak speed and the initial energy spread of 0.6 eV, it can be seen from Table II that the temporal resolution and temporal distortion are both subpicosecond and that these and the dynamic range are much superior to the corresponding values for the Photochron II. The pre-deflection temporal dispersions and temporal distortions have been calculated for several slit heights. From the results included in Tables III and IV it can be seen that while the performance of the Photochron IV is better than that of the Photochron II, it is nonetheless important to restrict the slit illumination at the photocathode to an overall extent ~4 mm to avoid appreciable slit curvature.

The theoretical estimates of the spatial resolution

TABLE I. Typical values of "focus" voltages applied to electrodes of Photochron IV streak tubes.

Electrode	Photocathode	Mesh	1st Focus electrode	1st Anode	2nd Focus electrode	2nd Anode
Potential (kV)	0	10	8	24	5	18

TABLE II. Comparison of salient performance characteristics of Photochron IV and II streak tubes.

Characteristic Image tube	Electric field at photocathode (kV/cm)	Static spatial resolution at photocathode (l p/mm)	Magnification	Deflection sensitivity (cm/kV)	Temporal resolution, τ_r (ps)	Temporal distortion at r_0 = 2 mm (ps)	Dynamic range τ_p = 3 ps[b] τ_r = 2 ps
Photochron IV	50	60	−2	3	0.48	0.77	911
Photochron II	20	33	−1.8	3	1.75	2.92	150

[b] τ_p ≡ pulse duration.

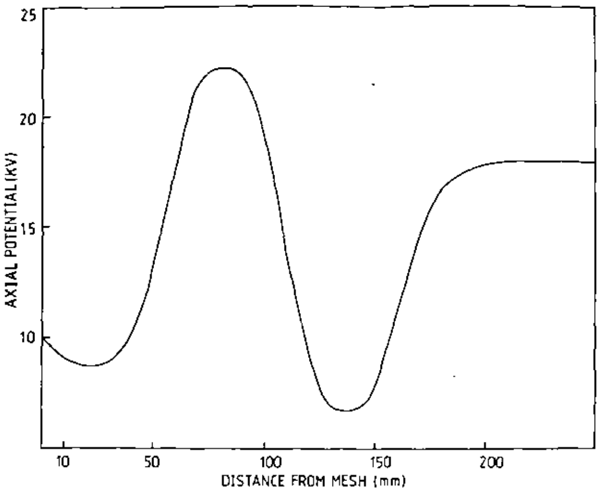

FIG. 3. Distribution of axial potentials in the mesh—anode region of Photochron IV.

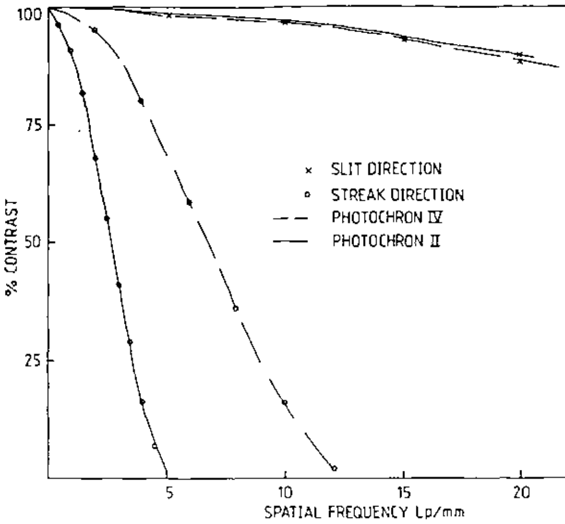

FIG. 4. Spatial modulation transfer functions for the Photochron II and IV streak tubes in slit and streak directions.

which are determined by the electron-optical systems can be inferred from the modulation transfer functions[14] shown in Fig. 4 for the Photochron II and IV image tubes. Although the spatial resolution is similar for both in the slit direction, it can be clearly seen that in the streak direction the performance of the Photochron IV is much superior. Similarly, from a consideration of the temporal modulation transfer functions it has been shown (see Fig. 5) that the temporal resolution of the Photochron IV is appreciably better than that of the Photochron II.

It is illustrated in Table V that an overall temporal resolution limit of <300 fs can be obtained under different operating conditions for the Photochron IV. When a photocathode is irradiated at a wavelength which is just shorter than the cutoff or threshold wavelength for photoemission, then the spread in energy ($\Delta\epsilon$) for the electrons is small and a limit of ~240 fs is possible. For shorter wavelengths, electric fields ~100 kV cm^{-1} are necessary at the cathode to ensure that a resolution limit of <300 fs is retained. (This suggested increase in applied electric field could be achieved by an appropriate reduction in the separation between the photocathode and mesh electrode.) It is interesting to note that for enhanced electric fields $\gtrsim$100 kV cm^{-1} near a gold cathode, then subpicosecond resolution could be achieved for ~1-keV x rays.

It has recently been shown from a theoretical analysis of space charge effects in Photochron streak cameras[15] that the dynamic range of the Photochron IV is better than that of Photochron I and II. The relevant data for the Photochron II and IV have been reproduced in Fig. 6 where it can be deduced, for example, that the dynamic range of the Photochron IV is approximately six times greater than that of the Photochron II for 3-ps light pulses and that a dynamic range ~60 is predicted for 1 ps pulses.

TABLE III. Values of temporal dispersion for several slit heights in Photochron IV and II streak tubes.

Temporal dispersion (ps) \ Slit height (mm) / Image tube	0	1	2	3	4	5
Photochron IV	0.26	0.31	0.35	0.45	0.51	0.6
Photochron II	0.76	1.06	1.37	1.85	2.5	3.1

TABLE IV. Values of temporal distortion for several slit heights in Photochron IV and II streak tubes.

Temporal distortion (ps) \ Slit height (mm) / Image tube	0	1	2	3	4	5
Photochron IV	0	0.2	0.77	1.72	3.08	4.76
Photochron II	0	0.74	2.92	6.57	11.69	18.27

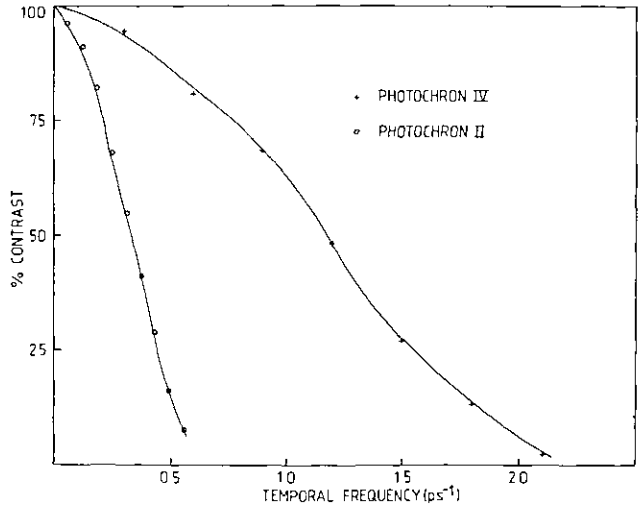

FIG. 5. Temporal modulation transfer function for Photochron II and IV tubes.

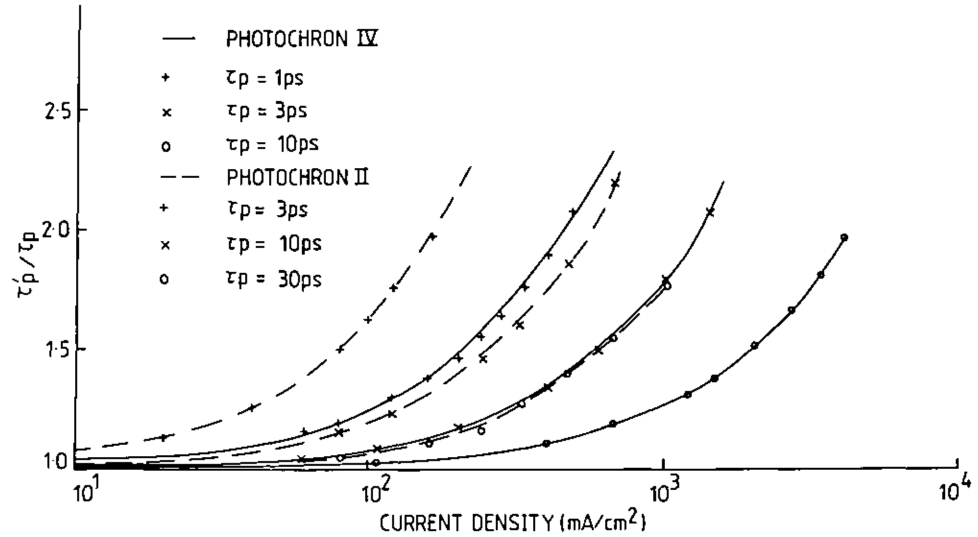

FIG. 6. Dependence of the ratio of measured streak pulse duration, τ_p', to actual light pulse duration, τ_p, on current density at the photocathode of Photochron II and IV tubes.

TABLE V. Values of temporal resolution for given initial photoelectron energy spreads and applied electric fields at photocathode of Photochron II and IV streak tubes.

Temporal resolution, τ_r (ps) / Photoelectron energy spread, $\Delta\epsilon$ (eV) / Image tube	0 ~ 0.2	0 ~ 0.6	0 ~ 5.0
Photochron II (20 kV/cm)	0.92	1.75	6.2
Photochron IV (50 kV/cm)	0.24	0.48	1.84
Photochron IV (100 kV/cm)	0.18	0.28	0.85

II. SUMMARY

In summary, therefore, it can be concluded that the expected performance of this newly developed Photochron IV streak tube is superior to that of previous designs. Current studies are being undertaken to evaluate the Photochron IV streak camera system experimentally.

ACKNOWLEDGMENTS

The financial support of the Paul Instrument Fund of the Royal Society of London and the Science and Engineering Research Council are acknowledged. One of us (MRB) was supported by an SERC CASE Studentship in collaboration with Thorn EMI Electron Tube Division, Ruislip, and another (HN) was supported by the Chinese Academy of Sciences.

---

[a] Permanent Address: Xian Institute of Optics and Precision Mechanics, Xian, China.

[1] D. J. Bradley, B. Liddy, and W. E. Sleat, Opt. Commun. **2**, 391 (1971).

[2] M. Ya. Schelev, M. C. Richardson, and A. J. Alcock, Appl. Phys. Lett. **18**, 354 (1971).

[3] D. J. Bradley, B. Liddy, W. Sibbett, and W. E. Sleat, Appl. Phys. Lett. **20**, 219 (1972).

[4] S. W. Thomas, G. R. Tripp, and L. W. Coleman, *Proceedings of the 10th International Congress on High Speed Photography* (1972), p. 127.

[5] M. Ya. Schelev, *Proceedings of the 11th International Congress on High Speed Photography* (1974), p. 32.

[6] R. Dupuy, N. Fleurot, J-P Gex, M. Lamy, and J-Y le Gall, *Proceedings of the 12th International Congress on High Speed Photography* (1976), p. 62.

[7] A. J. Lieber, H. D. Sutphin, C. B. Webb, and A. H. Williams, *Proceedings of the 12th International Congress on High Speed Photography* (1976), p. 194.

[8] Y. Tsuchiya, E. Inuzuka, and Y. Suzuki, *Proceedings of the 13th International Congress on High Speed Photography* (1978), pp. 5–7.

[9] D. J. Bradley and W. Sibbett, Appl. Phys. Lett. **27**, 382 (1975).

[10] G. I. Bryukhnevitch, N. S. Vorob'ev, V. V. Korobkin, A. M. Prokhorov, B. M. Stepanov, and M. Ya. Schelev, *Proceedings of the 12th International Congress on High Speed Photography* (1976), p. 17.

[11] R. L. Fork, B. I. Greene, and C. V. Shank, Appl. Phys. Lett. **38**, 671 (1981).

[12] C. V. Shank, E. P. Ippen, R. L. Fork, A. Migns, and T. Kobayashiv, Philos. Trans. R. Soc. London, Ser. A **298**, 303 (1980).

[13] M. H. Key, Philos. Trans. R. Soc. London, Ser. A **298**, 351 (1980).

[14] H. Niu, W. Sibbett and M. R. Baggs (to be published).

[15] H. Niu and W. Sibbett, Rev. Sci. Instrum. **52**, 1830 (1981).

[16] A. Lieber, *Proceedings of the 13th International Congress on High Speed Photography* (1978), p. 521.

Reprinted from SPIE Vol. 348—15th International Congress on High Speed Photography and Photonics

Picosecond framing image tube

W. Sibbett, M. R. Baggs, H. Niu*
Optics Section, Blackett Laboratory, Imperial College
Prince Consort Road, London SW7 2BZ, England

Abstract

The general features of the configuration and operating principle of a new framing image tube which has been designed to give picosecond resolution are described. Theoretically predicted performance characteristics are presented which indicate that a temporal resolution $\sim$100 ps and a spatial resolution $\sim$10 lp/mm should be attainable in a multiple-framing mode of operation.

Introduction

In applications such as the studies associated with laser-induced compression of matter and thermonuclear fusion [1], there is an obvious requirement for diagnostic devices with time resolution <100 ps and spatial resolution >10 lp/mm for a sequence of discrete two-dimensional images. For this reason, substantial research effort has concentrated on a variety of techniques by which picosecond frames can be obtained.[2-8] Using an image tube that has been designed specifically for framing operation, Kalibjian [4,5] has reported an exposure time of 125 ps for each of three discrete frames. In this tube, however, the image is dissected and then restored using a relatively complicated electrode arrangement. For our proposed framing tube, a simpler design has been investigated such that picosecond frames can be produced directly on the phosphor screen without recourse to image dissection and restoration. This has the advantage over previous approaches [3,8] in that elaborate data processing is no longer required and the absence of an image restoring section should ensure better image quality, although the time resolution and framing speed are likely to be somewhat inferior to that of our previously reported method.[8]

Framing tube design

The electrode configuration of the framing tube is shown schematically in figure 1. It will be shown later that it is required that the cross-over region of the photoelectron beam is positioned beyond the anode aperture, so this precludes the use of a curved photocathode. The initial temporal dispersion of the electrons is reduced by incorporating a mesh so that an electric field $>$20 kV cm^{-1} can be maintained in the cathode-mesh region. The remaining three cylindrical electrodes in the focussing section of the tube are designed to constitute a weak focussing lens which ensures that an extended narrow waist exists in the electron beam in the post-anode region. This allows us to use high-sensitivity deflectors and small apertures which are consistent with optimised exposure times.

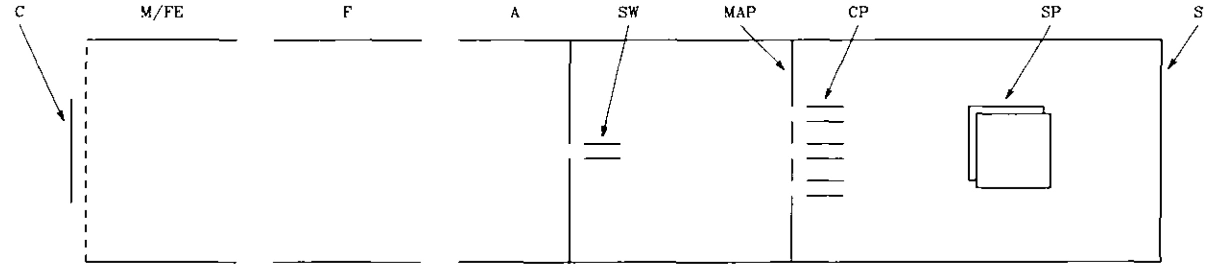

C	PHOTOCATHODE	A	ANODE	CP	COMPENSATING PLATES
M/FE	MESH/FIRST ELECTRODE	SW	SWEEP PLATES	SP	SHIFT PLATES
F	FOCUS ELECTRODE	MAP	MULTIPLEX APERTURE PLATE	S	SCREEN

Figure 1. Schematic of the framing tube.

The operating principle of the framing tube is as follows. A d.c. bias voltage applied to the sweep plates deflects the electrons to a pre-selected "off" position above or below the set of apertures in the multiplex aperture plate. When a single fast linearly

---

* Permanent address: Xian Institute of Optics and Precision Mechanics, Xian, China.

time-varying voltage ramp is applied across these deflectors, three short temporal transmissions of the electron beam are obtained. The imposed "smear" is then removed by supplying an identical voltage ramp of opposite polarity to the three pairs of compensating plates.[9,10] These compensating plates are configured so that their sensitivity of deflection and associated distributive capacitance and inductance are the same as those for the sweep deflectors. Spatial discrimination of the three discrete frames at the screen can then be carried out by one of several methods. One approach involves the inclusion of two extra pairs of deflector plates (the so-called "separator plates" indicated in figure 2). In this case the voltage waveforms supplied to the sweep and compensating deflectors have identical shape and opposite polarity whilst appropriate d.c. bias voltages of inverse polarities are maintained on the separator plates. This scheme has the disadvantage that the deflection section becomes more complicated. With some alternative techniques, no pairs of separator plates are necessary. For example, by a proper relative phasing of the inverse polarity voltage ramps applied to the sweep and compensating deflectors, a net d.c. voltage increment of $\pm\Delta V, 0$ can be established on the top/bottom and central pairs of compensating plates. A variation of this method is to match the phases of the applied voltages to the sweep and compensating deflectors, but to maintain suitable d.c. bias voltages on the top and bottom pairs of compensating plates. In all these cases, a staircase voltage waveform would be applied to a pair of shift plates orientated orthogonally to the other deflectors so that a sequential format of "triplet" frames would be displayed on the phosphor screen.

Another quite distinct practical approach to the framing operation is also under serious consideration. In this, the deflector network is further simplified by replacing the multiplex aperture plate and the three sets of compensating deflectors by a single aperture and just one pair of deflectors. A symmetrical triangular waveform is applied to the sweep plates so that two short exposures of the electron beam are obtained. The application of a suitably de-phased inverse triangular waveform to the compensation plates then leads to the display of two discrete framed images at the screen. Shift plates would still be included so that a sequence of "doublet" frames could be produced.

The following simplified qualitative analysis of the framing operation can be applied for both of the practical systems that have just been outlined. The streak speed v due to the sweep plates is given by

$$v = KS \tag{1}$$

where K denotes the slope of the streak voltage waveform (Vs^{-1}) and S denotes the deflection sensitivity of the sweep plates at the aperture plate (cm V^{-1}). For a parallel plate deflection network then:[11]

$$S = \frac{l\left(\frac{l}{2} + L\right)}{2dV} \tag{2}$$

the dimensions are as shown in figure 2 and V is the anode/screen voltage. If the diameter of an aperture in the aperture plate is, a, then the exposure time of each frame

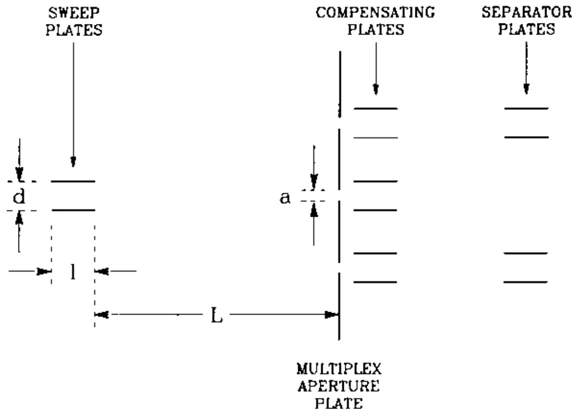

Figure 2. Deflection section geometry.

(T) is given by:

$$T = {}^{a}/v \tag{3}$$

and from equations (1), (2) and (3), we have:

$$T = \frac{2Vad}{Kl(^{l}/2 + L)} \qquad (4)$$

The obvious implications are that to obtain the shortest exposures it is required that for a particular operating anode/screen potential, V, (i) the speed of the streaking voltage ramp should be a maximum (e.g. use of Auston switches, [12,13]) (ii) the aperture size a, and plate separation d, should be small and this demands that an extended narrow waist must exist in the electron beam and,(iii) the distance L from the sweep plates and the aperture plate should be as large as possible. The length of the sweep plates can be selected by taking the structure of the compensation plates into consideration.

Theoretically predicted performance

The electron-optical system depicted in figure 1 has been designed and preliminarily analysed with the aid of a suite of computer programs. Computed results show that the beam cross-over is positioned $\sim$45 mm from the anode aperture. For an object size of 6 mm x 6 mm on the photocathode, L can be approximately 60 mm and the diameter of the electron beam is 1.8 mm at the aperture plate as indicated in figure 3. The overall electron-optical magnification of the tube is 1.5 and in the static or focus mode of operation the spatial resolution is expected to be $\sim$40 lp/mm at the screen (see figure 4).

In the framing mode of operation, the exposure time for each frame has been calculated to be $\sim$90 ps at a framing rate in excess of 3×10^9 frames s^{-1} by assuming that a streak speed of 2×10^9 cms^{-1} can be realized at the aperture plate. It is expected that under dynamic conditions, space charge effects, deflection-induced aberrations and non-perfect voltage waveforms applied to the deflection system will reduce the spatial resolution significantly below the static value. We would therefore predict that in the practical device, the spatial resolution at the screen should be $\gtrsim$10 lp/mm.

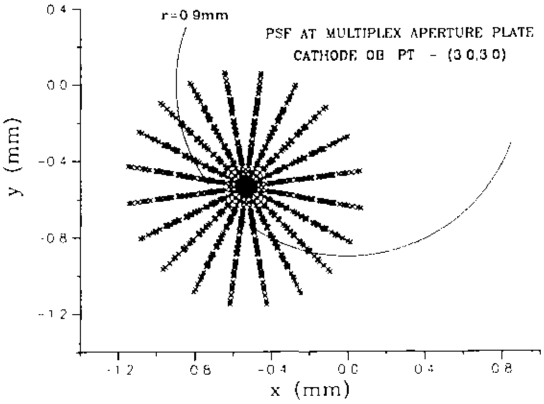

Figure 3. Point spread function.

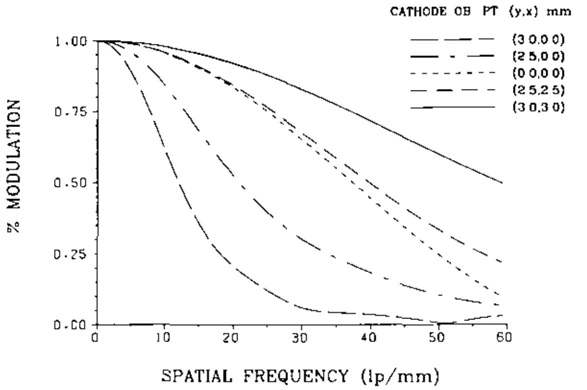

Figure 4. Static mode modulation transfer functions.

Acknowledgements

The financial support of the Paul Instrument Fund of the Royal Society of London and the Science and Engineering Research Council are acknowledged. One of us (MRB) was supported by an SERC CASE Studentship in collaboration with Thorn EMI Electron Tube Division, Ruislip, and another (HN) was supported by the Chinese Academy of Sciences.

References

1. Key M.H., "Some Topical Issues in Research on Short-Pulse Laser-Produced Plasmas", Phil. Trans. R. Soc. Lond. A., Vol. 298, pp. 351-364. 1980.
2. Richardson M.C. and Sala K., "Picosecond Framing Photography of a Laser-Produced Plasma", Appl. Phys. Lett., Vol. 23, pp. 420-422. 1973.
3. Cheng J.C., Multhauf L.G. and Tripp G.R., "Fiber Array Technique for Subnanosecond X-ray Framing Camera", Proc. 12th I.C.H.S.P., pp. 218-222. 1976.
4. Kalibjian R., "Optical/X-ray Framing Camera Tube", Proc. 12th I.C.H.S.P., pp. 269-274. 1976.
5. Kalibjian R. and Coleman L.W., "Framing-Camera Tube Development for the Sub-100 ps Range", Proc. 13th I.C.H.S.P.P., pp. 447-451. 1978.

6. Lieber A.J. and Sutphin H.D., "Picosecond Framing Camera Using a Passive Microchannel Plate", *Appl. Opt.*, Vol. 18, pp. 745-746. 1979.

7. Laviron E. and Delmare C., "Realization of an Image Converter with a 300 ps Exposure Time", *Proc. 9th I.C.H.S.P.*, pp. 198-201. 1970.

8. Niu H., Chao T. and Sibbett W., "Picosecond Framing Technique Using a Conventional Streak Camera", *Rev. Sci. Inst.*, Vol. 52, pp. 1190-1192. 1981.

9. Walters F., Chippendale R.A. and Brown R.P., "A Time-Resolving Image Converter", *Proc. 6th I.C.H.S.P.*, pp. 357-361. 1962.

10. Huston A.E., "A Multi-Frame Image Tube Camera", *Proc. 7th I.C.H.S.P.*, pp. 93-96. 1965.

11. Klemperer O., *Electron Optics*, Cambridge University Press. 1953.

12. Auston D.H., "Picosecond Optoelectronic Switching and Gating in Silicon", *Appl. Phys. Lett.*, Vol. 26, pp. 101-103. 1975.

13. Margulis W., Sibbett W., Taylor J.R. and Bradley D.J., "Reduction of Jitter in Streak-Camera Synchronization with Picosecond Laser Pulses", *Opt. Commun.*, Vol. 32, pp. 331-333. 1980.

Femtosecond streak image tube

W. Sibbett, H. Niu,* M. R. Baggs
Optics Section, Blackett Laboratory, Imperial College
Prince Consort Road, London SW7 2BZ, England

Abstract

Some design features and performance characteristics of a Photochron IV femtosecond streak image tube are presented. A more compact miniaturised version of the tube is also described and results from a preliminary theoretical evaluation of its performance are discussed.

Introduction

The direct[1,2] and indirect[3] generation of hypershort light pulses having durations below 100 fs have now made it possible to undertake time-domain studies in a femtosecond regime.[4] Although nonlinear measurement techniques based on autocorrelation, sum-frequency mixing etc,[5] have the adequate subpicosecond resolution, interpretation of the results can lead to serious uncertainties. In their present state of development, streak cameras have instrumental functions ≲1 ps in both single-shot[6] and synchroscan[7] modes of operation. They also possess the unique advantages of sensitivity and linearity of response over a wide spectral range (X-rays - NIR) and have an added facility for the simultaneous display of spectral/spatial versus temporal variations in intensity.[8] To further improve the time resolution of streak cameras, we have carried out extensive theoretical studies of the design and streak operation of image tubes.

The initial research was concentrated on the investigation of an electron-optical arrangement in which the photoelectron time dispersion would be small and which had the capability to provide high spatial resolution when space charge effects and the interactive dynamic influence of the deflection field were neglected. A time resolution ~200 fs was estimated for a preliminary design of tube (Photochron III[9]) in which the conditions of low initial photoelectron energy spread (0.1 eV FWHM) and fast streak velocity of 5×10^{10}cms^{-1} were assumed. However, in subsequent detailed theoretical analyses, when the importance of (i) the influence of space charge in respect of intensity-dependent temporal broadening of streak images[10] and (ii) a more realistic method (involving MTF) for evaluating temporal and spatial resolution[11] was confirmed, it was concluded that substantial re-design was necessary to ensure that femtosecond resolution could be achieved with useful dynamic range. The space charge effects which usually limit the dynamic range of picosecond and subpicosecond streak tubes can readily dominate in the post-mesh region[10] and these have been controlled in our new design (Photochron IV) by arranging that consistently high potentials and electric fields are maintained throughout the photocathode-to-anode section. It has also been significant that from our study we have established that an optimum streak speed exists for which the best temporal resolution can be achieved. For speeds above this value, the time resolution is observed to deteriorate quite rapidly.[11]

In this paper we have summarised the design features of the Photochron IV streak tube and some theoretical and experimental data are presented for the visible wavelength system, together with the predicted performance of X-ray camera tubes. A miniaturised version of the new tube (designated as the Photochron IV-M) which has been designed to have a similar physical length to that of the Photochron II, is also described and its theoretically predicted performance is compared to that of the standard size Photochron IV.

Photochron IV streak tube

The design and construction of the tube are illustrated photographically and schematically in figures 1 and 2 respectively. Because details of the electron-optical configuration and predicted performance have been presented elsewhere,[12] only a brief in-context description will be given here. A planar geometry for the photocathode and mesh have been retained, but the electron-lens arrangement is substantially different from the earlier Photochron I, II streak tubes. The four cylindrical electrodes in the pre-deflection section constitute two interdependent electron lenses that permit convenient optimisation of both static and dynamic characteristics.

When the maximum energy of the initial photoelectrons emitted at the cathode is assumed to be 0.6 eV, it has been shown from temporal modulation transfer functions that the time resolution is less than 0.5 ps at the optimum streak speed of 3×10^{10} cms^{-1}.[12] For illuminating wavelengths closer to the photosensitivity threshold of the cathode, the energy spreads are smaller (e.g. 0.2 eV) and a time resolution <0.2 ps should be achieved.

*Permanent Address: Xian Institute of Optics & Precision Mechanics, Xian, China.

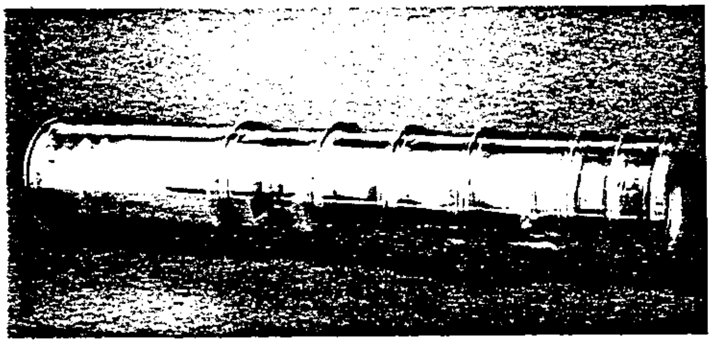

Figure 1. Photograph of the Photochron IV.

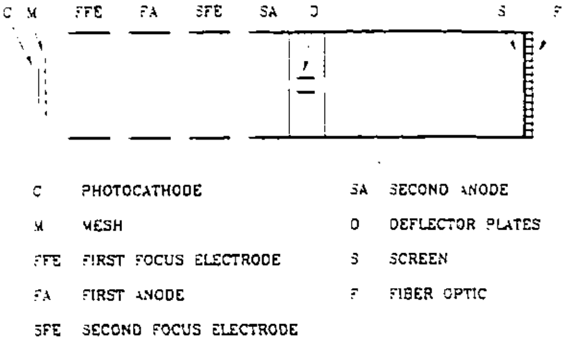

Figure 2. Schematic of the Photochron IV.

An experimental Photochron IV streak tube has been constructed and processed with an S20 photocathode. When operated at the voltages indicated in Table 1, the measured magnification and static spatial resolution at the phosphor screen are x2.1 and 33 lp/mm respectively. These are in excellent agreement with the predicted values.[12]

Table 1. Electrode voltages.

Electrode / Voltage (kV) / Image tube	P	M	FFE	FA	SFE	SA/S
Photochron IV	-18	-8	-10	+6	-13	0
Photochron IV-M	-18	-8	-10.5	+6	-12.3	0

A preliminary evaluation of the tube performance under the conditions of repetitive streak operation at 164 MHz has also been carried out, using the same passively mode-locked CW ring dye laser and basic experimental set-up that were employed for the Photochron IIA studies described in another paper at this conference.[7]

The intensity profiles of a pair of recorded streak images are reproduced in figure 3. In obtaining this result the applied RF power was 9W and the observed streak velocity was 4×10^9 cms^{-1}. (It is noteworthy that an RF power of 20W was required to produce a streak velocity of 4.5×10^9 cms^{-1} in the standard Photochron II, so the power efficiency of the Photochron IV is higher by a significant amount). The electric field between the mesh and photocathode of the S20 tube was restricted to 25 kV cm^{-1} in this first experimental version. Using our MTF method, the instrumental function of the camera at the laser wavelength of 615 nm and the above streak speed, was calculated to be 1.0 ps. This is in relatively good agreement with the preliminary streak duration measurement of 2.2 ps. The difference probably arose in the operation of the laser at less than optimum conditions.

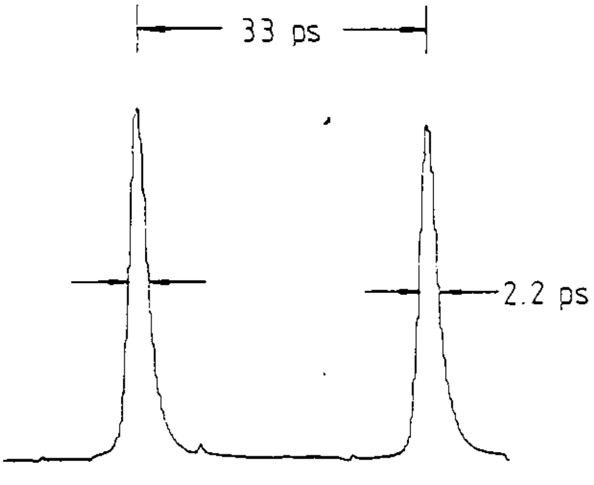

Figure 3. Recorded streak images.

When the streak tube has a gold photocathode which is illuminated by ~1 keV X-rays, then the expected energy spread in the initial photoelectrons is likely to be ~5 eV.[13] Under these conditions, it can be seen from the computed temporal modulation transfer function (see figure 4) that the performance of the Photochron IV is markedly superior to the Photochron II. Moreover, it has been calculated[12] that subpicosecond resolution at X-ray wavelengths could be achieved by doubling the usual electric field at the photocathode to 100 kV cm^{-1}. It is also worth noting that in applications where it is desirable to have maximum dynamic spatial resolution along the slit, the plane of the screen can be repositioned (+6 mm from plane for optimum temporal resolution) in such a way that the available spatial resolution is enhanced (see table 2) while the temporal resolution is only degraded to ~10% below the optimum value.

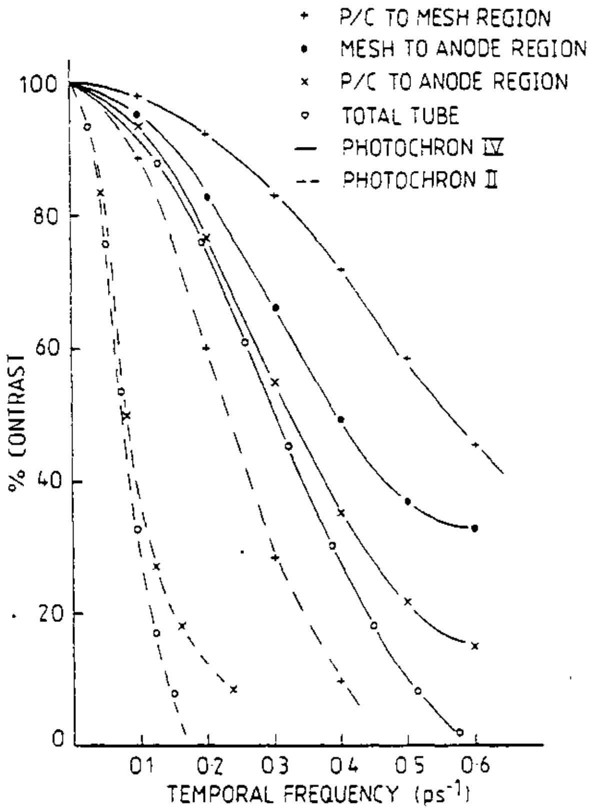

Figure 4. X-ray temporal modulation transfer functions.

Miniaturised Photochron IV (Photochron IV-M)

One possible short-coming of the Photochron IV is its physical size in that it may be too large for incorporation into a restricted diagnostics volume. This would be problematical, for example, in respect of an X-ray version of the tube that might be partially or fully enclosed in an evacuated (X-ray) target chamber. For this reason, we have investigated the performance of a miniaturised version called the Photochron IV-M which has an overall length that is comparable to that of the Photochron II.[14]

The electrode configuration of the Photochron IV-M has essentially the same format as the full-size counterpart, but the operating voltages and dimensions of the electrodes are somewhat altered as indicated in tables 1 and 2. Also included in table 2 are some comparative data which relate to the predicted performance characteristics of the two sizes of streak tube, where in both cases the electric field at the cathode is 50 kV cm^{-1}.

Table 2. Photochron IV tube characteristics.

Tube Characteristic	Photochron IV	Photochron IV-M
Length (mm)	395	274
Diameter (mm)	42	30
Magnification	-2	-2.2
Deflection sensitivity (cm kV^{-1})	3	2.5
Static spatial resolution at cathode (lp/mm)	60	60
Optimum temporal resolution (ps) ($\Delta\varepsilon$=0.6eV)	0.34 (on axis @ z=395mm)	0.27 (on axis @ z=274mm)
Optimum dynamic spatial resolution (lp/mm) in slit direction	>50 (on axis @ z=401mm)	>50 (on axis @ z=299mm)
Temporal distortion (ps) (r=2mm)	0.77	1.1
Dynamic range (τ_p=3ps, τ_r=2ps)	911	1700

The limiting static spatial resolution of both has its dependence on factors such as the cell density of the mesh, the alignment of the electrodes and the quality of the phosphor screen. It can be seen from the results presented in table 3 that the photoelectron temporal dispersion component of the overall time resolution of the Photochron IV-M is smaller and increases less markedly with slit height.

Table 3. Temporal dispersion

Temporal Dispersion (ps) \ Tube Slit height (mm)	Photochron IV	Photochron IV-M
0	0.26	0.24
1	0.31	0.26
2	0.35	0.29
3	0.45	0.34
4	0.51	0.40
5	0.60	0.41

This lower temporal dispersion is also reflected in the predicted dynamic range which is significantly higher for the miniaturised tube. The supplementary data for temporal distortions (or dynamic slit curvature) given in table 4 indicate the degree to which this facility of the Photochron IV-M is deficient to the standard-size counterpart. In order to minimise this effect, it would be necessary to limit the spatial extent of the slit image on the photocathode (or actual slit photocathode) to ~2mm.

Table 4. Temporal distortion.

Temporal Distortion (ps) \ Tube Slit height (mm)	Photochron IV	Photochron IV-M
1	0.20	0.28
2	0.77	1.1
3	1.72	2.4
4	3.08	4.3
5	4.76	6.8

In general, it may be concluded from the results of these studies that the overall performance of the miniaturised tube is comparable with that of the larger version. Thus, in all aspects, with the exception of deflection sensitivity, its performance is clearly superior to that of the Photochron II. It is therefore planned to continue our theoretical and experimental evaluation of both the Photochron IV and the more compact Photochron IV-M.

Acknowledgements

The financial support of the Paul Instrument Fund of the Royal Society and the Science and Engineering Research Council is gratefully acknowledged. One of us (MRB) was supported by an SERC CASE Studentship in collaboration with Thorn EMI Electron Tube Division, Ruislip, and another (HN) was supported by the Chinese Academy of Sciences. We would also wish to thank Dr. M. Adams and Mr. P. Grigg for their major contribution towards the construction of the experimental Photochron IV streak tube and particular thanks are due to Dr. W.E. Sleat and Mr. P. May for their assistance during the streak evaluations.

References

1. Fork R.L., Greene B.I. and Shank C.V., "Generation of Optical Pulses Shorter than 0.1 ps by Colliding Pulse Mode-Locking", Appl. Phys. Lett., Vol. 38, pp. 671-672. 1981.
2. Mourou G.A. and T. Sizer II, "Generation of Pulses Shorter than 70 fs with a Synchronously-Pumped CW Dye Laser", Opt. Commun., Vol. 41, pp. 47-48. 1982.
3. Shank C.V., Fork R.L., Yen R. and Stolen R.H., "Compression of Femtosecond Optical Pulses", Appl. Phys. Lett., Vol. 40, pp. 761-763. 1982.
4. Halbout J.-M. and Tang C.L., "Time-Resolved Observation of the Nonlinear Refractive Index of Molecular Liquids by Femtosecond Interferometry", Appl. Phys. B., Vol. B28, pp. 144-145. 1982.

5. Ippen E.P. and Shank C.V., *Ultrashort Light Pulses*, Ed. S.L. Shapiro, Topics in Applied Physics, Vol. 18, Springer-Verlag. 1977.

6. Bradley D.J. and Sibbett W., "Subpicosecond Chronoscopy", *Appl. Phys. Lett.*, Vol. 27, pp. 382-384. 1975.

7. Sibbett W., Sleat W.E., Taylor J.R. and Willson J.P., "Internally Intensified Photochron II Streak Tube", published in these proceedings.

8. Willson J.P., Sibbett W. and May P.G., "Synchroscan Streak Camera Measurements of Mode Propagation in Optical Fibres", to be published in "*Picosecond Phenomena III*", Ser. Chem. Phys., Springer-Verlag. 1982.

9. Bradley D.J., Jones K.W. and Sibbett W., "Picosecond and Femtosecond Streak Cameras: Present and Future Designs", *Phil. Trans. R. Soc.*, Vol. A298, pp. 281-285. 1980.

10. Niu H. and Sibbett W., "Theoretical Analysis of Space-Charge Effects in Photochron Streak Cameras", *Rev. Sci. Instrum.*, Vol. 52, pp. 1830-1836. 1981.

11. Niu H., Sibbett W. and Baggs M.R., "Theoretical Evaluation of the Temporal and Spatial Resolutions of Photochron Streak Image Tubes", *Rev. Sci. Instrum.*, Vol. 53, pp. 563-569. 1982.

12. Sibbett W., Niu H. and Baggs M.R., "Photochron IV Subpicosecond Streak Image Tube", *Rev. Sci. Instrum.*, Vol. 53, pp. 758-761. 1982.

13. Attwood D.T. and Coleman L.W., "Picosecond X-ray Spectral Studies", *Proc. 12th ICHSP*, pp. 318-324. 1976.

14. Bird P.R., Bradley D.J. and Sibbett W., "The Photochron II Streak Camera", *Proc. 11th ICHSP*, pp. 112-117. 1974.